Aluminum Surface and Bulk Nanocomposites

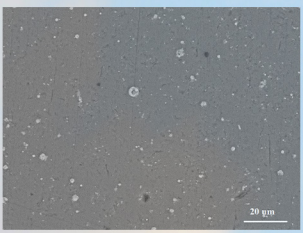

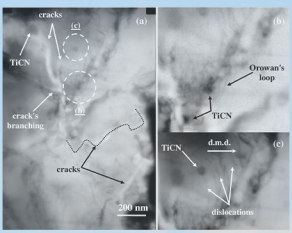

Rumyana Lazarova
Lubomir A. Anestiev

Aluminum Surface and Bulk Nanocomposites

Aluminum Surface and Bulk Nanocomposites

By

Rumyana Lazarova
and Lubomir A. Anestiev

Cambridge
Scholars
Publishing

Aluminum Surface and Bulk Nanocomposites

By Rumyana Lazarova and Lubomir A. Anestiev

This book first published 2022

Cambridge Scholars Publishing

Lady Stephenson Library, Newcastle upon Tyne, NE6 2PA, UK

British Library Cataloguing in Publication Data
A catalogue record for this book is available from the British Library

ISBN (10): 1-5275-8343-0
ISBN (13): 978-1-5275-8343-6

TABLE OF CONTENTS

Part I: Production and Investigation of Surface and Bulk Nanocomposites

PART I:
PRODUCTION AND INVESTIGATION OF SURFACE AND BULK NANOCOMPOSITES

RUMYANA LAZAROVA

I dedicate my research work to the Metropolitan of Triaditsa – His Eminence Photiy and my cleric - His Reverence Stefan (Andonov) as an expression of gratitude for the care, they make for my soul.
Prof., Ph.D. Rumyana Lazarova

PREFACE TO PART I

The terms “metal-matrix composite” and “metal-matrix nanocomposite” are defined in the general introduction to this part. Laboratory methods for obtaining bulk and surface nanocomposites with an aluminum matrix are considered. The possibilities for industrial production of bulk aluminum nanocomposites are also briefly clarified. The application of aluminum nanocomposites, which comes down mainly to the replacement of aluminum microcomposites by them, is discussed.

The second chapter is devoted to surface nanocomposites obtained by incorporating nanoparticles in a substrate of aluminum and piston alloy using electron beam treatment. The improvement of the surface’s properties is due to the presence of hard nanoparticles, which take in the external load and prevent the dislocation movement in the matrix.

The third chapter describes a method for the preparation of bulk nanocomposites with an aluminum matrix consisting of cold isostatic pressing and hot extrusion of aluminum powders containing different amounts of nanoparticles. It is found out that the main strengthening mechanism in the investigated nanocomposites is the Orowan mechanism.

The fourth chapter is devoted to the formation of the nucleus and microstructure in an aluminum nanocomposite reinforced with TiCN nanoparticles. The dependence of the rate of nucleation in aluminum on the size of nanoparticles with a cubic shape was determined. The process of growth and modification of dendrites and silicon crystals in aluminum alloy is described. The process of microstructure formation in a sample of AlSi12Cu2NiMg alloy subjected to electron beam treatment was simulated using the MAGMASOFT® software. Conclusions are made in the fifth chapter.

The first part of the book is intended for several groups of readers: researchers working on the development and research of nanocomposites based on aluminum and metal in general, university professors of metal science and materials science, students and Ph.D. students in materials science, metal science, nanosciences and nanotechnologies, manufacturers of metal-based nanocomposites and all readers who are interested in surface and bulk metal-based nanocomposites.

ACKNOWLEDGMENTS

This part of the book was financially supported by the Fund "Scientific Researches" at the Ministry of Education and Science, Bulgaria, Contract DH07/16.

About the Author

Dr. Rumyana L. Lazarova is a Professor of Materials Science at the Institute of Metal Science, Equipment and Technologies with Hydro- and Aerodynamics Centre (IMSETHAC), at the Bulgarian Academy of Sciences (BAS). She received her master's degree in engineering from the Technical University – Sofia, Bulgaria, and her Ph.D. degree from the Bulgarian Academy of Sciences. In 1995 Dr. R. Lazarova joined the department of Materials testing and Analysis at the Institute of Metal Science and Technology, BAS (the predecessor of IMSETHAC). During her employment at that time, Dr. R. Lazarova worked on several projects in materials science. From 1999 to 2000 she was a scholarship holder at UCL Louvain-la-Neuve, Belgium. Her research interests are currently focused on graphene-reinforced aluminum nanocomposites.

She is the author of over 110 scientific publications.

CHAPTER I-1

GENERAL INTRODUCTION

RUMYANA LAZAROVA

1.1 Aluminum matrix nanocomposite: definition and general characterization

The concept of composite material is sufficiently known and clarified in modern material science [1, 2, and 3]. It is assumed that "any material consisting of two or more components" with "distinct boundaries" between them and "different properties" is a composite material [3]. With greater precision, we could define it as follows:

- Composite material contains two or more chemically separate phases;
- The quantity, form, and distribution of the constituents are controlled in a predetermined manner during the composite manufacturing;
- The composite has unique properties, which are determined by the quantity, shape, and distribution of phases through the principles of mechanics.

The composite usually consists of base or matrix material which as a rule is homogenous and isotropic. Its properties and behavior could be described by the mechanics of conventional materials. The properties and the behavior of the matrix are improved by filling it with particles, fibers, or plates of another material which is named filler or reinforcement.

Metal matrix composites (MMCs) are divided into three groups: *particle reinforced*, *short fiber-reinforced,* and *continuous fiber-reinforced MMCs*. Particles contained in the first category MMCs are ranging from 10 nm up to 500 μm. **MMCs with a uniform dispersion of particles in the range of 10 nm to 1 μm are named — Metal Matrix Nanocomposites (MMNCs)**. On this basis, **nanocomposites can be defined as composites in which the filler has dimensions in the nanometric range (1 nm = 10^{-9} m)** [4]. This category includes nanocomposites with ultrafine particles. These are particles that are less than 100 nm in diameter. MMNCs possess more outstanding properties than MMCs which overcome the disadvantages

of MMCs for example poor ductility, low fracture toughness, and machinability.

The classification of nanomaterials can be made based on numerous characteristics. The main feature is the nature of the constituents - organic or inorganic. The second characteristic could be the dimensionality of constituents – one, two, or three-dimensional.

We investigate the case in which one constituent is a three-dimensional matrix and the other one represents nano-sized particles distributed in the matrix. The chemical nature of the matrix is metallic and the nanoparticles play the role of reinforcement - ceramic. That means metal matrix nanocomposite (MMNC) is a combination of metal matrix and nano-sized reinforcement (usually ceramics) [5]. Generally, MMNCs are metals reinforced with other metal, ceramic or organic compounds with nano-dimensions.

Metal matrix nanocomposites (MMNCs) consist of a ductile metal or alloy matrix in which nano-sized reinforcement material is incorporated. These materials combine metal and ceramic features - ductility and toughness with high strength and hardness. Because of the nano-metric size of the reinforcement phase, the interaction of particles with dislocations becomes of significant importance for strengthening and, when added to other strengthening effects typically found in conventional metal matrix composites (MMCs), leads to a significant improvement of mechanical properties [6-10].

The references on a micrometric particle in MMCs show that although micrometric dispersion is easier to achieve, these composites are less effective in strengthening compared to MMNCs. For example, the tensile strength of 1 vol. % Si_3N_4 (10nm) – aluminum MMNC is comparable to that of 15 vol. % SiCp (3.5μm) – aluminum MMC, while the yield stress of the MMNC is significantly higher than that of the micrometric particle dispersed MMC [11]. Moreover, particles larger than 1.5μm act as micro concentrators and cause cleavage between them and the matrix. Particles with dimensions between 200 and 1500 nm cause the formation of cavities and pits due to their poor interphase cohesion. But particles with a size less than 200 nm bond well with matrix and so that determine excellent mechanical properties of MMNCs [12]. We could conditionally assume that MMNCs have one-dimensional reinforcements because the particles have sizes below 200 nm, unlike MMCs in which the reinforcements are except particles with dimensions above 200 nm and fibers and plates.

Due to their nano-dimensionality, the particles that serve as reinforcements in MMNCs have special properties that need to be highlighted.

When the particle size is brought down to the nanometric length scale, surface energy is increased by three orders of magnitude [13]. This engenders instability in a gas-liquid-solid system, the Gibbs energy of which, is described by the following equation:

$\Delta G = (\mu G(T,P) - \mu L(T,P)) + \gamma_{LG}\,\Delta S_{LG} + \gamma_{SG}\,\Delta S_{SG} + \gamma_{SL}\,\Delta S_{SL}$,

where T is the temperature, P the pressure in the liquid, μG and μL the chemical potentials of gas and the liquid, and ΔS is the change in interfacial areas and γ surface energies.

In this situation, agglomeration of nanoparticles, which provides a smaller interfacial area, is proving to be an energy-efficient phenomenon: several nano-particle clusters in one microagglomerate.

The dynamics of the relative motion of two nano-sized particles have been extensively studied [14]. Due to the complexity of the problem, the analysis is usually limited to two main mechanisms: Brownian diffusion and inter-particle forces (electrostatic and Van der Waals).

Brownian diffusion, which is identified with aggregation limit factor, ensures the continuous collision between particles. The magnitude of the displacement follows a Gaussian statistic distribution according to the relation:

$$\theta = \frac{-Ar}{12H^2}$$

where A is the Hamaker constant, which depends on the polarization properties of the molecules on the particle surface, r is the reduced particle radius, and H the inter-particle distance [14]. When the particle dimension is smaller than 1 μm, Van der Waals's forces dominate. Coulomb's force of repulsion competes with Van der Waals force of attraction. The Van der Waals attraction force overcomes the electrostatic repulsion for an inter-particle distance down to 1 nm. For smaller values, the Born repulsion of adjacent electron clouds dominates [15].

The essential for an effective load transfer from the matrix to the particle and for delaying the onset of particle-matrix decohesion is the good interface bonding between particles and matrix.

Thus, MMNCs are suitable for the production of materials with high strength in shear-compression processes and wear resistance. They show extraordinary potential for application in many areas, such as the aerospace and automotive industries and the development of structural materials [16].

The matrix of composites we study is aluminum. Aluminum and aluminum alloys are of interest as parent metals in MMNCs. Commonly used reinforcements are carbides, borides, nitrides, and oxides, i.e, SiC, TiC, TiCN, Al_2O_3, WC, TiB_2, and others. The effectiveness of the

nanoparticles is expressed normally only between 0.5 and 5% addition by weight, but sometimes it reaches 10-15%.

The result of the addition of nanoparticles is a drastic improvement in properties such as mechanical strength, toughness, hardness, and wear resistance.

By surface aluminum nanocomposites we mean thin coatings or surface layers of nanocomposite on an aluminum substrate. Depending on whether the aluminum nanocomposite is bulk or surface, its purpose as a machine part in modern engineering could be different.

There are many applications in which only surface properties play an important role for example wear resistance. In this situation, only the surface layer needs to be reinforced by ceramic phases while the bulk of the component should retain the original composition and structure with higher toughness. There are several methods to fabricate particulate reinforced nanocomposites to create functional surfaces as well as many methods for the production of bulk metal nanocomposites. Below we have considered the possibilities for obtaining metal nanocomposites.

1.2 Methods for nanocomposites producing

1.2.1 Methods for bulk nanocomposites producing

There are two categories of metal matrix composites, respectively nanocomposites, depending on the manufacturing process: ex-situ and in-situ. Ex-situ composites are obtained when the reinforcement is externally added to the matrix. In-situ fabricated metal matrix composites are characterized by the production of reinforcements within the matrix during the fabrication process.

On the other side, the methods for metal matrix nanocomposites manufacturing could be classified depending upon the matrix state during the production process, which can be molten or solid [1, 17-20].

Solid-state processing

Solid-state processes for fabrication of bulk nanocomposites relate to powder metallurgy. This method provides better wetting of the nanoparticles and a better matrix-reinforcing particle bond. Furthermore, this processing route can incorporate a higher volume fraction of reinforcement.

- **High energy ball milling**

The raw materials are breaking up into nano-scale sizes and mixed then utilizing rotation and vibration of ball milling machine. The obtained

product is a pure element, alloy, or nano-composite powder. For producing bulk nano-materials hot extrusion or hot isostatic pressing could be used then.

- **Powder metallurgy (powder blending and consolidation)**

Powder metallurgy (PM) is a manufacturing approach, in which many kinds of powder technology can be used [21]. The constituent processes of this route are: blending matrix and reinforcing powders; compacting the blend, usually by cold pressing; degassing the compacted product to remove water vapor and gases; consolidation of the slugs by one of the following methods: direct sintering, hot isostatic pressing, vacuum hot isostatic pressing, hot extrusion, and cold sintering.

Nano-sized particles are manufactured first and then mixed with metal matrix powders. The next processes are used for obtaining a bulk product [22]. Powder metallurgy is a very attractive technique as it employs lower temperatures and thus, ensures better control of interface kinetics.

Powders of aluminum or aluminum alloy are blended with the nano-reinforcement. Blended powders are then compacted into a 'green form', using uniaxial pressing or cold isostatic pressing. The green body thus obtained is approximately 80% dense. The green body is heated usually in an inert atmosphere to a desired processing temperature to obtain a sintered body [23]. The sintered body has a 100% theoretical density.

- **Severe plastic deformation**

Severe plastic deformation (SPD) is a method by which nano-structured materials are fabricated. Extremely large refinement of the microstructure can be achieved through it. The refinement is expressed by structure elements size reduced into sub-micron or even nano-scale. This is obtained by the very large strains imposed on the specimen at a temperature usually less than the temperature of recrystallization. High densities of crystal lattice defects (particularly dislocations) are created as a result and form nano-sized grains and subgrains.

The two main fabrication routes for SPD are severe plastic torsional straining (SPTS) under high pressure and equal channel angular pressing (ECAP).

- **Mechanical alloying**

The blending of the powders in the traditional PM occurs without material transfer between the mixed components. It is possible, however, to incorporate hard ceramic particles into the matrix powder particles through a solid-state bonding [24] which performs a mechanical alloying. This process could be determined also as cold welding between the different types of particles. Mechanical alloying could be defined as a solid-state powder processing technique consisting of repeated cold

welding, fracturing, and rewelding of powder particles in a high-energy ball mill. Many types of aluminum-based nanocomposites were produced by this method for example Al–AlB_2, Al–Al_4C_3, Al–Al_xMo_y, Al–AlN, Al–Al_2O_3, Al–Al_3Ti, Al–BN, Al–C, Al–$CuAl_2$, Al–MgB_2, Al–SiC and Al–TiC [25].

- **Microwave and bi-directional hybrid microwave sintering**

These processes are based on the conversion of electromagnetic energy into thermal energy, which is rapidly and highly efficiently spreading. The heat is generated from within the powders and radiates outward due to the penetrative power of the microwaves. Higher temperatures exist at the core of sintered materials whereas the surfaces demonstrate lower temperatures. Because of that, the variation in microstructure along the thickness of the sample is observed which results in bad properties. This problem is resolved by using bi-directional hybrid microwave sintering, wherein microwave susceptors such as SiC particles/rods assist in the reduction of thermal gradient during sintering.

Semi-solid state processes

Semi-solid processes consist of shaping a partially solid mixture in which the solid fractions are between 20 and 60 % [20]. The advantages of these processes are low shrinkage and porosity, non-turbulent filling, and lower processing temperature. They can be divided into two main groups: thixo-processes and rheo-processes (compocasting). The thixo-processes use solid feedstock which is partially melted. The base material is obtained by partially solidifying a liquid melt under controlled conditions for inducing the formation of crystals in the slurry [20]. The thixo-processes need to be adapted and optimized for the production of metal matrix nanocomposites. The authors of [20] consider **thixoprocessing** as a key technology for the industrial scaling up of MMNCs production because significant effects on properties can be obtained at low volume fractions of particles. The prewetted feedstock, which can be prepared in several methods, allows handling nano-reinforcement on a smaller volume scale before diluting the master composite in a larger metal volume. Further research is needed for synthesizing the nanocomposites in an industrial process to utilize these promising materials in various applications. The rheocasting could be combined with squeeze casting for the production of aluminum nanocomposites reinforced with nanoparticles [26].

Liquid State Processes

Liquid state processing routes for MMNCs producing are relatively simple, cost-effective, and suitable for industrial use. These routes are as follows:

- **Stirring techniques**

It is indisputable that the **stir casting process** is a suitable method for micron-size reinforcement composites producing, but for nano-sized reinforcement's composites fabrication, it poses an especially great difficulty – the dispersion and uniform distribution of nanoparticles in industrial-scale melts due to the large surface-to-volume ratio [27].

The nanopowders are very often added to the liquid matrix and distributed in it by applying mechanical stirring through an impeller. Because of the poor wettability of nanoparticles within the molten metal and their tendency to agglomerate, it is usually difficult to obtain a homogeneous distribution of the nano-reinforcement. The difficulties in mixing and wetting nano-sized particles by metallic melts require particles pre-coating or cladding with metal-protector. The as-prepared molten alloy with the dispersed reinforcing nanoparticles may be used for sand casting or permanent mold casting for obtaining a bulk nanocomposite.

- **Droplet consolidation techniques**

Droplet consolidation could be defined as a "rapid" quenching from the liquid state. The cooling rate, which is usually greater than 1 mm s^{-1} characterizes these techniques.

- **Ultrasonic assisted casting**

The characteristic feature of this method is the melt treating with ultrasonic waves to disperse homogenously the reinforcement. This method is used for the production of aluminum-based nanocomposites reinforced with different types of nanoparticles. The ultrasonic-assisted casting is considered as a method providing better matrix–particle bonding, braking nano-particle clusters, and removing impurities from the surfaceof the particles, which assures good microstructural characteristics [20]. However, the ultrasonic casting is difficult to be scaled up to the industrial level as the volumes of castings are limited to the dimension of the ultrasonic probe and power of the ultrasonic source. These limitations could be overcome if ultrasonic flow processing could be adopted. This concept was used in developing a scaled-up ultrasonic processing system, aimed to produce MMNCs at an industrial scale [20].

- **Infiltration technique**

The infiltration process consists of preparing a porous "preform" of the reinforcement and infiltration its pores with the molten metal. The flow of molten metal is driven only by the forces of capillarity i.e. pressure is

needed to overcome the resisting forces due to drag and capillary. The required pressure is a function of the friction effects due to the viscosity of the molten matrix. Wetting the ceramic preform by the liquid alloy depends on different factors like alloy composition, ceramic preform material and surface morphology, temperature, and time. The pressure/vacuum infiltration method is already a widely used method for composites with micron-size reinforcements producing. However, its use for large-scale MMNCs production depends on the preparation of nano reinforcement preform, and the parameters of the infiltration process. Due to these reasons, the large-scale production of MMNCs by pressure/vacuum infiltration requires a highly standardized process procedure with accurate control of process parameters by which an eventual preform breakage, increased porosity and/or phase segregation could be avoided.

The infiltration technique could be applied in a pressureless configuration. In this case, a spontaneous infiltration of the ceramic preform acts without the aid of externally applied pressure, nor vacuum. B. Xiong et al. produced aluminum alloy-based nanocomposites reinforced with SiC particles by combining ball-milling and cold pressing to make the preform and then used a pressureless infiltration [28 and 29].

The infiltration techniques are characterized by long infiltration times and preform costs.

- **The disintegrated melt deposition technique** has some advantages in respect to MMNCs production - fine grain size, uniform nanoparticle distribution, minimum porosity, and superior mechanical properties [30]. Since the microstructural and mechanical properties depend on parameters of this process such as the disintegrating gas velocity, distance between the melt exit stream and the substrate, etc. which have to be varied according to the dimension of the final product, the DMD process is more suitable to produce MMNC ingots to be used as precursors for making wrought products. Also, due to its set-up (see Sect. 6.2), the DMD process is difficult to be automated and to be used for continuous casting operations [30].
- **High pressure die casting**

This method consists of feeling the die cavity by the molten metal under pressure. Both filling speeds and solidification rates are relatively high. The technique is suitable to obtain detailed components. It could be used for producing nanocomposites and especially aluminum nanocomposites but there are feu works as examples for that [31 and 32].

Homogenous distribution of the nano-sized reinforcement phase is difficult to achieve using liquid-processing methods because of the difference in densities between the two components of the composite. The

poor wettability of the reinforcement by the molten metal makes mixing very difficult leading to a heterogeneous structure that affects the properties of the composite.

Combined or hybrid methods

Nanocomposites can also be produced through a combination of the based processes discussed above. Powder-metallurgy techniques are usually applied to producing the nanocomposite which further is introduced and imported into the liquid or semi-liquid metal.

- **Friction stir processing**

Friction stir processing is based on friction stir welding which is a technique for surface metal matrix production. However, in recent years, it is used as a route to incorporate nanoparticles into the metal matrix to fabricate bulk nanocomposites. A rotating tool with a shoulder and a pin are plunged into the surface of the workpiece (the desired base matrix) with grooves filled with the desired volume fraction of nanoparticles [20].

- **Accumulative roll bonding**

In essence, this process presents a severe plastic deformation allowing producing nanostructured and ultrafine-grained materials. It consists of roll bonding stacked sheets sprinkled with nanoparticles, then cutting the sheets and rolling them again after stacking the pieces over each other.

As we have seen, when considering the individual methods for preparing metal-based nanocomposites, they are currently obtained mainly in the laboratory. Their production on an industrial scale is still a significant challenge for scientists and engineers [33]. This is due to their recent development. For this reason, it is good to look briefly at the problems of each method of producing aluminum matrix nanocomposites, its use in industrial conditions, and the fabrication of an industrial product.

1.2.2 Methods for surface nanocomposites producing

When the surface of the component is required to be of higher strength, hardness, and wear resistance, and the core to maintain its plasticity and toughness, it is appropriate to apply a superficial nanocomposite. The modified or applied surface layer is named surface metal matrix nanocomposites (SMMNCs).

Fabrication of SMMCs is usually performed using surface treatment techniques such as high energy laser beam, plasma spraying, cast sinter, and electron beam irradiation which have been developed over the last decades [34].

The methods for surface nanocomposites fabricating could be classified as follows [35]:

- **Cold spray method**

Cold spraying allows the fabrication of coatings at lower temperatures than the melting points of the used materials. Thus this method avoids the deterioration phenomenon of the materials such as oxidation and decomposition as well as phase transition during the process. The obtained coatings have low porosity (<1%) and low oxygen concentration. In addition, the coatings have high strength (>280MPa) and strong adhesion (>70MPa). This method is used to produce nanocomposite coatings with metallic or alloy matrices. The nanofillers, in this case, are nitride, carbide, boride, diamond, CNT, etc. For the production of nanocomposite powders, mechanical alloying is used with metallic matrix powders and other nanoparticles.

- **CVD (chemical vapor deposition) method**

This method is usually used for fabricating coatings of inorganic matrices and inorganic nanofillers. The aerosol-assisted CVD method can be used for improving the quality of the coating.

- **PVD (physical vapor deposition) method**

This method serves to produce nanocomposite coatings of inorganic matrices and inorganic nanoparticles. In this case, the PVD method includes the processes: laser ablation, thermal evaporation, ion beam deposition, ion implantation, laser-assisted deposition, and atom beam co-sputtering technique. For nanocomposite coating with organic matrix, aerosol-assisted plasma deposition is used [36].

- **Thermal spray method**

This method is often used to make nanocomposite coatings with a matrix of metal or alloy. The spray material is a nanosized alloy powder (formed by ball milling) and dispersed in a suspension solution using suspensions to conduct plasma thermal spraying.

- **Welding techniques**

Methods for the introduction of nanoparticles during manual arc welding, electron-beam welding, MIG/MAG, and TIG welding are presented in [37 and 38]. The manners for metal microstructure modifying are in principle the same as the manners for surface nanocomposites manufacturing.

Electron beam irradiation is an advanced technique for surface modification as laser beam irradiation, ion implantation, etc. [39]. We use this technique for surface nanocomposite production. The surface aluminum matrix nanocomposites we have produced and investigated have been obtained using coating the substrate surface with a mixture

containing nanoparticles and the following electron beam scanning treatment incorporating the reinforcement in the aluminum matrix.

1.3 Application of aluminum matrix nanocomposites

The wide use of aluminum matrix composites is determined by their properties which cannot be achieved by any monolithic material. It is logical to assume that aluminum matrix nanocomposites would find similar applications as those of aluminum composites. Here we would like to recall some industrial applications of aluminum composites:

1.3.1 Application in the automotive engineering industry

Aluminum matrix composites have a great application in the automotive engineering industry for the production of valves, piston rods, pistons, piston pins; covers: cylinder heads, crankshaft main bearings; engine blocks: part strengthen cylinder blocks; brake rotors, calipers, liners, propeller shafts, connecting rods, piston rings, rear brake drums, driveshaft, engine cradles, multichip electronic module. It is due to their properties as good strength to weight ratio, high specific strength, low coefficient thermal expansion, and high thermal resistance, good damping capacities, superior wear resistance, high specific stiffness, and satisfactory levels of corrosion resistance exceptional microstructure stability at high temperatures [40].

1.3.2 Aerospace and aircraft application

The aluminum matrix composites are applied for producing: wings and supporting structures in airlines, fuselage, military aircraft and cargo, aircraft electrical ac doors, heat sinks and missile fins [19].

1.3.3 Defense industry application

Passivated aluminum composites are used for enhancing desirable characteristics for propellant applications [41].

1.3.4 Building and construction materials

Strength and stiff-propeller shafts and brake disc are fabricated.

Others as: rail transport, marine transport, electrical transmission, sports and recreation, etc. [42].

As nanoparticle reinforced MMCs show higher mechanical properties than micro-particles reinforced composites without decreasing thermal and electrical conductivity, they are ideal candidates for substituting conventional MMCs or analogous monolithic alloys in structural and electrical applications. Lightweight metal matrix nanocomposites with their high wear resistance, and thermal conductivity, could be employed in automotive industries as brake system components, as well as piston liners owning to their high wear resistance, good thermal conductivity, and low coefficient of thermal expansion or as valves owning to their high creep resistance and resistance to sliding wear [43]. Furthermore, because of the high specific strength and elastic modulus of lightweight metal matrix nanocomposites, they could find good use in the sports industry, like rackets, bicycle frames, and other components. Another field of application is in electronic devices (heat sinks and solders thanks to their thermal properties or as antennas thanks to their electrical properties and stiffness) [43].

Thus, most of the products of conventional composites can be substituted by MMNCs. These are ventral fins for aircraft and exit guide vanes in the aerospace industry. Brake system components in the automotive industry, bumper beams, and connectors, inner hood, steering knuckle, crash support beams, wheels, etc. MMNCs are ideal candidates in thermal management and electronic packaging systems such as radiator panels and battery sleeves, power semiconductor packages, black box enclosures, and printed circuit board heat sinks [20].

The next few decades will reveal the widespread use of aluminum nanocomposites in many industries.

References

1. B. Gupta et al., Aerospace Materials, S. Chand Publishing, 2002.
2. M. A. Chaudhry et al., Development, and Characterization of Nanoparticle Metal Matrix Composites: A Review, International Journal of Scientific Research and Innovative Technology, Vol. 4, No. 8; 2017.
3. Advanced Mechanics of Composite Materials and Structures (Fourth Edition), Valery V. Vasiliev, Evgeny V. Morozov, 2018, https://doi.org/10.1016/B978-0-08-102209-2.00022-0.
4. Hu H, Onyebueke L, Abatan A, Characterizing and modeling mechanical properties of nanocomposites-review and evaluation, Journal of minerals and materials characterization and engineering, 2010; 9 (04):275.

5. P. Nguyen-Tri et al. Nanocomposite Coatings: Preparation, Characterization, Properties, and Applications, International Journal of Corrosion, vol. 2018, 19 p.
6. Z. Zhang, D. Chen, Contribution of Orowan strengthening effect in particulate-reinforced metal matrix nanocomposites, Mat. Sci. Eng. A 2008, 483–484, 148–152.
7. Z. Zhang, D. Chen, Consideration of Orowan strengthening effect in particulate-reinforced metal matrix nanocomposites: A model for predicting their yield strength. Scripta Mater. 2006, *54*, 1321–1326.
8. A. Sanaty-Zadeh, Comparison between current models for the strength of particulate-reinforced metal matrix nanocomposites with emphasis on consideration of Hall–Petch effect. Mat. Sci. Eng. A 2012, 531, 112–118.
9. P. Luo, Xu McDonald, S. Palanisamy, M. Dargusch, K. Xia, A modified Hall–Petch relationship in ultrafine-grained titanium recycled from chips by equal channel angular pressing. Scripta Mater. 2012, 66, 785–788.
10. A. Mortensen, T. Clyne, Metal-Matrix Composites: Challenges and Opportunities, Materials Synthesis and Processing, pp. 210-213, https://citeseerx.ist.psu.edu/viewdoc/download?doi=10.1.1.178.6870&rep=rep1&type=pdf.
11. Y.C. Kang, S.L. Chan, Tensile properties of nanometric Al2O3 particulate-reinforced aluminium matrix composites, Mater. Chem. Phys. 85 (2004) 438-443.
12. Subhranshu Chatterjee, Amitava Basu Mallick*Challenges in Manufacturing Aluminium Based Metal Matrix Nanocomposites via Stir Casting Route, Materials Science Forum Vol. 736 (2013) pp. 72-80.
13. S. Melis, M. Verduyn, G. Storti, M. Morbidelli, J. Bałdyga, Effect of fluid motion on the aggregation of small particles subject to interaction forces, AIChE J., 45 (1383 – 1393) 1999.
14. J. Szekely, “Fluid flow phenomena in metals processing”, Academic Press 1979.
15. Takemura, Matsumoto, “Dissolution of spherical carbon dioxide bubbles in strong alkaline solutions”, Chemical Engineering Science 55, pp. 3907-3917.
16. Ceschini L. et al., Ex Situ Production Routes for Metal Matrix Nanocomposites. In: Aluminum and Magnesium Metal Matrix Nanocomposites. Engineering Materials. Springer, Singapore, 2017.

17. Nouari Saheb, Spark Plasma Sintering of Metals and Metal Matrix Nanocomposites: A Review, Journal of Nanomaterials, 2012, 13 p.
18. S. Jayalakshmi, R. Arvind Singh, M. Gupta, Synthesis of Light Metal Nanocomposites: Challenges and Opportunities, Indian Journal of Advances in Chemical Science S1 (2016) 283-288.
19. Amitesh, V. C. Kale, Aluminium Based Metal Matrix Composites for Aerospace Application: A Literature Review, IOSR Journal of Mechanical and Civil Engineering, 2015, Vol. 12, Issue 6, pp 31-36.
20. Aluminum and Magnesium Metal Matrix Nanocomposites, Lorella Ceschini et al., Engineering Materials, Springer Nature Singapore Pte Ltd., 2017.
21. He. F., Han. Q. and Jackson, M. J., Nanoparticulate reinforced metal matrix nanocomposites-a review, Int. J. Nanoparticles, 2008, Vol.1, No.4, pp.301- 309.
22. R. Casati and M. Vedani, Metal Matrix Composites Reinforced by Nano-Particles—A Review. Metals (Basel), 2014, 4(1): 65-83.
23. Garg P, Gupta P, Kumar D, Parkash O. Structural and mechanical properties of graphene reinforced aluminum matrix composites. J Mater Environ Sci 2016;7(5):1461–73.
24. Ye, J., He, J., Schoenung, J. M.: Cryomilling for the fabrication of a particulate B 4 C reinforced Al nanocomposite: Part I. Effects of process conditions on the structure. Metall. Mater. Trans. A (2005).
25. C. Suryanarayana, N. Al-Aqeeli, Mechanically alloyed nanocomposites, Progress in Materials Science 58, 2013, 383–502
26. C. D. Marini, N. Fatchurrohman, A review on the fabrication techniques of aluminium matrix nanocomposites, Jurnal Teknologi (Sciences & Engineering) 74:10 (2015) 103–109.
27. Koli, D. K., Agnihotri, G., Purohit, R.: Properties and characterization of Al-Al_2O_3 composites processed by casting and powder metallurgy routes (review). Int J Latest Trends Eng Technol 2, 486–496 (2013).
28. Xiong, B., Xu, Z., Yan, Q., et al.: Fabrication of SiC nanoparticulates reinforced Al matrix composites by combining pressureless infiltration with ball-milling and cold-pressing technology. J Alloys Compd 497, L1–L4 (2010). doi:10.1016/j.jallcom.2010.02.184.
29. Xiong, B., Xu, Z., Yan, Q., et al.: Effects of SiC volume fraction and aluminum particulate size on interfacial reactions in SiC nanoparticulate reinforced aluminum matrix composites. J Alloys Compd 509, 1187–1191 (2011). doi:10.1016/j.jallcom.2010.09.171.

30. Gupta M, Sharon NML, 2011, Magnesium, magnesium alloys, and magnesium composites, Wiley.
31. Xixi Dong et al., Advanced heat treated die-cast aluminium composites fabricated by TiB_2 nanoparticle implantation, Materials and Design 186 (2020) 108372.
32. Li, Q., Rottmair, C.A., Singer, R.F.: CNT reinforced light metal composites produced by melt stirring and by high pressure die casting. Compos Sci Technol 70, 2242–2247 (2010). doi:10.1016/j.compscitech.2010.05.024.
33. Massoud Malaki et al., Advanced Metal Matrix Nanocomposites, Metals, 2019, 9, 330; doi: 10.3390/met9030330.
34. A Thangarasu et al., Microstructure and microhardness of AA1050/TiC surface composite fabricated using friction stir processing, Vol. 37, Part 5, October 2012, pp. 579–586.
35. Phuong Nguyen-Tri, Tuan Anh Nguyen, Pascal Carriere, and Cuong Ngo Xuan, Nanocomposite Coatings: Preparation, Characterization, Properties, and Applications, International Journal of Corrosion, Volume 2018, Article ID 4749501, 19 pages, https://doi.org/10.1155/2018/4749501
36. H. G. Schild, Poly(N-isopropylacrylamide): experiment, theory and application, Progress in Polymer Science, vol. 17, no. 2, pp. 163–249, 1992.
37. Introduction of nanoparticles in the liquid phase during welding, Plamen Tashev, Publisher: Prof. Marin Drinov Publishing House of Bulgarian Academy of Sciences, 2020, ISBN: 978-619-245-065-6.
38. Maximilian Sokoluk et al., Nanoparticle-enabled phase control for arc welding of unweldable aluminum alloy 7075, Nature Communications, https://doi.org/10.1038/s41467-018-07989-y.
39. M. Rahman, J.Haider, M.S.J.Hashmi, 8.03 - Health and Safety Issues in Emerging Surface Engineering Techniques, Reference Module in Materials Science and Materials Engineering Comprehensive Materials Processing, Volume 8, 2014, Pages 35-47.
40. S. T. Mavhungu, E. T. Akinlabi, M. A. Onitiri, F. M. Varachia, Aluminum Matrix Composites for Industrial Use: Advances and Trends, Procedia Manufacturing 7 (2017), 178-182.
41. S.W. Chung, P.A. Jelliss, S.W. Buckner, G.J. Place, J.M. Laktas, Aluminum Nanocomposite Materials for Propellant Applications, TechConnect Briefs 2016, TechConnect.org,, 142-144.

42. Pulkit Garg et al., Advance research progresses in aluminium matrix composites: manufacturing & applications, Journal of Materials Research and Technology, 8 (5), 2019, 4924-4939.
43. P. K. Rohatgi and B. Schultz, Lightweight Metal Matrix Nanocomposites - Stretching the Boundaries of Metals, Material Matters, 2007, 2.4, 16.

CHAPTER I-2

SURFACE NANOCOMPOSITES ON ALUMINUM AND PISTON ALLOY SUBSTRATE

RUMYANA LAZAROVA

For the development of this chapter, we have used the following articles with the kind consent of the publishers Taylor&Francis and IOP Conference Series: 1. R. Lazarova, R. Dimitrova, Y. Murdjeva, St. Valkov, P. Petrov, *Layers obtained on aluminum by nanopowder deposition and subsequent electron beam scanning*, Materials and Manufacturing Processes, Taylor&Francis, 2018, ISSN:1532-2475, DOI:10.1080/10426914.2018.1453148, 1-5; 2. Stefan Valkov, Ruslan Bezdushnyi, Rumiana Lazarova, Rossitza Dimitrova, and Peter Petrov, *Surface modification of Al substrate with TiCN nanopowder by electron-beam treatment*, AIP Conference Proceedings 2075, 160017 (2019); https://doi.org/10.1063/1.5091344 ; 3. R Lazarova, S Valkov, V Dyakova, and P Petrov, *Layers obtained on TiCN aluminum nanocomposites by electron-beam treatment*, in IOP Conference Series: Materials Science and Engineering, International Conference on Novel Functional Materials IOP Conf. Series: Materials Science and Engineering 733 (2020) 012017 IOP Publishing, doi:10.1088/1757-899X/733/1/012017, 1-9 and 4. Mihail Kolev, Stefan Valkov, Rumyana Lazarova, Peter Petrov, Rossitza Dimitrova, and Vanya Dyakova, Tribological Properties of TiCN Nanosized Powder Reinforced Aluminum, Journal of Physics: Conf. Series, 992, IOP Publishing, 2019, 1492(1), 012066

2.1 Introduction

The aluminum and aluminum alloy nanocomposites are designed to have better mechanical and tribological properties than aluminum and corresponding aluminum alloys used in automotive and aircraft engineering. Because of that their microstructure and properties should be characterized and then compared with those of the aluminum and respective alloys.

We have elucidated the methods for surface nanocomposites producing in Chapter 1.2.2 of this book. Now we will demonstrate the results we obtained using surface treatment of aluminum and aluminum alloy with

concentrated energy flows (or fluxes) as a method for manufacturing surface nanocomposites.

Surface treatment of metals and alloys with concentrated energy fluxes (CEF), such as laser beam and electron beams, has been intensively used over the last several decades. Their main advantage is the possibility of precise control of the technological conditions of processing, which in turn allows controlling the structure and properties of the processed materials. When the flow of accelerated electrons hits the surface to be treated, the kinetic energy of these particles is transformed into heat, which propagates into the volume of the sample [1-4]. The technological parameters can be selected so that the treatment will bring the modified surface to the liquid phase - formation of a liquid bath. In the preparation of composite materials based on aluminum and aluminum alloys with introduced nanoparticles, the nanoobjects are introduced into the liquid phase in powder form or pre-deposited on the surface as a coating. For their homogeneous distribution, the technological conditions of electron beam treatment (EBT), defined by the technological parameters, are of fundamental importance: accelerating voltage (U, kV); electron beam current (Ib, mA); the speed of movement of the sample during the EBT (V, mm / sec); scanning frequency (f, Hz).

It has been found that the distribution and homogenization of alloying elements in the case of introduction by electron beam treatment with the formation of a liquid bath are based on the intense convection of Marangoni generated by the high-temperature gradient in the liquid bath. The influence of technological conditions on the formation of aluminum nanocomposites was investigated, and it was determined that the speed of movement of the specimen was essential in their preparation. The high speed of movement of the sample results in a short lifetime of the liquid bath. In this case, the transfer of the elements in the liquid bath is extremely insufficient for their homogeneous distribution, which leads to the formation of highly inhomogeneous structures. At low sample movement rates during the EBP, the main mechanism for the transfer of elements in a liquid bath is based on the convection flows that exist due to the presence of a high-temperature gradient. The existence of the liquid bath is much larger, which leads to the formation of homogeneous composite structures. It has also been found that the application of high scanning electron beam frequencies leads to a longer lifetime of the liquid bath and significantly more suitable conditions for the introduction of the alloying elements as well as their homogeneous distribution. It has been proven that the technological parameters of the EBP have to be chosen so

that the treated material is brought to a liquid phase and a liquid bath is formed.

2.2 Surface nanocomposites producing on an aluminum substrate using electron beam treatment

The aluminum used by us as a substrate is of technical purity: 99.5% Al and 0.5% other elements: Cu, 0.003 wt%; Mg, 0.007 wt%: Si, 0.150 wt%; Fe, 0.28 wt%; Mn, 0.005 wt%: Ni, 0.004 wt%; Zn, 0.009 wt%; Ti, 0.009 wt%; Cr, 0.007 wt%; Pb, 0.003 wt%; Sn, 0.02 wt%.

The refractory nanosized TiCN powder was chosen as a layer component due to its excellent properties such as high melting point, high hardness (3000–3500 kg/mm^2), and good thermal conductivity. In addition, it has an FCC lattice-like aluminum. Both materials have close lattice constants, which is a requirement for the modifiers and parent metals. TiCN nanopowder has been produced by Neomat Co, Latvia. The mean particle size is 40 - 50 nm and the C: N ratio is 1:1.

Samples with dimensions ø 30 mm and thickness 10 mm – *fig.I-2-1* were wet ground on the flat surface to grinding paper #1200, cleaned with ethyl alcohol, and dried. Then three of them (No 1, 2, and 3 – *table I-2-1*) were smeared by a laboratory spatula with a mixture of three drops of $CHCl_3$, dissolved plastic rasping, and TiCN nanopowder for obtaining a film with concentration 0.03 mg/mm^2 TiCN. The obtained film is uniform and well adherent to the aluminum substrate after drying. The as-prepared samples were subjected to electron-beam treatment (EBT) in installation-type ESW300/60-15 (“Leybold-Heraeus”) [5].

The electron beam scanning movement is circular rotating. The scheme of selective electron beam treatment is shown in *fig.I-2-2* [6]. The electron beam rotates in a circle with a radius r (mm) and frequency f (kHz) on the surface of the moving aluminum specimen. The studied sample moves on axis x with a certain velocity v (cm/s). As a result of the interaction of electron beam with TiCN nanoparticles film layers were created on the surface of the aluminum specimen. Depending on electron beam parameters (accelerating voltage; electron beam current; electron beam scanning frequency; sample motion speed; and, respectively, beam power) zone with or without melting pool on the surface of specimens is formed. The parameters of the treatment process are shown in *table I-2-1*.

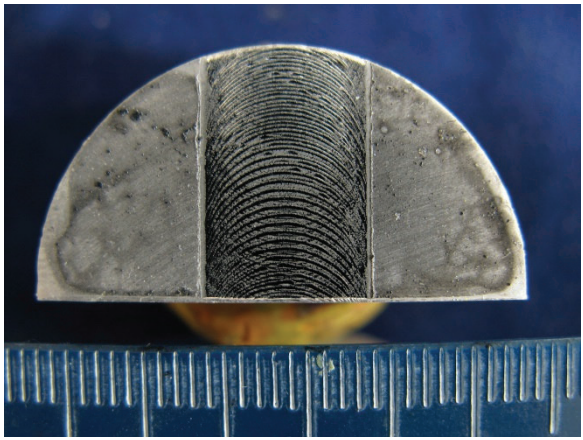

Figure I-2-1. Al sample smeared with TiCN nanoparticles containing mixture and electron beam treated

Table I-2-1. Treatment process parameters, microhardness, and layers thickness of samples

Nr of sample	I_b [mA]	v [cm/s]	f [kHz]	U [kV]	I_f [mA]	P [W]	$HV_{0.02}$ [kg/mm^2]	Δ [μm]
1 / 1-1	18	0.5	10	52	472	936	596 / 561	33 / 14
2 / 2-1	25	2	10	52	472	1300	636 / 624	25 / 18
3 / 3-1	25	5	10	52	472	1300	686 / 798	19 / 16

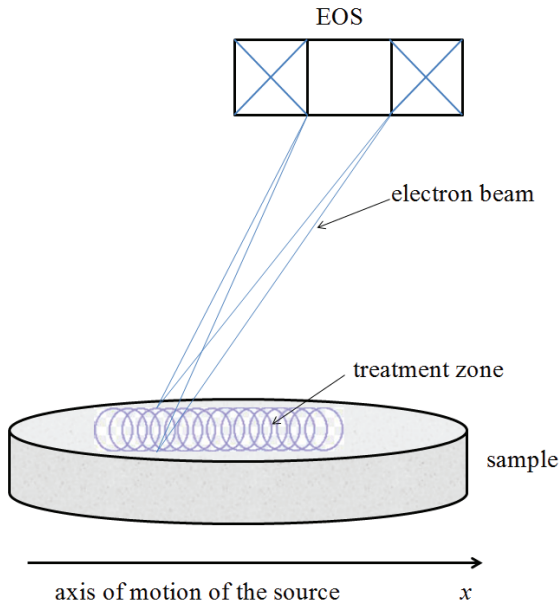

Figure I-2-2. Scheme of electron beam treatment

It should be noted that they are selected after the performance of several experiments where the power of the electron beam was varied within the range from 1 to 3 kW at different speeds of specimen motion during the alloying process. All experiments have been conducted at a rotational geometry of scanning of the electron beam, and after the investigation of the hardness of the obtained layers, those parameters which lead to the highest values have been selected. The other three samples (No 1-1, 2-1, and 3-1- *table I-2-1*) were smeared with the same mixture with concentration 0.015 mg/mm^2 TiCN and were treated with the same process parameters. After electron beam treatment, the metallographic samples were cut perpendicularly to the trace of the electron beam, wet ground on silicon carbide grinding paper #1200 ÷ #4000, and then electrolytic polished and etched by electropolishing device Lectropol (Struers) using the following electrolyte: 575 ml methyl alcohol, 25 ml $HClO_4$, 10 ml HNO_3.

2.3 Microstructure and microhardness of aluminum surface nanocomposites

The aluminum surface nanocomposite microstructure and phase composition are characterized using light microscope PolyvarMet with magnification up to 1000x, SEM FIB LYRAI XMU, TESCAN, equipped with an EDX detector (Quantax 200, Brucker) and XRD Seifert&Co with CuKα radiation. The HV microhardness is measured by device MicroDuromat (Reichert-Jung) with a load of 20g, time for reaching the load 10s, and holding time 10s.

Metallographic image of TiCN nanopowder layer on Al substrate is presented in *fig.I-2-3*. It is evident that a well-formed layer is obtained by the described method. It is visibly well adhered to the substrate and has a relatively uniform thickness.

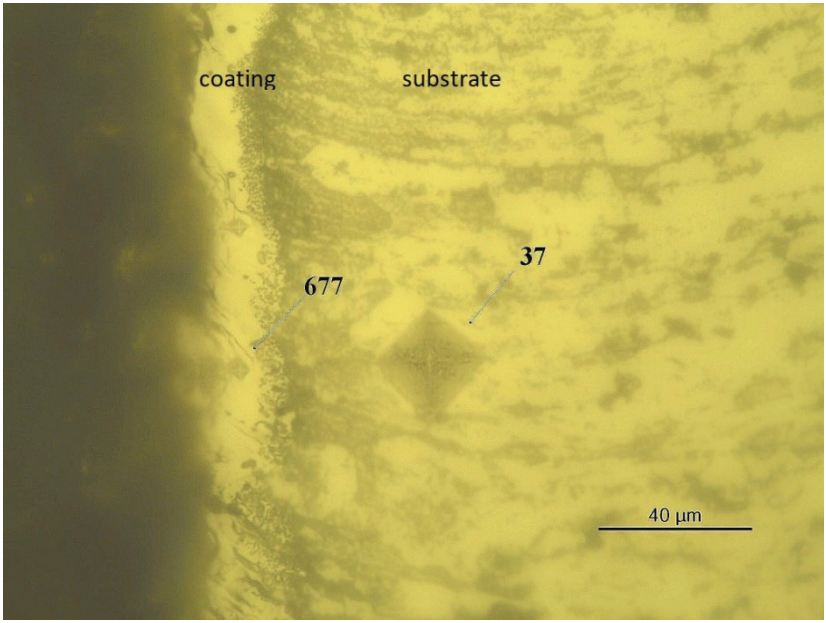

Fig.I-2-3. Metallographic image of TiCN nanopowder coating on Al substrate and microhardness imprints: sample 2, microhardness unit is kgf/mm^2

The results from microhardness measurements show that the used process parameters are appropriate for obtaining layers with sufficient thickness and high microhardness – *table I-2-1*. The mean substrate microhardness value is 35 kgf/mm^2 which means the microhardness of layers is 16-22 times higher than that of the aluminum. K.R. Ramkumar and S. Natarajan [7] achieved a significant increase in microhardness of 96% of 3% TiO_2 nanocomposite weldment compare to those of the based metal which is Al 3003 alloy. The TiO_2 nanoparticle adding is by gas tungsten arc welding. We could explain the very high individual microhardness values in our case with the presence of agglomerates of nanoparticles that have their hardness of 3000-3500 kgf/mm^2. We suppose that the main strengthening mechanism is the so-called Orowan mechanism which expresses the interaction of dislocations with nanoparticles [8] because the hard particles are an obstacle for dislocation movement in the metal matrix in principle. But other mechanisms, such as the load transfer effect and the mismatch in coefficient of thermal expansion and elastic modulus between the reinforcements and the metal matrix also contribute to strengthening augmentation. The question of the strengthening mechanism in aluminum-based nanoparticle reinforced composites is given particular attention in Part two in this book.

Sample 3 which has a relatively good combination of microhardness and thickness is subjected to SEM and EDX analysis.

The SEM investigations are carried out with SEM/FIB LYRAI XMU, TESCAN, equipped with an EDX detector (Quantax 200, Brucker).

The results are shown in *fig.I-2-4*.

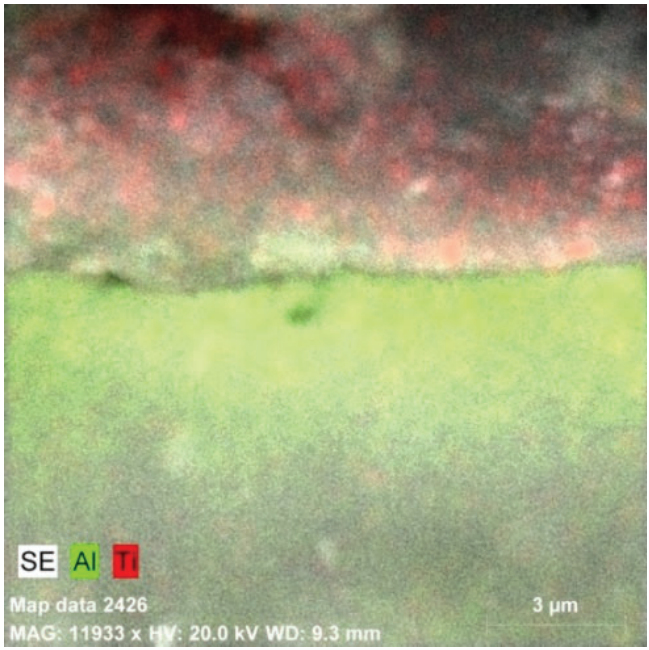

Figure I-2-4. Composition map of Al and Ti in the layer and below the layer of sample 3

The data from *fig.I-2-4* show the presence of titanium in all the coating thickness, as it is visible that the concentration of the particles increases with increasing the depth. The mechanism of the incorporation and distribution of TiCN nanoparticles can be evaluated by the intense Marangoni convection which is due to the high-temperature gradient in the melt pool [9]. In this case, driving forces from the upper parts to the depth exist and are responsible for the incorporation of the nanoparticles and, therefore, increased concentration of the TiCN in the depth is in correlation with the theory of the mass transport in the melt pool. The use of an electron beam with circular rotation is capable to increase the lifetime of the melt pool which leads to a significantly more homogeneous distribution of the incorporated particles. This indicates that TiCN nanoparticles are absorbed by the molten parent metal and a hard coating is formed. The unclad nanoparticles are difficult to adopt by the molten metal and they have low wettability in principle [10 ÷ 13]. For this reason, they are covered with metal-protector, which assists the wetting by the

molten metal. The metal-protector melts and the nanoparticles remain to act in the melt as centers of crystallization. We demonstrate that unclad nanoparticles are well wetted and adopted when an electron beam with rotating motion is used. Good nanoparticle incorporation in the substrate is realized. The TiCN nanoparticles have a high melting point temperature~ 2950ºC and they do not melt during processing and only aluminum melts. The nanoparticles which act as nucleating centers and refining factor during casting process should have the same roles in this case too. The nucleation process of crystals in Al-based composites is investigated by us in Chapter 4 of Part One.

Another sample treated in the same way and a layer of about 15 μm of thickness is shown in *fig.I-2-5*. 0.6 wt. % Ti are registered in the middle of the layer thickness using EDS analyses – *fig.I-2-6* and *fig.I-2-7*. This means that TiCN nano-sized particles penetrate undoubtedly in the layer depth thanks to the good stirring realized by the rotational movement of the electron beam.

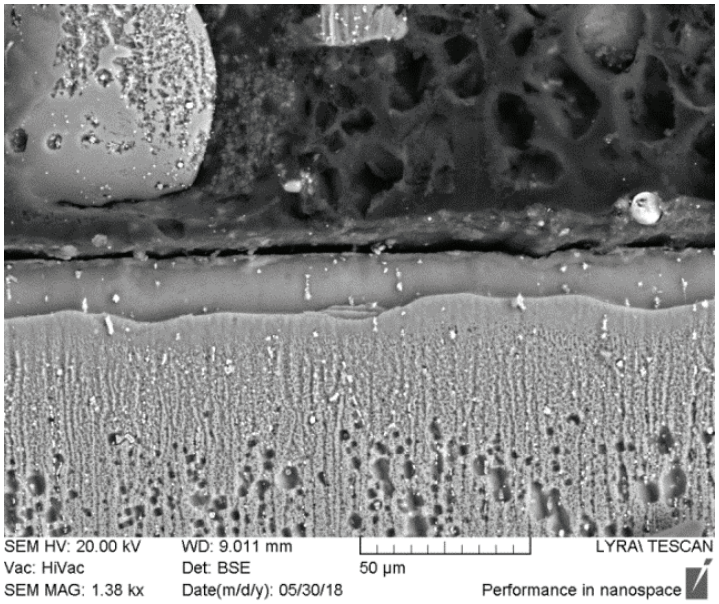

Figure I-2-5. Sample with aluminum nanocomposite layer

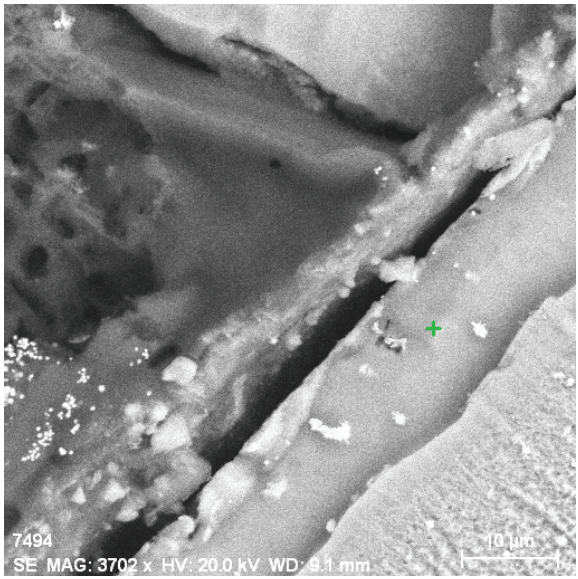

Figure I-2-6. Sample with aluminum nanocomposite layer and the tested point

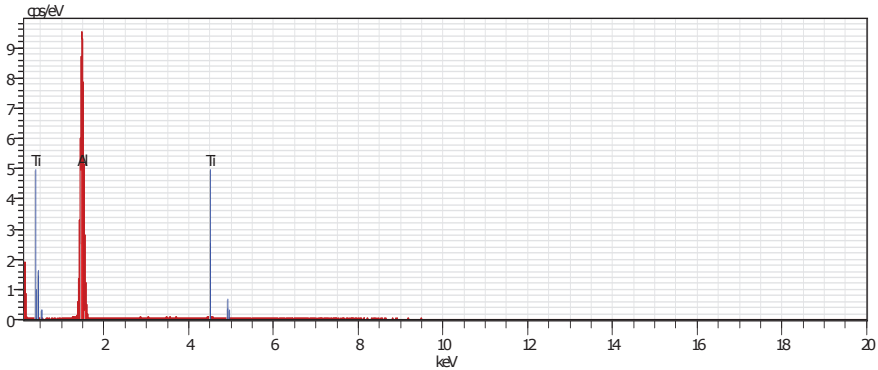

Figure I-2-7. EDS results in the marked in *fig.I-2-6* point showing a presence of Ti

Chemical composition in the marked point in *fig.I-2-6*:

El	AN	Series	unn. C [wt.%]	norm. C [wt.%]	Atom. C [at.%]	Error [%]
Al	13	K-series	72.07	99.17	99.53	3.5
Ti	22	K-series	0.60	0.83	0.47	0.1
Total:			72.68	100.00	100.00	

To prove the presence of TiCN nanoparticles in the surface layer of sample 3, we remove a surface material of about 5 μm thickness and subjected the sample to XRD analyses. X-ray diffraction patterns of sample 3 before and after withdraw of the surface material are shown in *fig.I-2-8.*

They exhibit diffraction maxima related to TiCN, pure Al, and δ-Al_2O_3 phases. It should be noted that the TiCN compound has a face-centered cubic structure, as both nitrogen and carbon atoms have occupied the octahedral sites of close-packed hexagonal Ti lattice, forming TiC_xN_{1-x} [14]. As it was already mentioned, the ratio of C: N atoms is 1:1 and, therefore, the identification of this phase has been done according to both TiN (JSPDS 38-1420) and TiC (JSPDS 32-1383). It should be noted that the penetration depth of the x-rays is limited due to the photo-electron absorption and therefore, the XRD method is appropriate for investigations of the phase composition on the surface but in-depth they cannot penetrate. For this reason, XRD measurements have been carried out before and after withdraw of about 5 μm of the surface to study the distribution of the TiCN particles. Diffraction peaks corresponding to TiCN are visible in both cases as considering the sample before withdrawing the maxima are much weaker which means that the concentration of the nanoparticles is much smaller on the surface in comparison to the depth of the melt pool. These results are completely in agreement with those obtained by EDX. Also, it should be noted that the shape and 2θ peak position of TiCN diffraction maxima are different before and after the withdrawal process. This means that the grain size, residual stresses, micro strains, etc. of the nanoparticles are different on the surface and in-depth of the melt pool, which can be due to the significantly more aggressive environment on the surface in comparison to the depth of the melt pool. The existence of the oxide Al_2O_3 phase is because the sample was retrieved directly from the vacuum chamber after the treatment process, as the specimen has not been cooled down to room

temperature. This oxide Al_2O_3 phase is commonly accepted as appropriate because it acts as a protective barrier to other reactive agents and organic pollutants.

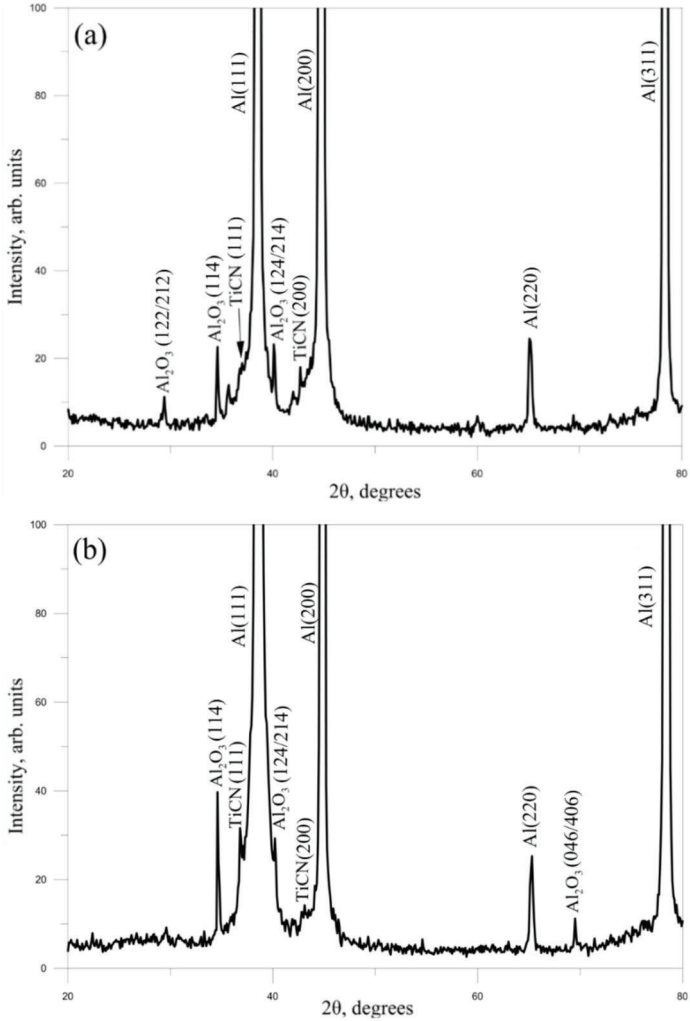

Figure I-2-8. X-ray diffraction patterns of Al sample 3 with TiCN incorporated nanoparticles: a) a spectrum obtained from sample 3 before withdrawal; b) spectrum obtained from sample 3 after withdrawal of about 5 µm of the surface

To prove and investigate the introduction of TiCN nanoparticles into an aluminum substrate, the following XRD analysis was performed by Dr. Konstantin Borodynskiy:

Three samples were examined by X-ray diffraction analysis:

1. Pure aluminum substrate, before electron beam and other treatments
2. Pure aluminum substrate after electron beam treatment (EBP)
3. Aluminum substrate with TiCN-embedded nanoparticles by EBP

The measurements are realized in two modes: B-B (the symmetric mode - Brag-Brentano) and AGIB (asymmetric geometry by the method of the sliding beam). X-ray diffraction patterns are presented in 2 theta-scales. The step is 0.02 degrees with 1 second measurement time at each step.

Fig.I-2-9 and *fig.I-2-10* show The X-ray diffraction patterns of technically pure aluminum before and after electron beam treatment (sample 1 and sample 2 resp.). In both cases, diffraction peaks corresponding to pure aluminum are observed. The phase is identified according to the International Crystallographic Database (ICDD 01-71-4008).

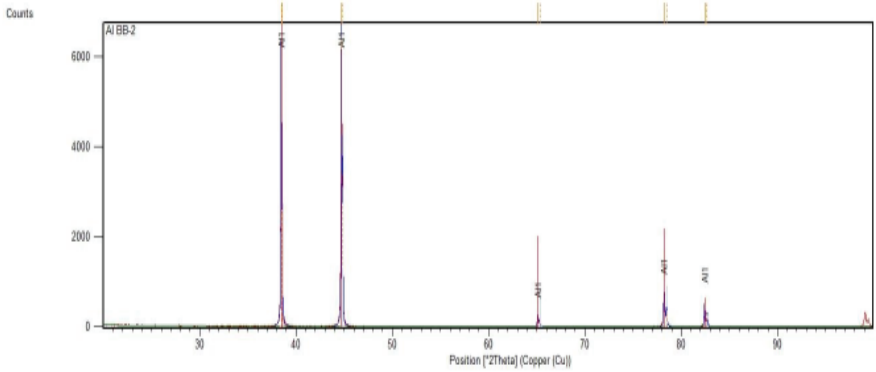

Figure I-2-9. X-ray diffraction pattern of sample 1 (a pure aluminum substrate)

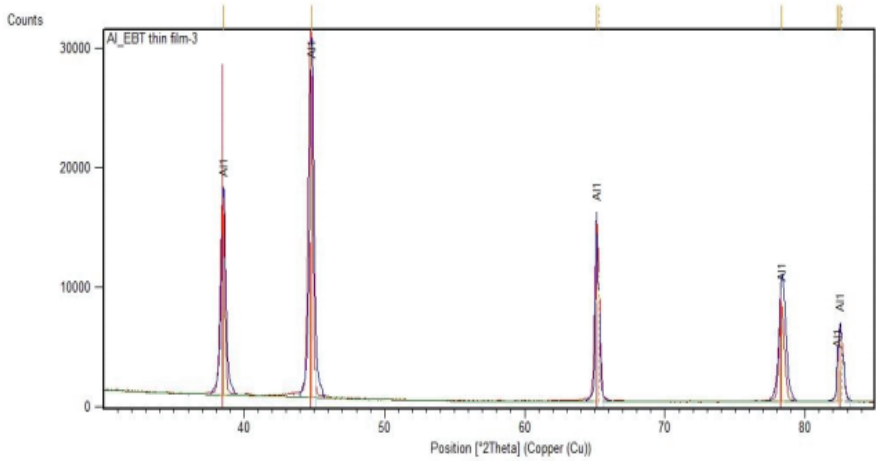

Figure I-2-10. X-ray diffraction pattern of sample 2 (pure aluminum substrate after EBT)

Fig.I-2-11 shows an X-ray diffraction pattern of sample 3 (pure aluminum substrate with embedded TiCN nanoparticles by EBP). Peaks corresponding to pure aluminum and traces of the Ti_2CN phase are observed. Quantitative phase analysis was also carried out, finding that the Ti_2CN content was 2%.

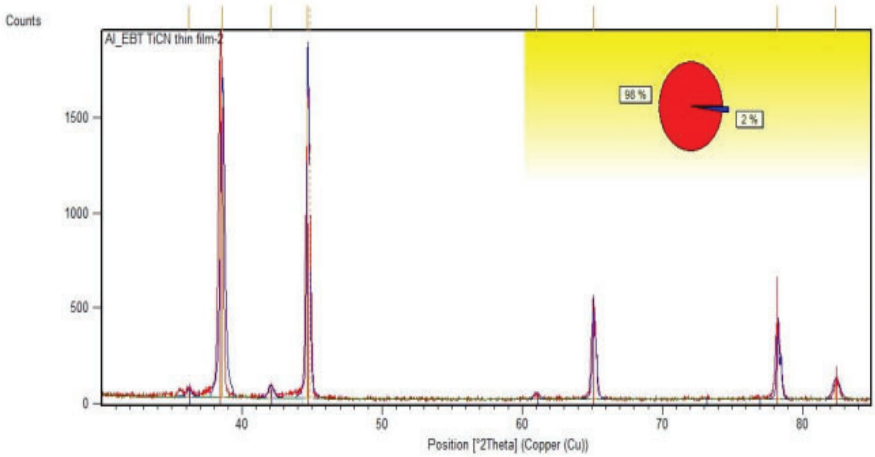

Figure I-2-11. X-ray diffraction pattern of sample 3 (aluminum with TiCN nanoparticles embedded by EBT)

We could draw the following conclusions based on the results:

- The X-ray diffraction analysis confirms the fact that the TiCN nanoparticles are incorporated into the aluminum matrix at a depth greater than 5 μm from the sample surface.

- The concentration of nanoparticles at a depth of the sample is greater than that of the surface, which is apparently due to the effect of the electron beam motion, whereby the surface metal layer melts and the nanoparticles are embedded inside the liquid metal layer.

The complex investigation was completed with TEM analysis. Sample 2 was unilaterally thinned by reaching a layer immediately adjacent to the applied surface coating and polished with an acetic acid flow. TEM images of nanoparticles were taken by TEM JEOL 1011 with an accelerating voltage of 100 kV. The electron diffraction investigation was performed by TEM JEOL 2100 with an accelerating voltage of 200 kV. X-ray energy-dispersive spectroscopy was performed as well.

The crystal structure of $TiC_{0.5}N_{0.5}$ and Al is FCC. The lattice constant of $TiC_{0.5}N_{0.5}$ is a = 4.282 Å [15]. *Fig.I-2-12 a)* shows the zone from the investigated sample of which composition maps are made and diffraction pattern – *fig.I-2-12 b)* is taken. The observed reflexes are characteristic of FCC. The measured distance values for directions: $\overline{1}11$ and $\overline{2}00$ are 2.396 Å and 2.063 Å respectively.

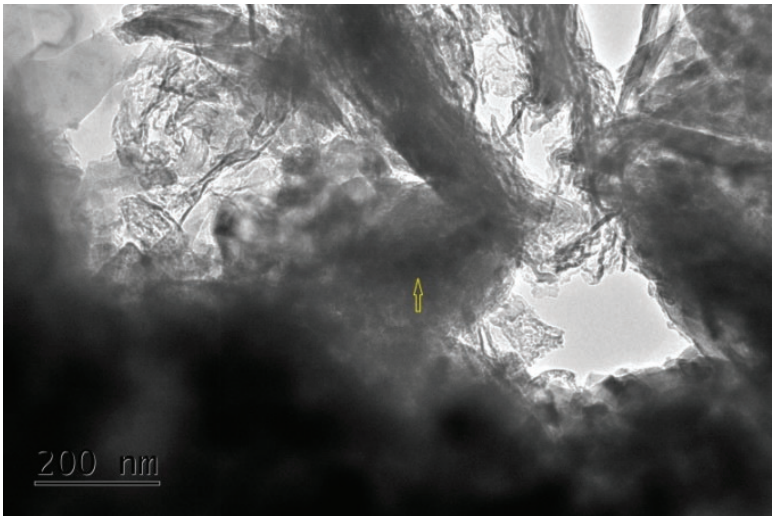

a

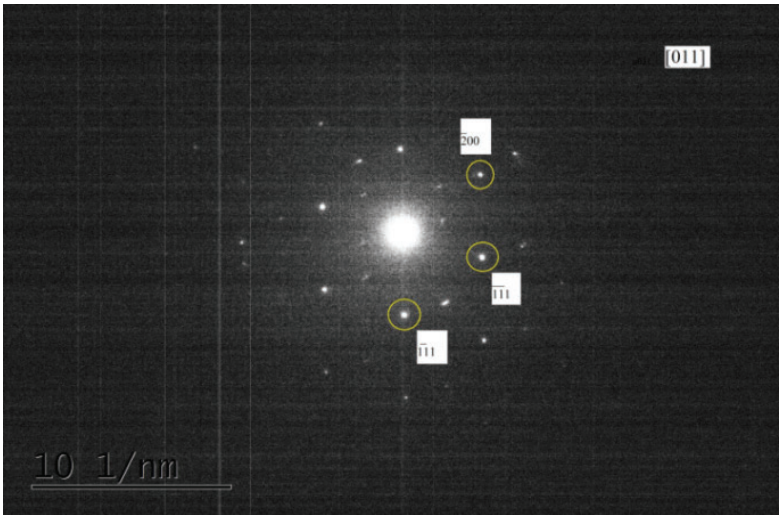

b

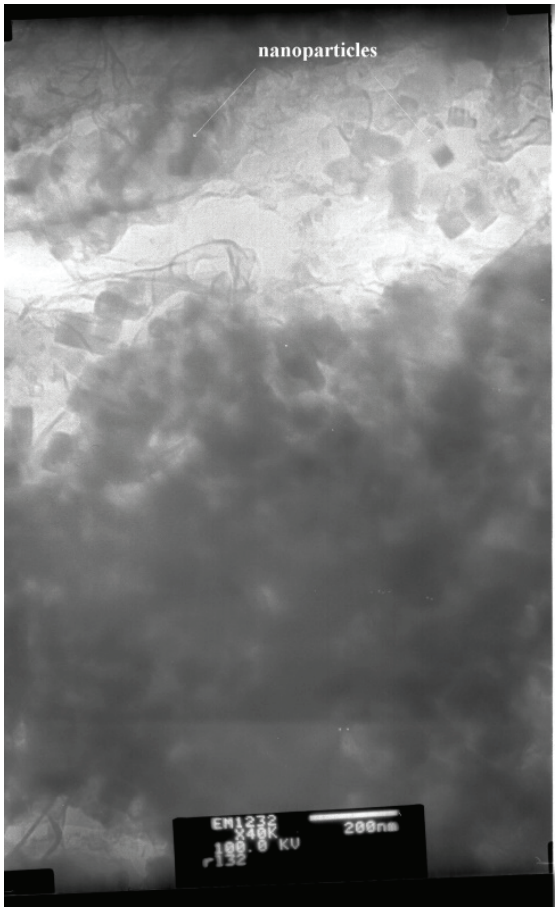

c

Figure I-2-12. TEM images of the investigated sample: a) area from which the diffraction pattern is taken; b) - reflections of TiCN nanoparticles; c - nanoparticles

According to the database of ICSD, No 181785 ($TiC_{0.5}N_{0.5}$) these values are 2.472 Å and 2.141 Å respectively. We consider that there is a good agreement between experimental and reference data and that the difference is due to the variation of the microscope constant.

Furthermore, the presence of Ti confirms the result of the XRD analysis. We can conclude that there are TiCN nanoparticles incorporated

in the layers of the investigated sample – *fig.I-2-12 c*. It is known that the dispersed particles in the metal matrix cause its strengthening and increases its hardness. It is claimed that the introduction of nanoparticles strongly increases the mechanical properties even though the nanoparticles are agglomerated [16]. In our case, these are refractory TiCN nanoparticles that act as barriers to dislocation movement which could explain the high microhardness of the coating. The second factor for strengthening increase is the presence of nanoparticles clusters where the volume fraction of hard TiCN nanoparticles is greater.

Following conclusions can be made from the performed analyses:

- The scanning circular rotating motion of the electron beam is successfully applied for alloying of a pure aluminum matrix with TiCN nanoparticles. The most appropriate treatment conditions for obtaining layers with significant thickness and high microhardness are reported.
- Treatment conditions are accelerating voltage U = 52 kV; electron beam current I_b = 18–25 mA; electron beam scanning frequency f = 10 kHz; and sample motion speed V = 0.5–5 cm/s.
- The used method allows obtaining layers on an aluminum substrate with thickness 14–33 μm and microhardness 562–798 kg/mm^2, which is 16–22 times higher than the substrate microhardness. Such details could be convenient for applications requiring high surface hardness and light, soft, and plastic parent metal, which means an increase in the surface hardness concerning the uncoated substrate.
- XRD and TEM analyses show that TiCN nanoparticles are incorporated in the layers which are responsible for increased hardness. The microhardness raising is mostly due to the presence of hard TiCN nanoparticles in the aluminum matrix as well as hard clusters. Possible strengthening mechanisms are discussed.

2.4 Tribological properties of surface aluminum composites with TiCN nanoparticles

Hosseini et al., have reported that the wear rate of Al6061-Al_2O_3 bulk composite decreases significantly with micro to nano-size variation of alumina particle (60 μm, 1 μm, 30 nm) – *fig. I-2-13* [17]. That means the particulates nanocomposites have better tribological properties than particulates composites.

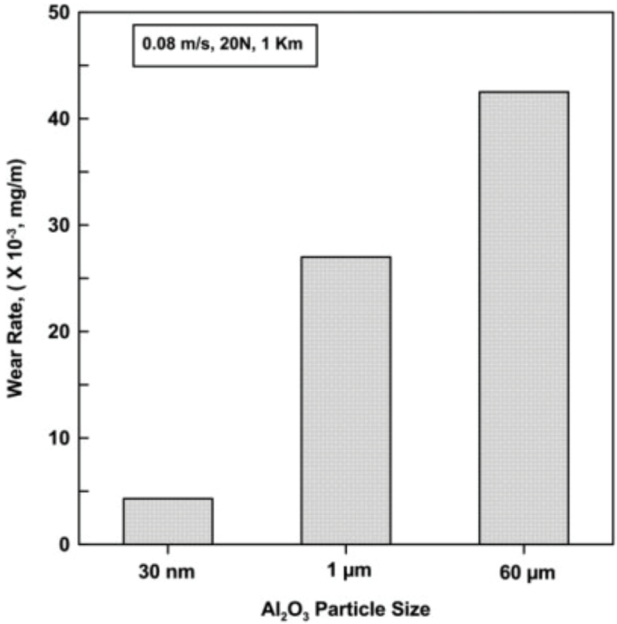

Figure I-2-14. Reinforcement particle size impact on the wear rate of Al6061-Al_2O_3 nanocomposite [17]

On the other hand, the nanocomposites exhibit reduced wear loss compared to the same alloys but without the nano-reinforcement phase [18 ÷ 21].

Nanocomposite surface demonstrates a large number of dislocations [22] as compared to the base alloy. This is attributed to the large mismatch in the elastic modulus and thermal coefficient of expansion between matrix and nanoparticles. Dislocations' presence increases strength and hardness and therefore improves the wear resistance of nanocomposites. A combination of adhesion and abrasion is found to be the dominant wear mechanism for nanocomposites.

In the present part, the effect of TiCN nanoparticles as reinforcing phase on the coefficient of friction (COF), friction force, and mass wear of specimen with and without surface coating are studied and compared [23].

2.4.1 Materials and methods

Three cylindrical specimens made of aluminum of technical purity (99.5% Al and 0.5% other elements) are tested under frictional lubrication conditions. The dimensions of the samples are 12 mm in diameter and 10 mm in height. The first sample is of untreated Al marked 1-Al. The second is of Al, subjected to electron beam treatment (EBT), marked 2-Al and the third is of Al, coated with a mixture, containing TiCN nanoparticles and subjected to electron beam surface treatment – 3-Al. The treated samples are prepared according to the method used in [24]. *Fig.I-2-14* shows the three experimental specimens before being subjected to tribological tests.

(a) **(b)** **(c)**

Figure I-2-15. Samples prepared for tribological tests: a) untreated Al, b) Al subjected to EBT, c) Al coated with the mixture, containing TiCN nanoparticles and subjected to EBT

Metallography

The cross-sections perpendicular to the flat surface were prepared for microstructure analysis. They were wet ground on the grinding paper up to 4000, mechanically polished, and etched with 0.5% aqueous solution of HF. The observations were carried out with a metallographic microscope PolyvarMet at magnifications up to 1000x. The microhardness is measured with device MicroDuromat 4000, a load of 20g, time of reaching the load 10s, and holding time 10s.

Tribology

The experiments were carried out on an installation certified by the American Society of Tribology and designed for "Pin/ball on the disk" tests of the company Ducom – *fig.I-2-16*.

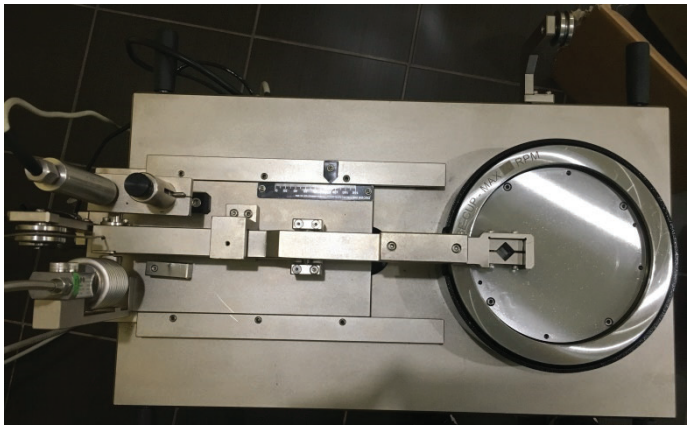

Figure I-2-16. Pin/Ball on Disk Tribometer by Ducom

The tribological installation shown in *fig.I-2-17* functions as follows: The cylindrical sample is positioned in the holder which is located at one end of the loading beam – *fig.I-2-17 a*. The test surface of the sample is in direct contact with the surface of a counterpart disk. The surface of the counterpart disk is hardened to 60 HRc. The counterpart is mounted on a special holder designed to conduct a lubricant test – *fig.I-2-17 b*. The drive is powered by an electric motor that rotates around its central axis with constant RPMs, and for our tests, we have chosen 65 rpm. At the opposite end of the loading beam, there is a static working load of 110N – *fig.I-2-17 c*. The installation has two sensors for precise measurement of and friction force – *fig.I-2-17 d*. The results are plotted in real-time using specialized software that calculates the friction coefficient after completing the test. All three experiments are conducted under frictional conditions with 50ml of 10W40 motor semisynthetic oil as a lubricant and the contact surface of all specimens is submerged under media.

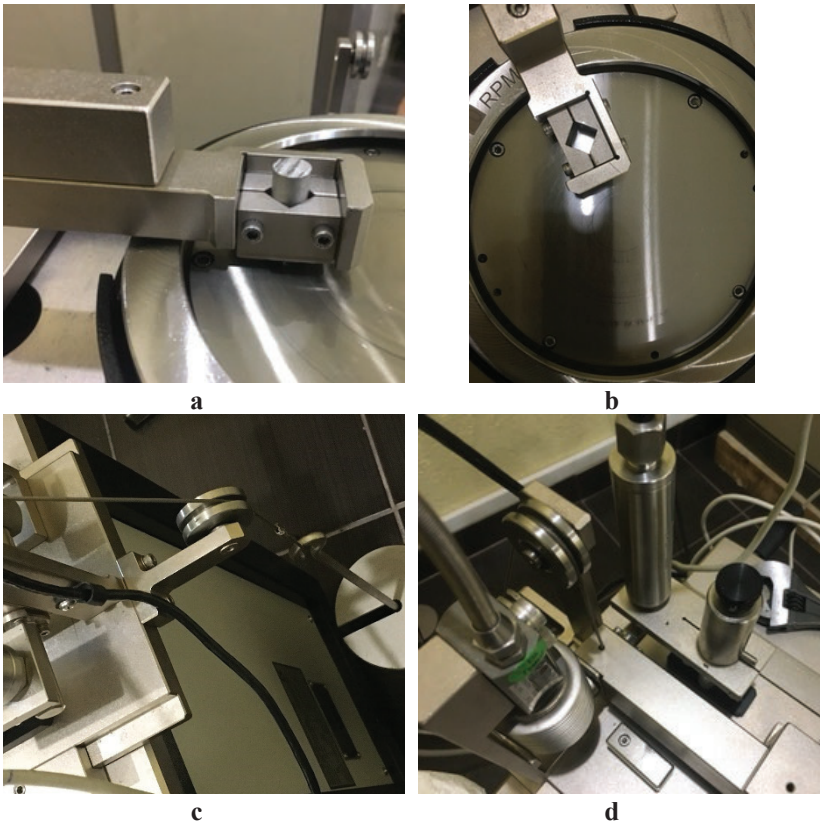

Figure I-2-17. Some nodes of the tribological test facility: a) specimen holder; b) an anti-gripping device; c) static working load and d) sensors for measuring linear wear and friction force

For determination of mass wear is used an electronic balance Boeco BAS32 Plus with a scale accuracy of 0.1mm and the possibility of automatic internal calibration.

The methodology for the tribological testing is expressed by the following steps:

Preparation of the experimental specimens

Each of the experimental bodies has the following dimensions: diameter 12 mm and height 10 mm. Their contact surfaces have been wet grounded with sandpaper size 2500.

Mass wear determination

The mass wear determination of the test specimens is carried out on an analytical balance with a precision of 0.1 mg. Before each measurement, the sample is cleaned and degreased by organic and mechanical particles and dried with ethyl alcohol to prevent electrostatic effects. The samples are measured before and immediately after the experiment and the difference in their masses is established.

$$m = m_0 - m_{f,} \text{ [mg]} \quad (1)$$

m is the difference between $\mathbf{m_0}$ initial (before friction) mass and $\mathbf{m_f}$ final (after the end of test) mass.

Experimental conditions:

- experiments under lubrication conditions were conducted at room temperature of 22 ° C;
- after determining the initial mass before the tests, the specimen was mounted on the installation holder and positioned at a diameter of 110 mm on the contact surface of the abrasive body;
- the contact surface of the test body is immersed in 10W40 engine-semi-synthetic motor oil for 2 hours;
- distance covered by each sample is 2700 m;
- speed of the counter disk is 65 rpm;
- selected stationary load is 110N.

Friction force measurement

The friction force is given automatically by the sensor in real-time by plotting the graphics: friction force (N) - time (sec) and friction force (N) - distance (m).

Measurement of friction coefficient

The friction coefficient is automatically calculated from the program after the end of the experiment and graphics: friction coefficient - time (s) and friction coefficient - distance (m) are plotted.

2.4.2 Results and discussions

Microstructure and microhardness

The matrix of the aluminum samples is an α- solid solution – *fig.I-2-18 a*. There are inclusions in it. The imprints from the microhardness measurements are visible. The microhardness values – near the edge and in the core of the sample are the same – 29 kg/mm^2. This means there is no difference in the microhardness in the two zones.

The microstructure of the aluminum samples consists of coarse grains – *fig.I-2-18.* A layer of about 20-25 μm is formed at the surface after electron beam treatment *fig.I-2-18 b*. Between the layer and the matrix,

there is a strong metallurgical bond. The microhardness of the layer in sample 2- Al is 78 kg/mm^2. The core's one is 29-30 kg/mm^2. It could be concluded that the EBT itself hardens the material 2.7 times. It could be seen that the layer is much harder (814 kg/mm^2) than the matrix (38 kg/mm^2) in sample 3-Al or 21.4 times – *fig.I-2-18 c*. This is due to the hard TiCN particles (~3 500 HV) incorporated in the layer as we have found out previously [24]. The nanoparticles diameter which is commensurate with the dislocations one represents obstacles for the movement of dislocations. The Orowan mechanism is the main straitening mechanism acting in aluminum nanocomposites. The strengthening effect is a result of the formation of multiple dislocations Orowan loops around the reinforcement particles, as argued by many researchers [25-27]. This could serve as a prerequisite for increasing the hardness, strength properties, and wear resistance that we study in the next part of the article.

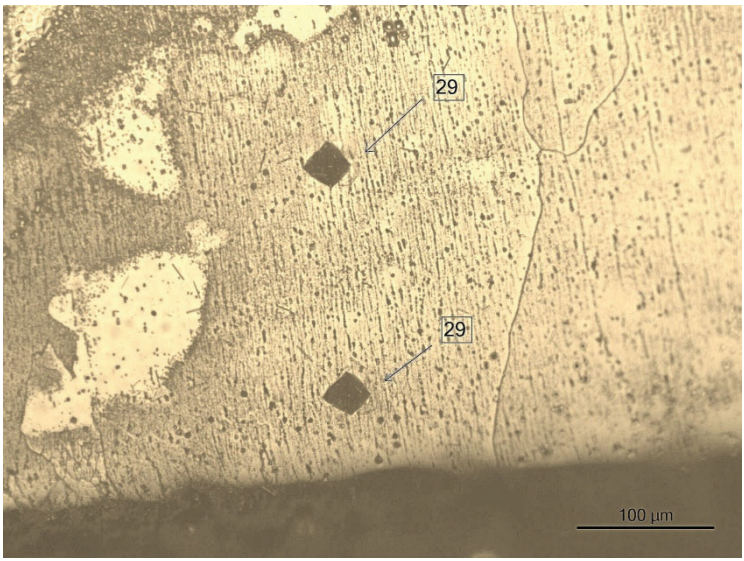

(a)

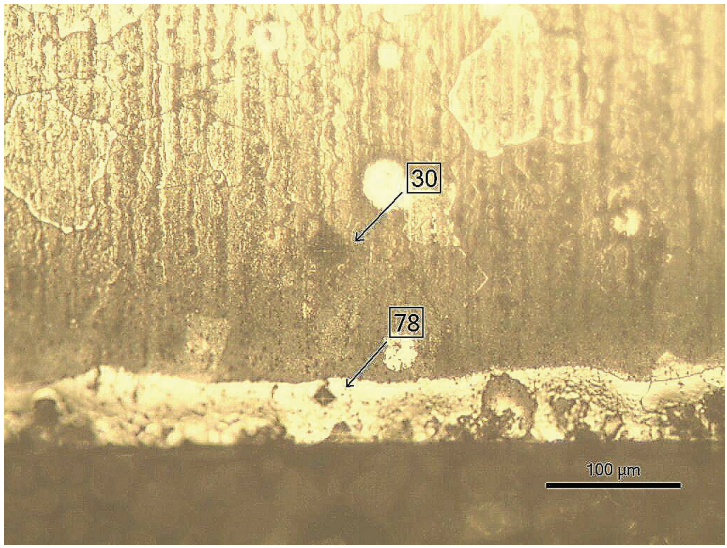

(b)

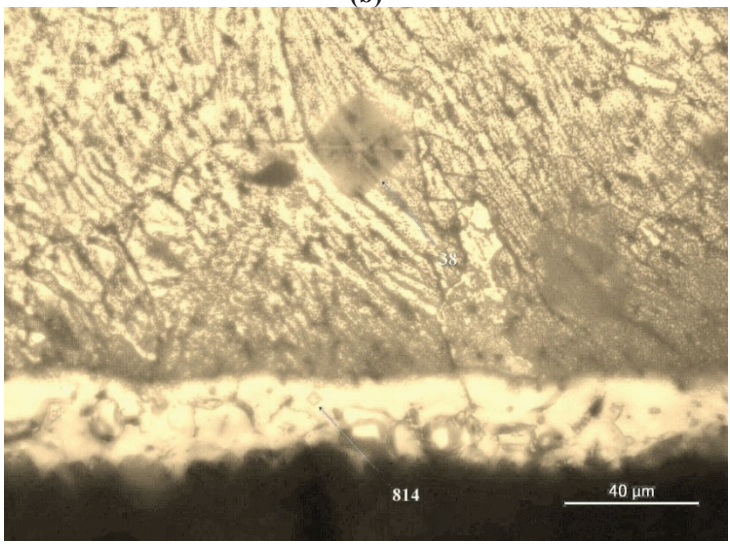

(c)

Figure 2-18. Metallographic images of a) sample 1-Al, b) sample 2-Al, and c) sample 3-Al

The SEM image of sample 3-Al is shown in *fig.I-2-18.* The layer is relatively smooth and with uniform thickness.

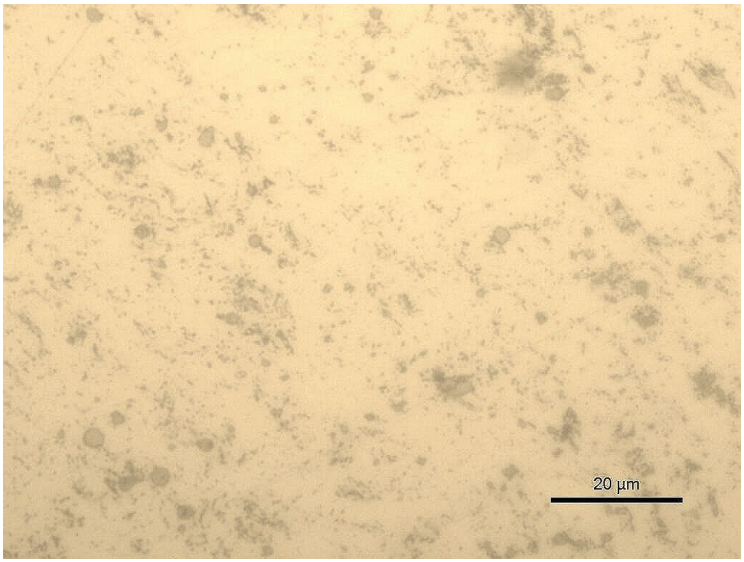

(a)

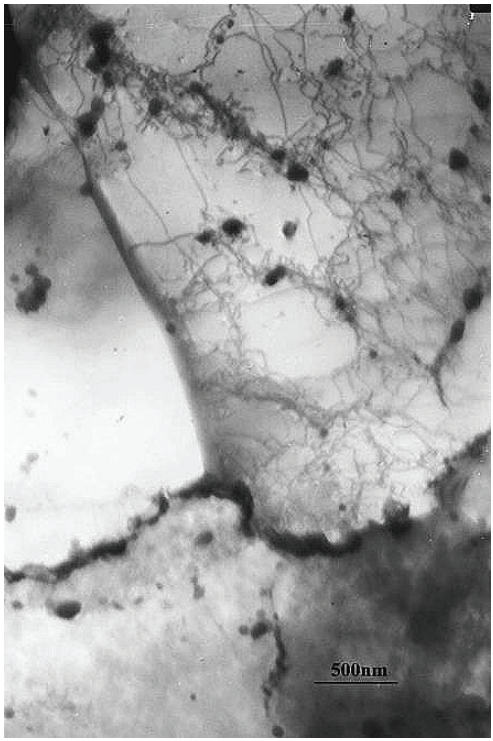

(b)

Figure I-2-19. **Images of sample 3-Al showing the nanoparticles in the Al matrix: a - LM, b - TEM**

Tribological properties

The obtained data for the mass wear graph for the entire experimental cycle are presented in *table I-2-2* and *fig.I-2-20*. The untreated sample has lost most of its mass compared to the other two samples. 1-Al reduced its mass due to surface friction with 0.0109g more than electron beam treated sample 2-Al and 0.0524 g more of the nanoparticle surface coated and electron beam treated sample. There is a significant difference in mass wear between the surface-treated samples. It could be concluded that the electron beam treatment increases the wear resistance of the aluminum sample 1.25 times. Electron beam treated sample 2-Al has lost 29 times more mass than sample 3-Al coated with nanoparticles. The most important result, however, is the difference between wear loss of the

untreated sample and sample coated with nanoparticles and electron beam treated. The last sample 3-Al has lost 36 times less mass than the untreated one. This shows that the hard nanoparticles are the main reason for the improved wear resistance of the aluminum nanocomposite. The hard nanoparticles which are dispersed in the soft aluminum matrix are difficult to overcome obstacles to the movement of dislocations. As it could be seen in *fig.I-2-19 b*, the dislocations create somewhat as *networks, meshes* around of the nanoparticles even as sub grain's boundaries. This could explain the higher wear resistance of the layers containing TiCN nanoparticles in comparison with the non-containing nanoparticles layers.

Table I-2-2. Experimental results of mass wear of the samples at test time/distance – 160 min / 2700m

Sample	Initial mass, g	Mass after friction, g	Mass wear, g
1-Al	1.7829	1.7290	0.0539
2-Al	2.9264	2.8833	0.0430
3-Al	3.1795	3.1778	0.0015

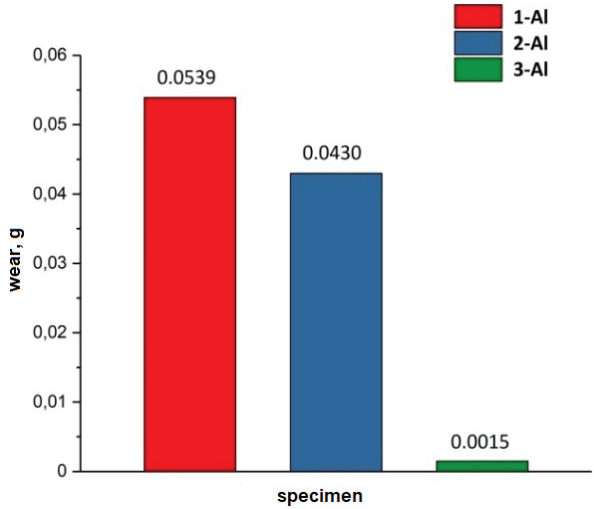

Figure I-2-20. Mass wear of experimental specimens: 1-Al; 2-Al; 3-Al

The mean experimental values for friction force and friction coefficient obtained using data after elapsed time/distance for each of the test samples at a load of 110 N are shown in *table I-2-3*. After 2 000 s of elapsed time

and respectively 800m of distance passed the surfaces of the sample and the wear disk have already reached good working contact. We can see that the friction force of sample 1-Al is 5N greater than 2-Al and 8N greater than 3-Al as shown *table I-2-3*. We can observe a similar difference in *fig.I-2-23* by comparing the friction coefficient for each of the test specimens. Sample 1-Al has the highest coefficient of friction 0.11 and sample 3-Al exhibits the lowest one 0.05. Thus, the sample coated with TiCN nanoparticles and electron beam treated has a 2.2 times lower friction coefficient than that of the untreated aluminum sample.

Table I-2-3. Average friction force and friction coefficient of test specimens at test time/distance 83 min / 1800 m.

Sample	Friction force, N	Coefficient of friction
1-Al	13	0.11
2-Al	8	0.07
3-Al	5	0.05

The reported coefficient of friction values are mainly in the range from 0.1 to 0.05, which is because the composites with added nano-sized reinforcement generally have a lower coefficient of friction and higher wear resistance than unreinforced matrix alloys [28].

Unfortunately, it would be incorrect to compare the coefficients of friction of the aluminum sample with TiCN coating obtained by electron beam treatment and the coefficient of friction of an aluminum sample with TiCN coating obtained by reactive plasma spraying [29] under a load of 110 N. The reason is that the authors of [29] have managed their experiment in the dry friction conditions while we have used 10W40 motor semisynthetic oil as a lubricant.

We cannot make a comparison between obtained by us tribological characteristics of aluminum nanocomposites and that of other researchers because of different conditions of experiments [30 and 31], but we would allow ourselves to compare the coefficients of friction with those of Ni–W plating sliding against 390 Al at 120 N [32] – *fig.I-2-21*. As well as the friction coefficient of our aluminum nanocomposite reinforced with TiCN nanoparticles and friction coefficient of tin-plated piston sample sliding against 390 Al – *fig.I-2-22*. From here we could conclude that the coefficient 0.05 is considerably low, which we consider a good achievement.

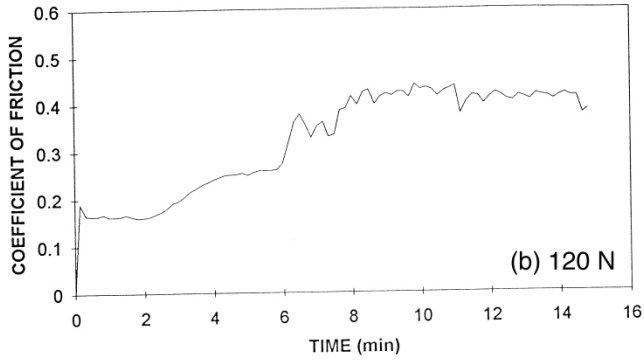

Figure I-2-21. Change of coefficient of friction with sliding time for Ni–W plating sliding against 390 Al at 120 N [32]

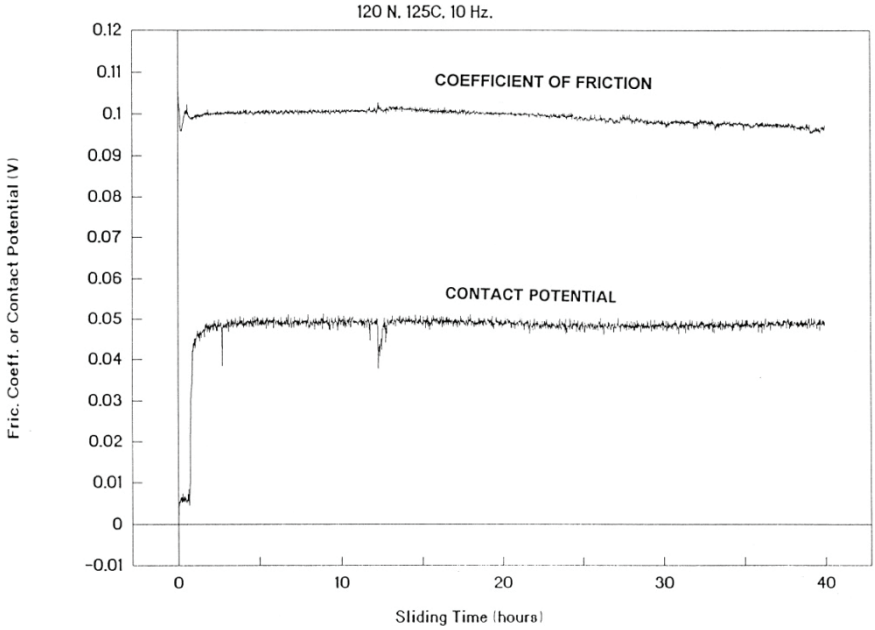

Figure I-2-22. The friction coefficient and electric contact potential measurements of tin-plated piston sample sliding against 390 Al at 400 K and 120 N [32]

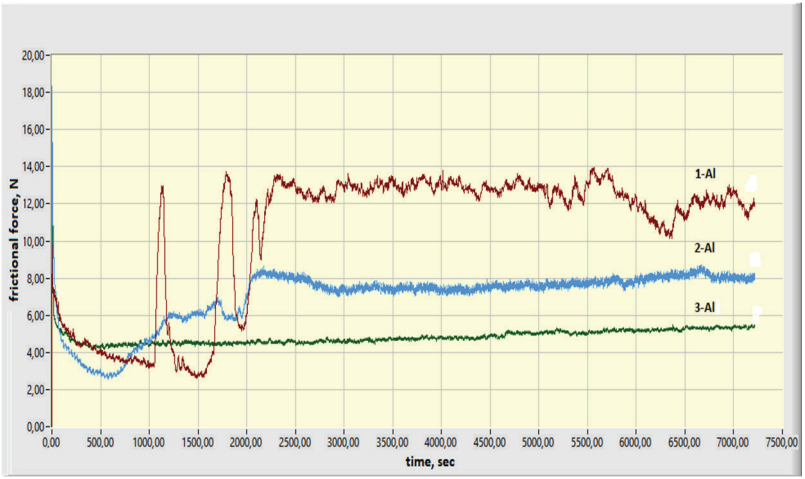

(a)

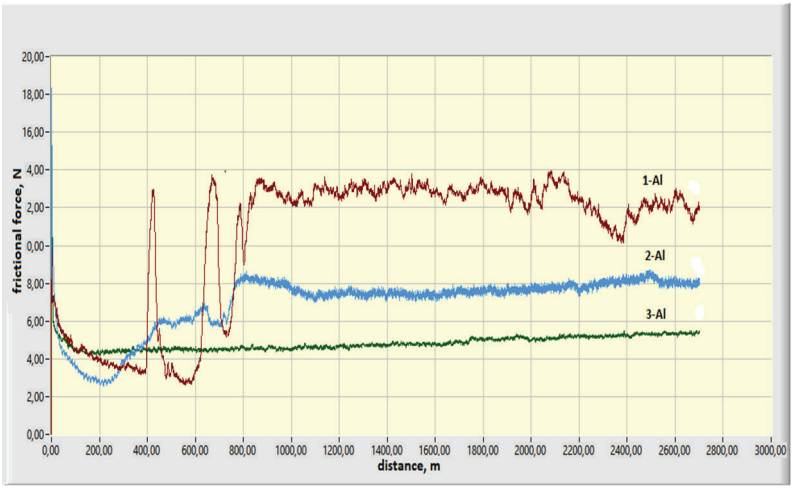

(b)

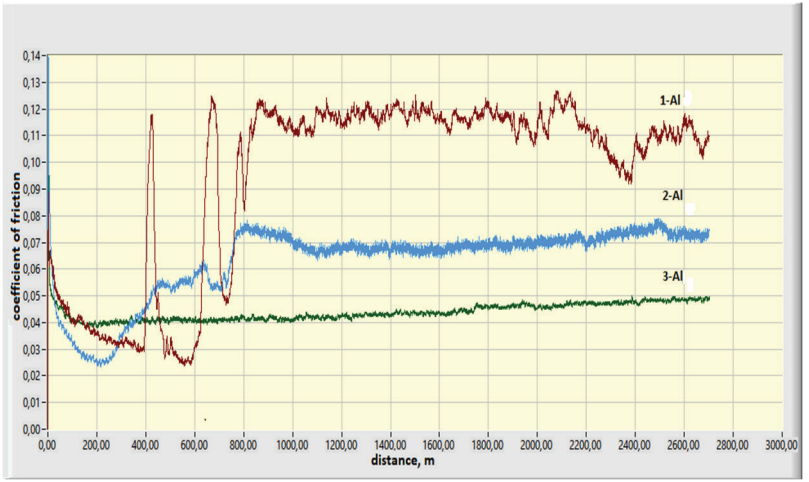

(b)

Figure I-2-23. Coefficient of friction: (a) for a time elapsed of 2 hours; (b) for a distance of 2700 m

The enhancement of wear resistance of 4.5% TO_2 reinforced aluminum compared to the Al is about two times according to any load in the interval 5÷25N [28].

The embedding of TiCN nanoparticles in an aluminum matrix increases the resistance of the material against friction because of the great nanoparticles' hardness and their commensurability with the dislocations' dimensions which is why they are obstacles to the movement of the dislocations and the material becomes stronger.

We have not investigated the variation of the friction coefficient with the increasing content of TiCN nanoparticles. But the reference shows that the researchers [33-35] have found a reduction in friction coefficient with increasing content of nanoparticles.

Conclusions

Following conclusions can be made from the performed analyses:

- The electron beam treatment of the surface of aluminum and aluminum alloy samples causes a layer formation. It is a surface zone in which TiCN nanoparticles are incorporated. Their presence determines the increase of microhardness.
- The studied tribological characteristics, such as mass wear, friction force, and coefficient of friction are improved of the samples with

nanocomposite layer compared to the same characteristics of the samples without a nanocomposite layer.

- The increased microhardness and improved tribological characteristics are due to the higher microhardness and better tribological characteristics of TiCN nanoparticles in comparison of Al- matrix and the obstruction of the movement of the dislocations by nanoparticles in the Al Matrix.

2.5 Two-layer coatings of TiCN nanoparticles on an aluminum substrate

TiCN nanoparticles were incorporated in pure Al substrate using electron-beam treatment [36]. The aluminum substrates were smeared by a laboratory spatula with a mixture of three drops of CHCl3, dissolved plastic rasping, and TiCN nanopowder for obtaining a film with a concentration of 0.03 mg/mm^2. The mean particle size is 40±5 nm, as the C: N ratio is 1:1. The samples are further subjected to electron-beam treatment with scanning electron beam as the scanning was realized in a circular geometry. During the process, the accelerating voltage was 52 kV, the speed of the specimen motion during the EBT process was from 0.5 cm/sec to 5cm/sec, the electron beam current was from 18 mA to 25 mA, the focusing current was 472 mA and the electron-beam scanning frequency was varied from 1 kHz to 10 kHz. A scheme of the electron beam treatment process is presented in *fig.I-2-1*. A description of the manufactured samples is provided in *table I-2-4*. A second layer of TiCN nanoparticles introduction was realized to increase the nanopowder concentration in the treated zone. The surface of the Al substrate with already introduced nanopowder was further coated with TiCN and then subjected to a second electron beam treatment process. During all experiments, the accelerating voltage was U = 52 kV and the focusing current was I_f = 472 mA. The processing is performed in a circular path, in which the electron beam scans the surface of the pads. The limits for changing the parameters were as follows: I [mA] = 18÷25; v [cm/s] = 0.5÷5; f [Hz] = 200÷10 000. The two most successful experiments out of 27 are of the following samples, which show the best mechanical properties – *table I-2-3*:

Table 2-4. Technological parameters of electron beam treatment of Al with TiCN containing layer

Sample	A current of the electron beam, I [mA]	Speed of the sample movement, v [cm/s]	Scanning frequency of the electron beam, f [Hz]
1.	18	2	1000
2.	25	5	10 000

The SEM images of the treated zones of both samples are shown in *fig.I-2-23,* where it could be found out that the depth of the treated zone (designed as A) of sample 1 is 80±10 μm and the depth of the treated zone of sample 2 is 20±3 μm. This difference could be explained by the different speeds of the sample motion during the EBP. Lower velocity leads to a higher penetration depth of the electrons since the input energy increases. This means that lower velocity values increase the thickness of the treated area.

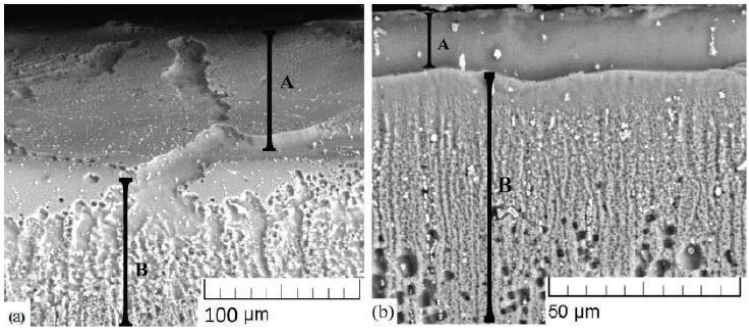

Figure I-2-23. SEM images of the surface zones of the treated samples: a) – sample 1 and b) – sample 2

To investigate the chemical composition of the treated area of the two specimens, energy dispersion spectrometer analysis was carried out. The results are summarized in *fig.I-2-24*. Only peaks of pure Al are seen and no other elements are recorded in specimen No. 1. The results for sample No. 2 show that in addition to Al, a small amount of Ti (~4%) is detected. Therefore, the nanoparticles are successfully embedded in the source matrix. These results are in agreement with those of the X-ray diffraction analysis showing the presence of TiCN particles in the substrate – *fig.I-2-25*.

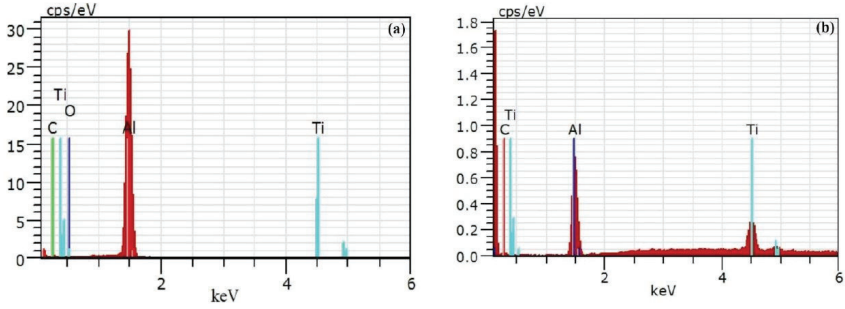

Figure I-2-24. Elemental composition of the treated area: a) specimen No 1 and b) specimen No 2

The phase composition of sample No 1 indicates the presence of a diffraction peak corresponding to pure Al. No peaks corresponding to TiCN or other phases were detected, proving that the nanoparticles were not successfully introduced into the Al matrix. The diffractogram of sample No 2 shows peaks of pure Al, as well as TiCN maxima, indicating the presence of nanoparticles in the surface layer of the substrate.

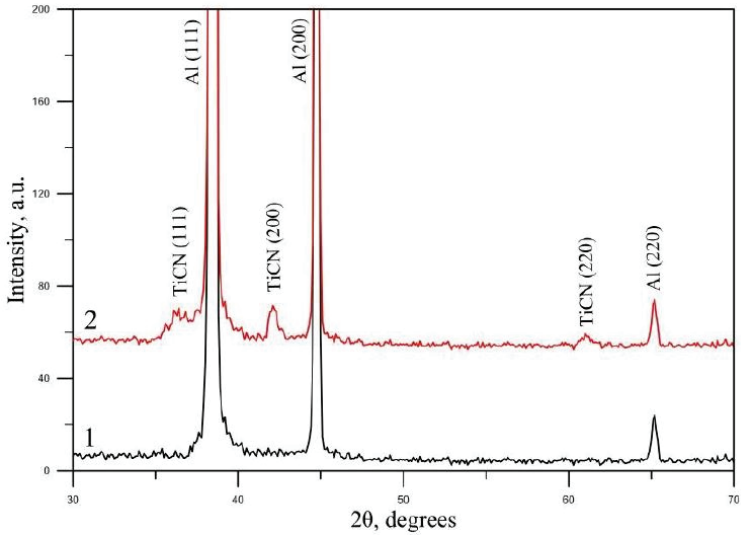

Figure I-2-25. X-ray diffraction analysis of specimens 1 and 2 after EBT

To increase the concentration of nanoparticles in the treated zone, a second layer of TiCN was applied to an already treated sample of Al + TiCN. For this purpose, the surface was subjected to secondary electron beam treatment under the same technological conditions.

Fig.I-2-26 shows the results of the post-repeated EBT sample obtained by X-ray diffraction analysis. It can be clearly seen that the diffraction peaks associated with TiCN are significantly higher, which means that the concentration of introduced particles is much higher than that of a single introduction cycle (sample No 2).

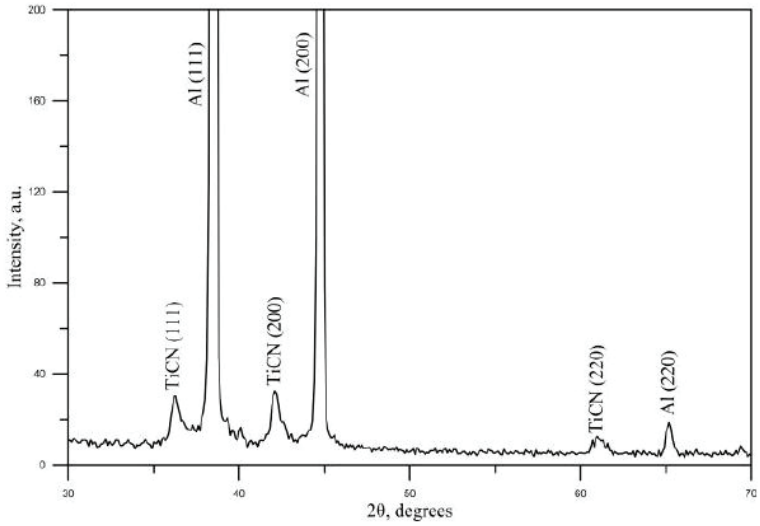

Figure I-2-26. X-ray diffraction analysis of sample No 2 after repeated EBT

The microhardness $HV_{0.02}$ of the initial material and the treated areas of both samples was investigated. The microhardness of Al is 30 ± 3 $HV_{0.02}$. Considering sample No 1, the hardness of the treated area is 101 ± 5 $HV_{0.02}$. It is about 3 times higher than that of aluminum. As already mentioned in the case of sample No 1, the nanoparticles were not successfully introduced, therefore, the increased microhardness is due only to electron beam processing of the material. The results for sample No 2 show a microhardness of 686 ± 7 $HV_{0.02}$. This means that the treated area is about 20 times stiffer than the aluminum pad. The higher value of the microhardness of sample No 2 compared to those of sample No 1 is due to

the aluminum nanoparticles of TiCN. The microhardness value of secondary treated sample No 2 reaches about 1150 $HV_{0.02}$. Therefore, with an increase in the amount of nanoparticles, the microhardness also increases.

The nanoparticles of TiCN are found to be successfully introduced into the aluminum matrix when the electron beam scanning is performed with a higher frequency. This in turn contributes to a longer lifetime of the liquid bath, as well as to good conditions for homogeneous distribution of the nanoparticles. The increase in microhardness in the treated zone is mainly due to the increase in The concentration of nanoparticles.

2.6 Surface modification of AlSi12Cu2NiMg alloy substrate with TiCN nanoparticles at two concentrations by electron beam irradiation

AlSi12Cu2NiMg alloy is mainly used for the production of pistons for internal combustion engines operating under high temperature and high wear conditions. Therefore, we believe that the application of a firm and durable coating on the pistons is appropriate for their practical use.

For the smearing of piston alloy samples, we used the same mixture as for the aluminum specimens, i.e. with TiCN nanoparticles.

34 Samples of AlSi12Cu2NiMg – *fig.I-2-27* were wet grounded to #1 200 grinding paper, dried with ethyl alcohol, coated with TiCN nanopowder mixture, and then treated with an electron beam in a circular incremental motion - d = 5.8 split circular development.

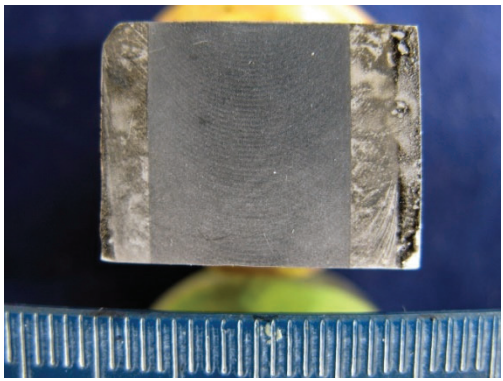

Figure I-2-27. Samples of AlSi12Cu2NiMg, coated with TiCN nanopowder mixture and electron beam treated

The conditions of EBT are the following: I_b = 18 ÷ 30 [mA], v = 0.5 ÷ 5 [cm/s], f = 1 ÷ 10 [kHz]; U = 52 [kv]; I_f = 472 [mA]; P = 1 300[W]

The designation of the samples and the conditions for electron beam processing (EBT) are given in *table I-2-5*.

Table 2-5. Electron beam processing conditions

Sample's designation	I_b[mA]	v [cm/s]	f [kHz]	U [kv]	I_f [mA]	P [W]
P2	25	2	10	52	472	1300
P9	25	1,5	10	52	472	1300
P10	30	2,5	10	52	472	1560
P21	25	3	10	52	472	1300
P23	25	5	10	52	472	1300
P25	25	1,5	1	52	472	1300
P26	25	3	1	52	472	1300

After subjecting the specimens to EBT they were grounded with #1 200 and #4 000 grinding paper and mechanically polished. The microstructure was revealed with a 0.5% solution of HF in water.

2.7 Investigation of the microstructure and properties of AlSi12Cu2NiMg alloy based nanocomposite, reinforced with TiCN nanoparticles

2.7.1 Light microscopy examination and microhardness test

Metallographic studies of the microstructure of the samples were performed using a PolyvarMet optical microscope at magnifications up to x1000. The microhardness was measured using a MicroDuromat 4000 microhardness meter with a load of 20 g, a loading time of 10 s, and a holding time of 10 s.

The microstructure of sample PB10 is shown in *fig.I-2-28*. It has a dense and even coating, and below - a modified zone with a refined dendritic structure of 100-150 μm thickness and increased microhardness compared to that of the matrix. The microhardness in the zone is 1720 MPa, in the matrix - 1157 MPa.

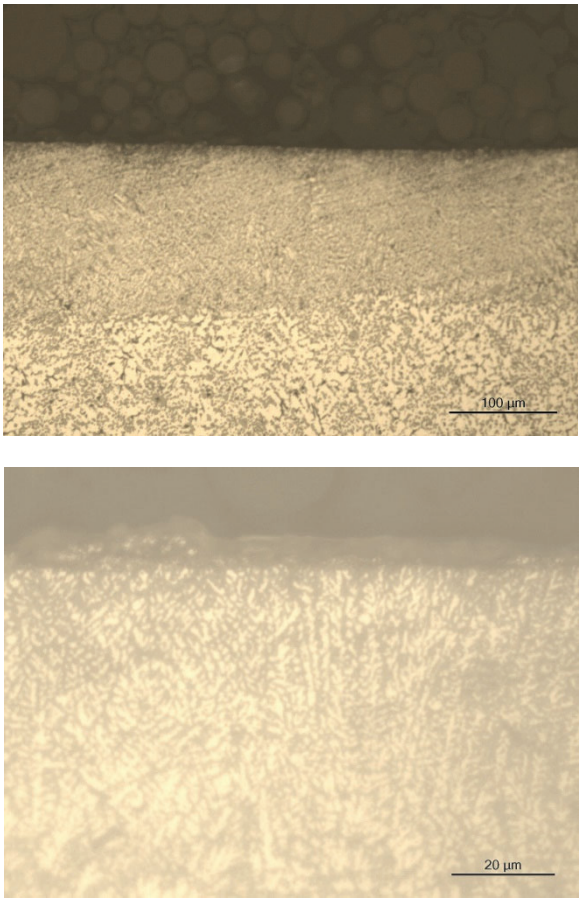

Figure I-2-28. Microstructure of sample P10

The microstructure of sample P25 is shown in *fig.I-2-28*. It has a modified area with a refined dendritic structure. The thickness of this zone is about 120 µm. The microhardness in this zone is 1943 MPa and in the matrix is 1152 MPa.

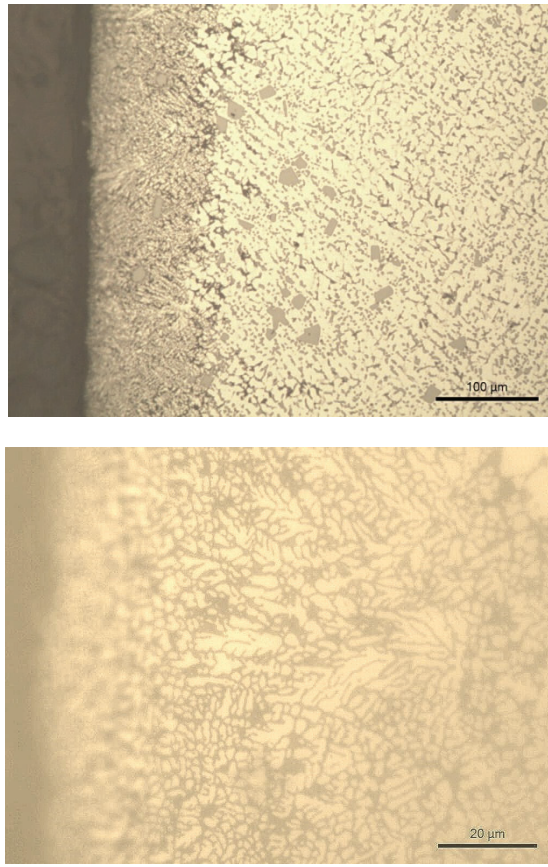

Figure I-2-29. Microstructure of sample P25

Fig.I-2-30 shows the microstructure of sample P26.

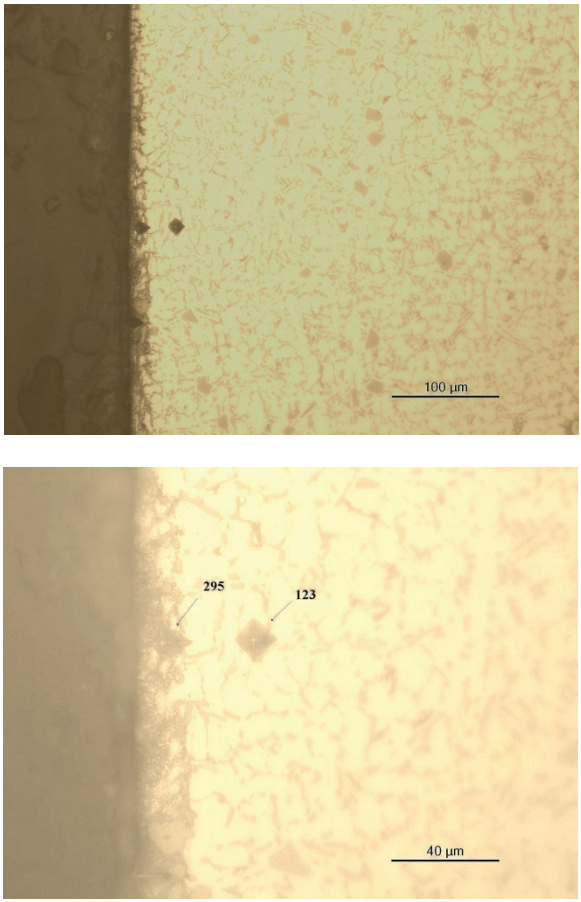

Figure I-2-30. Microstructure of sample P26

A modified zone of about 10-15 µm thickness was observed in sample P26, densely strewn with fine inclusions. In this zone, the microhardness is higher than that of the substrate - from 1206 MPa in the matrix to 2893 MPa in the modified zone – *fig.I-2-30*.

2.7.2 XRD investigation

XRD analysis was performed using a Panalytical X'Pert Pro X-ray powder diffractometer with Cu Kα radiation (λ = 0.154 nm). Full identification of the model was made using X'Pert HighScore Plus software, version 2.2e (2.2.5), PANalytical B.V. Material identification and analysis were performed using PDF-2 Release 2009 (Powder Diffraction File). These studies were conducted by Dr. Konstantin Borodianskiy, Ariel University, Israel. The following geometry is applied: Grazing Incidence (GI): 40mA, 40kV, angle - 1 °, step size - 0.02 °, step time - 1 sec.

Samples P0 (uncoated, treated with a beam current of 18 mA, a beam velocity of 0.5 cm / s, and a power of 936 W) and sample P1 (coated with 9 mg TiCN, i. concentration 0.045 mg / mm^2 treated at the same EBP parameters were subjected to XRD analysis.

An X-ray diffraction pattern of sample P0 (piston alloy after electron beam treatment) is observed in *fig.I-2- 31*. Peaks of pure aluminum and silicon are observed (ICDD: 01-071-4631).

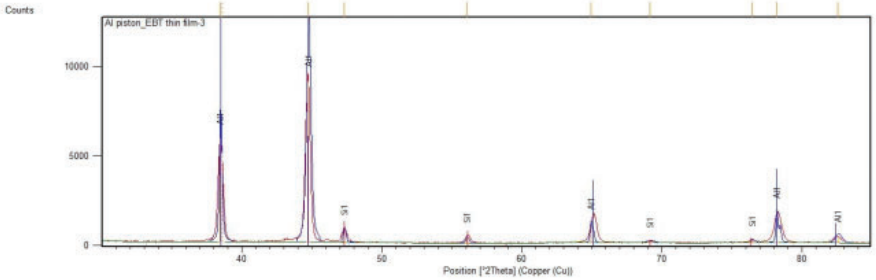

Figure I-2-31. X-ray diffraction pattern of sample P0 (Piston alloy after electron beam treatment)

Fig.I-2-32 shows an X-ray diffraction pattern of sample P1, a piston alloy with TiCN- nanoparticles embedded by EBP. Peaks of pure aluminum, silicon, and Ti_2CN are observed.

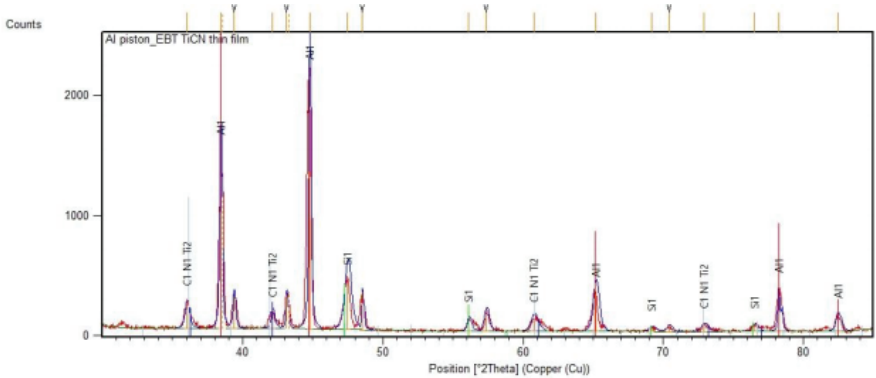

Figure I-2-32. X-ray diffraction pattern of sample P1 (piston alloy with TiCN nanoparticles embedded by EBT)

XRD study

XRD analysis was performed using a Panalytical X'Pert Pro X-ray powder diffractometer with Cu Kα radiation (λ = 0.154 nm). Full identification of the model was made using X'Pert HighScore Plus software, version 2.2e (2.2.5), PANalytical B.V. Material identification and analysis were done using PDF-2 Release 2009 (Powder Diffraction File). These studies were conducted by Dr. Konstantin Borodianskiy, Ariel University, Israel. The following geometry is applied: Grazing Incidence (GI): 40mA, 40kV, angle - 1 °, step size - 0.02 °, step time - 1 sec.

Two samples were subjected to XRD analysis: B0 - uncoated, treated with a beam current of 18 mA, a beam velocity of 0.5 cm / s and a power of 936 W, and sample B1 coated with 9 mg TiCN, i. concentration 0.045 mg / mm^2 treated at the same EBT parameters.

Fig.I-2-33 shows an X-ray diffraction pattern of sample B0 (piston alloy after EBT). Peaks of pure aluminum and silicon are observed (ICDD: 01-071-4631).

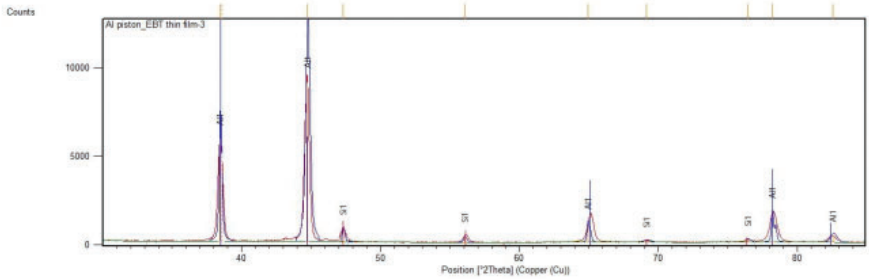

Figure I-2-33. X-ray diffraction pattern of sample P0 (Piston alloy after EBT)

Fig.I-2-34 shows an X-ray diffraction pattern of sample P1, a piston alloy with EBT- embedded TiCN nanoparticles. Peaks of pure aluminum, silicon, and Ti_2CN are observed.

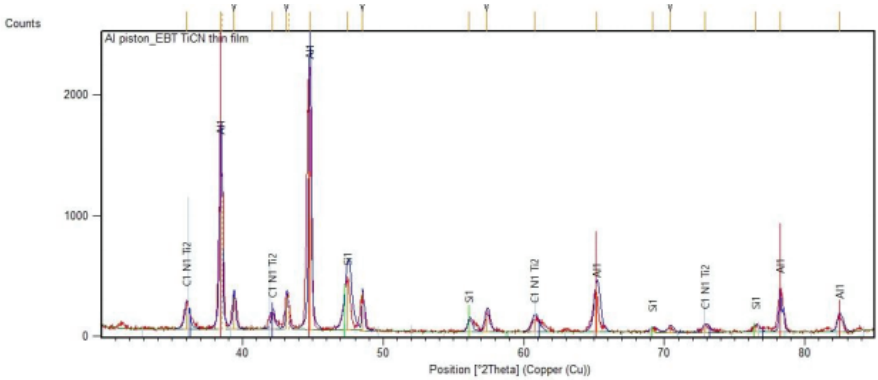

Figure I-2-34. X-ray diffraction pattern of sample B1 (piston alloy with TiCN-embedded nanoparticles by EBT)

Conclusions on the effect of modifying AlSi12Cu2NiMg alloy substrate with TiCN nanoparticles on microstructure and properties

The following samples can be listed as the most successful as a result of TiCN nanopowder coating and subsequent EBT:

• sample P2, (beam current 25 mA, beam motion speed 2 cm / s and power 1300 W) – the presence of a modified zone with a thickness of about 40 μm, the microhardness in this zone is higher than that of the matrix with 38 %;

• sample B10 (beam current 30 mA, beam motion speed 2.5 cm / s, frequency 10 kHz) – the presence of a dense layer and a modified zone below it (100-150 μm) on the surface. The microhardness of the modified zone is 49% higher than that of the matrix. The sample is subjected to SEM and EDX analyses, which demonstrate the penetration of nanoparticles into the metal matrix.

• sample P9 (beam current 25 mA, beam motion speed 1.5 cm / s, frequency 10 kHz) – the presence of a coating surface, below which there is a modified zone about 100 μm thick with increased microhardness - 40% higher than that of the matrix;

• sample P21 (beam current of 25 mA, beam motion speed of 3 cm / s, and frequency of 10 kHz) at which a coating with a uniform thickness of about 10 μm was detected was also examined by SEM and EDX analyses. The presence of Ti in the surface layer and in the area below it was detected.

• sample P23 (beam current 25 mA, beam motion speed 5 cm / s, frequency 10 kHz) - embossed coating with a relatively uniform but small thickness of about 3-4 μm. A modified area with a 60-70 μm thick dendritic structure is observed beneath the coating.

• sample P25 (beam current 25 mA, beam motion speed 1.5 cm / s, frequency 1 kHz) the thickness of the modified zone is about 120 μm, with 69% higher microhardness compared to that of the matrix.

• sample B26 (beam current 25 mA, beam motion speed 3 cm / s, frequency 1 kHz), modified zone with a thickness of about 10-15 μm. The largest difference in the microhardness of the modified zone compared to that measured on the substrate - 139% is measured in this sample.

As a general conclusion, it can be said that the coated specimens with a concentration of 0.03 mg / mm^2 TiCN do not perform better than those coated with 0.015 mg / mm^2 TiCN.

2.7.3 Conclusions regarding the effect of reinforcing AlSi12Cu2NiMg alloy substrate with TiCN nanoparticles on microstructure and properties

The following samples can be listed as the most successful as a result of TiCN nanopowder coating and subsequent EBP:

- sample P2, (beam current 25 mA, beam speed 2 cm / s and power 1300 W) – the presence of a modified zone with a thickness of about 40 μm, the microhardness in this zone is higher than that of the matrix by 38%;

- sample P10 (beam current 30 mA, beam travel speed 2.5 cm / s, frequency 10 kHz) – the presence of a dense surface and a modified area below it (100-150 μm). The microhardness of the modified zone is 49% higher than that of the matrix. The sample is subjected to EDX analyses, which demonstrate the penetration of nanoparticles into the metal matrix.
- sample P9 (beam current 25 mA, beam movement speed 1.5 cm / s, frequency 10 kHz) – the presence of a coating surface below which there is a modified zone about 100 μm thick with increased microhardness - by 40% more - higher than that of the matrix;
- sample P21 (beam current of 25 mA, beam speed of 3 cm / s, and frequency of 10 kHz) at which a coating with a uniform thickness of about 10 μm was detected was also examined by EDX analyses. The presence of Ti in the surface layer and in the area below it was detected.
- sample P23 (beam current 25 mA, beam speed 5 cm / s, frequency 10 kHz) - embossed coating with a relatively uniform but small thickness of about 3-4 μm. A modified area with a 60-70 μm thick dendritic structure is observed beneath the coating.
- sample P25 (beam current 25 mA, beam speed 1.5 cm / s, frequency 1 kHz) the thickness of the modified zone is about 120 μm, with microhardness higher by 69% compared to that of the matrix.
- sample P26 (beam current 25 mA, beam speed 3 cm / s, frequency 1 kHz), modified zone with a thickness of about 10-15 μm, with the biggest difference in the microhardness of the modified zone compared to that of the modified zone.

In conclusion, the piston alloy AlSi12Cu2NiMg substrate has surface coatings and surface modified areas up to 120μm thick, consisting of primary and secondary Si crystals and precipitates that are assumed to originate and grow on substrates - nanoparticles (in smaller quantities there are always other germs) and an α-solid solution matrix. The resulting surface areas have a microhardness up to 139% higher than that of the substrate. Studies performed with various modern methods have revealed the presence of TiCN in the coating and the effect of modifying the surface of the substrate with it. The most suitable treatment modes are determined, which for the piston alloy are: I_b - 25-30 mA, v - 1.5-5 cm / s, f - 1 - 10 kHz.

References

1. S. Hao, H. Wang, L. Zhao, Nucl. Instrum. Methods Phys. Res. B 368 (2016) 81-85.
2. R. Zenker, Modern thermal electron beam processes e research results and industrial application, La Metall. Ital. (3) (2009).
3. M. Ormanova, P. Petrov, D. Kovacheva, Vacuum 135 (2017) 7-12.
4. C.W. Draper, J.M. Poate, Int. Metal Rev., 30 (2) (1985) 85-108.
5. R. Lazarova, R. Dimitrova, St. Parshorov, P. Petrov, Surface Electron Beam Alloying Light Metals using TiCN Nanoparticles, International Scientific Conference UNITECH 2017 Gabrovo, Proceedings, vol. III, 129-133.
6. Layers obtained on aluminum by nanopowder deposition and subsequent electron beam scanning R. Lazarova, R. Dimitrova, Y. Murdjeva, St. Valkov, and P. Petrov, Materials and Manufacturing Processes, Taylor&Francis, 2018, ISSN:1532-2475, DOI:10.1080/10426914.2018.1453148, 1-5. https://doi.org/10.1080/10426914.2018.1453148.
7. K.R.Ramkumar and S. Natarajan, Tensile properties and strengthening effects of Al 3003 alloy weldment reinforced with TiO_2 nanoparticles, Composites, Part B, 175, 2019, 107159.
8. E. Orowan: The Inst. of Metals, London, 1948, p. 451.
9. Chan, C.; Mazumder, J.; Chen, M. A Two-Dimensional Transient Model for Convection in Laser Melted Pool. Metall. Trans. A. 1984, 15, 2175–2184.
10. Kuzmanov, P.; Dimitrova, R.; Lazarova, R.; Cherepanov A.; Manolov, V. Investigation of the Structure and Mechanical Properties of Castings of Alloy AlSi7Mg, Cast Iron GG15 and GG25 and steel 345 GX120Mn12, Modified by Nanosized Powders. J. Nano. Nanosyst. 2014, 228(I), 11–18. DOI: 10.1177/1740349913510295.
11. Dimitrova, R.; Kuzmanov, P.; Lazarova, R.; Manolov, V. Investigation of Nanopowders Application in Metal Casting. Adv. Mat. Res. 2013, 629, 284–291. DOI: 10.4028/www.scientific.net/amr.629.284. 350
12. Lazarova, R.; Bojanova, N.; Dimitrova, R.; Panov, I.; Manolov, V. Influence of Nanoparticles Introducing in the Melt of Aluminum Alloys on Castings Microstructure and Properties. Int. J. Metalcast. 2016, 10(4), 466–476.

13. Chen, L.-Y.; Xu, J.-Q.; Li, X.-C. Controlling Phase Growth during Solidification by Nanoparticles. Mater. Res. Lett. 2015, 3(1), 43–49. DOI: 10.1080/21663831.2014.956264.
14. 415 Shaflei, S.; Divandari, M.; Boutorabi, S.; Naghizadeh, R. Characterization of TiCN Thin Films Deposited by Dc-Pulsed PACVD Using Methane Precursor. Mater. Res. 2014, 17(6), 1651–1657. DOI: 10.1590/1516-1439.309514.
15. Wenxia, F.; Shouxin, C.; Haiquan, H.; Guiqing, Z.; Zengtao, L. Electronic Structure and Elastic Constants of TiCxN1−x, ZrxNb1−xC and 420 HfCxN1−x alloys: A First-Principles Study. Physica B 2011, 406,3631–3635. DOI: 10.1016/j.physb.2011.06.058.
16. Sehrt, J.; Kleszczynski, S. Nanoparticle Improved Metal Materials for Additive Manufacturing. Progress Add. Manuf. 2017, 2, 179–191. DOI: 10.1007/s40964-017-0028-9.
17. Hosseini N, Karimzadeh F, Abbasi MH, et al. Tribological properties of Al6061-Al_2O_3 nanocomposite prepared by milling and hot pressing, Mater Des 2010, 31: 4777–4785.
18. S. Veličković et al., Tribological properties of aluminium matrix nanocomposites, Applied Engineering Letters Vol. 1, No 3, 2016, 72-79.
19. A. Muley et al., Mechanical and tribological studies on nano particles reinforced hybrid aluminum based composite, Manufacturing Rev., 2015, 2 – 26.
20. A. Lekatou et al., Aluminium reinforced by WC and TiC nanoparticles (ex-situ) and aluminide particles (in-situ): Microstructure, wear and corrosion behavior, Materials and Design 65, 2015, 1121–1135.
21. S. Anvari et al., Wear characteristics of Al–Cr–O surface nano-composite layer fabricated on Al6061 plate by friction stir processing, Volume 304, Issues 1–2, 15 July 2013, Pages 144-151.
22. Poovazhagan L, Kalaichelvan K and Sornakumar T. Processing and performance characteristics of aluminum-nano boron carbide metal matrix nanocomposites. Mater Manuf Process, 2016; 31: 1275–1285.
23. Mihail Kolev, Stefan Valkov, Rumyana Lazarova, Peter Petrov, Rossitza Dimitrova, and Vanya Dyakova, Tribological Properties of TiCN Nanosized Powder Reinforced Aluminum, VEIT 2020.
24. R. Lazarova et al., Coatings obtained by TiCN nanopowder deposition on aluminum by electron beam treatment, Materials and Manufacturing Processes, 33(10), pp. 1128-1132, 2018.

25. J. C. Fisher, E. W. Hart and R. H. Pry: Acta Metall., 1953, vol. 1, 336.
26. E. W. Hart: Acta Met., 1972, vol. 20, p. 275.
27. R. H. Jones: Predicting the stress-strain behavior of polycrystalline α-iron-containing hard spherical particles, (U. S. Atomic Energy Commission, W-7405-ENG-48, Lawrence Berkeley National Laboratory, 1973) https://escholarship.org/uc/item/0gj769z4, Accessed January 2019.
28. Amal E. et al., 2017, Properties of aluminum matrix nanocomposites prepared by powder metallurgy processing J. King Saud Univ. – Eng. Sci. 29 295–99.
29. Y. Qin et al., Structure and wear characteristics of TiCN nanocomposite coatings fabricated by reactive plasma spraying, Surface & Coatings Technology 342 (2018) 137–145.
30. A. D. Moghadam et al., Effect of In-situ Processing Parameters on the Mechanical and Tribological Properties of Self-Lubricating Hybrid Aluminum Nanocomposites, Tribol Lett (2016) 62:25.
31. K. K. Ekka, S. R. Chauhan, Varun, Dry sliding wear characteristics of SiC and Al_2O_3 nanoparticulate aluminium matrix composite using Taguchi technique, Arab. J. Sci. Eng., 40 (2), 2015: 571–581.
32. Y. Wang, S. C. Tung, Scuffing and wear behavior of aluminum piston skirt coatings against aluminum cylinder bore, Wear, 225–229, 1999, 1100–1108.
33. Mosleh-Shirazi S., Akhlaghi F. and Li D., Effect of SiC content on dry sliding wear, corrosion and corrosive wear of Al/SiC nanocomposites, Trans Nonferrous Met Soc China 2016, 26: 1801–1808.
34. Nemati N., Khosroshahi R., Emamy M., et al., Investigation of microstructure, hardness and wear properties of Al-4.5 wt.% Cu-TiC nanocomposites produced by mechanical milling. Mater Des, 2011, 32: 3718–3729.
35. Sharifi E. M. and Karimzadeh F., Wear behavior of aluminum matrix hybrid nanocomposites fabricated by powder metallurgy, Wear, 2011, 271: 1072–1079.
36. Stefan Valkov, Ruslan Bezdushny, Rumiana Lazarova, Rossitza Dimitrova, and Peter Petrov, Surface Modification of Al Substrate with TiCN Nanopowder by Electron-beam Treatment, AIP Conference Proceedings 2075, 160017 (2019); https://doi.org/10.1063/1.5091344.

CHAPTER I-3

ALUMINUM BULK NANOCOMPOSITES

RUMYANA LAZAROVA

For the development of this chapter we have used the following articles with the kind consent of the publishers Taylor&Francis and IOP Conference Series: Lubomir Anestiev, Rumyana Lazarova, Peter Petrov, Vanya Dyakova, and Lenko Stanev, On the strengthening and the strength reducing mechanisms at Aluminium Matrix Composites, reinforced with TiCN nano-sized particulates, Philosophical Magazine & Philosophical Magazine Letters, https://www.tandfonline.com/doi/full/10.1080/14786435.2020.1821114 and R Lazarova, S Valkov, V Dyakova, and P Petrov, Layers obtained on TiCN aluminum nanocomposites by electron-beam treatment International Conference on Novel Functional MaterialsIOP Conf. Series: Materials Science and Engineering 733 (2020) 012017IOP Publishing doi:10.1088/1757-899X/733/1/012017, https://www.researchgate.net/publication/338718736_Layers_obtained_on_TiCN_aluminum_nanocomposites_by_electron-beam_treatment#fullTextFileContent.

3.1. Introduction

We have reviewed the methods of manufacturing nanocomposites in chapter 1 – "General introduction" on which base we could conclude that high energy ball milling succeeding by isostatic pressing and extrusion is a complex method providing homogenous powder dispersion and high density of the product. Powder metallurgy assures homogenous microstructure, proper bonding between the matrix material and reinforcements, avoids porosity and improves physical, mechanical, and tribological properties [1, 2]. This method is the easiest route to synthesis the metal matrix composites with hard and soft reinforcements in comparison with the other manufacturing techniques. The powder metallurgy technique was used to produce pure aluminum nanocomposite with TiO_2 nanoparticles which were uniformly distributed within the matrix alloy with a low degree of porosity [3]. The powder metallurgy route and conventionally vacuum

sintered were used for aluminum-carbon nanotube composite fabrication [4, 5]. This method is favorable for producing nanocomposites with two-dimensional reinforcement as graphene although the production of metal matrix nanocomposites with a uniform distribution of graphene, strong interfacial bonding, without unfavorable reactions, and with better isotropic properties is still a challenging topic [6]. Because of that, we chose this way to produce bulk nanocomposites on an aluminum base with TiCN nanoparticle reinforcement [7]. This chapter is devoted to this topic, investigation of as produced nanocomposites and layers obtaining of them using EBT.

3.2. Aluminum bulk nanocomposites produced by powder metallurgy

In this section, we will consider two types of bulk aluminum nanocomposites - those reinforced with nanoparticles and in particular nanoparticles of TiCN and those reinforced with two-dimensional particles and in particular graphene particles.

3.2.1. Aluminum bulk nanocomposite reinforced with nanoparticles

3.2.1.1. Materials

The composite was prepared by the powder metallurgy (PM) route. As incentive powders were used a commercially available Al powder (Al, min 99.5 wt. %; Fe, max. 1 wt. % with a mean particle diameter of ~ 37 μm) and TiCN (nano-sized powder with a particle diameter of ~50 nm). Before processing the incentive reinforcement and matrix, powders were mixed in different weight proportions. The TiCN weight represented the following proportions: w = 2, 5, 10, 15, and 20 wt. %. After the mechanical mixing, each mixture was subjected to a mill and mix (M&M) procedure in a planetary agate ball mill for 10 min, at rotating speed - 500 rpm, room temperature, and under inert gas atmosphere (Ar). (Ball weight to powder weight ratio (BPR) used was 0.4225; the total weight of the balls 67.6 g and weight of the powder mixture 160 g, per M&M cycle.) The purpose of the M&M procedure applied was to prevent the liquation (respectively, the accompanying agglomeration) of the reinforcement, by embedding the reinforcement particles in the incentive powder surface. That way it was ensured easy handling of the green powder during subsequent processing

and a homogeneous distribution of the reinforcement throughout the samples.

3.2.1.2. Processing of the green powders

The as-prepared green powder mixtures were compacted into bars by cold isostatic pressing – *fig. I-3-1*. The produced bars were hot extruded (RUE 250 SS hydraulic press supplied with a mold heater and molds allowing a variable degree of reduction) at temperatures varying between 0.8-0.85 of the aluminum melting temperature. The hold time of the extrudates in the mold was up to 20 minutes, which ensured equalization of the temperature through the whole assembly, mold-extrudates, and degassing of the pre-pressings. The extrusion ratio used was 6:1. The produced rods were 12 mm in diameter. The friction between the mold and the extrudates was reduced by applying a high-pressure lubricant, "Vapor". To achieve the best results optimization of the process has been carried out by varying the hot extrusion process parameters. The objective was to obtain extrudates with high density, small-grained structure, good plasticity, and, most important, without particle agglomeration. The best results were achieved at (1) Cold compaction (2) Hot extrusion.

Figure I-3-1. Extruded bars with w = 0, 2, 5, 10, 15 and 20 wt. % TiCN

The technology consists of two stages:

1. Cold volume compression with at 600 MPa force and holding time under load 1 min.

2. Hot pressing at 470 ° C ± 10 ° C for 10 minutes and cooling in the air.

The optimization of the process has been achieved through the above-mentioned parameters, while the structure is kept small-grained and good plasticity is achieved at the high density of the compacted materials obtained.

The molding of *fig.I- 3-2* consists of the following elements:

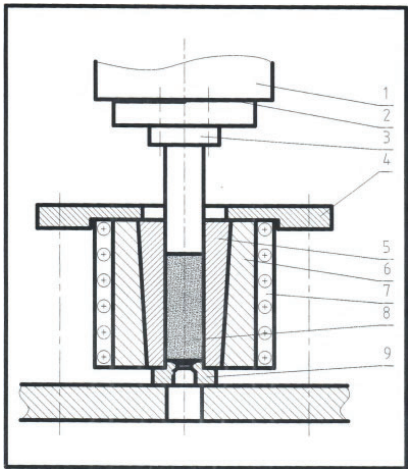

1. Piston
2. Insulation pad
3. Punch
4. Flange
5. Container
6. Bandage
7. Heating system
8. Preform
9. Matrix

Figure I-3-2. A scheme of obtaining round billets by right extrusion

As it could be seen from *fig.I-3-1* the surfaces of the extruded bars with 15% and 20% TiCN are too rough because of the large amount of powder. Which is why we excluded them from further studies?

3.2.1.3. Microstructure

Light microscopy

The LM samples were prepared using conventional grinding and polishing techniques; wet grounding (grinding paper up to # 2000) and electrolytic polishing and etching.

Quantitative measurements were performed using a metallographic microscope MIT 500, equipped with a digital camera DV500 and software for quantitative analysis. The mean grain diameter of samples of aluminum and reinforced with nanoparticles of TiCN aluminum was determined by quantitative metallographic analysis on five visual fields.

The metallographic photos of Al and Al+10% TiCN are shown in *fig. I-3-3* where the grains are embossed.

The mean grain diameter of aluminum samples is d = (1.925428 ± 0.569684) μm and the mean grain diameter of armed aluminum samples is d_{arm} = (1.93358 ± 0.601238) μm. Therefore, the addition of nanoparticles in the Al matrix does not lead to changes in the grain size during hot extrusion. Here we should note that the nanoparticles that are added during the casting of the metal cause refining of the grain during its crystallization. This effect has been repeatedly established by many researchers. K. Wang et al. [8] manage to decreases the mean grain diameter by ultrasonic-assisted casting from 1 500 μm to 78 μm at 2 vol. % TiCN nanoparticles in commercially pure aluminum. Therefore, the role of grain refining for composite strengthening, which is described by the Hall-Patch equation, is significant in composites fabricated by casting [8]. In hot extruded composites, as in our case, the greatest share of strengthening has the obstruction of the movement of dislocations, as we will see that in the next chapter.

The microhardness of the samples was measured using a MicroDuromat 4000 microhardness tester with a load of 20g, a time to reach the load of 10s, and a retention time of the load of 10s. The mean values of 10 measurements are shown in *table I-3-1*. Because of the great agglomeration of the nanoparticles in the composite with 20 wt. % TiCN, we consider the microhardness result to be irrelevant.

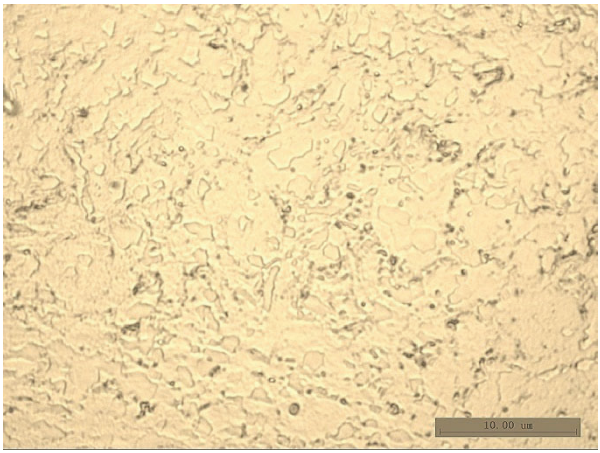

a

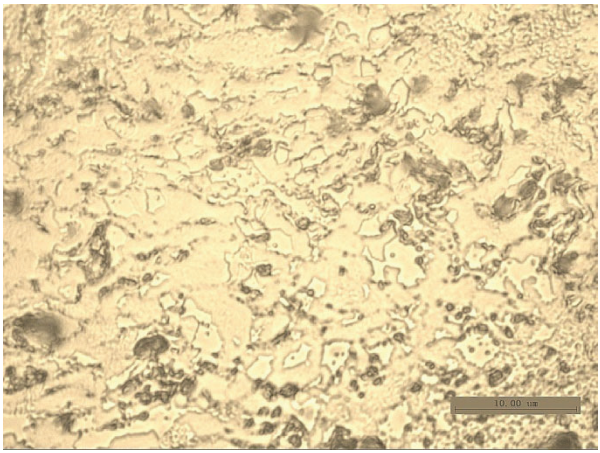

b

Figure I-3-3. Microstructures of: a) Al- sample and b) Al with 10 wt% TiCN nanoparticle sample

Table I-3-1. TiCN nanoparticles content and microhardness of aluminum samples

No of sample	TiCN nanoparticles content in the sample [wt%]	Microhardness HV [MPa]
1	0	412
2	2	432
3	5	490
4	10	539
5	15	608
6	20	-

It can be seen – *fig.I-3-4*, that the microhardness increases gradually from 412 MPa in the aluminum sample to 608 MPa in the sample with 15 wt. % TiCN nanoparticles. The microhardness of (432-608) MPa of the bulk samples with (2-15) wt. % TiCN is one order of magnitude lower than the microhardness of the surface nanocomposite samples of (5511-7826) MPa – *table I-2-1*. These results show that the electron beam treatment method is very effective for surface nanocomposite fabrication of products with very high microhardness. The EBT itself causes an increase in microhardness.

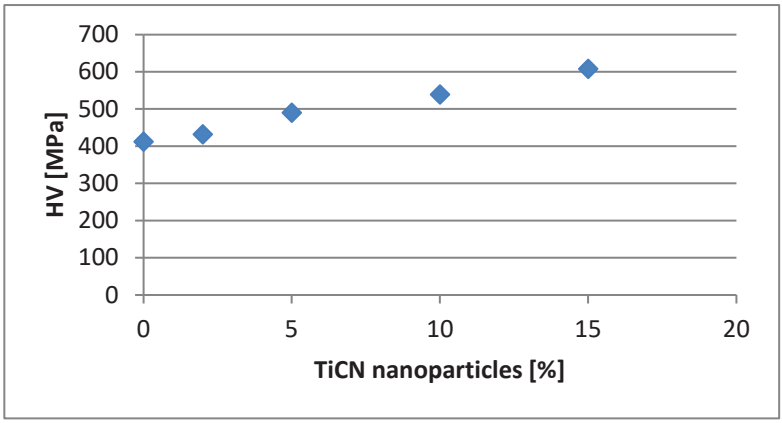

Figure I-3-4. Microhardness increasing with TiCN nanoparticles content in aluminum samples

The authors of [9] prepared Al-12Si composites with Al_2O_3 nanoparticles up to 10 wt. % of reinforcement by hot pressing and subsequent hot extrusion. The Vickers hardness of the composites increased first (for 2 and 5 wt. % reinforcement) and then decreased (for 10 wt. % reinforcement). The hardness decreasing is explained by the porosity and irregularities generated by the agglomeration of nanoparticles at 10 wt. % nanoparticles. Our results indicate a homogeneous microstructure, without agglomerates even at 10 and 15 wt. % TiCN nanoparticles which we consider a significant success.

Scanning electron microscopy

The *SEM* samples were prepared using conventional grinding and polishing techniques; wet grounding (grinding paper up to # 3000), mechanical polishing with diamond paste and etching, at room temperature, with 0.5% water solution of hydrofluoric acid. The microstructure of the aluminum matrix composites (AMCs) was studied by a scanning electron microscope (SEM/FIB LYRAI XMU, TESCAN) equipped with an EDX detector (Quantax 200, Brücker).

The SEM micrographs, taken from two of the specimens, those with weight fraction of TiCN, w=5 wt. % and w=10 wt. %, are shown in *fig.I-3-5 (a)* and *(b)*. The microstructure consists of α- matrix phase (fcc-Al), a negligible quantity of the $FeAl_3$ precipitates, and TiCN nano-particles. The $FeAl_3$ precipitates are in the form of ultrafine dispersoids, which are evenly distributed throughout the specimen's volume. They are not visible in the photo and the $FeAl_3$ peak is not registered on the EDX spectrum – *fig.I-3-5 (c)*. *Fig.I-3-5 (a)* shows the absence of agglomerates and an even distribution of the reinforcement particles throughout the specimen. This favorable result is attributed to the mill and mix procedure which was applied before the processing of the powder mixture. The micro-grooves observed in the figure were formed during sample preparation when some of the reinforcing particles were dragged by the abrasive of the grinding paper. Here we would like to add that the authors of [9] obtained an inhomogeneous microstructure, with agglomerates at 10 wt. % of Al_2O_3 nanoparticles, which degrades the hardness and mechanical properties of the material at this content of the reinforcement.

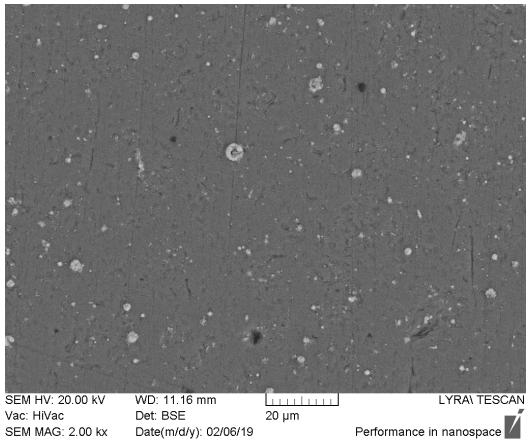

(a)

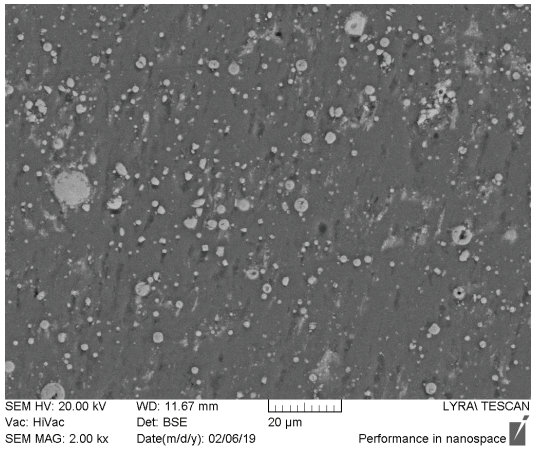

(b)

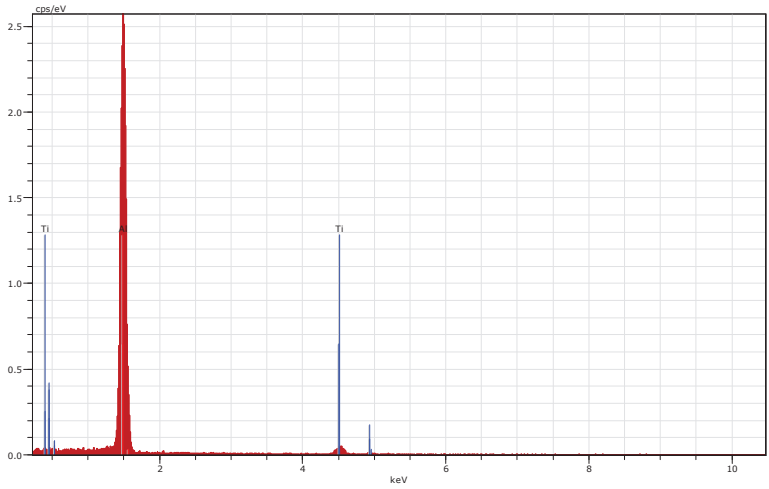

(c)

Figure I-3-5. SEM micrographs, taken from samples with *w*= 5 wt.% - (a), *w*= 10 wt.% - (b) and EDX spectrum of sample wuith *w*= 10 wt.% - (c)

Al6061/Al_2O_3 composites with concentrations of 5, 10, and 15 wt% Al_2O_3 nanoparticles were fabricated by stir casting technique in [10]. It was achieved good distribution of the Al_2O_3 reinforcement phase within the nanocomposite. But a great amount of clustering was occurring with increasing the percentage of Al_2O_3 nanoparticles to 15 wt%.

Transmission electron microscopy

Fig.I-3-6 shows images of structures of laser-deposited aluminum-matrix nanocomposite with 35 vol. % TiC [11]. It can be seen that this method of production of AMNCs also ensures an even distribution of the particles in the matrix and a strong bond between them and the matrix. During the nonequilibrium laser-induced rapid melting and solidification, similar to the electron beam processing processes we use, the nanoparticles do not agglomerate to form clusters.

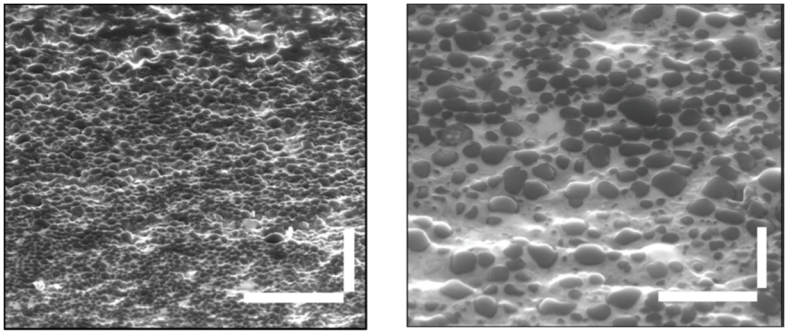

(a) **(b)**

Figure I-3-6. Surface and micro/nanostructure of laser-deposited aluminum matrix nanocomposites (AMNC) via laser-deposition of 35 vol. % TiC. 52° tilted cross-sectional SEM image of laser-processed AMNCs, showing that TiC nanoparticles are uniformly dispersed and distributed in aluminum – (a). FFT filtered high-resolution TEM image shows good bonding between TiC nanoparticle and aluminum – (b). Scale bar 1 μm in (a), 2 nm in (b)

The microstructure of the AMCs was studied also by transmission electron microscopy (TEM/ JEOL-JEM 1011, 100 KV). The microstructure was investigated in the deformed and no deformed states to understand the role of reinforced particles in the process of deformation. For this purpose standard specimens for the tensile test were subjected to tensile deformation.

The TEM specimens were prepared from plates cut perpendicularly to the load axis (ISOMET 1000, Bühler diamond disc saw) and close to the yield site of the tensile test specimens. The plates, with thickness ~700 μm, were mechanically thinned to foils, 20-30 μm thick, by grinding (SiC paper). From the foils were cut discs 3 mm in diameter, which were subsequently electrolytically polished at room temperature (Struers Tenupol Electropolisher, operating at 15V) in a solution of 20% $HClO_4$ and 80% CH_3COOH.

The TEM micrographs of two specimens reinforced with 10 wt. % TiCN are shown in *fig.I-3-7*. *Fig.I-3-7 (a)* shows the microstructure of a reference specimen, while *fig.I-3-7 (b)* shows the microstructure of a specimen after the tensile stress test. The reinforcement particles, embedded in the matrix, are clearly visible in both micrographs. An important result is that the reference specimen, *fig.I-3-7 (a)*, is void of dislocations, while the specimen undergone a tensile test shows a well-developed dislocation tangle around a group of reinforcement particles (the upper left corner in *fig.I-3-7 (b)*. It could, thus, be concluded that the

dislocations, seen in *fig.I-3-7 (b),* are generated during the tensile test, but not during the processing of the composites. It is also visible that the reinforcement particles have served their purpose as pinning points of the moving dislocations when the composite was under load. These results contradict the claims of some authors [12, 13], that the strengthening at AMCs, produced by hot extrusion, is mostly due to the difference between the thermal expansion coefficient of the reinforcement and the matrix, also known as, thermal mismatch effect (TME). According to these authors due to the TME inside the composite are produced thermal strains, which are accommodated by the generation of dislocations around the reinforcement particles. The results, shown in *fig.I-3-7 (a)* and *I-3-7 (b)*, however, do not support their arguments; Dislocations are not detected within the matrix, nor around the reinforcement particles in *fig.I-3-7 (a)*. Therefore, a conclusion could be drawn that the TME strengthening mechanism is not operative, at least in the case, studied here. For this reason, below it is excluded as a possible mechanism of the composite strengthening.

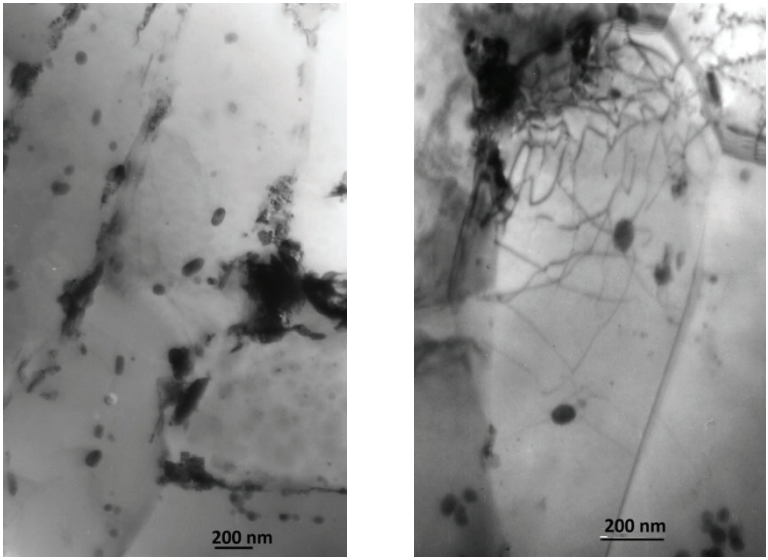

(a) **(b)**

Figure I-3-7. TEM micrographs of two specimens reinforced with 10 wt. % TiCN. (a) a reference specimen, (b) specimen after a tensile stress test. At the upper left corner of *fig.I-3-7 (b)* is seen a well-developed dislocations tangle around a group of reinforcement particles

All TEM observations were carried out in a bright field (BF-mode) at equally positioned samples (direct e-beam, perpendicular to the plane of the foils). *Fig.I-3-7* and *3-9* show TEM-micrographs obtained from foils prepared from samples that have undergone a tensile load (w = 10% TiCN; f = 0.0625). *Fig.I-3-7* shows embedded in the Al-matrix particles of the reinforcement. The bright halos around the reinforcement particles, the one in the center of *fig.I-3-7 (b)* and the one in *fig.I-3-7 (a)*, encircled in white, are due to deeper penetration of the etching agent in the Al-matrix during the electropolishing of the foil. The sketch in *fig.I-3-7 (c)* shows a cutoff of the foil along the A-A line and is intended to illustrate the origin of the halos seen in the micrograph. Several particles of the reinforcement TiCN embedded in the Al matrix are seen in *fig.I-3-7*. Two of those, the one in the center of *fig.I-3-7* and the one in *fig.I-3-7 (a)*, circled in white, are of special interest because of the bright halos surrounding them. This finding suggests that for some reason the Al-matrix around the reinforcement particles is much easily etched. Keeping in mind, that the etching depth depends on the free energy of the etched material [14] it could be concluded that the free energy of the Al-matrix in the vicinity of the reinforcement particles exceeds that of the Al-matrix in general. In this case, the matrix consists of pure Al. Therefore, the differences observed should be a result of an uneven deformation and/or an uneven distribution of microstructural defects induced by the tensile loading. The absence of a halo around the remaining particles is explained by the fact that the stress field, formed around them, is inaccessible to the etching agent, as illustrated in *fig.I-3-7 (c)*. The micrograph in *fig.I-3-7 (a)* shows a net of cracks in the Al-matrix formed between some of the reinforcement particles. It is seen that some of the cracks are branching in and that the branching occurs close to the reinforcement particles. Similar to particles in *fig.I-3-7* around most of the reinforcement particles are seen bright halos. At the center of the *fig.I-3-8 (a)*, is seen a TiCN particle (45-50 nm in diameter) with a dislocation tangle around it. A dislocation loop formed around that particle is also readily detected (see the blowup in *fig.I-3-8 (b)* for details). Just above a single particle (25-30 nm in diameter) is seen together with a series of parallel dislocations, presumably formed during the tensile loading of the specimen (see the blowup in *fig.I-3-8*. Note how one of the dislocations in *fig.I-3-8 (c)* passes through the particle by cutting it. From the minute disruptions on the dislocations, positioned at the right side of the particle, it could be figured out that the dislocations' movement direction (d.m.d.) is from left to right (as indicated in *fig.I-3-8 (c)*. The preceding findings indicate that the reinforcement particles with a size of nm and above serve as barriers to the free movement of the

dislocations, generated during tensile loading. On the contrary, the reinforcement particles below 20-30 nm in diameter, do not restrain the movement of dislocations because the latter does cut through them freely. *Fig.I-3-8* shows cracks formed in the Al-matrix. It is readily noticed that the cracks start and branch in the vicinity of the reinforcement particles. The dotted black line follows one of those cracks along its length. The blowups at the right side of *fig.I-3-8 (a)* show: *fig.I-3-8 (b)* - an Orowan's loop with a TiCN particle at the center; *fig.I-3-8 (c)* - series of linear dislocations, one of which at the moment of cutting through a TiCN particle (indicated with an arrow). The arrow (top center of *fig.I- 3-8 (c)*, indicated as d. m. d. - dislocations movement direction) shows the tentative direction of the dislocations' movement, which originated during the tensile loading of the specimen. The locations of the blowups, shown in *fig.I-3-8 (b)* and *I-3-8 (c)*, are indicated in *fig.I-3-8 (a)* with broken line circles. Due to the specificity of the foils examined (Recall that these are made of specimens that have undergone tensile loading.), the preparation of quality TEM foils and their study was accompanied by problems, some of which are listed below: (1) The tensile loading of the composite leads to a considerable overstressing of the Al-matrix near the reinforcement particles, thus, resulting in an uneven distribution of the plastic deformation throughout the sample. At electropolishing these parts of the Al-matrix are etched deeper [13], thus, forming around reinforcement a mushy zone of voids and remnants of the Al-matrix (see *fig.I-3-7*). The voids could penetrate the whole thickness of the foil in some cases. As a result, the adhesion forces, keeping the particles and the matrix together, are not strong enough which leads to the separation of some particles from the foil. Due to this circumstance, the TEM should be operated at the thicker parts of the foils, which deteriorates the micrographs' quality (the obtained images are without sufficient contrast), which makes the microstructural analysis difficult and labor-consuming. (2) A serious problem, usually encountered when working at low magnifications, is the e-beam diffraction (the Fraunhofer diffraction [14]), which occurs when the electrons are transmitted through the mushy zone formed around the reinforcement. (Recall, that due to the accumulated around the reinforcement stress the Al-matrix is etched easier and much deeper.) In this case, the diffracted e-beam is imaged on the TEM micrograph as a bright halo around the mushy zone, and the reinforcement particles' edges. Regrettably, this unwanted "optical" effect is unavoidable. Yet, when working with higher magnifications this unwanted effect is damped [15] and the quality of the micrographs return to their normal. (3) Another issue is the plastic deformation induced in the sample during the preparation of

the foil. However, these could be readily avoided keeping in mind that the depth of the damage produced inside the specimen during mechanical thinning is three times the grit size of the abrasive used [16]. Hence, using fine grinding paper at the mechanical thinning of the sample would eliminate the risk of inducing unwanted mechanical deformations in the TEM-foil. (4) The differences in the corrosion resistance of the matrix and the reinforcement could also lead to a problem, e.g., the protruding of the reinforcement above the matrix, or vice versa. The quality of the image, in this case, will be unaffected only if the protrusions are within the depth field of the microscope [16], which for a TEM are within 0.1 μm. Otherwise, the defocused parts of the foil will be blurred, hence, with low contrast. Therefore, one should be aware of the problems above that could arise when studying composites with nano-sized reinforcement. In the present research, we encountered two of the problems listed above (1) and (2). Yet the micrographs obtained (*fig.I-3-7* and *3-8*) allow drawing the following conclusions: (1) At tensile loading, the stress accumulated in the Al-matrix near the reinforcement particles, correlates with the VF of the reinforcement. (2) The stress field in the Al-matrix matches the geometry of the reinforcement particles (see *fig.I-3-7*). (3) The intensity of the stress field around the reinforcement particles gradually increases and reaches its maximum close to the particle-matrix boundary.

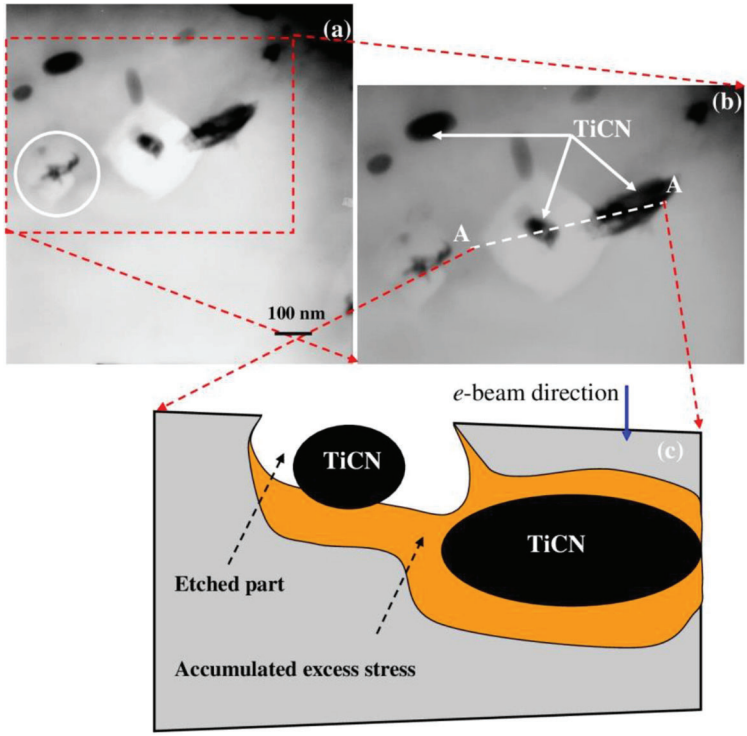

Figure I-3-8. A TEM micrograph showing embedded in the Al-matrix particles of the reinforcement. The bright halos around the reinforcement particles, the one in the center of *fig.I-3-8 (b)* and the one in *fig.I-3-7 (a)*, encircled in white, are due to deeper penetration of the etching agent in the Al-matrix during the electropolishing of the foil. The sketch in *fig.I-3-7 (c)* shows a cutoff of the foil along the A-A line and is intended to illustrate the origin of the halos seen in the micrograph.

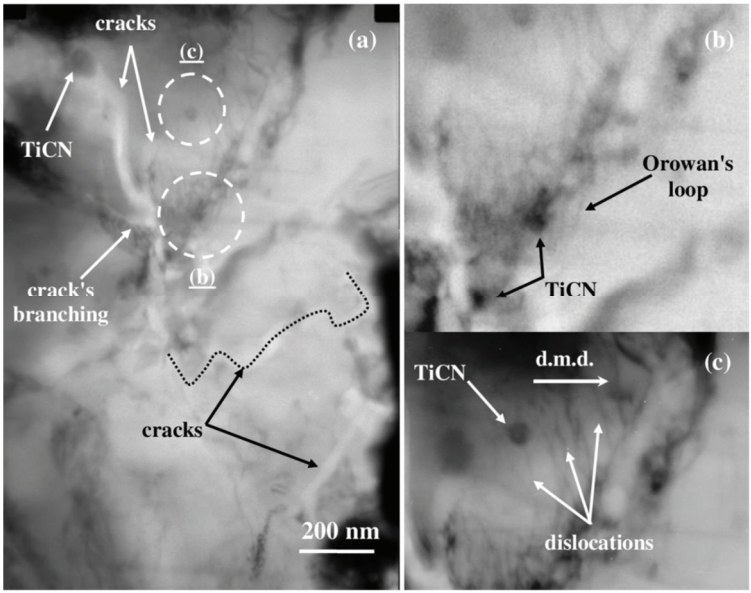

Figure I-3-9. A TEM micrograph showing cracks formed in the Al-matrix.

The interactions between dislocations and TiCN nanoparticles in the Al-TiCN nanocomposite that had previously been deformed by 0.2% are registered in *fig. I-3-10* [8]. *Fig.I-3-10 (a)* shows how the dislocations circumvent the nanoparticles and leave several Orowan loops surrounding them after crossing. The dislocation in *fig.I-3-10 (b)* is bypassing a nanoparticle through the Orowan mechanism and an Orowan loop is formed incipiently around it. The bowing out of the dislocation can also be observed in the matrix (*fig.I-3-10 (c)* and *(d)*). All this is in accordance with the reinforcement we have established by impeding the movement of dislocations in an aluminum-based nanocomposite with embedded TiCN nanoparticles.

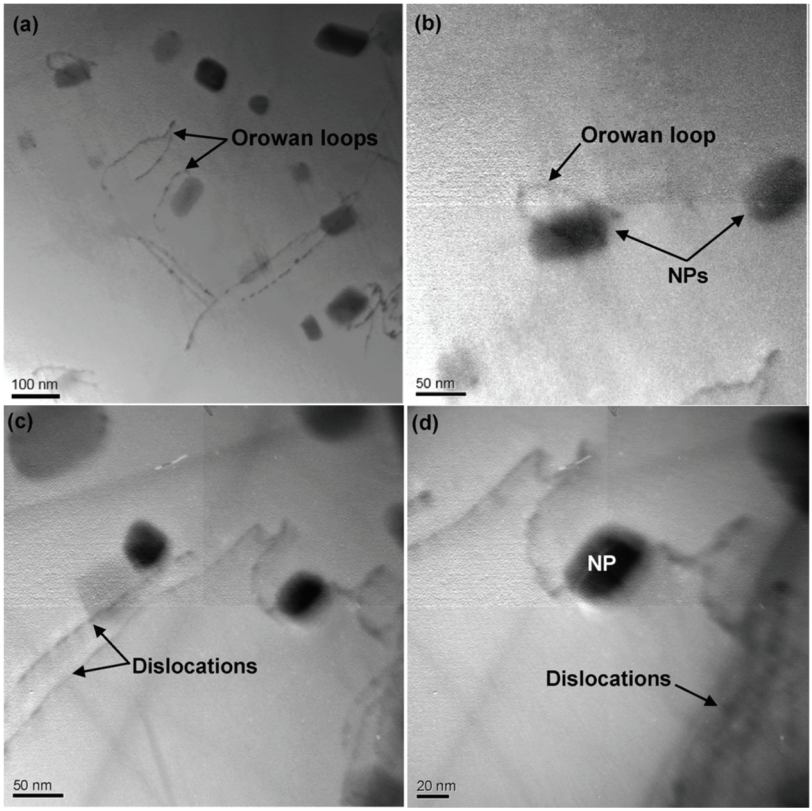

Figure I-3-10. [8] TEM images of the nanocomposite solidified at the average cooling rate of 60 K/s after tensile deformation (0.2% strained): (a) and (b) Dislocations circumvent nanoparticles and leave Orowan loops around them. (c) and (d) Dislocations bow out at the NP-matrix interface

3.2.1.4. Mechanical properties

The tensile stress tests were carried out on a Zwick-Roell (Z100) testing machine in an ISO-certified lab, which specialized in mechanical testing of aluminum-based materials. The tests were carried out at room temperature according to the standard EN ISO 6298-1 Method B with test parameters: Speed/yield point, 20 MPa s^{-1}, preload 5 Mpa, and a test speed of 0.0067 s^{-1}. The strain was determined by a laser extensometer.

The specimens for the stress-deformation (*s*-*e*) tests were prepared from the hot extruded rods, with different weight fractions of the reinforcement particles (TiCN): Three samples for the tensile tests, according to the requirements of the standard EN ISO 6892-1 (length 30 mm, diameter 6 mm); One sample, with the same dimensions, for reference purposes.

Tensile tests results

The results from the mechanical tests, the yield, and the ultimate tensile strength, of the studied composites, are summarized in *table I-3-2*.

Table I-3-2. Measured values of the mechanical properties of the studied specimens reinforced with different amounts of TiCN.

w TiCN wt. %	VF TiCN *f*	$s_{Y0.2\%}$ [MPa]			s_{UTS} [MPa]		
		Min.	Median	Max.	Min.	Median	Max.
0	0	74	74	74	96	96	96
2	0.0121	96	105	107	148	149	150
5	0.0306	110	113	116	154	153	145
10	0.0625	106	113	114	142	142	146
15	0.0957	103	104	105	127	122	128
20	0.1304	97	98	failed	114	113	failed

As seen, the experimental data for $s_{Y0.2\%}$ and s_{UTS}, depends on the volume fraction VF of the reinforcement, *f*, thus, it correlates with the results of the authors, who studied AMCs with nano-sized reinforcements so far; Initially, the composite strength increases with the increasing of the reinforcement's VF, but after f_{max}=0.0587 (9.4 wt.%), it decreases to values slightly above those of the matrix. Nevertheless, the obtained results clearly show that the addition of nano-sized TiCN particles into the pure Al-matrix results in a substantial increase of $s_{Y0.2\%}$ and s_{UTS}, compared to that of the matrix. For instance, the increase of $s_{Y0.2\%}$ at *w*= 5-10 wt.% TiCN is up to 57% and s_{UTS} is up to 60%, see *table I-3-2*.

The authors of [8] have managed to achieve a uniform dispersion of 2.0 vol. % TiCN nanoparticles in aluminum through a combination of ultrasonic dispersion and fast cooling processing. They claim that the intragranular distribution of NPs obtained by tuning cooling rates can yield about 391% and 18% enhancement in tensile strength and ductility, respectively, compared to that of Al. In our case, in the case of 3.0 vol. % TiCN nanoparticles in aluminum the tensile strength enhancement is 59 %.

The tensile test results show that the addition of nano TiO_2 particles to Al matrix composites increases the tensile strength of the alloy at room temperature along with an increase in the

TiO_2 particles' volume fraction from 0.5 to 4.5 vol. %. The measured maximum and minimum tensile strength of the composite samples were 250 and 198 MPa respectively. Great enhancement in tensile strength was observed due to the low degree of porosity and the good distribution of Nano ceramic particulates [16].

The maximum values of YS and UTS are obtained for the composites with 5 wt. % Al_2O_3 in [9]. They are 244 Mpa and 286 MPa, which showed an increase to about ~23% and 26%, compared with the Al-12Si matrix alloy. The increase of the same mechanical characteristics of our composites is 57% and 60% respectively. It was shown that there was a critical alumina content, above which the mechanical and tribological properties of composites in [9] were both lowered. The mechanical and tribological properties reach the maximum when the amount of Al_2O_3 nanoparticles comes to 10 wt%. The clusters formed by the addition of a high amount of Al_2O_3 act as stress concentration centers. The formation and dispersion of the clusters of nanoparticles within matrix material cause a decrease in the tensile properties.

The mechanical properties of the nanocomposite were increased with increasing the amount of Al_2O_3 nanoparticles into the Al6061 matrix [17]. They reach the maximum when the amount of Al_2O_3 nanoparticles comes to 10 wt% after this amount the mechanical and tribological properties of composites were both lowered. The increase of YTS and UTS was 37% and 30% respectively.

Lorella Ceschini et al. [18] have summarized a large amount of experimental data on the hardness, yield strength, and tensile strength of aluminum alloys-based nanocomposites obtained by different methods (traditional stir casting, compocasting, ultrasonic cavitation assisted casting, high pressure die casting, and others). These authors conclude that a common result for the different production techniques is that mechanical properties are generally enhanced with respect to the corresponding unreinforced alloys by adding reinforcing nanoparticles. The second important conclusion is that the improvement is generally superior to that obtained with micro-reinforcement at the same wt% fraction. In their opinion hardness, YS and UTS generally improve by increasing the reinforcement wt% content.

The data for the mechanical characteristic of two aluminum nanocomposites shown in *table I-3-3* could be compared. The aluminum, reinforced with 2 wt. % TiCN and produced by powder metallurgy (PM)

route has microhardness 324 % higher, yield strength - 128 % higher, and ultimate tensile strength - 63% higher compared with aluminum nanocomposites, reinforced with 2 wt. % Al_2O_3 and produced by Non-Contact Ultrasonic treatment (NC-US).

Table I-3-3. Mechanical characteristics of two aluminum nanocomposites reinforced with 2 wt. % different types of nanoparticles and produced by two different fabrication routes.

Nanocomposite	HV	YS	UTS	Reference
Al + 2 wt. % Al_2O_3 (NC-US)	102	47	92	[18, *table 4.3*]
Al + 2 wt. % TiCN (PM)	432	107	150	[*table 3-2*]

3.2.1.6. Conclusions

A detailed study of the influence of the volume fraction of the reinforcement additive on the microstructure, the mechanical properties, and the strengthening (strength reduction) mechanisms led to the following conclusions:

(1) The applied technological path allows producing composites with a relatively homogeneous distribution of the reinforcement particles in the matrix.

(2) The addition of nano-sized TiCN reinforcement particles into the Al-matrix leads to a substantial improvement of the mechanical properties. For instance, the obtained maximal increase of the yield strength of the composite was up to 57%, above that of the Al-matrix % at $w \approx 9$ wt. % TiCN.

3.3 Surface layers on aluminum bulk nanocomposites reinforced with TiCN nanoparticles [19]

It would be interesting to understand what would be the properties of surface layers on the bulk composites thus obtained after electron beam treatment. That is why we set ourselves the goal to investigate the microstructure and microhardness of aluminum nanocomposites layers containing 0%, 2%, 5%, and 10 wt. % TiCN nanoparticles formed after a surface treatment by electron beam irradiation with low and high energy power input.

3.3.1 Materials and methods

Aluminum nanocomposites containing 0, 2, 5, and 10 wt. % TiCN nanoparticles were produced as rods with 12 mm diameter using preliminary cold volume compression and succeeding hot pressing. Cylinders with a height of 10mm were cut from the rods. Their flat surfaces were treated by electron beam irradiation at following parameters: voltage (U) = 50 kV, speed of the specimen motion (V) = 50 mm/sec and scanning frequency (f) = 10 kHz. When the beam current I_b = 26 mA, the regime is low energy, designed as Q_1= 1300W. When the beam current I_b = 30 mA, the regime is high energy and designed as Q_2 =1500W. The experiments were carried out with Leybold Heraeus (EWS 300/15–60) electron beam equipment.

Metallographic samples were prepared by standard procedure: mounted in acrylic resin and wet ground up to 4000 grinding paper. Then the samples were electrolytic polished with the followed electrolyte: 575 ml methyl alcohol, 25 ml $HClO_4$, and 10 ml HNO_3. The metallographic observations were carried out by microscope PolyvarMet at magnifications up to 1000x.

The microhardness was determined by means of device MicroDuromat 4000 with a load of 20g, time for reaching the load - 10s, and time for holding the load - 10s.

The investigations by SEM and EDX were carried out using SEM/FIB LYRAI XMU.

Plates, with a thickness of ~700 μm, were mechanically thinned by grinding (SiC paper) to a thickness of 20÷30 μm. From the as-prepared foils were cut small discs of 3 mm in diameter, which were subsequently electrolytically polished at room temperature (Struers Tenupol Electropolisher, operating at 15V) in a solution of 20% $HClO_4$ and 80% CH_3COOH. These specimens were used for TEM analysis performed by TEM JEOL-JEM 1011 with 100 kV accelerating voltage.

The phase composition of the obtained samples was studied by X-ray diffraction (XRD). The experiments were carried out using CuKα characteristic radiation (1.54 Å). The measurements were conducted in the range from 5° to 90° at the 2θ scale with a step of 0.02° and counting time of 5 sec. per step.

3.3.2. Results and discussion

Temperature distribution during electron beam treatment

Fig. I-3-11 presents the results of the calculated temperature field distribution along with the depth of the electron beam treated area. The calculations are made by developing a heat model that is detailed in our previous work [20]. The numerical model is based on an analytical solution of the heat transfer equation using Green's functions.

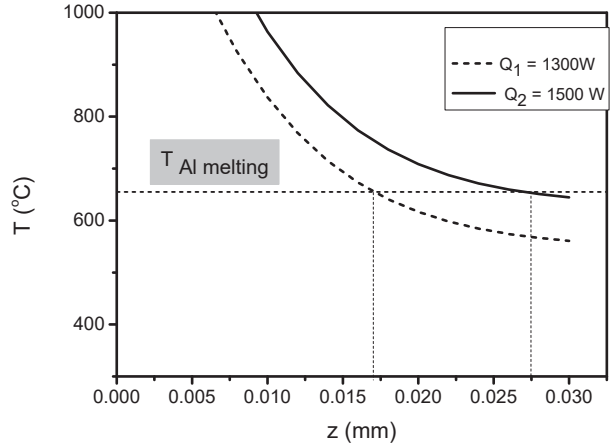

Figure I-3-11. Temperature distributions along the z-axis (depth of the treated zone) for different energy power input (V=50 mm/s, f=10 kHz)

The results presented in *fig.I-3-11* show that increasing the electron beam power leads to an increase in the alloyed layer thickness, which is expected. The molten zone depth decreases from 27 to 17 μm for energy power input variation from 1500 to 1300 W.

Samples treated with Q_1 (low energy power input)

The microstructures of samples with 0 and 10 wt. % TiCN treated with low energy power input Q_1 are shown in *fig.I-3-12.* The samples with (0 ÷ 10) wt. % TiCN have a clearly formed layer. The layers are too convex, so good focusing of the parent metal is impossible with a metallographic microscope. Such protrusive layers are formed during grinding and polishing samples because the hardness of layers is much higher than the hardness of the parent metal. It could be seen that the layer's microhardness of

the EBT aluminum sample is nearly two times higher than the microhardness of the parent metal. The tendency of microhardness alteration with TiCN content rising is shown in *fig.I-3-13*. The microhardness progressively increases with TiCN percentage and in the sample with 10 wt. % TiCN reaches a maximum of 1873HV after which it decreases. Analogic dependence of the strengthening from the weight fraction of TiCN nanoparticles contained in the parent metal is found out and explicated in [20].

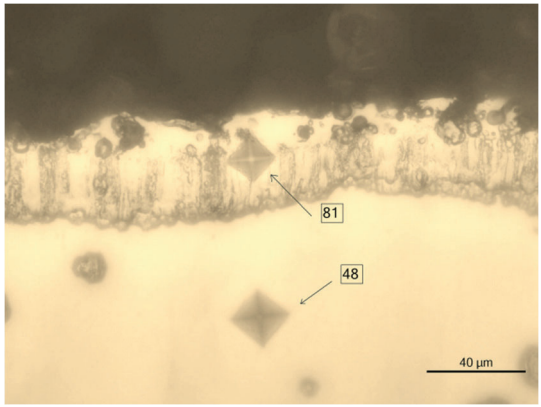

a

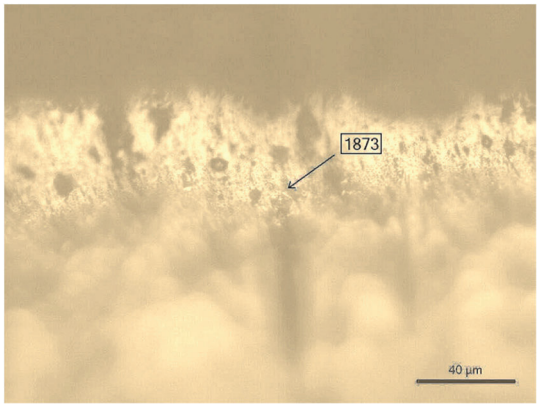

b

Figure I-3-12. Microstructures of samples treated with Q_1: (a) Al with 0 wt. % TiCN and (b) Al with 10 wt. % TiCN

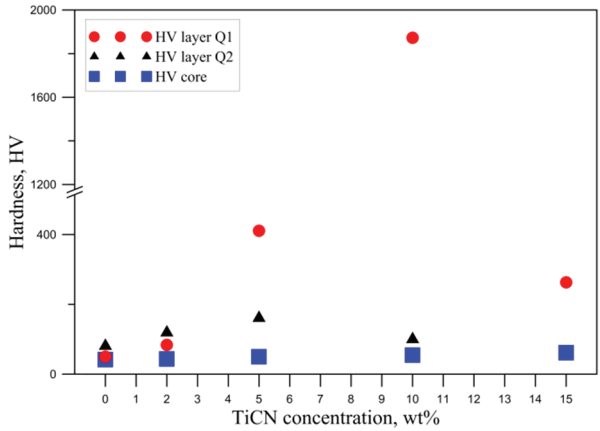

Figure I-3-13. Microhardness alteration with TiCN wt% in investigated aluminum nanocomposites

The EDX analyses show that there is 8.23 wt.% Ti in the sample with 10 wt. % TiCN – *fig.I-3-14,* which is an acceptable result, and the observed particles by SEM are precisely nanoparticles of TiCN – *fig. I-3-15 (a)*, *(b)* and *(c)*. The chemical spectrum unambiguously shows the sharp increase in titanium, carbon, and nitrogen content in the particles – *fig.I-3-15 (c)*. We have chosen to demonstrate larger particles to obtain clear results. TEM image – *fig.I-3-15 (d)* shows increased dislocation density around the nanoparticles, the formation of dislocation walls, and a substructure in the aluminum matrix. The TiCN nanoparticles prevent and stop the movement of dislocations resulting in the reinforcement of composites. TiCN particles can impede the dislocation motion through a variety of interaction mechanisms, some of which can operate simultaneously. The model of internal strain hardening distinguishes two main cases depending on the distribution of the obstacles: *a)* the stress fields are closely spaced and the dislocation line has to curl between them, or *b)* the fields are widely spaced and the dislocation line has to pass around them, subsequently leaving a dislocation loop, known as Orowan loop [21] around each of them. The strengthening effect of the reinforcement additive on the composite is a result of the formation of multiple dislocation Orowan loops around the nanoparticles, as argued by other researchers [22-24]. When the accumulated stresses around the particles exceed the strength limit of the matrix, the strength reduction begins. The accumulated stress is then relieved by the formation of nanosized cracks usually between the nanoparticles [7]. The strengthening effect depends on

the volume fraction of the additive f and is limited by a critical value, f_{max}, beyond which the strengthening decreases. This standpoint explains very well the gradual increase of the microhardness values to the maximum at 10 wt. % TiCN, and the next decrease.

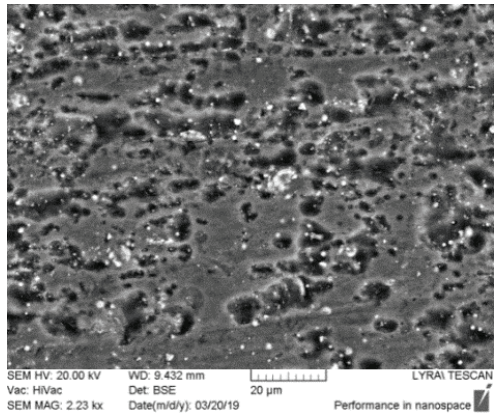

(a)

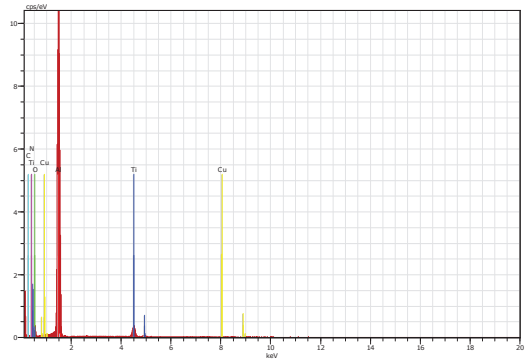

(b)

Figure I-3-14. An area in the sample with 10 wt.% TiCN nanoparticles – (a) and (b) EDX spectrum and content of chemical elements

Spectrum: Acquisition 9244

El	AN	Series	unn. C [wt.%]	norm. C [wt.%]	Atom. C [at.%]	Error [%]
Al	13	K-series	90.49	68.59	58.98	4.4
O	8	K-series	25.09	19.02	27.58	40.8
C	6	K-series	4.06	3.08	5.94	1.0
N	7	K-series	3.42	2.60	4.30	6.0
Ti	22	K-series	8.23	6.24	3.02	0.3
Cu	29	K-series	0.62	0.47	0.17	0.1
Total:			131.92	100.00	100.00	

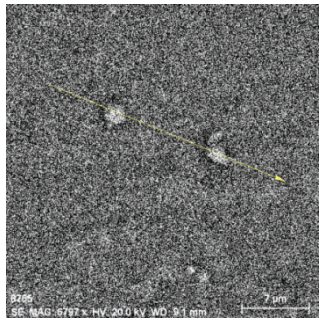

(a)

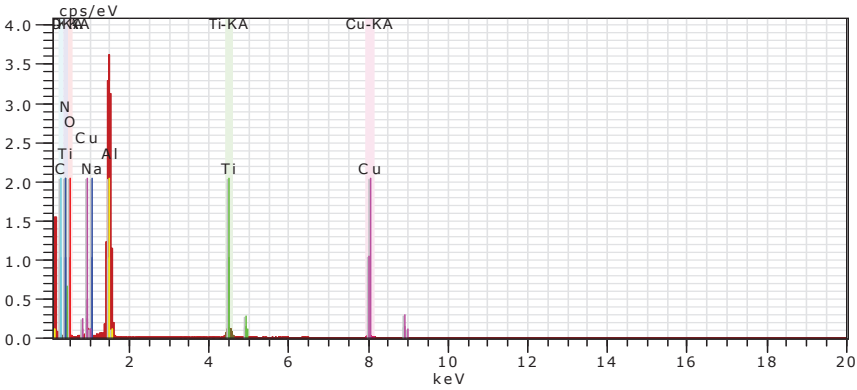

(b)

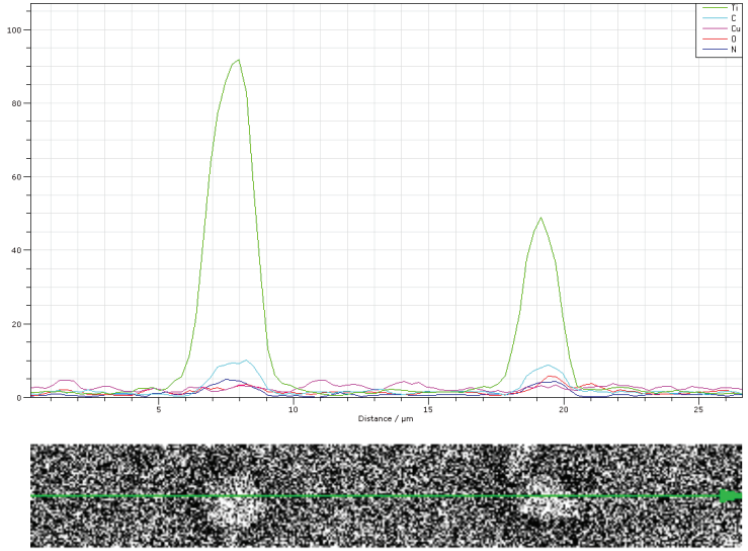

(c)

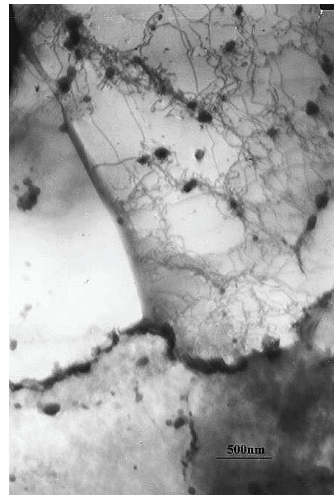

(d)

Figure I-3-15. The area around two TiCN particles in the sample with 10wt. %: (a); EDX spectrum of the chemical elements: (b); linear elements distribution: (c); a TEM image of nanoparticles and dislocations around them: (d)

Samples treated with Q_2 (high energy power input).

The results from the light microscopy investigation of samples treated with Q_2 are shown in *fig.I-3-16*. A layer with a thickness of 25 μm nearly is formed on the aluminum sample with 0 wt. % - *fig.I-3-16 (a)*. The layer's microhardness is 78HV which is 2, 6 times higher than the microhardness of the parent metal. This means the EBT itself causes a hardening. The sample with 10 wt. % TiCN nanoparticles layer is with about 80 μm thickness and 102 HV microhardness. The maximum microhardness after this type of treatment is achieved in the 5 wt. % TiCN sample. This means that the high energy displaces the maximum microhardness to the lower values of the nanoparticles' weight part.

Great particles are optically registered in the sample with 10 wt. % TiCN – *fig.I-3-16 (a)* and *(b)*. The TiCN nanoparticles are in principle refractory but in this case, favorable conditions are probably created for TiCN interfacial reaction with some elements from the molten matrix. *Fig.I-3-16 (a)* and *I-3-16 (b)* register a spherical nanoparticle in the layer and nanoparticles having a core and a cover. We assume that the high temperature of the liquid bath is kept in some places in the sample for a relatively long time under the electron beam impact, during which TiCN reacts with some elements of the melting and nanoparticles or a part of them do not exist yet as reinforcement. This could explain the lower microhardness of the samples treated with high energy - Q_2.

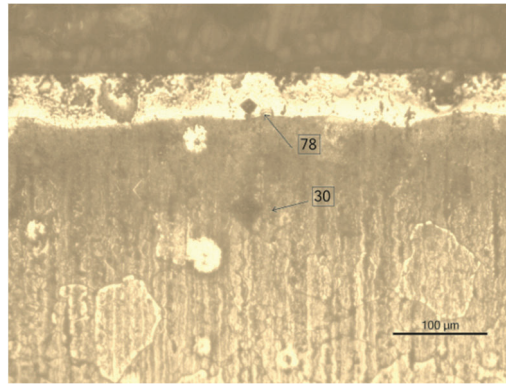

(a)

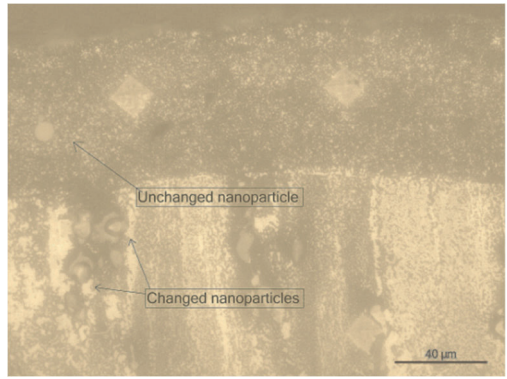

(b)

Figure I-3-16. Microstructures of samples treated with Q_2: (a) - Al with 0 wt. % TiCN and (b) - Al with 10 wt. % TiCN

Fig.I-3-17 represents a SEM image of the layer of the sample with 10 wt. % TiCN. The layer shows a dendritic-like microstructure at higher magnification.

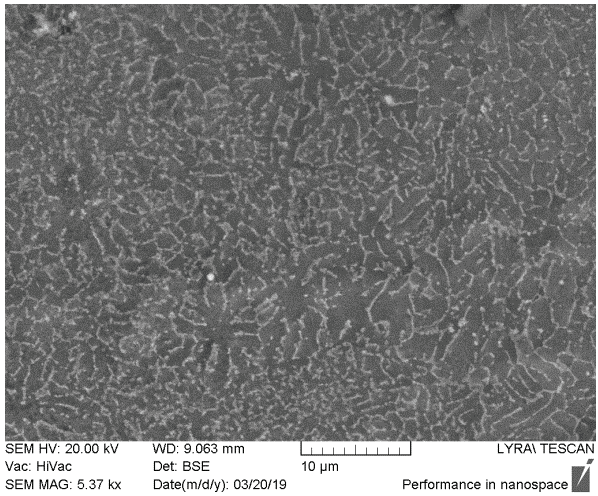

Figure I-3-17. SEM image of the layer of the sample with 10 wt. % TiCN

The XRD patterns of the samples with 10 wt. % TiCN, electron beam treated with Q_1 and Q_2 are shown in *fig.I-3-18 (a)* and *fig.I-3-18 (b)*, respectively. Both diffraction patterns exhibit peaks of pure Al and amorphous-like halos. In addition, at the sample treated with Q_1, peaks of the TiCN phase are present, which means that some amount of the nanoparticles exist in the layer formed by the lower energy, contrary to the case of electron beam treatment with Q_2. This result is another proof that the high energy promotes the interaction between particles and some elements from the matrix and converts them almost entirely into an amorphous phase. The TiCN phase has a body-centered cubic crystal structure where the carbon and nitrogen atoms occupied the octahedral sites of the closed-packed hexagonal Ti lattice forming TiC_xN_{1-x}. Therefore, the identification of the latter phase was done according to both TiN (ICDD PDF#38-1420) and TiC (ICDD PFD# 32-1383).

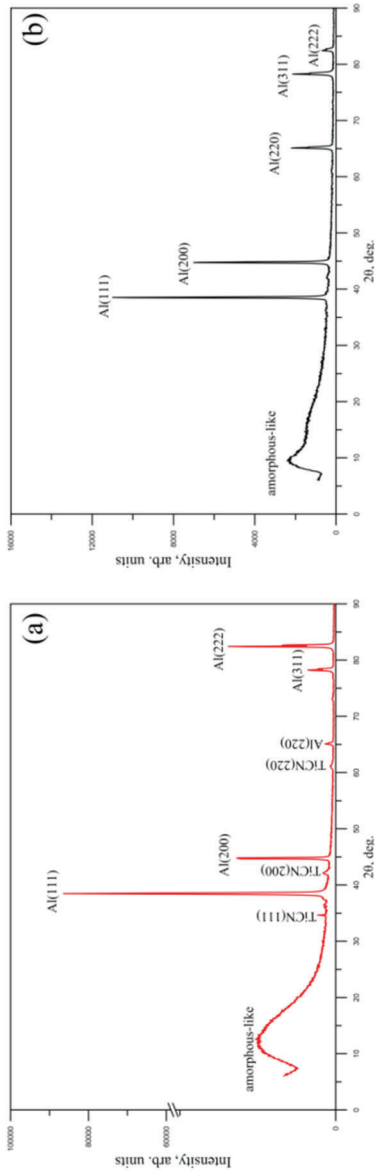

Figure I-3-18. XRD patterns of the samples with 10 wt. % TiCN and treated with: (a) - Q_1 and (b) - Q_2

3.3.3. Conclusions

- Layers obtained on aluminum nanocomposites containing 0%, 2%, 5%, and 10 wt. % TiCN nanoparticles were produced by electron beam treatment with low and high energy.
- The nanoparticles remain unchanged in the layers obtained by low energy irradiation, whereas in the layers obtained with high energy the interaction between particles and some elements from the matrix occurs and they almost entirely convert into an amorphous phase.
- The microhardness alteration in the samples treated with low energy is expressed in progressively increasing with TiCN content and in the sample with 10 wt. % of TiCN reaches a maximum of 1873HV after which it decreases. The main strengthening mechanism in the aluminum matrix nanocomposites is the Orowan mechanism. This is the cause of higher microhardness in the samples treated with low energy where the nanoparticles remain unchanged in comparison with the samples treated with high energy where the nanoparticles are transformed into an amorphous phase.
- The microhardness alteration in the samples treated with high energy is expressed in a progressively slight increase with TiCN content and in the sample with 5% wt. TiCN reaches a maximum of 161HV after which it decreases. The slight increase in microhardness is explained in this case by the transformation of the hard TiCN nanoparticles into an amorphous phase.
- This investigation confirms the fact that the strengthening effect depends on the volume fraction of the additive f and is limited by a critical value, f_{max}, beyond which the strengthening decreases.

3.4. Aluminum bulk nanocomposites reinforced with graphene

Aluminum bulk nanocomposites reinforced with graphene could be considered as a special case of aluminum bulk nanocomposites reinforced with nanoparticles – the case in which the particles are two-dimensional.

There has been increased research interest in graphene-reinforced metal composites and hybrid metal composites in the last few years. The interest in graphene-reinforced metal-based nanocomposites is because graphene, due to its unique properties, turned out to be a perfect reinforcement. These nanocomposites have strength properties that surpass those of the matrix material by several tens of percent. Tribological properties are also better. On the other hand, in recent years there has been

a strong interest of researchers in hybrid composites, which are either composites with the same type of reinforcement but with dimensions of a different order (e.g. micro- and nano-), or composites with two or more different types reinforcements.

Numerous studies of graphene-reinforced aluminum composites have been performed in the last few years [1-34]. The great interest of researchers in these composites is due to the unique physical properties of aluminum as a matrix - good corrosion resistance, low density (2.70 g / cm3), low melting point (659 °C), low weight, and high prevalence on the one hand, and the unique physical and mechanical properties of graphene as a hardener (density 1.06 g cm-3 [9], tensile strength 130 GPa and Young's modulus~1 TPa [26-28]) on the other. Graphene is considered to be the material with the highest strength properties, which is why it improves the poor mechanical and tribological properties of aluminum. The interest in graphene is determined also by the fact that it is a relatively new material (discovered in 2004).

Aluminum composites reinforced with reduced graphene oxide rGO (graphene oxide - GO is considered to be a form of graphene, which includes oxygen functional groups) have been obtained in the last few years [29-33]. To have a good dispersion of graphene in the liquid matrix and to achieve good homogenization of the material, as well as a better interaction of graphene with the liquid matrix, graphene oxide is reduced, which largely removes oxygen functional groups and reduces graphene oxide - rGO. Reduced graphene oxide can be used for the same applications as graphene, as it has similar properties to virgin graphene.

The most important features of aluminum nanocomposites reinforced with graphene or reduced graphene oxide can be summarized as follows:

- Some properties such as mechanical, thermal, and electrical can be improved by introducing graphene or rGO into a metal matrix;
- There are several difficulties in the production of these composites. Some of them are related to the nature of the initial materials and others to the production process: achieving a uniform distribution of graphene, preventing an adverse reaction between graphene and the matrix, obtaining a strong interfacial bond, and avoiding the preferred orientation of graphene;
- Even distribution of graphene in the matrix can be achieved by powder metallurgy and laser-based technologies for 3D printing. Powder-metallurgical methods create a better bond between the reinforcement and the matrix, as well as a better distribution of the reinforcing phase in the matrix, which leads to better mechanical properties. They also simplify the production of complex parts and provide excellent control over the

microstructure, including grain size, morphology, and volume of the reinforcing component [34]. Therefore, powder metallurgy is the preferred way to incorporate allotropic types of carbon into the metal matrix.

- The mechanical properties and thermal conductivity of composites strongly depend on the content of graphene, the dispersion of graphene, and the interfacial bond between graphene and the metal matrix. The low content of graphene leads to improved properties, and the higher content of graphene deteriorates the properties of composites, mainly due to the formation of graphene agglomerate.
- There is a critical limit for graphene content (0.7% for aluminum nanocomposites obtained by powder metallurgy [35]), up to which the properties of the composite can be improved, while at higher graphene content, all properties such as mechanical properties, tribological behavior, thermal conductivity, and electrical conductivity deteriorate.
- The critical limit of the rGO content in rGO / 7075 Al composites, for example, is 0.5 wt%, after which the strength properties decrease due to the formation of brittle Al4C3 and cracks [33].
- During the production of nanocomposites, graphene nanoplatelets are located mainly at the grain boundaries and lead to grain crushing, which is the main reinforcing source according to some authors [36].
- The preferred orientation of graphene nanoplatelets during compaction leads to anisotropic properties of the composites.
- Due to the large specific surface area of graphene and the excellent adhesion of the matrix to the nanofiller, the mechanical properties of aluminum nanocomposites with graphene are better than those of aluminum nanocomposites with carbon nanotubes [36].
- The tribological properties of aluminum composites with graphene and rGO have been poorly studied. Studies to date have shown that graphene can significantly reduce the degree of wear and friction coefficients of the composite with respect to the monolithic material.

The production of metal matrix nanocomposites with an even distribution of graphene, a strong interfacial bond, without adverse reactions, and with better isotropic properties is still a challenge for scientists.

Regarding the reinforcing mechanisms acting in aluminum nanocomposites with graphene, it is claimed in the literature [37] that they are the following: obstructing the movement of dislocations, the transmission of stress, and crushing of the grain.

First, graphene nano inclusions effectively prevent the movement of dislocations in the lattice as the predominant deformation mechanism in metals. This effect is manifested in all considered graphene metal

nanocomposites [31-36] and most likely has a dominant contribution to their strengthening.

The second strengthening mechanism in metal matrix nanocomposites reinforced with graphene is stress transfer. In general, the effect of this mechanism on both the strength and elastic properties of the nanocomposite is sensitive to the chemical interaction between graphene and the metal matrix. In addition, there are geometric factors that enhance the stress transfer in metallic graphene nanocomposites. The graphene platelets have a curved shape and large aspect ratio values. They are bent, anchored, and often wrapped around metal grains along the metal boundaries. As a consequence, graphene nano inclusions have a large contact area with a metal matrix and thus provide efficient stress transfer.

Third, because graphene nanoplatelets inhibit the migration of grain boundaries, grain growth slows during the production stage of the material and its plastic deformation. As a result, nanocomposites with a metal matrix and graphene have a smaller grain size than that of pure metals. At the same time, according to the classic Hall-Patch relationship, the strength of materials increases with decreasing grain size.

References

1. A. E. Nassar, E. E. Nassar, Properties of aluminum matrix Nanocomposites prepared by powder metallurgy processing, Journal of King Saud University – Engineering Sciences (2017) 29, 295–299.
2. Triratna Shrestha, Enhanced properties of metal matrix nanocomposites. Applying carbon nanotube reinforced aluminum-based nanocomposite via the powder metallurgy route., Thermal Processing, June 15, 2019, pp 18-19.
3. Íris Carneiro, Filomena Viana, Manuel F. Vieira, José V. Fernandes, and Sónia Simões, EBSD Analysis of Metal Matrix Nanocomposite Microstructure Produced by Powder Metallurgy, Nanomaterials (Basel). 2019 Jun; 9(6): 878.
4. Daniela Penther, Sepideh Kamrani, Alireza Ghasemi, Ralf Riedel, and Claudia Fleck Microstructural characterization of Mg-SiC nanocomposites produced by powder metallurgy techniques, Research & Reviews: Journal of Material Sciences, 2017, vol. 5, Iss. 7, 42
5. M. Meignanamoorthy, Synthesis of Metal Matrix Composites via Powder Metallurgy Route: a Review, Mechanics and Mechanical Engineering, Vol. 22, No. 1 (2018) 65–75

6. Mehran Dadkhah, Abdollah Saboori, and Paolo Fino, An Overview of the Recent Developments in Metal Matrix Nanocomposites Reinforced by Graphene, Materials 2019, 12, 2823; doi:10.3390/ma12172823.
7. Lubomir Anestiev, Rumyana Lazarova, Peter Petrov, Vanya Dyakova, and Lenko Stanev, On the strengthening and the strength reducing mechanisms at Aluminium Matrix Composites, reinforced with TiCN nano-sized particulates, Philosophical Magazine & Philosophical Magazine Letters, https://www.tandfonline.com/doi/full/10.1080/14786435.2020.1821114.
8. K. Wang, et al., Development of Al-TiCN nanocomposites via ultrasonic-assisted casting route, Ultrasonics - Sonochemistry 58 (2019) 104626.
9. Pan Ma et al., Effect of Al_2O_3 Nanoparticles as Reinforcement on the Tensile Behavior of Al-12Si Composites, Metals 2017, 7, 359.
10. Huda A. Al-Salihi and Hadia Kadhim Judran, Effect of Al_2O_3 reinforcement nanoparticles on the tribological behavior and mechanical properties of Al6061 alloy, AIMS Materials Science, Volume 7, Issue 4, 486–498.
11. Ting-Chiang Lin et al., Aluminum with dispersed nanoparticles by laser additive manufacturing, NATURE COMMUNICATIONS | https://doi.org/10.1038/s41467-019-12047-2
12. J. G. Park, D. H. Keum and Y. H. Lee: Carbon. 2015, vol. 95, pp. 690–698.
13. C. Carreño-Gallardo, J.M. Mendoza-Duarte, C. López-Meléndez, I. Estrada-Guel and R. Martínez-Sánchez: Microsc. Microanal. (Microscopy Society of America 2015), 2015, vol. 21 (Suppl. 3), pp. 1041-1042, https://www.cambridge.org/core. Accessed 04 May 2018.
14. N. Perez: Electrochemistry and Corrosion Science, 2nd ed., Springer International Publishing, Switzerland 2016, ch. 1.4 Galvanic Corrosion.
15. M. Born and E. Wolf, Principles of Optics, 6th edition, Pergamon Press, 1980, ch. 8.5 Fraunhofer diffraction at apertures of various forms and ch. A.II.4 The application of optical principles to electron optics.
16. D. B. Williams and C. B. Carter; "Transmission Electron Microscopy: A Textbook for Materials Science, 2nd edition, Springer Science-Business Media, LLC, 2009, Ch. 10.3. A Forming a Thin Slice from the Bulk Sample".

17. Amal E. Nassar, Properties of aluminum matrix Nanocomposites prepared by powder metallurgy processing, Journal of King Saud University – Engineering Sciences (2017) 29, 295–299.
18. Aluminum and Magnesium Metal Matrix Nanocomposites, Lorella Ceschini et al., Springer Nature Singapore Pte Ltd. 2017.
19. R Lazarova, S Valkov, V Dyakova, and P Petrov, Layers obtained on TiCN aluminum nanocomposites by electron-beam treatment International Conference on Novel Functional MaterialsIOP Conf. Series: Materials Science and Engineering733 (2020) 012017IOP Publishingdoi:10.1088/1757-899X/733/1/012017, https://www.researchgate.net/publication/338718736_Layers_obtained_on_TiCN_aluminum_nanocomposites_by_electron-beam_treatment#fullTextFileContent.
20. Angelov V., Ormanova M., Kaisheva D., Lazarova R., Dimitrova R., Petrov P., 2019, Selective electron beam surface alloying of aluminum with TiCN nanoparticles, Nuclear Instruments, and Methods in Physics Research, B 440, pp 88-94.
21. Orowan E., 1934, Z. für Kristall. - Crystalline Materials vol. 89, No1, pp 327–343.
22. Fisher J. C., Hart E. W. and Pry R. H. 1953 Acta Metallurgica vol. 1 p. 336.
23. Hart E. W. 1972 Acta Metallurgica vol. 20 p. 275.
24. Ashby M. F., 1970, Philosophical Magazine, vol. 21, No 170, pp 399–424.
25. M. A. Rafiee, J. Rafiee, Z. Wang, H. Song, Z.-Z. Yu, and N. Koratkar, Enhanced mechanical properties of nanocomposites at low graphene content, ACS Nano, 2009, 3, (12), 3884–3890.
26. S. F. Bartolucci, J. Paras, M. A. Rafiee, J. Rafiee, S. Lee, D. Kapoor, and N. Koratkar, Graphene–aluminum nanocomposites, Mater. Sci. Eng. A, 2011, 528, (27), 7933–7937.
27. Wang, Z. Li, G. Fan, H. Pan, Z. Chen, and D. Zhang, Reinforcement with graphene nanosheets in aluminum matrix composites, Scr. Mater., 2012, 66, (8), 594–597.
28. R. Guan, C. Lian, Z. Zhao, R. Chao, and C. Liu, Study on the preparation of graphene and Al-graphene Composite, Rare Met. Mater., 2012, 41, (Suppl. 2), 607–611.
29. M. Bastwros, G.-Y. Kim, K. Zhang, and S. Wang, Fabrication of graphene reinforced aluminum composite by semi-solid processing, International Mechanical Engineering Congress and Exposition, San Diego, CA, USA, 2013, ASME, 1–7.

30. I.A. Ovid' ko, Metal-graphene nanocomposites with enhanced mechanical properties: a review, Adv. Mater. Sci. 34 (2013), 190-200.
31. Abdollah Saboori et al., An Overview of Metal Matrix Nanocomposites Reinforced with Graphene Nanoplatelets; Mechanical, Electrical, and Thermophysical Properties, Metals **2018**, 8, 423, 1-33
32. Mehran Dadkhah et al., An Overview of the Recent Developments in Metal Matrix Nanocomposites Reinforced by Graphene, Materials 2019, 12, 2823, 1-38
33. Yi Huang et al., The fabrication of graphene-reinforced Al-based nanocomposites using high-pressure torsion, Acta Materialia 164 (2019) 499e511
34. Miao, and C. N. Lau: Superior thermal conductivity of single-layer graphene, Nano Lett., 2008, 8, (3), 902–907.
35. C. Lee, X.Wei, J.W. Kysar, and J. Hone: 'Measurement of the elastic properties and intrinsic strength of monolayer graphene', Science, 2008, 321, (5887), 385–388.
36. C. Lee, X. Wei, Q. Li, R. Carpick, J.W. Kysar, and J. Hone: Elastic and frictional properties of graphene, Phys. Status Solidi (B), 2009, 246, (11–12), 2562–2567.

CHAPTER I-4

NUCLEATION AND MICROSTRUCTURE FORMATION IN ALUMINUM NANOCOMPOSITE REINFORCED WITH TiCN NANOPARTICLES

RUMYANA LAZAROVA

In approaching the above question, we should consider that the crystallization in the presence of high melts, refractory nanoparticles (NPs) is heterogeneous.

4.1. Nucleation process

In recent years, efforts have been made to investigate the effect of NPs in the melt on the microstructure formed during crystallization and the mechanical properties of the solid metal [1-8]. It is found that the solidified microstructure containing NPs is finer than the corresponding NPs free microstructures [9-11]. This means that NPs have a refining effect on the crystallites. Another established effect is the modification of the surface of the dendrite by nanopowders [12]. These observations are supported by theoretical analyses, suggesting that nanopowders may block solvent diffusion during solidification [13]. Experimental studies prove this also.

The results of the reference literature indicate that the addition of NPs increases the rate of nuclei formation. It also limits the growth of the dendrites and alters their morphology. For example, it was found in [14] that these changes in the microstructure upon solidification result from an NPs-induced restriction in the effective diffusion of Zn at the tip of the dendrite, which reduces the rate of increase at the tip.

The very mechanism of nucleation in liquid metal with the addition of cubic shaped NPs is described in [15] and we consider it reliable. The numerical calculations there are made for liquid aluminum and TiN.

Nuclei formation in Al and AlSi12Cu2NiMg alloy

The TiCN NPs used by us when introducing them in Al and AlSi12Cu2NiMg alloy, have cubic form – Figure 1 and certificate of Neomat Co.

Particle walls are characterized by a wetting angle $0^0 < \theta < 90^0$ – *fig.I-4-1*. According to Rebinder [16], refractory NPs are potential centers of crystallization, on the surface of which individual clusters are formed, which under certain conditions are transformed into solid-phase nuclei. We assume, as in [17], that the nucleus is in the form of a spherical segment whose contact spot has a diameter not exceeding the length l_p at the edge of the cubic particle:

$$2R\text{c}\sin\theta \le l_\text{p}, \quad (1),$$

where R_c is the critical radius of the nucleus.

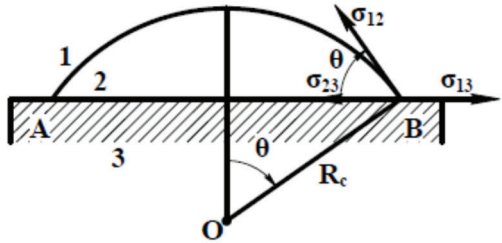

Figure I-4-1. Schematic of a solid-phase nucleus on a flat wall of a nanoparticle. 1 - melt, 2 - nucleus, 3 - NP [17]

For the heterogeneous nucleation rate in a metallic melt with NPs, the following equation is valid:

$$I = n_p \frac{12\pi D_0}{l_a^4}\left(\frac{l_p}{l_c}\right)^2 R_c^2(1-cos\theta)exp\left[\frac{-(E+\Delta G^*)}{k_B T}\right], \qquad (4\text{-}1)$$

where $0^0 < \theta < 90^0$, and $n_p = m_p\rho/100\rho_p l_p^3$ (4-2)

Gibbs' free nucleus energy is:

$$\Delta G^* = \frac{1}{3}\pi\sigma_{12}^{\infty}R_0^2\left(1-\frac{6\delta}{R_0}\right)(1-cos\theta)^2(2+cos\theta), \qquad (4\text{-}3)$$

and the value of R_c (critical nucleus diameter at heterogeneous crystallization) is determined by:

$$R_c = \frac{R_0}{2}\left\{1 + \sqrt{1 - \frac{4\delta}{R_0}}\right\} \approx R_0\left(1 - \frac{\delta}{R_0}\right) \quad (4\text{-}4),$$

where:

T –current temperature,

σ_{12} – surface tension melt-nucleus,

σ_{12}^{∞} - surface tension for a flat surface,

δ - a Tolman parameter characterizing the size of the interfacial transition layer,

$R_0 -$ the critical diameter of the nucleus at a homogeneous crystallization,

$R_0 = 2\sigma_{12}^{\infty}T_s/(k\rho\Delta T)$,

ΔT –supercooling,

T_s - crystallization temperature,

ρ –density of metal,

ρ_p –density of nanoparticle,

k – the heat of crystallization,

l_a - diameter of the liquid metal atom,

l_c - interatomic distance for the substrate,

E – activation energy of the diffusion process,

k_B – Boltzmann constant.

The dependence of the nucleation rate on the size of the nano-substrate – *fig.I-4-2* is determined for three values of the Tolman parameter, the wetting angle is chosen θ = 10^0, supercooling ΔT = 2 K and concentration 0.03g / mm^2, which for the modified layer thickness of 100μm is 0.013 wt%. The analysis of the calculated curves shows that the small Tolman parameter (2δ / R0 <0.01) has almost no effect on the rate of nucleation and the reduction of the size of the cubic nano-substrate at a fixed value of the mass fraction of the substrate material in the melt causes it to increase, i.e. the smaller the NPs, the higher the nucleation rate.

To find the rate of nucleation in aluminum with the addition of cubic shaped TiCN NPs and I, average size l_p = 40nm, as in our case, supercooling 2 K and wetting angle 10 °, we substitute with the following numerical values:

T_s = 933K, ρ = 2600 kg / m^3, k = 4.02x10^5J/kg, D_0 = $10^{-7}m^2/s$, E = 4.2x10^{-20}J, σ_{12}^{∞} = 0.093Jm^2, l_a = 2.86x10^{-10}m, l_c = 4.235x10^{-10}m, ρ_p = 5080 kg/m^3, m_p = 0.013 wt%, k_B = 1.38x10^{-23} J/K,

ΔT = 2K and we derived:

$$n_p = \frac{6{,}65354.10^{-5}}{l_p^3} \text{ [numbers / m}^3\text{]}$$
$$R_0 = 0{,}8302.10^{-7} \text{ [m]}$$
$$R_c = 827{,}31.10^{-10} \text{ [m]}$$
$$\Delta G^* = 45{,}2830.10^{-20} \text{ [J]}$$
$$I = 1.10^{22} [s^{-1}.m^{-3}]$$

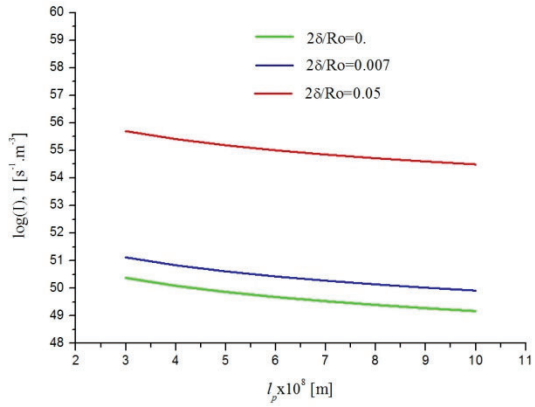

Figure I-4-2. Nucleation velocity dependence on the nanosubstrate size at $2\delta/R_0 = 0 - 1$, $2\delta/R_0 = 0.007 - 2$, $2\delta/R_0 = 0.05 - 3$ and $m_p = 0.013$ wt%

The issue of nucleation rate in the AlSi12Cu2NiMg alloy is more complicated, since the Tolman parameter, in this case, should be determined by the atomic diameters of the elements involved in the alloy, and the nucleation of the different phases occurs under different supercooling.

As the processes of nucleation and grain growth are mutually competitive, the issue of grain growth in a metal melt with NPs must also be addressed. In addition, some studies in recent years have shown that NPs play a role in the crystallization of the liquid metal as a refiner and the modifier, i.e. they simultaneously shred and alter the shape of the microstructural elements [12, 14, 18].

4.2. Process of growing and modifying dendrites and silicon crystals

Dendrites growth and modification

In [14], NPs were found to reduce the effective diffusivity of Zn in the liquid, acting as an effective limiter of dendritic growth. NPs have also been found to alter the morphology of the microstructure, changing it from dendritic to hyperbranched with many spacer tips. Quantification of dendritic tip growth rates by X-ray tomographic datasets in combination with analytical calculations - using the LGK model shows that the change in dendritic growth morphology results from the fact that NPs reduce the effective solubility of the liquid in the solid/liquid interface. This limits the redistribution of the dissolved elements and increases their concentration at the tips of the dendrites, leading to hyperbranched morphology of the grain.

In our case of surface modification of an AlSi12Cu2NiMg alloy with two concentrations of NPs from TiCN, it is found that the geometric parameter of the microstructure DAS at the low concentration of 0.015 mg / mm^2 in sample B9 is 1.98 μm and in sample B12 treated with the same process parameters is 1.02 μm – *fig.I-4-3* a and b, and *table I-4-1*. This shows that the microstructure is refined by 52% at twice the concentration of NP in the matrix. However, in sample B0, which is free of NPs, the DAS is even smaller - 0.92μm, and it is even difficult to determine the microstructure as dendritic because the eutectic is extremely dispersed. This result shows that the frequency of the current, which is the only different technological parameter in the three samples, is more strongly influencing the microstructure factor. For sample B0 it is 1 kHz and for others, it is 10 kHz.

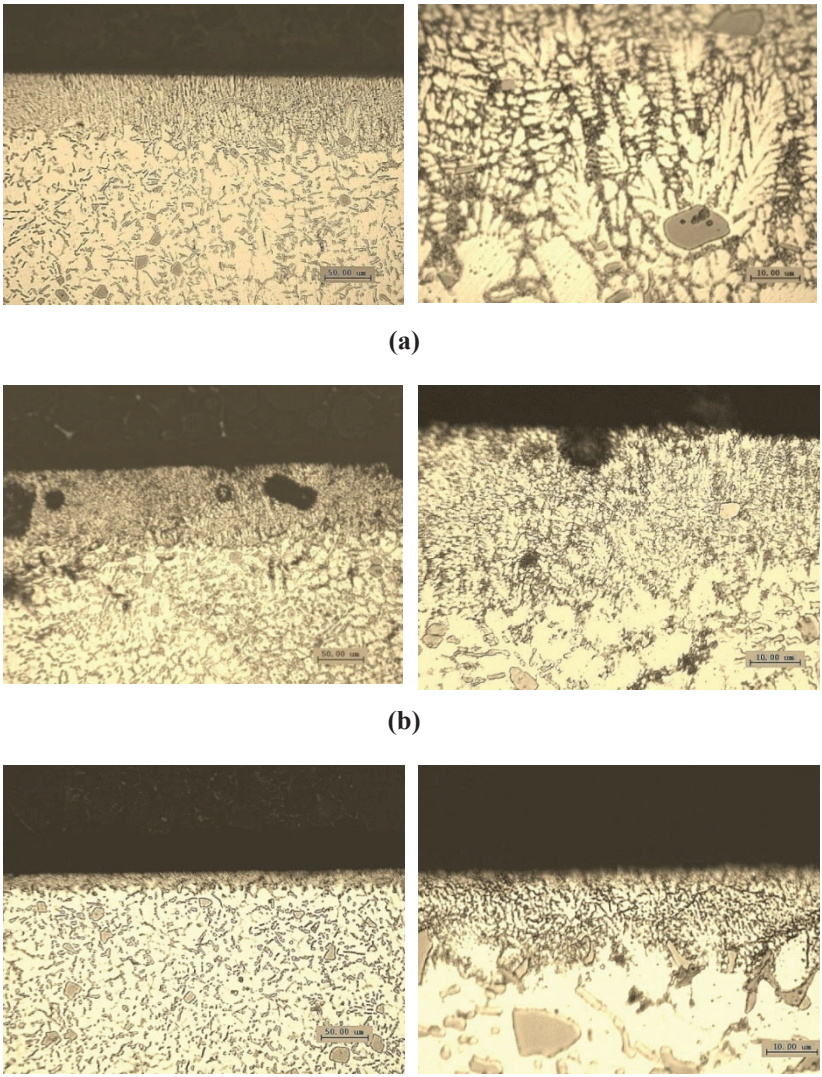

Figure I-4-3. Microstructures of the surface layer of samples: B9 – (a), B12 – (b), and B30 – (c)

Growth and modification of silicon crystals

It was shown in [19 and 20] that NPs can control the growth of the eutectic Si phase during solidification. And in [21 and 22] it was shown that NPs, Al_2O_3, and TiCN impede the growth of the eutectic Si phase by distributing them along the Al/Si interface and thus lead to the refinement of the eutectic phase. In addition, the refinement of the eutectic Si phase in the Al - Si alloys is also related to the heterogeneous nucleus of the TiCN NPs.

In [18] it was shown that the addition of SiC NPs induces the simultaneous modification and fragmentation of eutectic Si in SiC NPs / A356 samples, which becomes more significant with the increasing addition of SiC NPs. The effect of the addition of SiC NPs was primarily investigated by the results obtained from differential scanning calorimetry and high-resolution electron microscopy. The modification and refinement of eutectic Si are closely related to the interaction between SiC NPs and the solidification front (SF). When the particle size of SiC NPs is larger than the critical size, SiC NPs tend to move forward with respect to SF, while smaller SiC NPs tend to be enveloped. Here, SiC NPs that move in the interface between the eutectic Si/Al phases impede the growth of eutectic Si. At the same time, SiC NPs have been observed to act as heterogeneous nucleation sites for eutectic Si. Therefore, the simultaneous modification and refinement of eutectic Si are mainly facilitated by a combination of the above two separate effects of the addition of SiC NPs.

Comparative qualitative microscopic analysis of AlSi12Cu2NiMg alloy specimens – *fig.I-4-3 (a), (b),* and *(c)* shows that the primary and eutectic silicon crystals are crushed in the surface modified zone in specimens B9 and B12 with the addition of NPs. However, in sample B0, which is free of NPs but electron-beam treated, silicon crystals are also crushed, indicating that the EBP itself leads to crushing and is a strong factor for this.

Table I-4-1. Processing conditions of the tested AlSi12Cu2NiMg alloy samples

Designation of the sample	Concentration of TiCN, mg/mm^2	I_b [mA]	v [cm/s]	f [kHz]	U [kv]	I_f [mA]	P [W]	DAS [µm]	Δ [µm]
B9	0.015	25	1.5	10	52	472	1300	1.98	90
B12	0.03	25	1.5	10	52	472	1300	1.02	90
Br30	0	25	1.5	1	52	472	1300	0.92	25

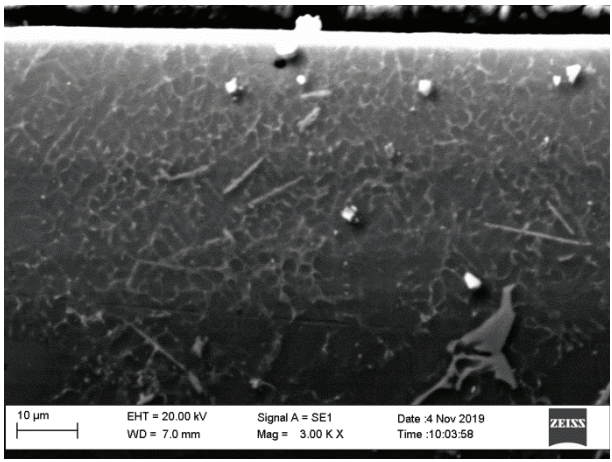

Figure I-4-4. Microstructure of the surface layer of sample B9

Fig.I-4-4 shows an image of the microstructure of sample B9 obtained by SEM, where the refining of the modified zone is visible.

Fig.I-4-5 (b) shows the result of EDS at the point indicated in *fig.I- 4-5 (a)*. The presence of titanium is found out which is proof of incorporated TiNPs in the sample's surface layer.

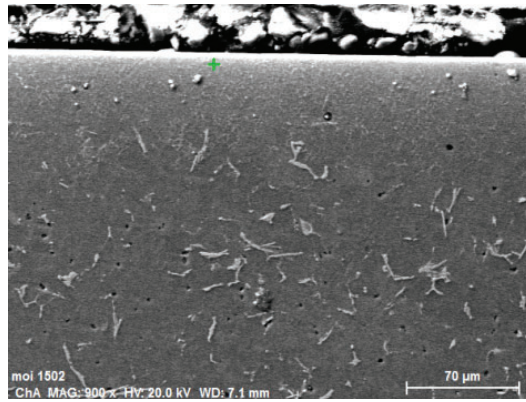

(a)

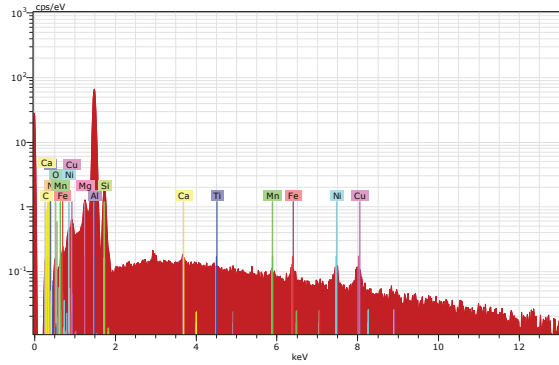

(b)

Figure I-4-5. SEM image – (a) and EDS results at the point of the surface layer of sample B9 – (b)

4.3. Simulation of the structure formation process in a sample of AlSi12Cu2NiMg alloy subjected to electron beam treatment (EBT) using the MAGMASOFT® software

Fig.I-4-6 presents a three-dimensional coordinate system of the AlSi12Cu2NiMg alloy sample we use. The control points in which thermocouples are marked are indicated by T1 to T10.

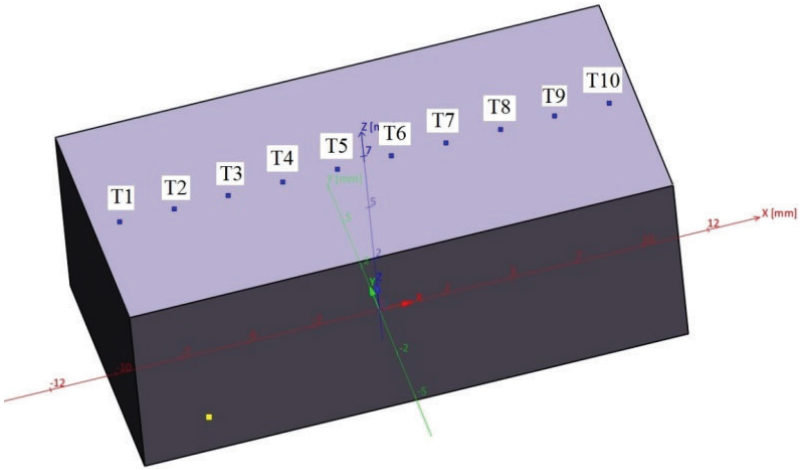

Figure I-4-6. Sample of AlSi12Cu2NiMg alloy subjected to EBT

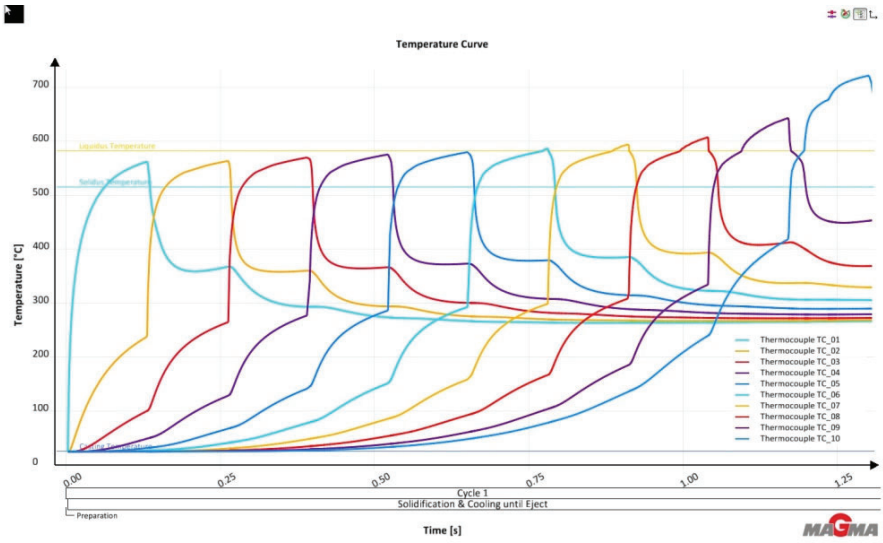

Figure I-4-7. Time-temperature curves captured by the ten thermocouples at the control points

Fig.I-4-7 shows the time-temperature curves captured by the ten thermocouples at the control points. They represent the change in temperature in them for the time of 1.33s, during which the electron beam scans the surface of the sample. The time during which the respective area was in the two-phase region i.e. between the solidus and liquidus temperature and the time when the metal is already solidified can be taken into account. This is completed for the nine points before the full-length scan is complete. The microstructure has already formed there and we should expect a very fine one.

The grain size in the sample of AlSi12Cu2NiMg alloy subjected to electron beam treatment can be read from *fig.I- 4-8*. It can be seen that in the 100 μm surface layer the grain size is about 1. 15 μm and it increases to 1.85 μm in-depth, which is an extremely fine-grained structure. These results are acceptable given our measured DAS sizes of 0. 92μm (sample B0).

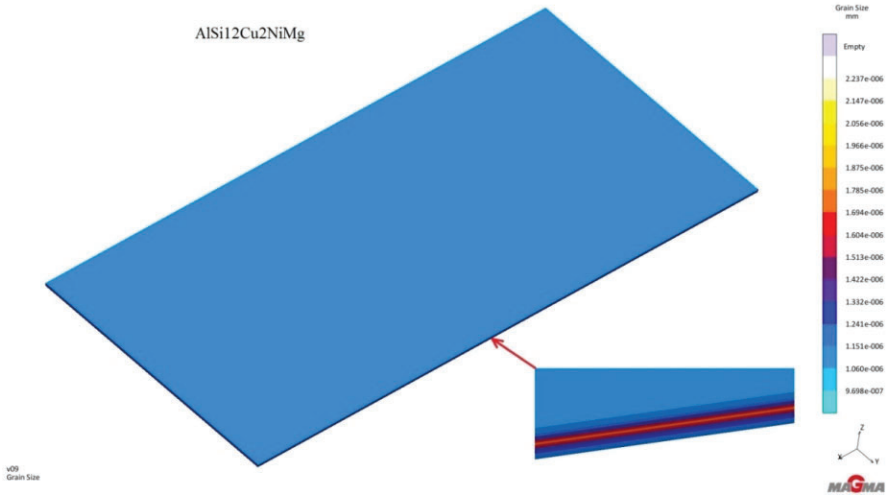

Figure I-4-8. Grain size in the surface layer of a sample of AlSi12Cu2NiMg alloy subjected to EBT

Fig.I-4-9 shows an enlarged element of *fig.I-4-8*.

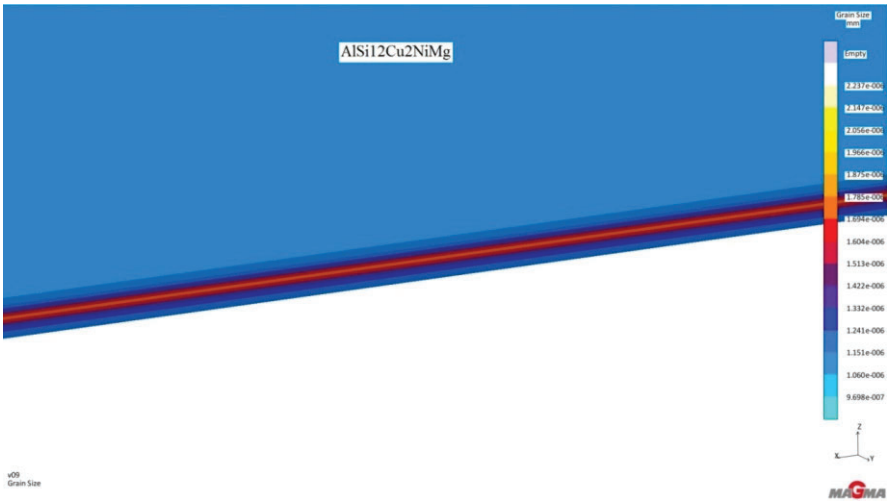

Figure I-4-9. Grain size in the surface layer of an AlSi12Cu2NiMg alloy sample subjected to EBT

4.4. Conclusion

The following conclusion can be drawn from the study of the nucleation and structure formation in aluminum and AlSi12Cu2NiMg alloy:

In the process of cooling the liquid aluminum and AlSi12Cu2NiMg alloy, the imported NPs serve as substrates on which crystallization nuclei are formed. The rate of nucleation depends on the size of the NPs and the atomic diameters of the elements constituting the liquid metal, as well as on the other physicochemical characteristics of the liquid metal. This speed is determined precisely for the liquid aluminum. A higher concentration of NPs results in a finer dendritic structure. Surface electron beam treatment in itself contributes to the fragmentation of the microstructure, with the frequency of current being a stronger factor in this respect than the presence of NPs. NPs are nucleation's centers also of the silicon phase and impede the growth of eutectic silicon. The obtained new properties of the surface of the treated metal are explained by the refined, modified, and strengthened microstructure due to the introduction of NPs and surface EBT.

The structure formation process in a sample of AlSi12Cu2NiMg alloy subjected to electron beam treatment (EBT) using the MAGMASOFT® software is simulated successfully. The simulated grain size in the 100 μm surface layer is about 1. 15 μm which is close to the experimental result of 0. 92μm.

References

1. H. Dieringa, Properties of magnesium alloys reinforced with nanoparticles and carbon nanotubes: a review, J. Mater. Sci. 46 (2) (2011) 289e306.
2. W.H. Sillekens, D.J. Jarvis, A. Vorozhtsov, V. Bojarevics, C.F. Badini, M. Pavese, S. Terzi, L. Salvo, L. Katsarou, H. Dieringa, The ExoMet project: EU/ESA research on high-performance light-metal alloys and nanocomposites, Metall. Mater. Trans. A 45A (8) (2014) 3349e3361.
3. B.F. Schultz, J.B. Ferguson, P.K. Rohatgi, Microstructure and hardness of Al2O3 nanoparticle reinforced Al-Mg composites fabricated by reactive wetting and stir mixing, Mater. Sci. Eng. A 530 (2011) 87e97.
4. X.Y. Jia, S.Y. Liu, F.P. Gao, Q.Y. Zhang, W.Z. Li, Magnesium matrix nanocomposites fabricated by ultrasonic-assisted casting, Int. J. Cast Metal Res. 22 (1e4) (2009) 196e199.
5. L. Katsarou, M. Mounib, W. Lefebvre, S. Vorozhtsov, M. Pavese, C. Badini, J.M. Molina-Aldareguia, C.C. Jimenez, M.T.P. Prado, H. Dieringa, Microstructure, mechanical properties and creep of magnesium alloy Elektron21 reinforced with AlN nanoparticles by ultrasound-assisted stirring, Mater. Sci. Eng. A 659 (2016) 84e92.
6. D.K. Wang, M.P. De Cicco, X.C. Li, Using diluted master nanocomposites to achieve grain refinement and mechanical property enhancement in as-cast Al-9Mg, Mater. Sci. Eng. A 532 (2012) 396e400.
7. H. Men, B. Jiang, Z. Fan, Mechanisms of grain refinement by intensive shearing of AZ91 alloy melt, Acta Mater. 58 (19) (2010) 6526e6534.
8. W. Mirihanage, W.W. Xu, J. Tamayo-Ariztondo, D. Eskin, M. Garcia-Fernandez, P. Srirangam, P. Lee, Synchrotron radiographic studies of ultrasonic melt processing of metal matrix nanocomposites, Mater. Lett. 164 (2016) 484e487.

9. X.Y. Jia, S.Y. Liu, F.P. Gao, Q.Y. Zhang, W.Z. Li, Magnesium matrix nanocomposites fabricated by ultrasonic-assisted casting, Int. J. Cast Metal Res. 22 (1e4) (2009) 196e199.
10. D.K. Wang, M.P. De Cicco, X.C. Li, Using diluted master nanocomposites to achieve grain refinement and mechanical property enhancement in as-cast Al-9Mg, Mater. Sci. Eng. A 532 (2012) 396e400.
11. L.Y. Chen, J.Y. Peng, J.Q. Xu, H. Choi, X.C. Li, Achieving uniform distribution and dispersion of a high percentage of nanoparticles in metal matrix nanocomposites by solidification processing, Scripta Mater. 69 (8) (2013) 634e637.
12. R. Daudin, S. Terzi, P. Lhuissier, J. Tamayo, M. Scheel, N. Hari Babu, D.G. Eskin, L. Salvo, Particle-induced morphological modification of Al alloy equiaxed dendrites revealed by sub-second in situ microtomography, Acta Mater. 125 (2017) 303e310.
13. L.Y. Chen, J.Q. Xu, H. Choi, H. Konishi, S. Jin, X.C. Li, Rapid control of phase growth by nanoparticles, Nat. Commun. 5 (2014) 3879.
14. Enyu Guo et al., The influence of nanoparticles on dendritic grain growth in Mg alloys, Acta Materialia, 152, 2018, 127-137
15. A Cherepanov, V Cherepanova, V Manolov and L Yovkov, On crystallization of a metal inoculated with nanoparticles, IOP Conf. Series: Journal of Physics: Conf. Series 1115 (2018) 042042
16. Rebinder P A, *Qualitative Steel* **3,** 1939, 31–4 [in Russian]
17. Fletcher N H, *J. Chem. Phys*. **29,** 1958, 572–76
18. Dapeng Jiang, Jiakang Yu, Simultaneous refinement and modification of the eutectic Si in hypoeutectic Al–Si alloys achieved via the addition of SiC nanoparticles, Journal of material researches technology, 2019, 8(3), 2930–2943
19. Chen LY, Xu JQ, Li XC. Controlling phase growth during solidification by nanoparticles. Mater Res Lett 2015;3(1):43–9.
20. Wang K, Jiang HY. Nanoparticle-inhibited growth of primary aluminum in Al–10Si alloys. Acta Mater 2016;103:252–63.
21. Choi H, Li X. Refinement of primary Si and modification of eutectic Si for enhanced ductility of hypereutectic Al–20Si–4.5Cu alloy with addition of Al2O3 nanoparticles. J. Mater. Sci. 2012;47(7):3096–102.
22. Wang K, Jiang HY. Microstructure and mechanical properties of hypoeutectic Al–Si composite reinforced with TiCN nanoparticles. Mater Des 2016;95:545–54.

CHAPTER I-5

GENERAL CONCLUSION

RUMYANA LAZAROVA

Based on our research work on the topic of aluminum-based surface and bulk nanocomposites, we can draw some important conclusions:

1. The electron beam treatment with scanning circular rotating motion of the electron beam is an appropriate method for successfully alloying pure aluminum matrix with hard and refractory nanoparticles and by this way producing surface aluminum nanocomposites. The most appropriate treatment conditions for obtaining layers with significant thickness and high microhardness are found out.
2. The used method allows obtaining layers on an aluminum substrate with thickness up to 33 μm and microhardness up to 22 times higher than the substrate microhardness. Such details could be convenient for applications requiring high surface hardness and light, soft, and plastic parent metal, which means an increase in the surface hardness with respect to the uncoated substrate.
3. The carried-out analyses show that nanoparticles are incorporated in the layers. The microhardness raising is mostly due to the presence of hard nanoparticles in the aluminum matrix as well as hard clusters.
4. The studied tribological characteristics, such as mass wear, friction force, and coefficient of friction are improved of the samples with nanocomposite layer compared to the same characteristics of the samples without a nanocomposite layer.
5. The increased microhardness and improved tribological characteristics are due to the higher microhardness and better tribological characteristics of nanoparticles in comparison to the aluminum matrix, which mostly takes the load and wear, as well as to the obstruction of the movement of dislocations by nanoparticles in the aluminum matrix.
6. The second cycle of incorporation of TiCN tends to increase the amount of the nanoparticles in the layer and further increasing the microhardness.

7. The powder metallurgy route (cold isostatic pressing and hot extrusion) is appropriate for bulk aluminum matrix nanocomposite obtaining up to about 10 wt. % nanoparticles reinforcement. This method allows producing nanocomposites with a homogeneous distribution of the reinforcement particles in the matrix.

8. Layers obtained on aluminum nanocomposites containing 0%, 2%, 5%, and 10 wt. % TiCN nanoparticles were produced by electron beam treatment with low and high energy.

9. The nanoparticles remain unchanged in the layers obtained by low energy irradiation, whereas in the layers obtained with high energy the interaction between particles and some elements from the matrix occurs and they almost entirely convert into an amorphous phase.

10. The microhardness alteration in the samples treated with low energy is expressed in progressively increasing with TiCN content and in the sample with 10 wt. % of TiCN reaches a maximum of 1873HV after which it decreases. The main strengthening mechanism in the aluminum matrix nanocomposites is the Orowan mechanism. This is the cause of higher microhardness in the samples treated with low energy where the nanoparticles remain unchanged in comparison with the samples treated with high energy where the nanoparticles are transformed into an amorphous phase.

11. The microhardness alteration in the samples treated with high energy is expressed in a progressively slight increase in TiCN content and in the sample with 5% wt. TiCN reaches a maximum of 161HV after which it decreases. The slight increase in microhardness is explained in this case by the transformation of the hard TiCN nanoparticles into an amorphous phase.

12. The addition of nano-sized TiCN reinforcement particles into the Al-matrix leads to a substantial improvement of the mechanical properties. For instance, the obtained maximal increase of the yield strength of the composite was up to 57%, above that of the Al-matrix.

13. The strengthening effect depends on the volume fraction of the additive f and is limited by a critical value, f_{max} (in the case here, Al-TiCN, $f_{max} \approx 0.06$, (9 wt. % TiCN)). Beyond f_{max}, the increase of the VF of the reinforcement led to a decrease in the strengthening effect.

14. The strengthening effect is a result of the formation of multiple dislocation loops around the reinforcement particles, as argued by Fisher, Hart and Pry, and Ashby.

15. The strength reduction occurs when the stresses, accumulated around the reinforcement particles, exceed the strength limit of the matrix.

The accumulated stress is then relieved by the formation of micro-, or nano- cracks in the matrix.

16. The yield strength of a composite, as a function of the reinforcement volume fraction, is readily described by an equation, Eq. 7, which combines the Orowan strengthening model (as modified by Melander and Ardell), and a Griffiths' expression, which renders an account of the stress reduction due to crack formation.

17. Concerning the topic of nucleation and microstructure formation, we could affirm that the imported nanoparticles in a liquid aluminum and AlSi12Cu2NiMg alloy serve as substrates on which crystallization nuclei are formed.

18. The rate of nucleation depends on the size of the NPs and the atomic diameters of the elements constituting the liquid metal, as well as on the other physicochemical characteristics of the liquid metal. This speed is determined precisely for the liquid aluminum. A higher concentration of NPs results in a finer dendritic structure. Surface electron beam treatment in itself contributes to the fragmentation of the microstructure, with the frequency of current being a stronger factor in this respect than the presence of NPs.

19. The structure formation process in a sample of AlSi12Cu2NiMg alloy subjected to electron beam treatment (EBT) using the MAGMASOFT® software is simulated successfully. The simulated grain size in the 100 μm surface layer is about 1. 15 μm which is close to the experimental result of 0. 92μm.

In this work, we have reviewed the methods for the preparation of the aluminum surface and bulk nanocomposites with nanoparticle filler. We have demonstrated the use of the powder metallurgy method for producing bulk aluminum matrix nanocomposites and electron beam treatment for the surface aluminum nanocomposites. We have clarified the nature of surface and bulk nanocomposites on the aluminum base - their composition, microstructure, and properties. We have elucidated the role of nanoparticles in the process of microstructure formation during electron beam treatment and in the process of strengthening during the extrusion of aluminum matrix nanocomposite. We have shown the improvement of microhardness, mechanical and tribological properties of nanocomposites in comparison with the parent metal and clarified the strengthening mechanism in aluminum – TiCN nanoparticles composites. We have simulated successfully the structure formation process in a sample of AlSi12Cu2NiMg alloy subjected to electron beam treatment using the MAGMASOFT® software and demonstrated a good agreement between

simulated and measured results. Finally, we were convinced of the great importance of aluminum matrix nanocomposites for the development of materials with unique properties and the prospects of their application in the modern industry.

PART II:
STRENGTHENING AND STRENGTH-REDUCTION AT METAL MATRIX COMPOSITES REINFORCED WITH NANO-SIZED PARTICULATES

LUBOMIR A. ANESTIEV

This part is dedicated to my parents Christina and Andrej

PREFACE TO PART II

This part of the book treats a new fast-developing field of materials science – metal composites reinforced with nano-sized particulates. As any of the newly emerging fields of research, this type of metal composites has already attracted the attention of many researchers and technologists, who are interested in and willing to contribute to this field of materials science.

In the distant 80s of the last century, the present author was one of these, willing to contribute to the very modern, at that time, a new field of materials science - the rapidly quenched materials. Thus, by personal experience, I know how difficult is to quickly step into a new field of science, which as a rule requires a very good background in fundamental and applied sciences, e.g., physics, chemistry, physical metallurgy, materials engineering, etc. The curriculum of a would-be materials researcher is usually in only one of the sciences above, while the others are not studied or are studied at a basic level. It is also well understood that most of the graduate, or the postgraduate, students, and especially those of the researchers who are working as technology-developers are not having the luxury of allocating a sufficient amount of time to go through the vast amount of scientific literature, to select the information which is required for the job at hand.

Thus, this book intends to help such individuals to step in fast into the problematics of nano-particulates reinforced metal composites by offering them the essentials of the well-established theories needed for that quick start in this field of materials science. I hope very much that the reader of this part of the book will find the topics discussed appropriate and helpful in her or his endeavors.

ACKNOWLEDGMENTS

This Part of the book was supported by the European Regional Development Fund within the OP "Science and Education for Smart Growth 2014 - 2020", Project CoE "National center of mechatronics and clean technologies", № BG05M2OP001-1.001-0008-C08.

About the Author

Dr. Lubomir A. Anestiev is a full Professor of Physical Metallurgy and Materials Engineering at the Institute of Metal Science Technologies and Equipment with Hydro- and Aerodynamic Centre (IMSTEHAC), at the Bulgarian Academy of Sciences (BAS) - Sofia. He received his master's degree in engineering from the Moscow Steel and Alloys Institute, USSR (now National University of Science and Technology "MISiS", Moscow, the Russian Federation), and his Ph.D. degree from the Bulgarian Academy of Sciences. In 1982 Dr. Anestiev joined the department of Physical-Chemistry of Metals and Alloys at the Institute of Metal Science and Technology, BAS (the predecessor of IMSTEHAC). During his employment at that time, Dr. Anestiev worked on several projects in materials and materials engineering. During his carrier as a researcher, he applied to and received several research grants and post-doctoral fellowships from research-supporting organizations from Bulgaria and abroad; DAAD-Germany (1991), The Office of the Prime Minister of Belgium OSTC-Scholarship (1997), and KULeuven (1999-2001). Between 2002 and 2006, Dr. Anestiev was employed at the McMaster University, Hamilton, Canada, where he worked on different projects, mainly in the utilization of the Al-alloys by the automotive industry. In 2008 he rejoined IMSTEHAC-BAS.

The research of Dr. Anestiev is primarily directed to the physical chemistry of metals and their alloys, physical metallurgy, casting, and the phase transformation in metals. He is an author and co-author of over 80 publications in the research fields above.

INTRODUCTION TO PART II

LUBOMIR A. ANESTIEV

The main subject of this part of the book is the strengthening and strength reduction that occurs when introducing ceramic or metal-ceramic particles into a metal matrix.

The term 'composite' generally refers to a material system composed of discrete particles (hereinafter referred to as reinforcing elements or reinforcement) distributed in a continuous phase (called a matrix). The composite material derives its distinctive characteristics from the properties of the composite components, their geometry, the “architecture” of the components, their distribution in the matrix, and the properties of the boundaries (contact surfaces) formed between the reinforcement and the metal matrix.

Depending on the physical or more often chemical nature of the matrix phase, composites are classified as polymeric, metallic, and ceramic.

Metal Matrix Composites (MMC) are a new class of composite materials that in many cases show excellent properties compared to “classic” metal materials, for example, excellent mechanical properties, good thermal conductivity, improved corrosion resistance, and wear resistance. The main disadvantages of this type of materials are their poor ductility and their tendency to break under mechanical stress. Unfortunately, these and other similar disadvantages of composites are inevitable, as their genesis is in the presence of boundary surfaces between the reinforcement and the matrix. The unresolved problems listed above related to the reliability of this type of composites due to material’s fatigue, tendency to fracture, etc., is an obstacle to their wider practical application.

This part of the book gives an overview of some basic aspects related to the mechanical properties of MMC, especially one of them, the broad class of composites; MMCs based on aluminum matrices (shortened - AMCs). Of particular interest is the topic; how the mechanical properties of the composite are influenced by the volume part of the reinforcement

and what are the mechanisms behind the improvement or deterioration of these properties.

The idea of reinforcing metals with micro-, and later with nanosized particles is based on the experience gained by researchers and technologists when they studied the hardening due to precipitation during heat treatment of some alloys from practical interest (e.g. cast iron, duralumin). It has been observed that the precipitations formed during the cooling from the liquid state of certain alloys or during their heat treatment in the solid-state (e.g. duralumin) lead to an overall improvement in the mechanical properties of the treated material. Initially, the direction followed by materials researchers and technologists developing new types of materials with higher strength and durability was the synthesis of new alloys, in which, for instance, by heat treatment to stimulate the formation of phase(s), contributing to the desired improvement of the mechanical properties of the material as a whole. From the description itself, it is obvious that this is a very difficult path to follow because it involves; synthesis of new alloys from a limited list of suitable metals and the development of specific procedures for their alloying and heat treatment. It later became clear that the same effect could be achieved not only by forming new phases in the matrix, but also by adding micron-sized particles (and later nano-sized ones). This approach has proven to be much more effective as it is universal and makes it much easier to control the production of the material, (i) the choice of reinforcement material and the amount of reinforcement is determined by the manufacturer, (ii) no special procedure is required for temperature and time control, with which to stimulate the release of specific strengthening phases and/or to avoid the coarsening of the precipitates. Recall that in conventional reinforcement methods, the increase in the size of the precipitates usually leads to a serious deterioration of the mechanical properties (see Fig. II-1-5 in Chapter II-1).

The development of composites with reinforced matrices with artificial reinforcement initially began with the use of different types of polymers as a matrix material. Later, when the beneficial effect of artificial reinforcement on the mechanical properties of the composite was realized and confirmed, the reinforcement of metals and alloys of practical interest (for example, steels and of course aluminum and its alloys) was started.

In conclusion of this section, it could be said that the main advantages of the MMCs over non-reinforced metals and alloys is that they have the following useful properties:

- Improved yield and ultimate tensile strengths,
- Improved hardness,

- Reduced density (weight) valid for the Al-, and Ti-based composites,
- Improved mechanical properties at elevated temperatures,
- Improved friction and wear resistance.

CHAPTER II-1

METHODS OF THE MMC'S PRODUCTION

LUBOMIR A. ANESTIEV

From the brief review of composites with metal matrices made in the Introduction section, it is clear that the development of useful mechanical properties in the composite depends to a large extent on the method of its production. The most commonly used and generally accepted methods for the production of MMC can be divided into the following two major groups: (i) powder metallurgy (PM) production methods and (ii) casting methods. Recently, the first group of production methods has gained popularity because it allows almost seamless production of MMCs using nanosized particles as an armament. Regardless of which of the methods is used, powder metallurgy or casting, one should keep in mind the following; at high temperatures, the surface energy of nanosized particles, due to their large curvature, is particularly high. Therefore, they are extremely unstable and, as a consequence, prone to decomposition and/or dissolution in the matrix during the production of the composite.

1.1 Overview of the methods of MMC's production

1.1.1 Methods, based on classical powder metallurgy (PM)

(i) *The classical PM method*. The classical PM method, as its name suggests, is based on the application of the standard PM technique which is: (a) mixing of the matrix and reinforcement powders, (b) compaction of the thus obtained green powder mixture, and (c) sintering at an appropriate temperature. The disadvantages of the direct PM approach, when applied to the production of nanoparticulate composites, are obvious - the reinforcement tends to agglomerate, thus deteriorating the mechanical properties of the composite. The reasons for agglomeration in the PM case are as follows: (a) "specific-weight-liquation" arising from the differences

in the specific weights of the basic powders. The result of that type of liquation, which occurs during the mixing of the powders, is that the powder particles with a higher specific weight do assemble at the bottom of the mixer, thus leading to spatial heterogeneities in the final product, (b) "size-caused-liquation" this type of liquation takes place when the sizes of the particles in the powders mixture differ considerably (e.g., when mixing nano- and micron-sized powders) the smaller particles literally "ooze" (due to the gravity, vibrations during handling, etc.) through the interstices formed between the larger powder particles. In the case of micro-nano-sized particulates mixtures, the ratio between the sizes of the reinforcement (nano-sized particles) and the matrix powder (micron-sized particles) is ~1:1000. This problem, however, could be overcome by replacing the powders mixing with a mix and milling (M&M) procedure which reduces that type of liquation and allows an even distribution of the reinforcement inside the green powder mixture. (c) The classical PM approach requires long processing times at elevated temperatures. As above, due to the high surface energy of the nano-particulates, these would disintegrate and their constitutional elements would dissolve into the surrounding matrix, thus making the whole process of composite production meaningless. However, this problem could be avoided by selecting reinforcement materials whose Gibbs energy, at the processing temperature, is lower than that of the matrix (see Section 2).

Summing up the aforesaid it is obvious that a direct utilization of the classical PM method is a subject of several restricting conditions, which could be satisfied only in a limited number of cases.

(ii) *The hot extrusion method*. The hot extrusion method is an alternative to the classical PM method which recently gained popularity among researchers and the producers of MMCs reinforced with nano-sized particulates. It owes its popularity to the fact that it allows avoiding the deficiencies of the classical PM, and as we will see below, the casting methods. The main advantages of this method are (a) the processing temperatures are below the melting temperature of the matrix and (b) the extrudates are cooled relatively fast. Thus in both cases, are avoided the decomposition processes of the reinforcement.

A typical processing route to fabricate particulate- or whisker-reinforced MMCs by hot extrusion involves the following steps (see also Fig. II-1-1): (a) the basic powders, those of the matrix and the reinforcement, are blended in a homogeneous mixture. Due to the "size-liquation", however, serious inhomogeneities inside the composite could occur. Thus recently, instead of step (a) is applied a procedure referred to as the "mix and mill procedure" (M&M) which drastically improves the

homogenous distribution of the reinforcement particles throughout the composite, (b) the as-prepared green powder is then cold-pressed which produces a green compact that could be easily handled, (c) the as-pressed compact is put in a sealed container and degassed, after which it is (d) hot pressed, uniaxially or isostatically, thus a fully dense compact is produced, (e) the most important step of the process is the hot-extrusion itself which in essence is "squeezing" of the as-produced compact through a calibrated orifice and (f) the last step of the hot-extrusion process is cooling of the extrudate. A flow chart scheme of the hot-extrusion process is shown in Fig. II-1-1.

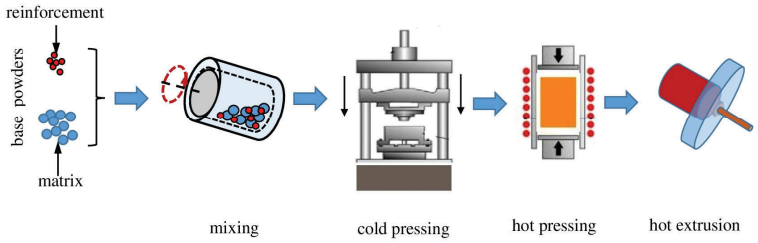

Figure II-1-1 Flow chart of the hot-extrusion process.

1.1.2 Production methods, based on casting

The casting methods. Regardless of their drawbacks (e.g., liquation and/ or decomposition of the reinforcement), the casting methods are still widely used in the fabrication of MMCs. The casting methods which nowadays find practical application are:

(i) *Stir casting*. In this method, the reinforcement, usually pre-treated ceramic particles or short fibers are added to the molten matrix material, the latter could be metal or plastic depending on what kind of a composite is intended to be produced. The as-obtained slurry (mixture of liquid matrix material and reinforcement powder) is homogenized by a vigorous mechanical stirring via, e.g., a rotating impeller. When sufficient homogeneity is achieved, the slurry is cast into the desired shape by some of the conventional casting methods and left to solidify.

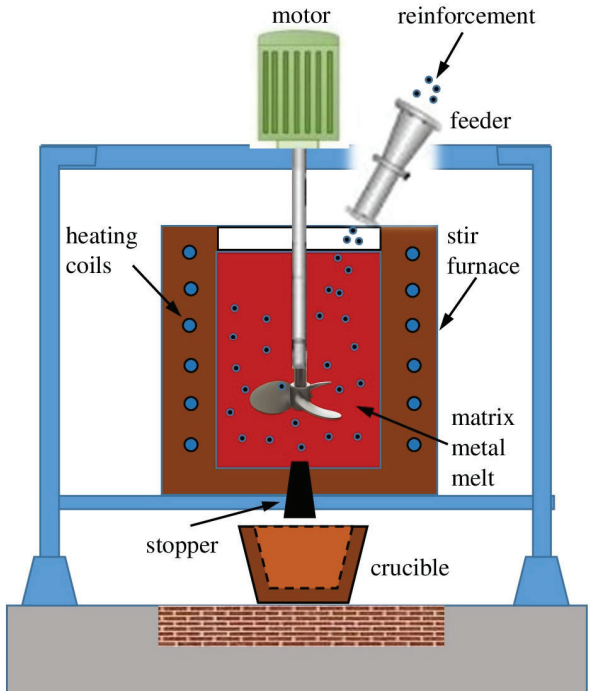

Figure II-1-2 An illustration of the stir casting method for the production of composites reinforced with micro-, or nano-sized, particulates.

The stir casting process is illustrated in Fig. II-1-2. It is considered the simplest and the most cost-effective method of MMCs production, from all methods which utilize the liquid state fabrication route. A drawback of the stir-cast method, which frequently arises during the stirring stage of the production process, is the possibility of non-uniform distribution of the reinforcements into the melt (see Section 6.2 in Ch. II-6). Thus, a formation of agglomerates and/or sediments inside the molten alloy are frequently observed, when applying this method. Typically, the method allows incorporating into the metal matrix of up to 30%, by volume, of reinforcement particles which size could vary between 5-100 μm. Recently, the method was adapted in incorporating into the melt nano-sized particulates.

(ii) *Infiltration casting*. In that method, the MMCs are fabricated by pressing the molten matrix material through a "mesh" formed by dispersed solid-phase materials (e.g., ceramic or metal-ceramic powders, fibers, woven wires, etc.), which serve as reinforcement in the composite to be produced. During the process of infiltration, the liquid metal wets the reinforcement and fills the space between the "mesh". The driving force of the infiltration could be, (a) a spontaneous infiltration, due to the capillary force, or (b) forced infiltration, (see Fig. II-1-3 and Fig. II-1-4) due to the application of external pressure (gaseous, mechanical, electromagnetic, centrifugal, or ultrasonic) to the free "mirror" surface of the liquid matrix material. In this specific method, the volume fraction of the reinforcements could range from 10 % to 70%, depending on the level of porosity of the reinforcement.

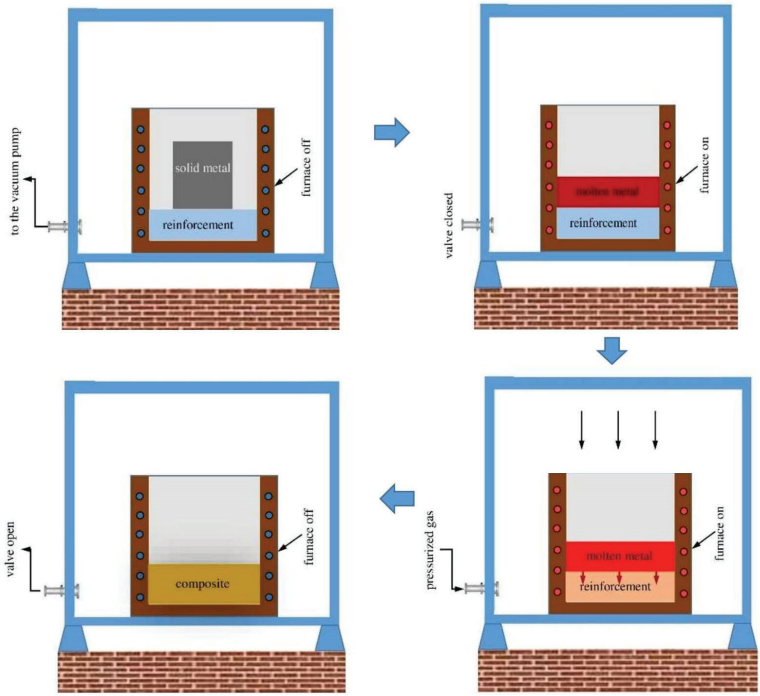

Figure II-1-3 Flow chart of the gas pressure infiltration casting method.

Two versions of the infiltration casting method, depending on the way the molten matrix material is squeezed through the reinforcement, are practicable; (a) *gas pressure infiltration casting* (see Fig. II-1-3) - the molten matrix material is forced through the voids formed between the dispersed reinforcement phase by applying a pressurized gas on the face of the molten metal. This approach is usually used in manufacturing large composite parts, and (b) *squeeze casting* (*pressure die infiltration*) – the flow of the molten material is accomplished by a movable piston (ram) that applies pressure on the molten metal surface, thus, forcing it to flow through the dispersed reinforcement phase. At the end of the "flow" phase of the process, the piston is left in contact with the metal and under pressure for two reasons; to absorb the heat from the molten metal and to follow the shrinkage of the molten material during its solidification, thus, reducing the porosity of the final product. In that way, are produced fine-grain castings with low porosity. This version of the method is especially suitable for the manufacturing of small parts with uncomplicated shapes, e.g., automotive engine pistons.

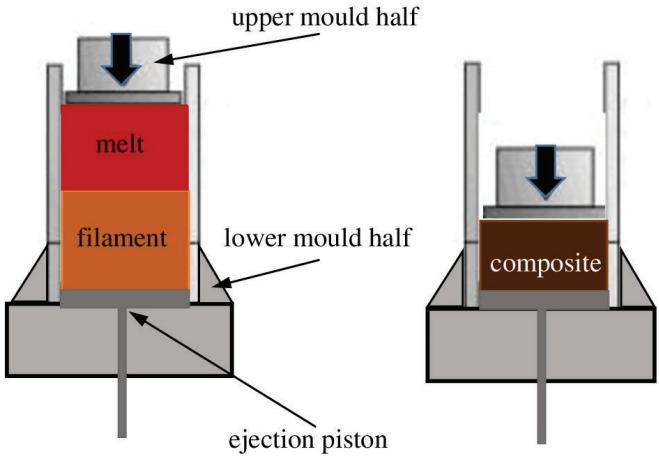

Figure II-1-4 Squeeze casting (pressure die infiltration casting)

1.1.3 In-situ fabrication of metal matrix composites

In that technique, the reinforcement is produced during the process of the composite's production, e.g., via chemical reaction which is initiated by; (a) introduction into the matrix chemical elements or compounds with

which the matrix chemically reacts to produce new phases. The latter is, therefore, precipitating inside the matrix, thus forming the desired reinforcement, (b) via changing of the external processing parameters (e.g. temperature, pressure), or (c) both of the preceding (see Fig. II-1-5).

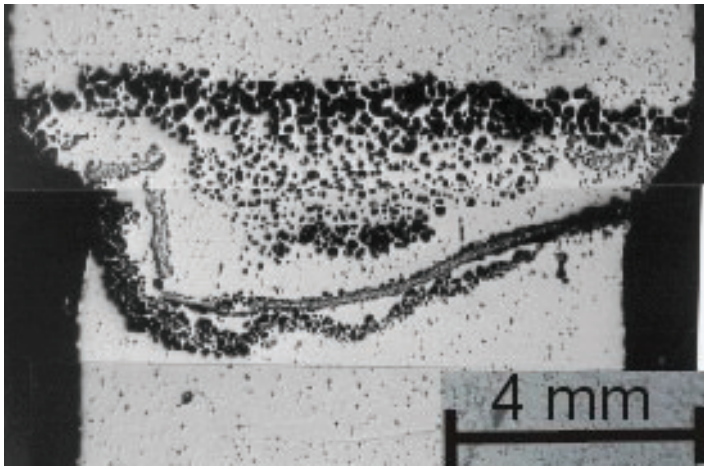

Figure II-1-5 A metal matrix composite Al-TiB_2 produced by the *in-situ* method in a low gravity environment (Froyen, Van Vugt – Grebolder [1]). The precipitates of TiB_2 (the black dots with different sizes) are visible at the central part of the micrograph. Notice the considerable Ostwald ripening undergone by a part of the TiB_2 precipitates.

In this way, the composite material is produced in one step and all the compatibility issues between the matrix and the compounds/phases, associated with differences in the chemical and physical properties, are avoided; the reinforcements are formed by precipitation inside the melt, or inside the solid phase, which ensures (a) thermodynamic compatibility between the matrix and the reinforcement, (b) free of contamination matrix-dispersoids/precipitates surface. In that way, a stronger bonding between the matrix and the reinforcement is achieved. A drawback of the method is again the control of the process parameters during the production of the composite.

1.1.4 Other methods of MMC's production

(i) *Diffusion Bonding*. This is a common solid-state technique used widely at the joining of metals with similar or dissimilar physicochemical properties. The diffusion bonding method relies on the cohesion bonds, formed between the reinforcement and the matrix material. Keeping in mind, that the strength of these bonds is achieved by enhancing the interdiffusion between reinforcement and the matrix, it could be thus possible to achieve the desired microstructure by varying the processing parameters, say, the temperature and the pressure. The principal advantage of this technique is that in its essence it allows the control of the spatial distribution of the reinforcement. Therefore, by varying the production parameters, MMCs with a predetermined spatial distribution of the volume fraction of the reinforcement could be produced (e.g., with "sandwich" or layered structure).

(ii) *Deposition techniques*. Those methods of composites' fabrication are based upon the coating of the reinforcement particulates with a layer of the matrix material. The coating procedure intends to achieve easier incorporation of the reinforcement into the composite matrix. The main disadvantage of these techniques is that they are time-consuming and expensive. Several deposition techniques are available:

(ii-1) *Spray forming*. Spray forming emerged as a viable technology for the discontinuous fabrication of reinforced MMCs. Advantages of this hybrid powder metallurgy approach are in their capability of (a) producing a near-net-shape product, (b) developing fine-scale microstructures, devoid of macro-segregation and porosity, (c) instigating a uniform distribution of the reinforcing constituents in the matrix, without compromising the interfacial properties of the matrix and the reinforcement, and (d) the health hazards connected with the handling of nano-sized powders is eliminated. Two adaptations of the spray forming process, used at the production of reinforced metal matrix composites, exist; reactive spray forming, and inert spray forming. The former, as its name suggests, combines the spraying with an attendant *in situ* reaction which provides the reinforcement phase, while at the second the reinforcement is added to the liquid matrix metal before the spraying.

(ii-2) *Reinforcement plating and deposition*. This technique is similar to the preceding one. The difference is that in this case, instead of unprocessed reinforcement, one with a metal coating deposited on it is used. The as-processed reinforcement is then used in the spray-deposition process; sprayed together with the matrix material onto a metal substrate. As a result, a layer of the composite on the surface of the substrate is created. The porosity in this technique is quite high, it can vary between 5

and 10%, which necessitates additional operations to consolidate the composite to a higher density, which makes this process economically inefficient.

(ii-3) *Electroplating*. The electroplating method of composites' production is based on the passing of electric current through electrolyte that contains ions of the desired matrix material. The matrix material serves as an anode, while as cathode serves mandrel with fibers (reinforcement) wound around it. By applying an electric voltage to both electrodes an electric current occurs which transports and deposits the matrix ions from the cathode on the anode, thus forming on the cathode the desired composite.

(ii-4) *Spray deposition*. In this technique, the reinforcement (fibers) is wound onto a foil-coated drum The drum is then set into rotation, and a jet of molten matrix material is sprayed on its surface, thus forming a tape-like ingot on the drum surface. The advantage of the method is that the matrix and the reinforcement are evenly distributed within the composite. The source of molten metal could be powder or wire feedstock (similar to those used in welding) which is melted in a flame, arc, or plasma torch.

1.2 General rules at the selection of the reinforcement for MMCs

Which of the above methods would be most suitable in the production of an MMC depends on the stability (mechanical, chemical, thermal, etc.) of the reinforcement during the production of the MMC and the planned time for use of the MMC product. As discussed, the decrease in the reinforcement's size leads to an increase in the surface energy of the reinforcement. It could happen that at a certain, size of the reinforcement and/or processing condition, the total energy, which is the sum of the surface energy and the Gibbs free energy, could exceed that of the matrix, thus making the reinforcement particles thermodynamically unstable. In that case, depending on the rate of decay of the reinforcement particle, the reinforcement could disintegrate and the products of disintegration dissolve into the surrounding matrix. Thence, the composite production would be meaningless due to the disappearance of the reinforcing agent. Since most of the methods, currently used to produce MMCs, involves the treatment of nano-sized particulates at elevated temperatures, it is highly desirable to discuss their thermal stability as a function of the temperature and their size.

From the course of physical chemistry, is known that the thermodynamic stability of a phase depends on its Gibbs free energy. The composite,

however, consists at least of two phases, which are in close contact with each other. Therefore, together with the Gibbs energies of the reinforcements and the matrix, the surface energies at the contact of these phases should be taken into account. The free energy of the reinforcement particle is equal to its volume multiplied by the Gibbs energy of the reinforcement's material, G^p in Jm^{-3}, thence, V^pG^p in J. By immersing the reinforcement into the matrix, the total energy, U, of the thermodynamic system particle-matrix changes due to: (i) the Gibbs energy of the system reinforcement-melt reduces by the amount of V^pG^m i.e., proportionally to the volume displaced by the reinforcement particle, and (ii) increases with the energy of the newly created surface, S^p, which is equal to the created new surface multiplied by the surface tension, σ, i.e., σS^p. For the total energy U in [J] of a spherical particle with a radius R_p is then valid:

$$U\left(R_p,T\right)=\frac{4}{3}\pi R_p^3\left(G^p-G^m\right)+4\pi\sigma R_p^2. \qquad (1)$$

Depending on the sign of $U\left(R_p,T\right)$ three possible types of system behavior exist; (i) $U\left(R_p,T\right)>0$ (Recall that both, G^p and G^m, are negative.), the reinforcement will dissolve in the matrix, (ii) $U\left(R_p,T\right)=0$, the matrix and the particle are in equilibrium, and (iii) $U\left(R_p,T\right)<0$ the reinforcement will be thermodynamically stable, i.e., it will not disintegrate during the processing of the composite. To conceive, the preceding, one could draw an analogy with the behavior of, say, tiny copper and sugar pieces immersed in water. The reason that the sugar will dissolve into the water but copper would not is that $G^{sugar}-G^{H_2O}$ is positive while $G^{Cu}-G^{H_2O}$ is negative. In both of those cases, the contribution of the surface tension member could be considered negligible.

To illustrate the application of Eq. 1, let us consider the suitability of SiC as a reinforcer in the following metals/alloy; Aluminium, $Al_{0.9}Si_{0.1}$ (Silumin), and iron. Let the utilized production method be one of the casting methods (see Section 1.1.2), which implies that the reinforcement is added to the melts of these metals/alloy. The calculated, $U\left(R_p,T\right)$,

for the case of SiC particles, immersed into the molten metals/alloy, are listed below:

$$U^{Al-SiC}\left(R_p,1250\right) = -1.54110^{10} R_p^3 + 18.84R_p^2 , \qquad (2a)$$

$$U^{AlSi_{0.1}-SiC}\left(R_p,1250\right) = -1.7110^{10} R_p^3 + 18.84R_p^2 , \qquad (2b)$$

$$U^{Fe-SiC}\left(R_p,1750\right) = 9.09210^{10} R_p^3 + 18.84R_p^2 . \qquad (2c)$$

The temperatures (in Kelvin) of the melts, used in the preceding calculations, are those most frequently used at the production of these MMCs. The composition of the Silumin is in at. %, the particle's radii are in [m] and for the sake of simplicity the surface tension at the contact, molten metal - reinforcement, is assumed to be the same for all composites, say, 1 J m^{-2}. The thermodynamic data used in the calculations above is taken from [2] and [3].

The first two equations show that the SiC-particulates will be stable up to the "critical" size of ~2 nm ($R_{p,\,crit}$ ~ 1 nm), thence, the production of Al-SiC and $Al_{0.9}Si_{0.1}$-SiC composites will be problem-free, for sizes of the reinforcement which are above 2 nm (actually, such small sizes are never used in the practice). This is not the case with the would-be Fe-SiC composite. As seen from the third of the equations above $U^{Fe-SiC} > 0$, regardless of the size of the reinforcement. Therefore, in this case, the reinforcement SiC is thermodynamically unstable and will dissolve into the molten iron during the processing of the composite. How fast that will happen depends on the dissolution rate according to the reaction: SiC → Fe-(Si)-(C) (The round parentheses around Si and C are used to indicate that these two elements are dissolved into the molten iron.)

In the analysis above it was presumed that the reinforcement particles are spherical. In the practice, however, this is not the case. Yet, when the reinforcing shape differs significantly from that of a sphere, i.e., when there are parts on the surface of the particle whose radii of curvature tend to zero (e.g., the presence of sharp edges such as the tips of the mustache-shaped reinforcements), even if the overall dimensions of the reinforcement are above the critical size, at those sharp edges a local disintegration of the reinforcement could occur, which eventually could lead to the disintegration of the reinforcement as a whole. Therefore, a careful analysis, similar to the one above, should be carried out and the results obtained taken into account when selecting; reinforcer, geometrical

shape, and size of the reinforcer, processing temperature, and the processing time.

The analysis carried out could be extended further to allow evaluation of the time for which an unstable reinforcement particle will dissolve in the surrounding liquid/solid matrix. The rate of decay, as a function of the thermodynamic properties of the matrix-reinforcement system and the reinforcement size, could be assessed by a set of equations [4-6], discussed in detail in Ch. II-4 Section 4.1. For the sake of simplicity, in the analysis below will be assumed: (i) the reinforcement and the matrix are compounds (e.g., pure metals or stoichiometric substances), (ii) the rate of dissolution of the reinforcement is much smaller than the kinetic parameter - v_0, (iii) the temperature is a constant, and (iv) by dissolving into the matrix the products from the reinforcement's decay do not change significantly the matrix composition. When the conditions (i) to (iv) are fulfilled for the reaction at hand, SiC → Fe-(Si)-(C), the as-mentioned kinetic equations yield:

$$G^{Fe} - G^{SiC} = -RT \ln\left(1 - \frac{\dot{R}_p}{v_0^{SiC}}\right) + \frac{2\sigma V_m^{SiC}}{R_p}, \tag{3}$$

In the reality the inequality, $\frac{\dot{R}_p}{v_0^{SiC}} << 1$, is always fulfilled, (see condition (ii)), thence, the differential equation above is readily rewritten as:

$$\dot{R}_p = \frac{v_0^{SiC}}{RT}\left(G^{Fe} - G^{SiC} - \frac{2\sigma V_m^{SiC}}{R_p}\right). \tag{4}$$

In the case discussed here, $\dot{R}_p$ is the decay rate of the SiC particle (presumed to be spherical). Eq. 4 allows the separation of the variables, thence, an analytical solution is obtainable. Assuming that the initial radius of the armament is R_{p0}, it could be shown that the decay time t_{decay} of the particle is:

$$t_{decay} = \frac{R_{p0}}{a v_0^{ph}}\left[\frac{b}{a}\ln\left(\frac{b}{|a|+b}\right) - 1\right]. \tag{5}$$

The symbols used in the equation above refer to, $a = \frac{G^{Fe} - G^{SiC}}{RT}$, and $b = \frac{2\sigma V_m^{SiC}}{R_{p0} RT}$.

From (2c) follows that in the case of the Fe-SiC system $|a| >> b$, respectively, $\frac{b}{a} \ln\left(\frac{b}{|a|+b}\right) << 1$. Thence, the dissolution time is, $t_{decay} = \frac{R_{p0}}{|a| v_0^{SiC}}$. Notice that the preceding relation is valid only for $a < 0$. By taking into account that in the reality $v_0 \approx 10^{-6}$ [ms^{-1}] and that $|a| \approx 5.10^5$ (see Eq. 2c), it could be argued that $t_{decay} \cong 2R_{p0}$ s (in the preceding relation R_{p0} should be in [m]). Thence, for the decay time of a SiC nanoparticle with a size, say R_{p0} =10^{-7} m, is obtained ~ 2.10^{-7} s.

Suggested additional reading to Ch. II-1

1. K. U. Kainer, Basics of Metal Matrix Composites, Custom-made Materials for Automotive and Aerospace Engineering. Edited by K. U. Kainer, 2006 WILEY-VCH Verlag GmbH & Co., Weinheim ISBN: 3-527-31360-5.
2. K. K. Chawla, Composite Materials. Science and Engineering, Third Edition, Springer New York, Heidelberg, Dordrecht, London 2013, ISBN 978-0-387-74365-3 (eBook).
3. D. R. Askeland and P. P. Fulay, Essentials of Materials Science and Engineering, Second Edition, Cengage Learning 2009, ISBN-13: 978-0-495-24446-2.
4. T. W. Clyne, Metallic Composite Materials in Physical Metallurgy Robert W. Cahn and Peter Haasen eds., vol. 3, Ch.30, Elsevier Science B.V. ISBN 0 444 89875 1.
5. M. F. Ashby and D. R. H. Jones, Engineering materials. Vol.1 and 2, Butterworth-Heinemann (2002) ISBN 0 7506 3081 7.

6. T. Kobayashi, Strength and Toughness of Materials, Ch. 8 Metal Matrix Composites, Springer Japan 2004, ISBN 978-4-431-53973-5 (eBook).
7. R. E. Smallman and R. J. Bishop, Modern Physical Metallurgy and Materials Engineering, Sixth Edition, Butterworth-Heinemann 1999, ISBN 0 7506 4564 4.
8. L. S. Darken and R. W. Gurry, Physical chemistry of metals. McGraw-Hill (1953), ISBN 978-0070153554.
9. S. L. Pramod, S. R. Bakshi, and B. S. Murty, Aluminum-Based Cast In Situ Composites: A Review, JMEPEG DOI: 10.1007/s11665-015-1424-2, ASM International (2015).
10. B. Ch. Kandpal, J. Kumar, H. Singh, Production Technologies of Metal Matrix Composite: A Review, International Journal of Research in Mechanical Engineering & Technology, 4 (2) 27-32 (2014).
11. T. Khorshid, "Nano-Crystalline Metal Matrix Nano-Composites Reinforced By Graphene and Alumina: Effect of Reinforcement Properties and Concentration on Mechanical Behavior" (2016). Theses and Dissertations. Paper 1314.
12. S. N. Trinh and S. Shankar, "Processing and Properties of Metal Matrix Composites" (2016). Mechanical Engineering and Materials Science Independent Study. 10. https://openscholarship.wustl.edu/mems500/10.
13. M. Hillert, Thermodynamics and Phase Transformations: Selected Works, Scientific Editors: J. Ågren, Y. Bréchet, Ch. Hutchinson, J. Philibert, G. Purdy, EDP Sciences 2006, ISBN: 2-86883-889-8.

References to Ch. II-1

1. L. Froyen and L. Van Vugt – Grebolder, KULeuven, private communication (2000).
2. Thermochemical database for light metal alloys, edited by I. Ansara, A. T. Dinsdale, M. H. Rand, Published by the Office for Official Publications of the European Communities, vol. 2 (1998). ISBN 92-828-3902-8.
3. A. T. Dinsdale, Calphad, 15, 4, 317-425 (1991).
4. L. A. Anestiev On the solute redistribution at thermally activated phase transition processes I. Theory, J. Crystal Growth 140, p.167-174 (1994).

5. L. A. Anestiev On the solute redistribution at the thermally activated phase transition processes II. Applications, J. Crystal Growth 140, p.175-181 (1994).
6. L. A. Anestiev, D. Malakhov Growth rate at first-order phase transformation processes in multi-component systems J. Crystal Growth 276, p.643-651 (2005).

CHAPTER II-2

STRUCTURE AND MECHANICAL PROPERTIES OF THE MATERIALS: A SHORT OVERVIEW

LUBOMIR A. ANESTIEV

As from the Introduction section of this part, this part of the book will be mainly concerned with selected topics on the mechanical properties of materials, thus, in the present chapter, the stress will be placed mainly on (i) the microstructure of the materials and how the mechanical properties and their microstructure are related, (ii) testing of the mechanical properties of the materials, tensile and hardness tests (iii) definition of the main mechanical properties of the materials and the concepts of stress, strain, deformation, yield strength, Young modulus, etc., (iv) plasticity and fracture of materials, (v) specificity in the mechanical properties of MMCs and (vi) essentials from the theory of elasticity. In case that the reader feels confident in his/her knowledge of the topics listed above, he/she could skip this chapter of the book without that precluding him from understanding the theories which are discussed/used in the next chapters of this book.

The mechanical properties are strongly dependent on microstructure (e.g., grain size, the constitutional phases distribution, etc.), the crystals structure of the constituent phases (i.e., the arrangement of atoms in the crystal lattice, the presence of defects of the crystalline structure, etc.), and the chemical composition (e.g., distribution of the alloying elements in the matrix, the impurity level, etc.). The interrelation between the microstructure and the mechanical properties of the material could be illustrated by the observed increase/decrease, say, of the yield strength with the decrease/increase of the grain size, or the presence of micro-, or nano-, particulates in the metal matrix. Therefore, obtaining relationships that connect the metal structure and the materials' properties is of great importance in the science of materials, as these determine the material's

performance at processing (e.g., metalworking), failure and failure prevention, and suitability for advanced applications.

2.1 The structure of the Materials (Metals)

At their most, the metallic materials (as well as many nonmetallic ones) are crystalline solids. The basic structural unit of a crystal material is the crystal lattice which consists of unit cells. Some examples of basic unit cells found in crystalline materials are shown in Fig. II-2-1 (a) through (d). By repeating these basic cell arrangements in three dimensions, as illustrated in Fig. II-2-2, the crystal lattice of the specific solid is formed.

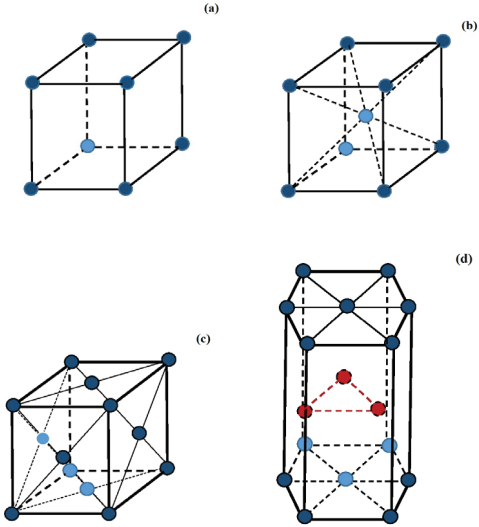

Figure II-2-1 Some of the most frequently encountered in reality basic cells and the atom arrangements in them. (II-2-1a) cubic, (II-2-1b) body-centered cubic (bcc), (II-2-1c) face-centered cubic (fcc), and (II-2-1d) hexagonal close-packed (hcp). The "invisible" atoms are circled with a broken line (hcp) or shown in brighter color (cubic, bcc, fcc).

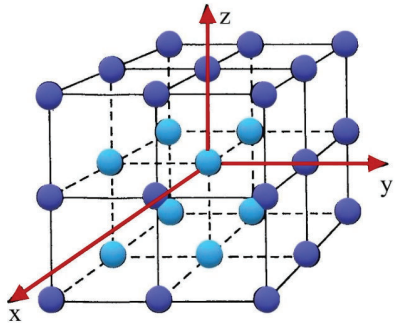

Figure II-2-2 Formation of the structure of crystalline material by repeating basic cell arrangement (here the cubic basic cells).

It was found (by Bravais) that the atoms' arrangement in the unit cells is not done arbitrarily. By analyzing different crystalline materials structures he found that the structure of the unit cells could be described by fourteen basic types. In crystallography, these are known as Bravais lattices. Yet, in the metals, with which we will be mostly concerned throughout this part of the book, three of the Bravais lattices are most frequently encountered; the face-centered cube (fcc) (e.g., nickel, aluminum), body-centered cube (bcc) (e.g., α-iron, tungsten, molybdenum), or hexagonal close-packed (hcp) (e.g., titanium, magnesium).

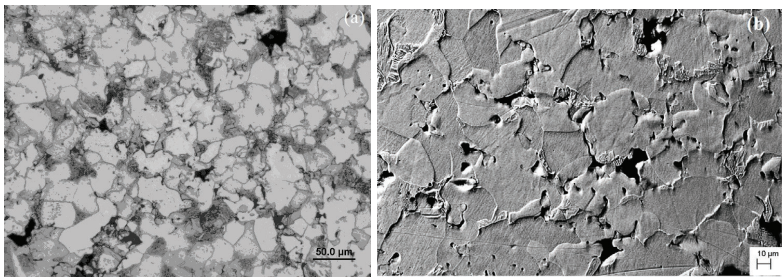

Figure II-2-3 Examples of metallic microstructures: (3a) Optical micrograph of the grains microstructure in low carbon steel; (3b) Embossed SEM image of the grains in the same steel, obtained after prolonged etching with a strong chemical etchant.

However, crystalline materials, made of a single crystal, also known as monocrystals, are rarely met in nature. Most of the materials encountered

in reality and used in engineering are constituted from many tiny monocrystals, or grains, as illustrated by Fig. II-2-3a and Fig. II-2-3b. Depending on the composition of the source material and the thermomechanical processing applied, the grain size in the final product could range between 1 and 1000 μm.

2.2 Common structural defects present in materials

Crystals are never free of defects, which is a consequence of the laws of thermodynamics, that state; at equilibrium, the free energy of the system crystal - defects should be minimal.

Different kinds of defects in the crystal structure could be distinguished most important of which are; vacancies and interstitials (point defects), dislocations (line defects), and intercrystallite, grain, and phase boundaries (planar defects). It is the existence of the crystal defects above that determine the properties, especially the mechanical ones, of the crystalline material.

2.2.1 Vacancies and interstitial atoms

Three types of point defects exist; (i) a vacant lattice site (vacancy), (ii) the placement of an atom in an interstitial site (interstitial atom(s)), and (iii) a combination of the first two, placement of a “foreign” atom in a vacant lattice site. Yet the most significant point defects of the three are the vacancies, since these control one of the most important transport processes in solids, the atom’s diffusion. It is also believed that these are a source or sink of the atoms when the dislocations, everpresent in material, are generated, shrunk, or grown. It should be noted that in the environment of a point defect the atoms are forced to rearrange, thus perturbing the original energy field of the crystal. It is the interaction between the disturbances in the energy field, caused by the point defects, with, say, the migrating dislocations that are responsible for the phenomenon known as solution strengthening (see Section 4.2 in Ch. II-4).

2.2.2 Dislocations

This structural defect is given detailed consideration in Ch. II-3 because of its importance in the description of the dislocations’ induced strengthening phenomena.

2.2.3 Crystallites

The grains themselves are not perfect crystals either. These also contain imperfections, much smaller than the grains, one of which is the crystallites. The crystallites could be defined as; very small monocrystals which are an integral part of the grain. As a rule, their orientation in the grain differs from one crystallite to another. The boundaries between the crystallites of the grain are considered defects of the grain structure and sometimes in the specialized literature are referred to as *low-angle boundary defects* (see below). A conceivable microstructure of two crystallites inside a grain is shown in Fig. II-2-4.

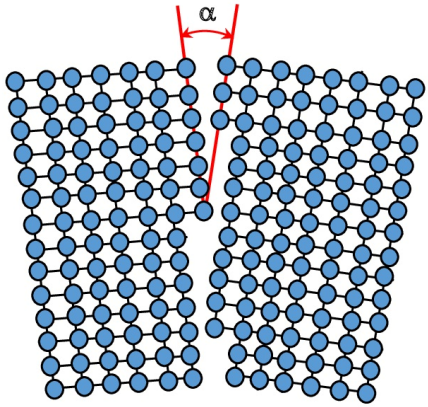

Figure II-2-4 Sketch of a low-angle boundary defect, known as crystallite. The figure shows two crystallites and the boundary formed between them.

2.2.4 Grain boundaries

Grain boundaries are one of the most easily detectable lattice defects. The grain boundary could be defined as a surface separating two differently oriented regions in the same crystal. Although they are easily distinguished, even by a naked eye, the grain boundaries are less studied and understood than all defects listed so far. The problem is in their complex structure, which requires the introduction of an extensive set of parameters to characterize them. For instance, the mathematical description of a grain boundary in the simplest case, a 2-D grain, requires four parameters, namely

a rotation angle that describes the orientation difference between the adjacent crystals (orientation relationship), an angle that defines the spatial orientation of the grain boundary "plane" (grain boundary orientation) and a 2 component translation vector accounting for the displacement of the two adjacent crystals to each other. Fig. II-2-5 shows a sketch of a 2-D grain, drawn from a bearing balls model, which illustrates the concepts of a *low angle* (small angle of misalignment between the adjacent crystal lattices) and *high angle* (large angle of misalignment) boundaries. The role of the grains in the materials' strengthening lies in their interaction with the moving dislocations. This interaction gives rise to the Hall-Petch effect, discussed in Section 4.6 of Ch. II-4. Ahead of the detailed discussion concerning the Hall-Petch effect, it should be noted that the latter is due to the interaction of the energy field at the grain boundary with that of the migrating dislocation.

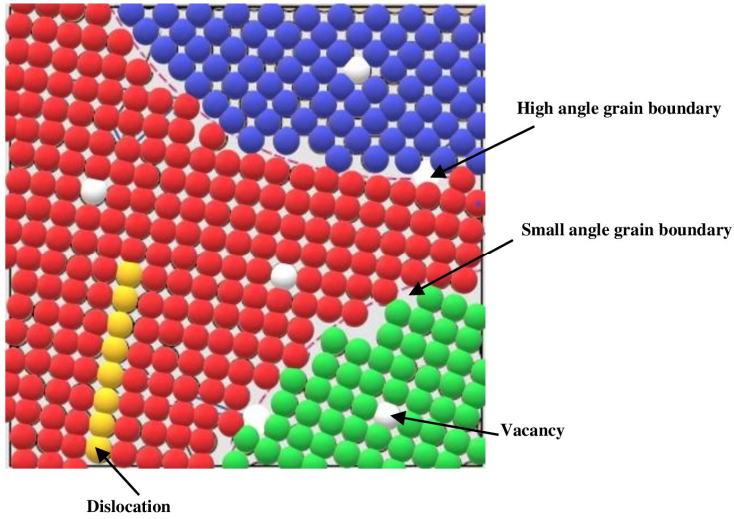

Figure II-2-5 A sketch of "real" grains found in a polycrystalline material showing, vacancies (white), a dislocation (yellow), a low angle (small angle of misalignment between the adjacent crystal lattices), and high angle boundaries (large angle of misalignment).

2.3 Methods of improving the mechanical properties

The mechanical properties of pure metals are rarely good enough to be used directly as structural materials. Therefore, a necessity arises, these to

be improved by the application of some additional processing. Three of the most commonly used ones are (i) alloying, (ii) reinforcement with material(s) that possess mechanical characteristics superior to these of the material which is subject to improvement, or (iii) a combination of the preceding two.

(i) *Alloying*. Alloying, i.e., adding chemical elements that differ from the basic chemical element composing the material (e.g., adding carbon to iron), is one of the commonest ways to improve the mechanical or other properties of a metal. In the reality, these mixtures (the metal alloys) may consist of over ten different chemical elements added in different proportions (concentrations). Depending on the ratio of the composing parts, during a specific way of processing or treatment (e.g., casting, or heat treatment) of an alloy, new phases may precipitate within the base metal (at the grain boundaries or in the grain interior, see Fig. II-2-6). These as a rule lead to considerable changes, not only in the microstructure but also in the mechanical properties of the alloy. Typically, minor alloying additions do not change drastically the basic crystal structure; the alloying elements at small concentrations usually form solid solutions by dissolving in the basic (matrix) element of the alloy (the solvent). However, if some concentration limits are exceeded, other phases (either with the same or different crystallographic lattices) may precipitate, as shown in Fig. II-2-6.

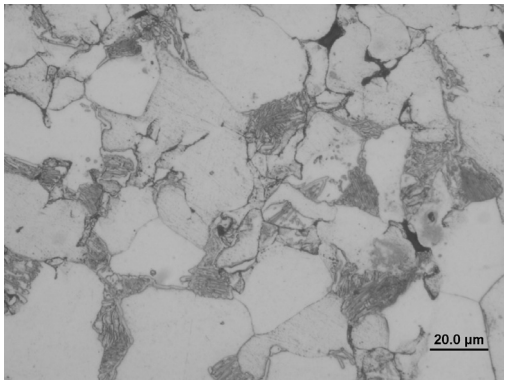

Figure II-2-6 Optical micrograph of precipitated and grown from austenite (γ- solution of carbon in iron) grains during sintering of a compact, formed from Fe and C powders. The white grains are α-Fe (ferrite) while these seen in different grades of grey are pearlite, a eutectoid composed of α-Fe and Fe_3C lamellas.

The final microstructure of an alloy depends on the chemical composition and the processing route. When the alloy is prepared at conditions close to that of the equilibrium between the constituent phases (e.g., produced at sufficiently slow cooling), the alloy phase structure is readily determined (or the phases that form are readily predicted) by consulting the equilibrium phase diagram of the studied system. In the cases, when the processing conditions differ considerably from those of equilibrium, the time-temperature transformation (TTT) or continuous cooling transformation (CCT) [1] diagrams, if available, are used in designing and improving the final microstructure of the alloy.

(ii) *Metal matrix composites*. Another way in improving the mechanical properties of the metals and the alloys is by incorporating into the basic metal or alloy (e.g., by the PM route) of micron-, or nano-sized ceramics or intermetallic particulates. The as-obtained materials are known as metal matrix composites (MMCs) and today, their synthesis and the study of their properties, is one of the fastest-growing areas in materials science.

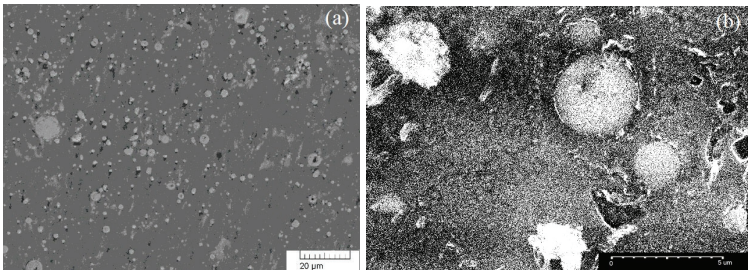

Figure II-2-7 Examples of the microstructures of a metallic matrix composite (MMC): (7a) SEM micrograph of the embedded in an Al-matrix TiCN powder particles (micrograph provided by R. Lazarova). (7b) SEM micrograph of the same composite but in a larger magnification showing details of the embedded in the matrix reinforcement particles (micrograph provided by V. Dyakova [2]).

Fig. II-2-7 shows an Al-based MMC, which utilizes as reinforcement micron- and nano-sized TiCN particulates. Besides reinforcement in form of particulates, as shown in the figure above, in MMCs could also be utilized whiskers, short, or long, fibers (e.g., rods or different kinds of filaments), etc. Processing of these composites typically entails the incorporation of the reinforcement material into the metal matrix by using ingot metallurgy or powder metallurgy techniques (see Ch. II-1). Because

of their importance, the mechanical properties of the MMCs are discussed in detail in Section 2.7 of this chapter.

2.4 Mechanical properties and testing of the materials

The ability of the metal/material to meet design and service requirements and to be fabricated to the proper dimensions is determined by its mechanical and physical properties. The reason for materials testing, therefore, is to determine whether the studied material fits the requirements of a specific application. The testing methods, thus, are various and depend upon the point of view in which the materials' testing is approached; theoretical calculations, obtaining physical constants of the material, obtaining of data concerning specific properties of materials from the application point of view, etc. The *physical properties* of a material are those measured by methods not requiring the application of an external mechanical force (or load). Typical examples are density, electric (e.g. resistivity) magnetic properties (e.g. permeability), thermal conductivity, specific heat, and the coefficient of thermal expansion. *Mechanical properties* are those which give a relationship between the loads applied to the material (or stresses) and the response of the material to these loads.

2.4.1 Mechanical testing

When metals, or materials in general, are subject to an external force, their response depends on several factors; the type of loading (e.g., tension, compression, shear, or combinations of those), the strain rate, temperature, the way of loading (e.g. axial or bulk), presence of defects on the sample surface (e.g., notches, cracks, corrosion, products of traces of chemical reactions), etc.

In this chapter of the book, our attention will be focused mainly on the relationship between the microstructure of a metal/alloy composite and the properties measured during mechanical testing. For the sake of simplicity, the basic principles and definitions concerning the deformation and fracturing in materials/metals will be studied on the example of uniaxial tensile loading. In general, tensile tests are performed on specimens, which are prepared or shaped according to the specific standards, adopted by the country or the organization, where the tensile experiments are carried out. Fig. II-2-8 shows a specimen shaped for uniaxial load testing. (The shape of the test piece, shown in Fig. II-2-8, is typical for most of the testing standards used.).

Figure II-2-8 A photograph of a typical form of a test piece (test specimen) used in the mechanical testing of metals/alloys (provided by R. Lazarova).

Figure II-2-9 A test piece subjected to uniaxially tensile loading.

The term "uniaxial loading" means that the studied test piece (sample) is subjected to two equal colinear forces acting in opposite directions, as shown in Fig. II-2-9. During that test at least two parameters are simultaneously monitored, the applied load and the extension (the change in length) of the test piece. The load and the displacements measured during the tests are then used in calculating the dependence between the stress, that is induced in the sample (σ), and the sustained strain (ε). The obtained $\sigma(\varepsilon)$ dependence is referred to as the *stress-strain* relationship, σ - ε, or in words, *sigma* – *epsilon* relationship. In materials science and structural mechanics the strain ε and stress σ are defined by the following expressions:

$$\sigma = \frac{P}{S}, \text{ and } \varepsilon = \ln\left(\frac{l_i}{l_0}\right) = \ln\left(\frac{l_0 + \Delta l}{l_0}\right) \cong \frac{\Delta l}{l_0},$$

where P is the applied load, l_0 is the initial length of the specimen, l_i is the current length measured during the test, S is the cross-sectional area of the specimen and Δl is the change in length due to the applied load. From that

definition is seen that the strain is a dimensionless variable, while the stress has the same dimension as the pressure, Pascals – [Nm^{-2}]. A typical σ - ε dependence of a plastically deformable material (mild steel) is shown in Fig. II-2-10 together with the changes taking place in the test piece during loading.

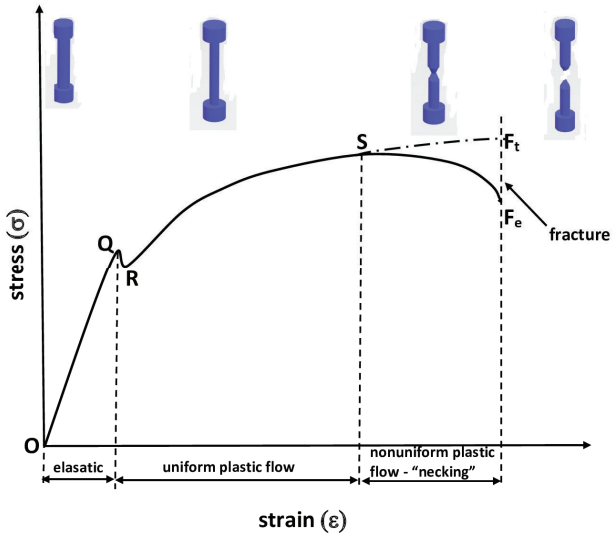

Figure II-2-10 σ-ε diagram for a test piece of a ductile alloy (e.g. mild steel) obtained during a uniaxial tensile test. Above are shown the different stages in the deformation undergone by the test piece during the tests. The σ-ε engineering diagram is shown as a solid line, while the true σ-ε diagram, as a dash-dotted line. The meaning of the letters used in the figure is explained in the text.

As seen from the σ - ε diagram, the induced stress is a complicated function of the strain. Notice, that between the points O and Q the dependence $\sigma(\varepsilon)$ is linear. Point Q is thus known as the elastic limit (or limit of proportionality) of the tested material. In case when the material is stressed beyond the Q point the, $\sigma(\varepsilon)$ curve deviates from linearity. At first, the extension of the tested material occurs without increasing the applied force (see Fig. II-2-10). For that reason, point Q is also referred to as the yield point of the material and from here on the plastic deformation region begins. The stress value at that point is termed - "yield strength of the material" and is considered in engineering as one of the material's

most important mechanical characteristics. In the structural mechanics and the materials testing it is denoted as σ_Y. If the load is removed before reaching the yield strength limit, the tested specimen returns to its initial length without visible changes of its shape (length, width, etc.). Beyond σ_Y, however, the changes in the material are irreversible, the test piece remains permanently deformed even after the removal of the load, i.e., beyond *Q* the plastic deformation of the material begins. The further increase of the tensile load, beyond that point, indicated on the diagram with *R*, leads to rapid stretching of the test piece. That stage of the deformation is sketched above the σ - ε graph in Fig. II-2-10 with a small icon of the test piece. At first, the stretching is uniform, along the entire length of the tested specimen, but after that, at the most stressed part local narrowing is formed which is referred to as "neck". It was found that a visually detectable "necking" takes place just after the maximum force value has been reached, indicated on the σ - ε graph as *S*. After that in the vicinity of the necking point a rapid decrease of the cross-section of the test specimen begins, as illustrated by the sketched icon in Fig. II-2-10, which leads to a rapid increase of the stress in the neighborhood of the neck. In other words, at a constant tensile load of the test specimen, the stress in the neck region will be always higher than that observed elsewhere. Recalling, that the induced in the material stress is evaluated by dividing the applied load on the specimen's cross-sectional area, two types of $\sigma(\varepsilon)$ stress-strain diagrams could be constructed; (i) *engineering stress-strain* diagram, in which the changes of the cross-section (the "necking") of the specimen are not taken into account (shown in Fig. II-2-10 as a solid line), and (ii) *true stress-strain* diagram, in which the reduction of the sample's cross-section, is accounted for (shown in Fig. II-2-10 with a dash-dotted line). The difference between the engineering and the true stress-strain diagrams is particularly well-distinguished after the non-uniform flow limit is reached, i.e. beyond the point indicated on the diagram with *S*. The presumable behavior of the test specimen, i.e., the neck formation and the test-piece breaking, are again visualized in Fig. II-2-10 with small icons of the test piece. The mechanical test ends with the fracturing of the test piece, indicated on the σ - ε graph as *F*. The subscripts "e" and "t" at *F* refer to engineering and true stress-strain.

Note: The form of the $\sigma(\varepsilon)$ diagram shown in Fig. II-2-10 is a special case of the material's behavior under load. In general, most of the alloys, do not show a definite elastic limit or yield point.

2.4.2 The elastic behavior of the materials. Elastic moduli

As above, in the region of the elastic deformation, the stress is a linear function of the strain, $\sigma = E\varepsilon$. The first derivative of $\sigma(\varepsilon)$, with respect to ε, the strain, therefore, should be a constant, $\frac{d\sigma}{d\varepsilon} = E$. The constant, E, is termed - Young modulus, and together with σ_Y, is one of the most important mechanical characteristics of a material. It characterizes the stiffness of the material in tension, and by the virtue of the dependency $\sigma(\varepsilon)$ it is measured in the same units as those of the stress, i.e., Pa (The values of the Young modulus are tabulated and are available for a wide range of materials.). The dependency, $\sigma = E\varepsilon$, is one of the fundamental dependencies in the mechanics of materials and is known as Hooke's law.

Another mechanical characteristic of importance, that characterizes a material, is the bulk modulus. The bulk modulus of a material, usually denoted with K, is a measure of the material's resistance to compression. It is defined as a ratio of the material's volume change at the infinitesimal change of the applied hydrostatic pressure, P. Thence, the bulk modulus is formally defined as, $K^{-1} = -\frac{1}{V_i}\left(\frac{\partial V}{\partial P}\right)$, where V_i is the initial volume of the tested piece and V is the change of the sample's volume due to the pressure applied. Depending on the thermal conditions at which K is measured, the bulk modulus could be isothermal, or adiabatic. If the Young and the bulk moduli of a material are known, the outstanding two mechanical parameters of importance; the Poisson ratio, ν, and the shear modulus, G are readily determined. Each of those is defined as: $\nu = \frac{3K - E}{6K}$, and $G = \frac{3KE}{9K - E}$.

The *Poisson ratio* is defined as a ratio of the lateral, ε' and the axial, ε, strains, i.e. $\nu = -\frac{\varepsilon'}{\varepsilon}$. The minus sign accounts for the experimental fact that ε' and ε as a rule have opposite signs. For all known materials the Poisson's ratio never exceeds 0.5, while for the most important, from the practical point of view metals, its value is approximately 0.3. It is worth noting that for a particular material, Poisson's ratio remains constant throughout the linearly elastic range. A condition, however, applies that the material must be homogeneous, that is, it must have the same composition (hence the same elastic properties) at every point. Such

materials are referred to as *isotropic*. The *shear modulus* of elasticity G (also called the modulus of rigidity) accounts for the properties of a material when the latter is subjected to shear stress. It can be determined experimentally from direct-shear tests or from torsion tests (twisting hollow, circular tubes, thus, producing a state of pure shear). As a result, shear-stress - shear-strain diagrams are obtained, which at its linear part closely resemble Hooke's law; $\tau = G\gamma$ (also referred to as Hooke's law in shear). Here, with τ is denoted the shear stress, and with γ the shear strain.

2.4.3 The plastic behavior of the materials

For most of the metallic materials, the elastic deformation does not exceed strains of about 0.005. As seen from the $\sigma(\varepsilon)$ diagram in Fig. II-2-10, beyond that limit the stress is no longer proportional to the strain (i.e. the Hooke's law is no longer valid). The plastic deformation of the material leads to a permanent change of the initial shape of the tested piece, thus when the load is removed, the metal will not return to its original shape (on the $\sigma(\varepsilon)$ diagram, see Fig. II-2-10, this region is denoted as the "uniform plastic flow"). The plastic deformation takes place, due to the rearrangements in the metal's structure; a movement of the atoms into new positions, e.g., gliding of entire atomic planes respectively to their adjacent neighbors. The plastic deformation starts immediately after the elastic region (after the point Q on the $\sigma(\varepsilon)$ diagram) and ends when the endurance limit of the material is exhausted, that is with the fracturing of the tested piece, i.e., at the points F_e (F_t) on Fig. II-2-10.

Once the existence of an atomic structure, in particular atomic planes, in metals has been firmly established, it has been suggested that the plastic deformation is due to some sort of rearrangement of atoms in the crystal lattice as a result of the applied external load. It was assumed, which was later confirmed experimentally, that the deformation of the material occurs by the following mechanism; (a) disruption of the atomic bonds between adjacent atomic planes in the crystal lattice, (b) subsequent sliding of these planes relative to each other and finally (c) establishing new interatomic links with the newly acquired neighbors. Early calculations of the strength of the metal, based on this mechanism, however, led to extremely high values of the yield strength, in fact, many times larger than those measured experimentally. Thence a conclusion was drawn that the plastic deformation of the crystal material/metal must proceed by a mechanism different from that described above.

In the 1930s, it was inferred that the crystal structure in metals is not perfect and that the latter contains various structural defects (see Ch. II-3). By the early 1950s, the existence of such structural defects (see Section 2.2 of this chapter) was experimentally confirmed by studying the microstructure of the metals using transmission electron microscopy.

Based on the above-mentioned presence of certain defects in the crystal lattice, it was assumed that the latter, in particular one of those – the dislocation, plays a key role in the plasticity of metals. It has been suggested that the presence of a certain number of dislocations in the interplanar region would lead to a reduction in the adhesion forces between the individual atomic planes, which would significantly facilitate the migration of these planes relative to each other. Therefore, the role of dislocations in the plastic deformation of metals resembles that of a lubricant, placed between the sliding atomic planes of the crystal. Indeed, the interatomic forces of attraction act at a very short distance, so it can be easily assumed that at the place, where the dislocation is located, interatomic bonds practically do not exist. From the above, it can be concluded that the greater the dislocations density in the interplanar space, the easier it would be for these planes to slide relative to each other. Given the above, the plastic deformation of materials having a crystalline structure is easily explained. Consider two atomic planes A and B. When the shear stress is applied, say, to the upper plane A, the latter will be forced to move in the direction of the shear force. (Recall that the shear force is defined as the product of the shear stress and the area to which it is applied.) If the shear force is large enough, the interatomic bonds between the atomic planes A and B will be disrupted, thus allowing these planes to move at one lattice-period distance to each other. If the shear force continues with time, the above process is repeated in successive discrete steps, which on a macroscopic scale are visually perceived as plastic deformation of the material. We specify that the above mechanism of plastic deformation applies only to crystalline materials. Amorphous materials (metallic glasses) are deformed plastically by a mechanism different from the one described above, actually, they flow [3]. The interatomic interaction, in that case, is accounted for by the viscosity, a physicochemical property that results from the statistical averaging of the interatomic forces acting between different layers of the material when those are sheared relative to each other.

The number of dislocations per unit volume of material is called the "*dislocation density*" and it is defined as the ratio of the total length of the dislocations to that volume. It follows from the above that the dislocation density is measured in [m^{-2}], i.e., units per square meter. Since in the

following chapters, in explaining various properties/processes in composites, we will return repeatedly to the concept of dislocation density, it is useful to note that at room temperature all metals and alloys contain a certain number of dislocations. It is assumed that the latter is generated during the solidification of the metal, for example by the thermal stresses arising locally as a result of the differences in the cooling rates. In practice, dislocation density is determined by counting the number of dislocations intersecting a unit area of an arbitrarily drawn plane in the material. In the case of slowly solidified metal crystals, the dislocation density is about 10^3 mm^{-2}, while in the case of strongly deformed metals it could reach up to 10^9 mm^{-2}.

2.4.4 The fracturing of the materials

Fracture of material occurs when it loses its load-carrying capability. The latter is characterized by the disintegration of the material into separate pieces. On the $\sigma(\varepsilon)$ diagram (see Fig. II-2-10) the fracture stage begins with the formation of a visible "neck" on the test piece, denoted on the diagram with the point *S*, and ends with the test piece disintegration, denoted on the diagram as *F*. Fracture is commonly categorized as ductile or brittle. The former is associated with an extensive plastic deformation along certain crystallographic planes, while the brittle fracture is associated with negligible plastic deformation and cleavages (splittings) on certain crystallographic planes. The fracturing process is a response to the imposed stress and involves two steps; (i) crack formation and (ii) crack propagation. The way of fracturing, ductile or brittle, depends on the mechanism of crack propagation. Ductile fracture is characterized by extensive plastic deformation in the vicinity of an advancing crack. It proceeds relatively slowly as the crack length is extended. At the brittle fracturing, the cracks spread very rapidly, with little or missing plastic deformation. Due to the spontaneous and rapid crack propagation, brittle fracturing occurs suddenly and as a rule catastrophically. Under tensile stress, most metals and their alloys fracture by the ductile mechanism, whereas the ceramics are cracking by the brittle fracturing mechanism. As we will see, the circumstances above play a crucial role in the mechanical behavior of the MMCs, which as a rule are based on a ductile metal matrix and a ceramic reinforcement.

Similar to the mechanical parameters, characterizing the elastic behavior of a material, in materials science a mechanical parameter is introduced, which characterizes the resistance of the material to fracture - the *fracture toughness*. For that purpose, using fracture mechanics

principles, an expression was developed that relates the fracture toughness, K_c, with the critical stress required for a crack propagation σ_c and the crack length produced by the application of that stress, l: $K_c = Y\sigma_c\sqrt{\pi l}$ (measured in Pa.m$^{1/2}$). Here Y is a dimensionless parameter that depends on; how the applied to the test piece load affects the crack, the specimen size, and the specimen's geometry. Thence, the fracture toughness could be defined as the material's resistance to brittle fracture when a crack is already present. By definition, the value of the fracture toughness will depend, via the parameter Y, on the geometry of the specimen and the spatial orientation of the crack. For instance, at relatively thin specimens, K_c depends on the specimen's thickness. Conversely, when the specimen thickness is much greater than the crack's dimensions, K_c is independent of the thickness. Furthermore, the load could operate on the crack in three different ways; (i) perpendicular to the crack's walls, (ii) tangential along the crack's length, and (iii) tangential along the crack's width. Therefore, depending on the mutual geometrical orientation of the crack's normal and tangent, and the vector of the applied force, three different values for K_c will be obtained for the same material. In the practice, however, the first way of determining K_c is most frequently used. In the materials handbooks, it is termed "*plane strain fracture toughness*" and is denoted with K_{Ic} to distinguish it from the other two ways in determining the fracture toughness. Fracture toughness varies considerably, by approximately 4 orders of magnitude, depending on the material; being very high at the metals and lower at the ceramics. A detailed description of the first phase of fracturing, the formation of cracks in a material, is given in the last section of this chapter.

2.4.5 Determining the yield strength of a material

Since the concept of yield strength is extensively used in this book it seems necessary to describe how to determine it from an experimental sigma-epsilon diagram. The σ_Y, (also termed "proof stress") determination procedure is illustrated in Fig. II-2-11. The following steps should be followed: (i) from a pre-determined point B of the epsilon axis, usually 0.1% or 0.2% of the engineering strain, is drawn a line parallel to the proportionality line (the line BC in Fig. II-2-11), (ii) the stress, corresponding to the point of intersection of that line with the σ - ε curve, determines the position of the point C and the sought value of the yield strength, σ_Y, of the material. The value of the selected predetermined strain, 0.1% or 0.2%, is added to the index of the as-determined σ_Y. For

instance, if the predetermined strain was chosen to be 0.1% then σ_Y is indexed as $\sigma_{Y0.1\%}$. It is accepted that the tested material fulfills the "0.1%" test specification when; after the proof force is applied for fifteen seconds the produced permanent set of the gauge length of the test piece (the permanent deformation) should be less, or equal, to 0.1%. The time limit of 15 seconds is specified in a way to allow sufficient time for the extension to be complete under the proof force.

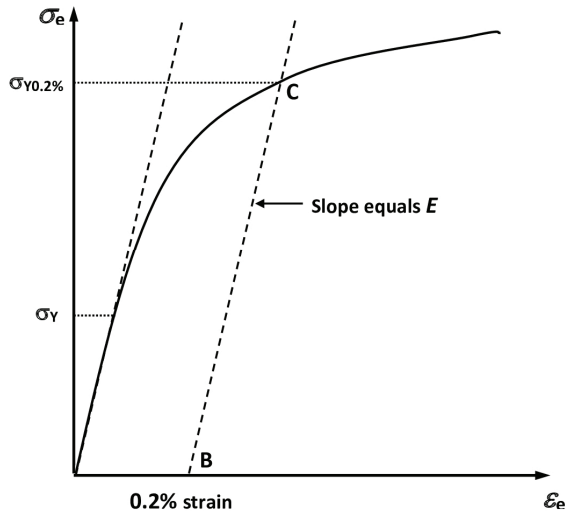

Figure II-2-11 Graph illustrating the determination procedure of the $\sigma_{Y0.2\%}$ yield strength from an engineering σ-ε diagram.

Besides, the yield strength (or yield stress, proof stress) usually are also determined: the tensile strength of the material, i.e., the maximal stress that it could sustain, and the elongation of the sample at fracture (measured in percent's of the initial length of the test piece). The latter could be regarded as an almost direct measure of the ductility of the studied material.

2.4.6 Hardness tests

The hardness tests used in materials science are a simple and cheap non-destructive way of evaluating the mechanical properties of the

materials. They do not require purposedly machined test pieces, and as a rule, the test probe used in these methods is so small that the tested material is not damaged. That is the reason why these tests are very popular among researchers and technologists and widely used for routine tests on materials as we will see in Ch. II-5. Under the hardness testing is understood the ability of a material to resist permanent indentation or deformation when in contact with a probe that is under load. The hardness test procedure consists of pressing into the surface of the tested material a pre-shaped sharp piece, aka 'indenter', made of diamond or hardened steel. Therefore, the softer the material and lower its yield strength, the further into the material the indenter sinks. The true hardness is defined as the load divided by the projected area of the 'indent'. There exist several methods of hardness measurement. The most widely used are the Brinell, the Vickers - Knoop, and the Rockwell tests. The difference between these methods is in the shape of the indenter used; spherical (Brinell test), pyramidal (Vickers - Knoop tests), or conical (Rockwell test). In all of the preceding testing methods, the hardness is evaluated by the area of the indentation, and optionally the penetration depth achieved when the indenter is loaded with a prescribed load for a specific time. The measured area and depth of the indentation are then converted to a hardness number which is specific for the hardness method used. As the reader already guesses the differences between the methods above follow from the shape and the depth of the indenter's mark left on the tested material. Hence, the difference between the scales used by these methods in the evaluation of the material's hardness.

The value of the hardness testing methods above is that they allow estimating the yield strength of a material, σ_Y, without damaging the test piece. Regrettably, a more detailed discussion on the methods for the hardness evaluation and the relationships used in the process of evaluation of the σ_Y is beyond the scope of this book. The interested reader is referred to the extensive literature covering this subject, e.g. [4].

2.5 Essentials from the theory of elasticity

Consider the distribution of the temperature in a solid or liquid body. To describe the temperature distribution inside that body one has to define a function (to be correct a scalar function) $T(x,y,z)$ that determines explicitly the spatial distribution of the temperature at every point of the body. To explicitly determine the flow of a liquid at a certain point of the space occupied by that liquid, however, one has to define a velocity vector, i.e., three different functions for every vector component - $v_i(x,y,z)$; $i \in \{x,y,z\}$.

The definition of the spatial distribution of the stresses and the strains in a solid body requires nine different functions of the spatial coordinates. These nine functions are usually represented in the form of a matrix and are termed stress, $\begin{pmatrix} \sigma_x & \tau_{xy} & \tau_{xz} \\ \tau_{yx} & \sigma_y & \tau_{yz} \\ \tau_{zx} & \tau_{zy} & \sigma_z \end{pmatrix}$, and strain $\begin{pmatrix} \varepsilon_x & \gamma_{xy}/2 & \gamma_{xz}/2 \\ \gamma_{yx}/2 & \varepsilon_y & \gamma_{yz}/2 \\ \gamma_{zx}/2 & \gamma_{zy}/2 & \varepsilon_z \end{pmatrix}$ tensors. The members of these matrices are known as tensor components and their value depends on the coordinate system used. The notations and the indexing used in the text above are typical for those used in structural engineering. The diagonal members of the matrices represent the normal stresses and strains, while the non-diagonal components represent the tangential ones (aka shear components). In the practice, for the sake of brevity, the components of the matrices above are written in a shortened form, σ_i, ε_i, τ_{ij}, and γ_{ij} (where $i,j \in \{ x,y,z \}$. From a mathematician's point of view, the tensors above are three-dimensional second-rank tensors, while the vectors $v_i(x,y,z)$ and the scalar $T(x,y,z)$ are three-dimensional tensors of the first- and the zero-rank tensors, respectively.

In a body made of isotropic material, which will be presumed in this book, the functions defining the stresses and the strains reduce to six and the tensor is said to be a "symmetrical tensor". In a symmetrical tensor, three of the non-diagonal tensor components are equal to the other three non-diagonal components, i.e., $\tau_{ij} = \tau_{ji}$ and $\gamma_{ij} = \gamma_{ji}$, (see e.g. A. Sommerfeld 1950) whence, the reduction of the functions required for the description of the stresses and the strains in a homogeneous body.

As with the axial load, so in the general case of a deformed body, the stresses and strains are not independent of each other. They obey the generalized Hooke's law which, written in tensor notations, states:

$$\varepsilon_i = \frac{1}{E}\left[(1+\nu)\sigma_i - \nu \sum_{j=1}^{3} \sigma_j \right],$$

$$\sigma_i = \frac{E}{(1-2\nu)(1+\nu)}\left[(1-2\nu)\varepsilon_i + \nu \sum_{j=1}^{3} \varepsilon_j \right], \qquad (1)$$

$$\gamma_{ij} = \frac{\varepsilon_{ij}}{G} = \frac{2(1+\nu)}{E}\varepsilon_{ij}, \text{ and } \tau_{ij} = G\gamma_{ij} = \frac{E}{2(1+\nu)}\gamma_{ij}.$$

The deformation sustained by a solid body under load is determined by a displacement vector, $\vec{u}$. In Cartesian coordinates, between u_i, ($i \in \{x,y,z\}$) from one side and the strains from the other, the following relations are valid:

$$\varepsilon_i = \frac{\partial u_i}{\partial x_i} \quad \text{and} \quad \gamma_{ij} = \frac{\partial u_i}{\partial x_j} + \frac{\partial u_j}{\partial x_i} \quad \text{where } (i, j \in \{x,y,z\}),$$

and ($u_{i=x,y,z}$ and $x_{i=x,y,z}$).

Understandably, the components of the tensors above would change when the coordinate system is changed (e.g., by rotation, translation, etc.). In the tensor calculus, however, is proved that there exist specific combinations of the tensor's components which do not change with the changing of the coordinates, known as *tensor's invariants*. In the mechanics of materials, the invariants constructed from the components of the stress tensor are of special importance, because these allow calculating the cumulative stress at a certain point of the material. In Cartesian coordinates the tensor invariants (denoted below as I_1, I_2, I_3), are expressed via the components of the stress tensor as follows:

$$I_1 = \sum_{j=1}^{3} \sigma_j$$

$$I_2 = \sigma_x\sigma_y + \sigma_y\sigma_z + \sigma_x\sigma_z - \tau_{xy}^2 - \tau_{yz}^2 - \tau_{zx}^2, \text{ and} \qquad (2)$$

$$I_3 = \sigma_x\sigma_y\sigma_z - \sigma_z\tau_{xy}^2 - \sigma_x\tau_{yz}^2 - \sigma_y\tau_{zx}^2 + 2\tau_x\tau_y\tau_z.$$

The significance of stress-tensor invariants is that they are independent of the chosen coordinate system, which allows calculating the maximums of the tensile stresses, σ_i, $i \in \{1..3\}$, and the equivalent tensile stress σ_E (the Von Mises stress) in a fixed point of the loaded body:

$$\sigma_1 = \frac{I_1}{3} + \frac{2}{3}\sqrt{I_1^2 - 3I_2}\cos\left(\frac{\varphi}{3}\right),$$

$$\sigma_2 = \frac{I_1}{3} + \frac{2}{3}\sqrt{I_1^2 - 3I_2}\cos\left(\frac{\varphi}{3} + \frac{2\pi}{3}\right),$$

$$\sigma_3 = \frac{I_1}{3} + \frac{2}{3}\sqrt{I_1^2 - 3I_2}\cos\left(\frac{\varphi}{3} + \frac{4\pi}{3}\right), \qquad (3)$$

$$\varphi = \arccos\left[\frac{2I_1^3 - 9I_1I_2 + 27I_3}{2\left(I_1^2 - 3I_2\right)^{3/2}}\right], \text{ and}$$

$$\sigma_E = \sqrt{I_1^2 - 3I_2} = \sqrt{\frac{\left(\sigma_x - \sigma_y\right)^2 + \left(\sigma_y - \sigma_z\right)^2 + \left(\sigma_z - \sigma_x\right)^2 + 6\left(\tau_{xy}^2 + \tau_{yz}^2 + \tau_{zx}^2\right)}{2}}.$$

The importance of the equivalent tensile stress σ_E follows from the Von Mises yield criterion which states that yield will occur at a point in a multiaxial loaded body when σ_E reaches the yield stress of the material at that point.

As pointed out above, in a stressed body the components of stress usually vary from point to point. These variations are governed by a set of differential equations, known as equilibrium equations. In Cartesian coordinates these read:

$$\frac{\partial \sigma_x}{\partial x} + \frac{\partial \tau_{xy}}{\partial y} + \frac{\partial \tau_{xz}}{\partial z} + F_x = 0 \qquad (4a)$$

$$\frac{\partial \sigma_y}{\partial y} + \frac{\partial \tau_{xy}}{\partial x} + \frac{\partial \tau_{yz}}{\partial z} + F_y = 0 \qquad (4b)$$

$$\frac{\partial \sigma_z}{\partial z} + \frac{\partial \tau_{xz}}{\partial x} + \frac{\partial \tau_{yz}}{\partial y} + F_z = 0 \qquad (4c)$$

Here F_i ($i = x,y,z$) denote the components of the cumulative internal forces applied to the body (The external forces are usually accounted for by the boundary conditions.).

In the practice, however, most three-dimensional problems are treated in terms of displacements instead of strains and stress, because such an approach satisfies the requirement of compatibility identically (see, e.g., Timoshenko and Goodier, 1970). Thence, by replacing the stress components in the equations above with those from the generalized Hooke's equations and keeping in mind the relations between the components of the strain tensor and the displacements, it is possible to rewrite the system above in the form of a vector differential equation:

$$\left(1 - 2\nu\right)\Delta\vec{u} + \nabla\left(\nabla.\vec{u}\right) = 0. \qquad (5)$$

By applying to that equation the operators of divergence and Laplace, one obtains two new equations:

$$\Delta\left(\nabla.\vec{u}\right) = 0, \text{ and } \Delta\Delta\vec{u} = 0, \qquad (6)$$

which, when appropriate boundary conditions are defined, allow determining the displacement at every point in an elastically deformed body. The interested reader could find an extensive number of examples of the application of these equations in the references listed at the end of this chapter. In the next chapter, these will be used to determine the deformations, generated in the surrounding material by a dislocation.

In the special case of plane deformation, i.e., when u_z=0, the stress and the strain components of the stress and the strain tensors with indices that contain z, except σ_z, turn identically to zero (e.g., the tensor components, τ_{iz}, γ_{iz}, etc., are all equal to zero). In that case, the system of equations above, $\Delta\Delta\vec{u} = 0$, could be readily reduced to a single biharmonical equation of a scalar function, χ(x,y), known as Airy's stress function, which is related to the components of the stress tensor as:

$$\sigma_x = \frac{\partial^2 \chi}{\partial y^2},\ \sigma_y = \frac{\partial^2 \chi}{\partial x^2},\ \sigma_z = \nu\Delta\chi,\ \text{and}\ \tau_{xy} = -\frac{\partial^2 \chi}{\partial x \partial y}. \quad (7)$$

By substituting in Eqs. 5 σ_x, σ_y, and τ_{xy} with their equals from the relations above for the sought scalar biharmonic equation, in Cartesian coordinates, is readily obtained:

$$\Delta\Delta\chi = \left(\frac{\partial^2}{\partial x^2} + \frac{\partial^2}{\partial y^2}\right)^2 \chi = 0. \quad (8)$$

Notice that by definition the equation above is valid only in the case of plane deformation. In the case of three-dimensional (spatial) deformation, the system of Eqs 7 should be solved to determine the stresses and the strains in an elastic body.

The work done on an elastic solid by the surface and body forces is stored inside the body in the form of strain energy. For an elastic body, this energy is recoverable when the body is unloaded and returned to its original shape. The strain energy accumulated, could be expressed via the resulting stress, strain, or both. The following dependencies, in Cartesian coordinates, are valid:

$$U_{\sigma\tau} = \frac{1+\nu}{2E}\left(\sigma_x^2 + \sigma_y^2 + \sigma_z^2 + 2\left(\tau_{xy}^2 + \tau_{yz}^2 + \tau_{zx}^2\right)\right) - \frac{\nu}{2E}\left(\sigma_x + \sigma_y + \sigma_z\right)^2 \quad (9a)$$

$$U_{\varepsilon\gamma} = \frac{\nu E}{(1-2\nu)(1+\nu)}\left(\varepsilon_x + \varepsilon_y + \varepsilon_z\right)^2 + \frac{E}{2(1+\nu)}\left(\varepsilon_x^2 + \varepsilon_y^2 + \varepsilon_z^2 + \frac{1}{2}\left(\gamma_{xy}^2 + \gamma_{yz}^2 + \gamma_{zx}^2\right)\right) \quad (9b)$$

$$U_{\varepsilon\gamma\sigma\tau} = \frac{1}{2}\left(\sigma_x\varepsilon_x + \sigma_y\varepsilon_y + \sigma_z\varepsilon_z + \tau_x\gamma_x + \tau_y\gamma_y + \tau_z\gamma_z\right) \quad (9c)$$

The indices at U indicate which tensor components are used as variables.

2.6 The Schmid law and the Schmid factor

Schmid's law and the associated with it Schmid factor allow defining the slip plane and the slip direction in a stressed material which resolves to the largest shear stress in that plane.

As above, when the crystal is under a tensile load, the plastic deformation occurs by displacement (slip) of the adjacent crystal planes relative to each other in well defined directions (slip directions) which lay in a plane, known as a *slip plane*. The combination of slip plane and slip direction is known as a *slip system*. The slip is due to the dislocation migration, which requires the application of certain stress to overcome the resistance to that migration. Schmid's law states that the shear stress τ at which slip occurs in a given material with specified dislocation density and purity is a constant, known as the 'critical resolved shear stress', τ_C. The relationship between the applied stress σ_{app} and the shear stress τ is determined by the equation, $\tau = \sigma_{app}\cos\varphi\cos\lambda$, where φ and λ are, respectively, the angles between the normal of the slip plane and the slip direction with the direction of the applied load. The quantity $m = c\,\mathrm{os}\varphi\cos\lambda$ is known as the Schmid factor. Thence, from the Schmid law, follows the important relation:

$$\tau_C = \sigma_Y \cos\varphi\cos\lambda = \sigma_Y m\,. \quad (10)$$

Taking into account that $\cos\varphi \le 1$ and $\cos\lambda \le 1$ it could be deduced that $\tau_C \le \sigma_Y$.

2.7 Specific reactions of the MMC's materials under mechanical loading

In contrast with the monolith materials, discussed so far, the MMC materials behave differently to the applied stress; the microstructure and the interfaces formed between the reinforcement and the matrix are mutually related, thus, at the MMCs they cannot be considered separately. Indeed, the chemical interactions and the reactions between the matrix and the reinforcement predetermine the interface adhesion forces, thus, modifying the characteristics of the composite and significantly affecting the mechanical characteristics. This is especially true when the endurance limit of an MMC is reached. At that point, the mechanical response of the MMC to loading exhibits some specific features which are typical only for that type of material. These include the formation of voids in the matrix, fracture of the reinforcement, and detachment of the reinforcement from the matrix.

2.7.1 Formation of voids

Void formation usually takes place in the matrix when the geometrical shape of the reinforcement differs from that of a sphere, i.e., when sharp edges, dents, or notches are present on the reinforcement surface. For instance, the nucleation and the growth of voids are frequently observed at the tips of the reinforcements when the latter has an elongated shape (e.g. whiskers, platelike ellipsoids, etc.). From the preceding follows that this type of mechanical behavior should be met frequently at the MMCs, reinforced with micro-, and nano-sized particulates because the shape of these particulates, as a rule, deviates from that of a sphere. Thence, at the contact area between the reinforcement and the matrix are formed critical points serving as effective stress σ_{eff} concentrators. These stress concentrators predetermine the specific mechanical behavior of the composite; the restraints, imposed on the elastic deformation of the matrix at the critical points. Thence, the transitioning from elastic to plastic deformation, which causes the formation of voids near these critical points. Recall, that effective hydrostatic stress is defined as - $\sigma = \frac{1}{3}\sum_{j=1}^{3}\sigma_j = \frac{I_1}{3}$.

2.7.2 Fracture of the reinforcement

This specific type of failure of the MMCs usually occurs when the reinforcement is not correctly chosen. In that case, when the material is loaded the stresses induced inside the material could exceed the fracture strength limit of the reinforcement, thus, leading to the formation of cracks and eventually to the disintegration of the reinforcement. The presence of interior defects inside the reinforcement is another factor that could lead to a similar failure of the composite.

2.7.3 Interface debonding

The interface debonding usually occurs when the local shear forces acting on the matrix-reinforcement interface with area A, $\tau_{ij} A$, exceed the strength of the adhesion forces acting between the matrix and the reinforcement.

2.8 The crack formation in metals: Griffith's theory

The crack formation, or cracking, in a solid body could be defined as the separation of the body into two or more parts under the action of accumulated stress. The process of the cracking of material involves two separate processes, (i) crack initiation and (ii) crack propagation. In the present part of the book, under material will be understood the metal matrix of the composite. It is established so far that the cracks formation and propagation in metals depend on the material, its crystalline structure, the temperature, the state of stress applied, and the rate of loading.

The micrograph in Fig. II-2-12 shows cracks formed inside the Al-matrix in an Al-TiCN composite. Notice, that the cracks propagated in a plane coplanar with the foil's surfaces (this could be deduced by the images of some of the TiCN particles; for instance, the image of the particle seen on the left side of the micrograph coincides with the image of the crack, which means that it is positioned above or below the crack.)

In the most basic terms, the strength of a metal is due to the bond forces between the atoms. Generally speaking, the stronger bond forces between the atoms of the metal' lattice lead to larger elastic constants, higher melting points, and small coefficients of thermal expansion. Based on the assumption above, the estimates intended to predict the strength of a metal, $\sigma_{\max}$, led to the following analytical dependence:

$$\sigma_{max} = \left(\frac{E\gamma}{a_0} \right)^{1/2} . \qquad (11)$$

Where: a_0 is the interatomic spacing of the atoms in an unstrained state of the lattice, and γ is the surface energy (Jm^2), which originates as a consequence of the formation of the crack's surfaces, and the disruption of the bonds between the lattice's atoms.

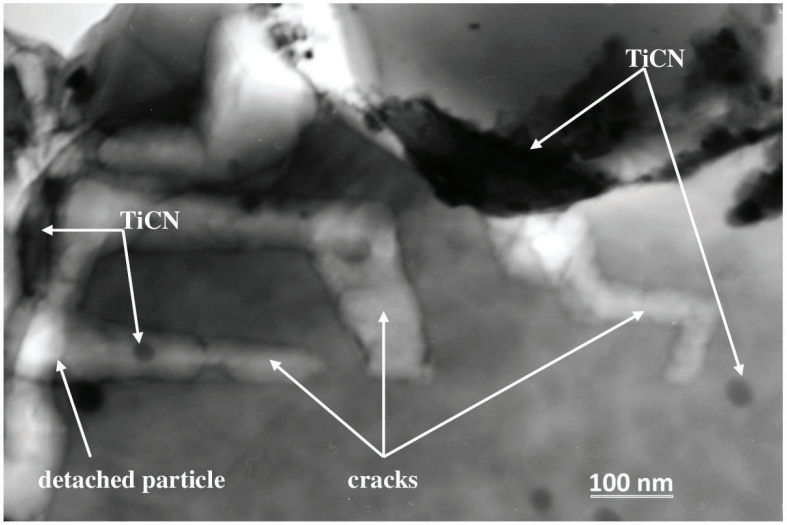

Figure II-2-12 TEM micrograph showing micro-cracks formed inside the matrix of an Al-TiCN composite after uniaxial loading of a test piece made from that composite, (V. Dyakova [10]).

Substituting in the expression above some reasonable values for the quantities involved a bonding strength of 10 to 1000 times greater than that measured in metals is obtained. The first who gave a successful explanation of why such a discrepancy occurs was Griffith. Griffith's theory in its original form, however, applies only to a perfectly brittle material such as glass. Yet, on a micro-sized level, all materials could be considered brittle, recall, e.g., that the metal plasticity is a phenomenon occurring at scales that exceed considerably the micro-level. Therefore, the results of Griffith's theory and the ideas on which it is based could be

readily applied to the metal matrix of the composite, as it is done in the strength reduction theory developed further in this part of the book.

In his celebrated theory, Griffith presumed that in a brittle material a population of fine cracks is inherently present. These micro-cracks, according to Griffith, generate in their vicinity high-stress regions. When the stress accumulated in these regions reaches a sufficiently high magnitude, so that the theoretical cohesive strength is exceeded, a crack spreads. The creation of new surfaces, those on both sides of the crack, requires work to be done against the cohesion forces. These, which before the formation of the crack did hold the separated sides together. The work spent in the crack's formation is done at the expense of the stress accumulated in the material. Thence, the formation of a crack would lead to a reduction of the accumulated stress. Making use of the preceding considerations, Griffith established the following criterion for the propagation of a crack: *A crack will propagate when the decrease in elastic strain energy is at least equal to the energy required to create the new crack surface*. This criterion allows determining the magnitude of the tensile stress which is just sufficient to cause the propagation of a crack of a certain size inside a brittle material. The problem could be thus treated as a plane stress problem which is much easier to be treated, from a mathematical point of view (see section 2.7 of the present chapter). Griffith's theory of crack formation considers a micro-crack with an elliptical form, formed in a plate of negligible thickness, whose major axis is equal to 2*l*. The as-formulated problem was solved by Inglis [5], who, in doing so, succeeded in obtaining the stress distribution around the crack. The obtained stress distribution, allows, by a contour integration around the crack, to determine the elastic strain energy released by the formation of the crack, U_E. The result obtained by Inglis for U_E, per unit of plate thickness, is:

$$U_E = -\frac{\pi l^2 \sigma^2}{E}, \tag{12}$$

where: σ is the tensile stress acting normal to the crack of length 2*l*. The negative sign indicates the decrease in the strain energy resulting from the formation of the crack. To the as-determined U_E one should add the gain in the energy resulting in by the formation of the crack surfaces which is:

$$U_S = 4l\gamma\,. \tag{13}$$

Thence, the total change in the energy resulting from the creation of the crack is:

$$\Delta U = -\frac{\pi l^2 \sigma^2}{E} + 4l\gamma \,. \tag{14}$$

In this context, Griffith's criterion above should read; the increased surface energy, due to the crack growth, should be compensated by the decrease in the elastic strain energy. Thence, the fulfillment of Griffith's criterion implies the validity of the following chain of equations:

$$\frac{d\Delta U}{dl} = \frac{d}{dl}\left(-\frac{\pi l^2 \sigma^2}{E} + 4l\gamma\right) = 4\gamma - \frac{2\pi l \sigma^2}{E} = 0\,, \tag{15}$$

or

$$\sigma = \left(\frac{2E\gamma}{\pi l}\right)^{1/2} . \tag{16}$$

The equation above determines the amount of the accumulated stress required to propagate a micro-crack with length l in a brittle material. Notice that this equation indicates that the fracture stress is inversely proportional to the square root of the crack length, thus, increasing the crack length by a factor of 4 reduces the fracture stress by one-half.

For a plate which thickness is comparable with the length of the crack (plane strain) Griffith's equation changes to:

$$\sigma = \left(\frac{2E\gamma}{(1-\nu)^2 \pi l}\right)^{1/2} . \tag{17}$$

An extension of the analysis above to three-dimensions (the crack was modeled under a very flat oblate spheroid) yielded only a slight modification of Griffith's equation above (confined to the appearance of a constant in the equation above) which, however, did not affect its analytical appearance [6]. Therefore, the simplification of Griffith's problem above, by reducing the three-dimensional to a two-dimensional problem, is not introducing large errors. This result will be used in Ch. II-6 of this part of the book at the explanation of the experimental fact; why the increase of the volume fraction (VF) of the reinforcement, beyond some critical value, leads to a reduction in the MMC's strength. In the course of the research, carried out in studying the crack forming phenomena, several improvements and revisions of Griffith's equation have been proposed by different authors.

One of the improvements, that fits most fully the objectives of the present monograph, has been proposed by Orowan [7]. He suggested that the Griffith equation could be made more suitable in describing brittle

fracture in metals, if it includes a term, p, expressing the plastic work required to extend the crack wall:

$$\sigma = \left(\frac{2E(\gamma + p)}{\pi l} \right)^{1/2} \cong \left(\frac{Ep}{l} \right)^{1/2} . \quad (18)$$

In the second equation above the surface-energy term is neglected because the estimates of the plastic work carried out showed that $p >> \gamma$ i.e. the plastic work term exceeds considerably surface-energy term. Some experimental evidence exists that p is a temperature-dependent quantity that decreases with the decreasing of the temperature.

Another extension of the Griffith theory has been proposed by Irwin [8,9]. This theory, however, deals with macro cracks i.e. cracks that are several centimeters in length or greater. The reader interested in the processes of growth of macro-sized cracks could find the information of interest in the original publication of Irwin (cited above).

In Eqs 16 to 18, the numerator is unknown because the values of γ and/or p are rarely known. However, by recalling that it characterizes the resistance of the material to fracture and keeping in mind the definition of the fracture toughness K_c, the mechanical parameter introduced in Section 2.4.4, these equations could be readily rewritten in a very compact form:

$$\sigma_{cr} = \left(\frac{2E\gamma}{\pi l} \right)^{1/2} = \frac{K_c}{(\pi l)^{1/2}} . \quad (19)$$

As above, σ_{cr} in Eq. 19 is the amount of the accumulated stress required to propagate a micro-crack with length l in a material with a fracture toughness, K_c. Thence, in this case, K_c could be regarded as a proportionality factor.

Suggested additional reading to Ch. II-2

1. J. M. Gere, B. J. Goodno, Mechanics of Materials, Seventh Edition, Cengage Learning 2009, ISBN-13: 978-0-534-55397-5.
2. W. D. Callister, Jr., Fundamentals of Materials Science and Engineering, Fifth Edition, John Wiley & Sons, Inc. 2001, ISBN 0-471-39551-X.
3. G. Gottstein, Physical Foundations of Materials Science, Springer-Verlag Berlin Heidelberg GmbH 2004, ISBN 978-3-662-09291-0 (eBook).
4. Ch. Kittel, Introduction to Solid State Physics, Eighth Edition, John Wiley & Sons Inc. 2005, ISBN 0-471-41526-X.
5. T. Kobayashi, Strength and Toughness of Materials, Ch. 8 Metal Matrix Composites, Springer Japan 2004, ISBN 978-4-431-53973-5 (eBook).
6. N. E. Dowling, Mechanical Behavior of Materials Engineering: Methods for Deformation, Fracture, and Fatigue, Fourth Edition, Pearson Education Limited 2013, ISBN 10: 0-273-76455-1.
7. Th. H. Courtney, Mechanical Behavior of Materials, Second Edition, Waveland Press, Inc. 2005, ISBN 1-57766-425-6.
8. J. W. Christian, The Theory Of Transformations in Metals and Alloys, Pergamon an Imprint of Elsevier Science 2002, ISBN: 0-08-044019-3.
9. L. D. Landau and E. M. Lifshitz, Course of Theoretical Physics vol. 7: Theory of Elasticity, Second Edition in English, Pergamon Press 1970.
10. S. P. Timoshenko and J. N. Goodier, Theory of Elasticity, Third Edition, McGraw-Hill, New York, 1970.
11. A. Sommerfeld, Lectures on Theoretical Physics vol. 2, Mechanics of deformable bodies, Academic Press 1950.
12. ASM Handbook Volume 8, Mechanical Testing and Evaluation ASM International 2000, ISBN 0-87170-389-0.
13. S. Stølen, T. Grande, N. L. Allan, Chemical Thermodynamics of Materials: Macroscopic and Microscopic Aspects, John Wiley & Sons Ltd, (2004), ISBN 0-471-49230-2.
14. D. A. Porter and K. E. Easterling, Phase Transformations in Metals and Alloys, Second Edition, Chapman and Hall (1996) ISBN 0-412-45030-5.
15. B. S. Bockstein, M. I. Mendelev, and D. J. Srolovitz, Thermodynamics, and Kinetics in Materials Science, A short course, Oxford University Press (2005), ISBN 0-19-852803-5.

References to Ch. II-2

1. D. R. Askeland, P. P. Fulay, W. J. Wright, The Science and Engineering of Materials, Sixth Edition, (2006) Cengage Learning, ISBN-13: 978-0-495-29602-7.
2. V. Dyakova, private communication (2018).
3. K. A. Russew and L. Stoyanova, Glassy metals, Springer, 2016, ISBN 978-3-662-47882-0.
4. Hardness Testing, Second Edition, Harry Chandler ed., ASM International 1999, ISBN: 978-0-87170-640-9.
5. C. E. Inglis, Trans. Inst. Naval Architects, vol. 55, pt. I, pp. 219-230 (1913).
6. R. A. Sack, Proc. Phys. Soc. (London), vol. 58, p. 729 (1946).
7. E. Orowan, in "Fatigue and Fracture of Metals," symposium at Massachusetts Institute of Technology, John Wiley & Sons, Inc., New York, 1950.
8. G. R. Irwin, Naval Research Lab. Rept. 4763, May 1956, available from Office of Technical Services, PB 121224. 9. G. R. Irwin, J. A. Kies, and H. L. Smith, Proc. ASTM, vol. 58, pp. 640-660, 1958.
10. V. Dyakova, private communication, (2019).

CHAPTER II-3

DISLOCATIONS

LUBOMIR A. ANESTIEV

3.1 General description of a dislocation and definitions used in the dislocation theory

The dislocation is a line defect of the metal's (alloy) lattice structure. The introduction of the dislocation formalism, in the mid-thirties of the past century, helped in the theoretical explanation of numerous processes that determine the mechanical behavior of the solid materials under load. It should be noted that the postulates of the theory of dislocations were originally formulated to give a satisfactory explanation of the plastic deformation phenomena in the metals and the alloys. Much later, in the mid-1950s, the dislocation theory has been applied to give an explanation of the strengthening in the metals and alloys, observed after mechanical deformation or after heat treatment.

The prerequisite to the development of the dislocations theory was the attempts to evaluate the strength of the materials. At first, these attempts were carried out by assuming a "perfect crystal" lattice structure. The evaluations showed that the strength of the materials is proportional to the Young modulus and that it should be of the order of $E/15$, see e.g., [1]. Yet, the results obtained were considerably higher, e.g., by one to two orders of magnitude than that measured experimentally. It did not take long to be figured out that the problem is in the assumption of the "ideality" of the crystal lattice. The crystals are not perfect (as it was already discussed, see Section 2.2 of Ch. II-2) they are never free of defects, which is a consequence of the laws of the thermodynamics, that state; at equilibrium, the free energy of the system crystal - defects should be minimal.

It was Volterra who first employed the classical theory of elasticity to develop a theory describing the stress field around a dislocation in a crystal [2]. The contemporary understanding of the dislocations as a defect

of the crystal structure on an atom-scale level, however, was developed later (the mid-thirties and the forties of the last century) by Taylor [3] Burgers [4], Orowan [5], and others.

The present author does not intend to cover in one chapter the extensive field of theoretical and experimental research carried up to now in the field of dislocations. That would be an impossible task. Here the intention is to summarize the main results obtained so far and emphasizing those used in explaining the role of the dislocations in the strengthening of the metals and alloys.

As discussed in Section 2.2, Ch. II-2, the dislocation could be defined as a linear crystallographic defect or irregularity within the regular crystal structure which is characterized by (i) an abrupt change in the arrangement of the atoms in the crystal lattice, and (ii) by a significant elongation in one specific direction. While the crystalline order is restored on either side of the dislocation the atoms ordering on one of the dislocation's sides are not; depending on the dislocation type they are either moved or slipped in respect to each other. The dislocation boundaries are, therefore, localized between the moved, or slipped, and the unchanged regions of the material.

From the preceding follows that the dislocation could be formed in two different ways; (i) by removing an entire atomic plane from an arbitrary place of the crystal lattice with a subsequent joining of the neighboring atomic planes, forming in this way a dislocation line. These are termed *edge*-dislocations and are illustrated with Fig. II-3-1a, or (ii) by moving two adjacent atomic planes of an arbitrary side of the crystal lattice, with respect to each other, and then joining them. These are termed *screw*-dislocations and are illustrated with Fig. II-3-1b. A detailed description of those two types of dislocations is given below.

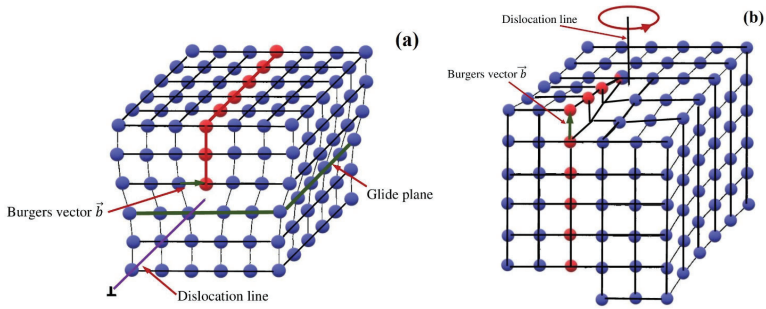

Figure II-3-1 Sketches illustrating the structure around an edge (1a) and a screw (1b) dislocations formed inside a crystal lattice.

By the definitions above it follows that the dislocation disrupts the typical, for the "perfect" crystal lattice, continuity. Thence, the formation of dislocation in a crystal implies that the "original" lattice structure is not any longer preserved. Expressed in mathematical terms the definition above reads; a contour integral, evaluated along a closed contour, *C*, drawn around a dislocation and which crosses the dislocation line, is different from zero, $\int_C d\vec{r} \neq 0$. Conversely, if the contour is not crossing the dislocation line the contour integral is equal to zero, $\int_C d\vec{r} = 0$. The dislocation thus could be characterized by a vector, which is a result of the integration performed by following the closed contour *C*. This vector is usually denoted with $\vec{b}$ and is termed "Burgers-vector". Its scalar magnitude $\left|\vec{b}\right|$ is considered as a measure of the dislocation's "strength". The Burgers-vector of the two types of dislocations discussed above is shown in Fig. II-3-1a and II-3-1b in green. As from the definition above, these are defined as the difference in the relative atomic positions when circling the dislocation line.

By the description above it could be expected that the Burgers vector should equal the interatomic distance in the glide plane. Dislocations of this kind are called perfect or lattice dislocations.

3.1.1 The edge dislocation

As above, the edge dislocation is formed by removing part of an atomic plane from an ideal (perfect) crystal lattice. As a result, one of the edges of the removed plane will originate inside the lattice, thence, when circling a contour in the crystal lattice around the missing plane edge, a difference of one interatomic distance will occur which is equal to the absolute value of the Burgers vector. Depending on the direction of the Burgers vector two types of edge dislocation are distinguished; edge dislocation with positive, or negative signs. That sign is determined by the direction of the Burgers vector, which is obtained when the integration contour *C* is traversed anticlockwise. The dislocation shown in Fig. II-3-1a is therefore positive, because its Burgers vector point in a positive direction, i.e., along the positive direction of, say, the x-axis. Due to the atoms' interactions, the ordered structure of the lattice will be restored by the atoms laying at both sides of the removed plane. However, despite the

restoration of the atomic lattice structure, the presence of an extra atomic plane in the crystal will cause stresses at the edge of the residual atomic plane; compressive at the side of the extra atomic plane, and tensile at the side of the missing plane. By the aforesaid follows that considerable energy is required for the formation of an edge dislocation. However, once formed, the dislocation in a close-packed structure can move inside the crystal with relative ease, even when relatively low shear stress is applied.

The plane that separates the regions of the crystal along which that movement takes place is termed; *glide* or *slip* plane, in Fig. II-3-1a this plane is marked with green. The slip plane is readily distinguished, it is the plane that contains both the dislocation and its Burgers vector.

3.1.2 The screw dislocation

The arrangement of atoms around a screw dislocation can be simulated as follows. Consider an axis (coinciding with one of the crystal directions) in an ideal (perfect) crystal lattice. A screw dislocation then could be formed by cutting the crystal through the half-plane, formed by that axis and the two remaining directions, and moving one side of the cut by one unit cell distance relative to the other (see Fig. II-3-1b). By applying the procedure above a single surface helicoid is formed that characterizes the screw dislocation. Depending on the selected direction of the dislocation axis two kinds of screw dislocations could be distinguished when looking down the dislocation line; right-oriented, when the helix advances one plane by completing a full clockwise circuit, and left-oriented if the opposite is true. In contrast with the edge dislocation, the Burgers vector of the screw dislocation is parallel to the dislocation axis, thence, when moving the screw dislocation glides in a direction parallel to its dislocation line.

3.1.3 The migration of edge and screw dislocation through the crystal

Both types of dislocations move (migrate) in directions parallel to their Burgers-vector. Thus, the edge dislocation moves in a direction perpendicular to its dislocation line, while the screw dislocation moves along it. It should be noted that the number of the slip planes and their orientation in a specific crystal, depends on the crystal system to which that crystal belongs. It follows, therefore, that the edge dislocation can glide easily only in a plane (termed *slip plane*), defined by the dislocation itself and its Burgers vector. The preceding statement is confirmed by the

fact that "climbing" of the dislocation in an interatomic distance, say, in a direction perpendicular to the slip plane would require: (i) removal of a considerable amount of atoms from their normal sites, (ii) moving them into interstitial sites, and (iii) subsequent diffusion of these atoms through the surrounding lattice to vacant lattice sites (to vacancies or other dislocations) where they will be incorporated in the lattice. Moving an edge dislocation in a direction out of its slip plane should be, thus, a very slow process that will depend on the diffusion of vacancies or interstitial atoms. From the preceding follows that two edge dislocations that have a common slip plane and opposite signs will attract each other and given sufficient time to migrate (which depends on the temperature, the load applied, etc.) they would annihilate, thus lowering the free energy of the crystal-two-dislocations system, and producing an "unslipped" perfect crystal.

3.1.4 Complex dislocations

The description of the screw and edge dislocations above, as a straight line, is an idealization. There is no reason to presume that the dislocations should be straight-line objects. On the contrary, the experimental evidence shows that the form of the dislocations observed is far from linear, see Fig. II-3-2.

It is believed, and the experimental evidence confirms it, that the general form of the dislocation in the glide plane is a combination of edge and screw elements. So in its commonest form, the dislocation will appear as a complex-shaped curve (as in Fig. II-3-2) rather than a straight line. From the preceding follows that at any point the complex dislocation could be regarded as being composed of two coincident elements of an edge and screw dislocation. Therefore, the Burgers vector of the complex dislocation (termed below as "composite Burgers vector") would be a sum of two Burgers vectors, one parallel (tangent) and the other normal to the complex dislocation line. In mathematical terms, that concept is interpreted as follows. Consider an element of the dislocation line curve. Let, $\vec{j}$ to be a unit vector coinciding with the direction of the tangent drawn at an arbitrary point of the dislocation curve and let $\vec{b}$ to be the composite Burgers vector at that point. By resolving the composite Burgers vector $\vec{b}$ in components in a coordinate system formed by the $\vec{j}$ -vector and a vector $\vec{i}$, which is normal to $\vec{j}$ and which lays in the slip

plane specified by $\vec{b}$ and $\vec{j}$, it could be shown that the edge component of the Burgers vector $\vec{b}$ is parallel to $\vec{i}$, while the screw component is parallel to $\vec{j}$. The screw, $\vec{b}_s$, and the edge, $\vec{b}_e$, components of the Burgers vector are then readily expressed via the composite Burgers vector by the following relations:

$$\vec{b}_s = \left(\vec{b}.\vec{j}\right)\vec{j} \quad \text{(1a) and } \vec{b}_e = \vec{b} - \vec{b}_s = \left(\vec{b} \times \vec{j}\right) \times \vec{j} \quad \text{(1b)} \qquad (1)$$

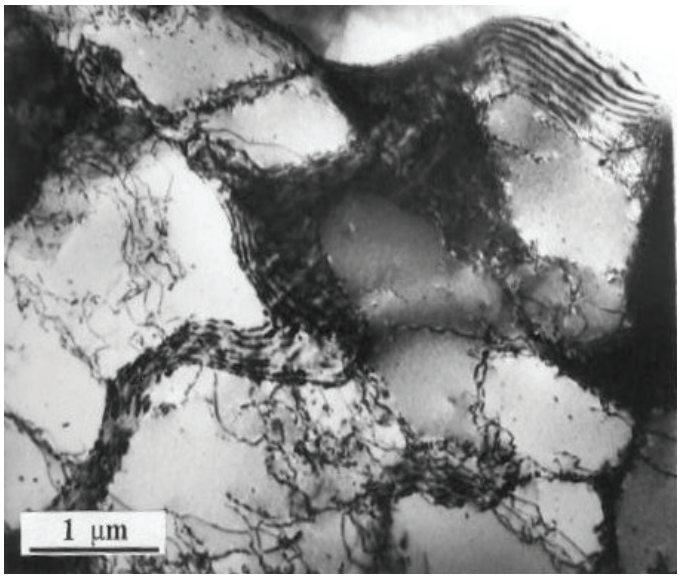

Figure II-3-2 TEM micrograph showing the incidental dislocation boundaries (IDB) and dense dislocation walls (DDW) in a plastically deformed aluminum, V. Dyakova [6]. Notice the intense dislocation density and the complex form of the dislocations in the Al subgrains, which resulted from the severe plastic deformation applied.

It is understandable that; when one of these components of the Burgers vector is zero, then that specific part of the dislocation is either a screw or edge dislocation. As we will see later these dependencies are very useful in identifying the dislocations on transmission electron microscopy (TEM) micrographs and/or establishing the direction of the Burgers vector when analyzing these micrographs.

3.2 Stress field and strain energy of a linear dislocation

When studying dislocations, it is sometimes useful to abstract from the atomic structure of the crystal (as done by Volterra) and considering the latter as an elastic continuous medium. The formation of dislocation in such a continuous medium can be represented in the following way. A slit is cut over part of a plane, then a thin layer with a thickness equal to that of the Burgers vector $\vec{b}$ is removed. The as-constructed new surfaces of the cut are then rejoined again, thus forming a narrow cylinder in diameter of a few atomic spacing's which is void of material. A dislocation loop could be constructed similarly; the difference is that the cut is done over any surface which has as its limit the dislocation line (this concept is used in the evaluation of the energy of a loop formed around an obstacle, see below). The concept of neglecting the atomic structure of the crystal and considering the latter as an elastic continuum allows, by using the formalism of the theory of elasticity (see Section 2.5 in Ch. II-2), to calculate the stress field around a dislocation. (Recall that the same approach was used in Section 2.8, Ch. II-2), when considering the formation and propagation of cracks in a material.). Obtaining an analytical solution of the equations of the elasticity for an arbitrary form of the dislocation is at present an impossible, from the mathematical point of view, task. However, as shown below, for linear dislocations, an analytical solution could be readily obtained. For that purpose, the equation of mechanical equilibrium within an elastic medium and in the absence of internal forces, see Section 2.5 in Ch. II-2 should be solved by applying appropriate boundary conditions. Understandably, these should reflect the specific geometry of the studied dislocation.

3.2.1 Stress field and energy of an edge dislocation

The stress field of an edge dislocation could be calculated by assuming that the dislocation edge is an axis of a cylinder. The use of the polar coordinates is then the logical choice, with the z-axis parallel to the direction of the dislocation axis. From the definition of an edge dislocation, thus, follows, Burgers [4] and Koehler, [7,8]; (i) the direction of the Burgers vector will be along the *r*-axis, (ii) over most of the cylinder, the displacements in the z-axis direction are zero, u_z=0, (iii) all stresses containing in their indexing z are equal to zero τ_{iz}=0 (where, $i \in \{r, \theta\}$), except that of the normal stress σ_z because it guarantees the conservation of the length of the elastic body along the z-axis, and (iv) the

external surface of the cylinder (at infinity) is free from stresses, σ_i=0 and τ_{ik}=0 (where $i,k \in \{r,\theta\}$). In the theory of elasticity is shown that the system of the tensor differential equations describing a planar stress problem (similar to that defined by the boundary conditions above) could be transformed into a single biharmonic scalar equation (see Section 2.5 in Ch. II-2), which in polar coordinates reads:

$$\left[\frac{1}{r}\frac{\partial}{\partial r}\left(r\frac{\partial}{\partial r}\right)+\frac{1}{r^2}\frac{\partial^2}{\partial\theta^2}\right]^2\chi=0\ . \qquad (2)$$

Where, $\chi=\chi(r,\theta)$ is the Airy stress functions in polar coordinates. The latter is related to the components of the stress tensor as:

$$\sigma_r=\left(\frac{1}{r}\frac{\partial}{\partial r}+\frac{1}{r^2}\frac{\partial^2}{\partial\theta^2}\right)\chi\,, \qquad (3a)$$

$$\sigma_\theta=\frac{\partial^2\chi}{\partial r^2}\,, \qquad (3b)$$

$$\sigma_z=\nu\left(\frac{\partial^2}{\partial r^2}+\frac{1}{r}\frac{\partial}{\partial r}+\frac{1}{r^2}\frac{\partial^2}{\partial\theta^2}\right)\chi\ , \qquad (3c)$$

and $$\tau_{r\theta}=\left(\frac{1}{r^2}\frac{\partial}{\partial\theta}-\frac{1}{r}\frac{\partial^2}{\partial r\partial\theta}\right)\chi\ . \qquad (3d).$$

It could be shown that the stresses satisfy the mandatory conditions for equilibrium and compatibility when used in conjunction with Hooke's equations.

The solution of Eq. 2 yields for χ; $\chi(r,\theta)=\dfrac{Gb}{2\pi(1-\nu)}r\cos\theta\ln(r)$.

Thence, for the stresses, strains, and displacements around an edge dislocation is valid:

stresses: $\sigma_r=\sigma_\theta=-C\dfrac{\sin\theta}{r}$, $\sigma_z=-2C\nu\dfrac{\sin\theta}{r}$,

and $\tau_{r\theta}=C\dfrac{\cos\theta}{r}$; (4)

strains: $\varepsilon_r = \varepsilon_\theta = -D\frac{\sin\theta}{r}$, and $\gamma_{r\theta} = 2D\frac{\cos\theta}{r}$; (5)

displacements: $u_x = D\left[2(1-\nu)tg^{-1}\left(\frac{y}{x}\right)+\frac{xy}{x^2+y^2}\right]$, (6a)

and $u_y = -D\left[\frac{(1-2\nu)}{2}\ln\left(\frac{x^2+y^2}{r_0^2}\right)+\frac{x^2}{x^2+y^2}\right]$. (6b)

Here, $C = \frac{Gb}{2\pi(1-\nu)}$, $D = \frac{b}{4\pi(1+\nu)}$, and r_0 is the radius of a hollow tube which axis coincides with the dislocation line.

From the stress relations above follows that at $r\to 0$ the induced by a dislocation stresses should tend to infinity. Therefore, it is assumed that around the dislocation axis exists a space, void of any material, closely resembling the inner part of a pipe on which internal surface the stresses do not disappear but have some finite value. Hence, the appearance in the displacement equations of the radius r_0 characterizing this cylinder-like void. The estimates show, r_0, should be a few interatomic distances wide (few Burgers vectors). The strain-stress relations suffice in calculating the energy accumulated in the region surrounding the dislocation. Recalling the Eqs 9 (a to c) from Section 2.5 of Ch. II-2, for the stored around the dislocation excess free energy, U_{edge}, (in J per unit length of the dislocation), is readily obtained:

$$U_{edge} = \frac{Gb^2}{4\pi(1-\nu)}\ln\left(\frac{r}{r_0}\right). \quad (7)$$

3.2.2 Stress field and energy of screw dislocations

The elastic field around a screw dislocation is obtained using similar concepts as above; the dislocation axis is assumed collinear with the axis of a cylinder forming the core of the dislocation. The difference in this case, however, is that the deformation arises due to; cutting along the generatrix and moving rigidly one of the cuts at a distance equal to the Burgers vector. From the construction described, therefore, follows; (i) in contrast with the edge dislocation the Burgers vector of the screw dislocation is parallel to the dislocation axis - z, (ii) the displacements in

the *x* and the *y* directions, u_x, and u_y are equal to zero, (iii) as θ changes from 0 to 2π, the displacement in the *z*-axis direction increases from zero to *b*. The preceding allows writing for the displacement u_z,

$$u_z = \frac{b\theta}{2\pi} \ . \tag{8}$$

By taking advantage of the dependencies between the displacement and the strain, $\gamma_{\theta z} = \frac{1}{2}\left(\frac{1}{r}\frac{\partial u_z}{\partial \theta} + \frac{\partial u_\theta}{\partial r}\right)$, and between the shear stress and the strain, $\tau_{\theta z} = G\gamma_{\theta z}$, for the stress field around the screw dislocation is obtained:

$$\tau_{\theta z} = \frac{Gb}{4\pi r}. \tag{9}$$

Thence, by integrating through the whole stress field around the screw dislocation for the total stress-energy is readily obtained:

$$U_{screw} = \frac{Gb^2}{4\pi}\ln\left(\frac{r}{r_0}\right) . \tag{10}$$

3.3 Glide force acting on dislocation

When a material (e.g., a crystal) containing dislocations is subjected to loading, a dislocations migration is initiated, thus, resulting in plastic deformation of the material. It is established that the work done by the applied stress in moving (gliding) the dislocation through the crystal is spent in overcoming the resistance to the dislocation migration. These resistances arise because of the displacement of the crystal planes above and below the slip plane. The force, which is behind the work spent in moving the dislocations, is termed gliding force, F_g. The gliding force is evaluated by equating the work done, at moving a small unit of the dislocation at a small distance, with the work performed by the external forces in displacing the crystal planes at a distance equal to a Burgers vector. Thence, for the gliding force, per unit length of the dislocation, is readily obtained:

$$\vec{F}_g = \tau\vec{b} \ , \tag{11}$$

where: τ is the resolved shear stress on the Burgers vector. Thence, the glide force $\vec{F}_g$ is coplanar with the glide plane and acts normal to the dislocation at every point along its length. The force, so defined, is virtual but the concept is useful in understanding the dislocation's behavior.

3.4 Line tension of a dislocation

In a section above (Section 3.1.4) was argued that the dislocation shape could differ from a straight line. The general notion of dislocations, which form is not a straight line, allows, analogously to thermodynamic quantity - surface tension, the introduction of the concept of *line tension* of a dislocation. The dislocation, therefore, could be considered as a stretched piece of an elastic string. Of particular interest in the concept of curved-dislocation is the possibility latter to form closed loops (or a loop). The line tension of a dislocation then could be defined as, $T = \frac{d\left(Ul\right)}{dl} = U \propto Gb^2$. Recall that the strain energy of the dislocation is proportional to its length. By solving the corresponding equations of the theory of elasticity and utilizing the chain of equations above, the following dependencies were obtained for the line tension of dislocations with different geometries (Kuhlmann-Wilsdorf, 1965):

Straight linear dislocation: $T_{line} = Gb^2$; (12a)

Circular-loop dislocation: $T_{loop} \cong \frac{Gb^2\left(1-0.5\nu\right)}{4\pi\left(1-\nu\right)}\left(\ln\left(\frac{R_l}{b}\right)+1\right)$; (12b)

Slightly curved dislocation: $T_{curved} \cong \frac{Gb^2\left(1-\nu\cos^2\omega\right)}{4\pi\left(1-\nu\right)}\ln\left(\frac{\omega}{b}\right)$; (12c)

Where R_l is the loop's radius and ω is the deviation of the dislocation axis from the straight line.

From the energy point of view, the last two dislocations' patterns will be very unstable, i.e., they could exist only in the stress field generated by an external load. For instance, if no energy is supplied to sustain the equilibrium, a loop dislocation would disappear and leave a perfect crystal. However, when external shear stress is applied, the loop would not disappear but grow in size, spreading over the slip plane in which it lies. The concept of a curved and flexible dislocation line is widely used in many applications of the theory. Within the present book, it will be used when explaining the strength reduction effect in composites reinforced with nano-sized particulates.

3.5 Intersections of migrating dislocations

In the real metal (material) the dislocations form a three-dimensional network of linear faults. Due to the considerable density of the dislocations, a significant probability exists that there will be a certain number of dislocations laying in the same plane. Thence, when suitable conditions are present, these would be capable of moving (slipping) along that plane. It can therefore be assumed that many of the other dislocations, present in the crystal, could intersect the slip-plane of these dislocations simultaneously with them and at angles varying in a wide range. As a result, when a dislocation moves it will be forced to pass through a net of other dislocations that intersect its slip plane. Because of the stress field, inherent to the vicinity of any dislocation, it is apparent that these intersections would require some work to be done, to make them possible. The preceding could be readily illustrated as follows. Consider a dislocation loop in a crystal. In the case when the volume of the crystal that contains the loop dislocation is sheared by another dislocation the loop dislocation length should increase by two Burgers vectors, i.e., 2*b*. The latter statement is based on a rule that a line dislocation cannot end inside the crystal volume, i.e., it should start and end on the surface of the crystal. For this reason, the shearing dislocation cannot end inside the loop.

Two basic ways of dislocation intersections could be distinguished; (i) *kink* – a step that lies in the slip plane of a dislocation, and (ii) *jog* – a step that is normal to the slip plane of a dislocation.

3.5.1 *Kinks*

Due to the differences in the mutual orientation between the dislocation axis and the Burgers vector; the kink in the edge dislocation has a screw orientation (the step is parallel to the Burgers vector of the migrating dislocation), while the step in the screw dislocation has an edge orientation (the step is normal to the Burgers vector). The energy required for the slipping of the kinks, respectively, for the elimination of these steps, is less than the excess strain energy associated with this type of dislocation's intersections. Therefore, it can be assumed that steps of this type may tend to disappear.

3.5.2 *Jogs*

From the preceding follows that the jogs on a dislocation could also tend to disappear if the dislocation can move in a plane normal to the indicated slip plane, that is, to move in a vertical plane; in this specific case the stepped dislocation could be viewed as lying in a vertical plane. Yet, when both dislocations are incapable of gliding in a vertical plane, two specific types of dislocations movement could be distinguished, depending on the way these dislocations interact with each other:

(i) The first of the specific cases is when both interacting dislocations are edge dislocations. In that specific case, all three segments of the shearing dislocation are in fact edge dislocations, with their respective Burgers vectors lying in the crystal planes that contain the segments of the first dislocation. The only difference between that three-piece and an ordinary edge dislocation is that the former glides over all three segments, the unperturbed, the perturbed, and the stepped surfaces. (Here, by perturbed glide-surface is meant the glide surface which resulted after the interaction of the two dislocations).

(ii) The second of the specific cases occur when an edge dislocation intersects with a screw dislocation. As a result, the axis of the screw dislocation will be cut into two parts which would be displaced in a distance equal to a Burgers vector. The helical arrangement of the atoms around the screw dislocation axis would be thus discontinued which would lead to excess or deficiency of atoms at the vicinity of the dislocations intersection. Which side of the screw dislocation is enriched or depleted of atoms depends on the mutual orientation of the Burgers vectors of the intersecting dislocations. The essence of the above is that the jog on the screw dislocation, which is a tiny edge dislocation, will be restricted in moving (gliding) along the vertical step surface. The reason for that is because its Burgers vector is not laying on the surface of the step but is normal to it. The only way that the jog can move across the surface of the step is by a dislocation climb. Recall, (see Section 3.1.3) that this type of migration requires adding or removing vacancies and atoms to the respective side of the step surface which could be done by diffusing those from other parts of the crystal. As a result, behind the intersecting dislocations are left various defects or “debris”.

The interested reader could find additional information about the dislocations intersections in the book of W. T. Read [9] (see also the list of books in Suggested readings to this chapter).

3.6 Dislocations' sources

3.6.1 Solidification mechanism of dislocations' generation

The dislocation line energy is relatively high, so it is presumed that it is very unlikely that stresses of reasonable magnitude would lead to the creation of new dislocations in the regions void of dislocations. Thus, it is generally believed that the crystals, should initially contain a considerable number of dislocations. It is assumed that these "innate" dislocations are generated in the solid metals/alloys during their crystallization. However, it was soon realized that the dislocation density in a cast material is insufficient to explain the surface displacement at a slip band. The latter requires about 10^3 dislocations over a slip plane so that process to take place. Thus, the developers of the dislocation theory should have had to find/formulate some new mechanism by which the loaded metal produces (generates) the required dislocations. A feasible mechanism by which the dislocations are generated from those already existing in the crystal was proposed by Frank and Read [10]. Respectively, the sources generating the new dislocations are commonly referred to as Frank-Read sources.

3.6.2 The dislocations' generation under stress: the Frank-Read mechanism

The Frank-Read mechanism is based on the ideas and concepts discussed in the previous subsections. Their theory presumes that the crystal is imperfect i.e. containing inclusions that could serve as obstacles to the gliding of the dislocations. They surmised that under the action of applied stress the dislocation line could freely glide in its plane until encountering the obstacles. When these are met, the ends of the dislocation are anchored at them and their gliding stops. However, the central part (the unobstructed one) is still free to move and expand in the glide plane. As a result, a dislocation bow is formed which winds around the obstacles until the two branches of that bow are joined together. Eventually, a closed dislocation loop is formed, which spreads out freely over the glide plane. At the end of the process, the original dislocation length is restored, due to the natural propensity of decreasing the tension in the dislocation line. If the external stress is not removed the process repeats again and again, thus, increasing the dislocation's density in the stressed material. The various stages of the Frank-Read mechanism are illustrated in Fig. II-3-3. The work required for the creation of the new dislocation comes from the external source generating the stress. From preceding follows that the

work done by the source is spent on increasing the line tension of the dislocation, which results from the increase of the dislocation length (Recall that the stretched dislocation strives to minimize its length.). By analogy with the surface tension, the larger the curvature (i.e. the smallest the radius of curvature) the larger the stress, required to push the dislocation between the obstacles. Therefore, the greater the distance between the anchoring points, the lower the stress needed to activate a Frank-Read source.

In mathematical terms, the idea of Frank-Read could be represented as follows: From Section 3.4 follows that the line tension of an expanding dislocation should be equal to, $T = Gb^2$. That tension should be balanced by a line bending force, which results from the shear stress applied, $\vec{F}_g = \tau \vec{b} l$ (Eq. 11 in Section 3.3). Here, l is the distance between the anchoring obstacles. Hence, for the critical shear stress required for the operation of a Frank-Read source, it is valid:

$$\tau_{F-R} \approx \frac{T}{bl} = \frac{Gb}{l}. \qquad (13)$$

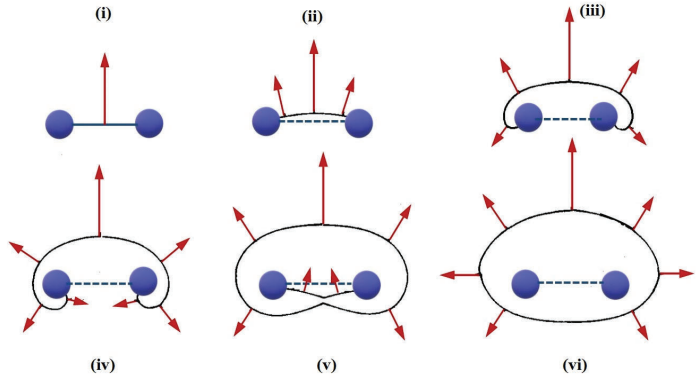

Figure II-3-3 A scheme of the successive stages in the operation of a double-ended Frank-Read source. The forces acting normally to the expanding dislocation are shown in red (here the length of the arrows does not match the real value of the force).

3.7 Interaction between the dislocations

As above, depending on the position of the extra atomic plane inserted (edge dislocations) or shifted (screw dislocations), the dislocations could be divided into two classes, positive and negative. The dislocations of opposite signs gliding on the same slip plane will attract each other, move toward each other, and annihilate. Conversely, the dislocations with an equal sign gliding on the same slip plane will repulse each other.

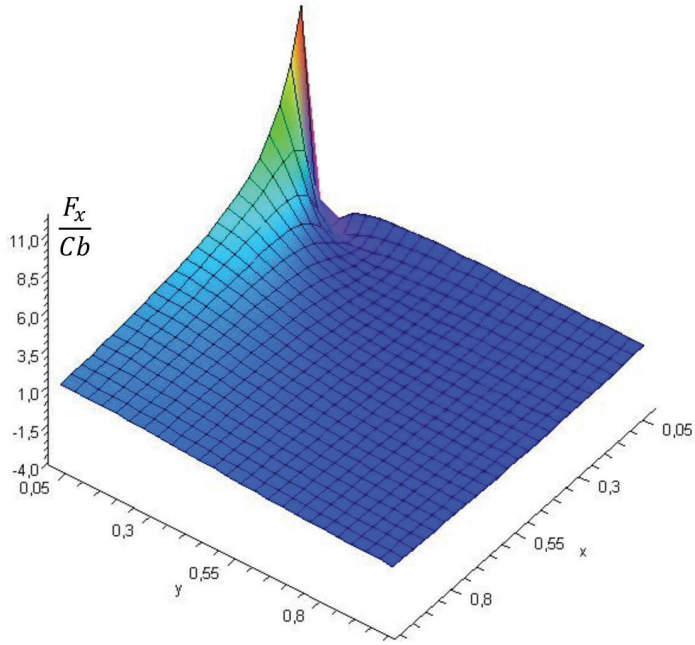

Figure II-3-4 3D-graph showing the interaction force, in F_x/Cb units, between two edge dislocations of the same sign along their slip direction, as calculated by Cottrell in [11]. Notice the existence of a small area of negative interaction (attraction). The minimum of the function is positioned at $x \sim 0.05$ and $y \sim 0.05$. Otherwise, the interaction is repulsive.

3.7.1 The force of interaction between two screw dislocations

That is the simplest case to consider. Since the stress field around a screw dislocation is $\tau = \tau_{\theta z} = \dfrac{Gb}{4\pi r}$ for the force acting between two screw dislocations is readily obtained:

$$\vec{F}_g = \tau \vec{b} = \frac{Gb^2}{2\pi r} \ . \tag{14}$$

This force is attractive for dislocations with opposite signs (antiparallel screws) and repulsive for dislocations with equal signs (parallel screws).

3.7.2 Interaction force, between two edge dislocations

Consider two parallel edge dislocations with the same Burgers vectors pointing, say, along the x-axis and their dislocations lines lined along the z-axis. In this case, the interaction force has not a central symmetry, thus, it should have a radial and a tangential component. According to Cottrell [11], the radial F_r and the tangential F_θ components of that force per unit length are equal to:

$$F_r = \frac{Cb}{r} \ \text{(15a), and} \ F_\theta = \frac{Cb}{r}\sin 2\theta \ \text{(15b).} \tag{15}$$

Recall that, $C = \dfrac{Gb}{2\pi\left(1-\nu\right)}$.

The force component along the *x*-axis, which by definition is the slip direction of the two dislocations considered, is thus equal to:

$$F_x = F_r \cos\theta - F_\theta \sin\theta = Cb\frac{x\left(x^2 - y^2\right)}{\left(x^2 + y^2\right)^2} . \tag{16}$$

Fig. II-3-4 shows a 3D graph of the dimensionless interacting force, $\dfrac{F_x}{Cb}$, between two dislocations as a function of the distance between them, i.e., the distance between their *x* and *y* coordinates.

The situation when two edge dislocations are laying in a common vertical plane above each other is a condition of equilibrium; $x = 0$. Thus, the theory predicts that a vertical array of edge dislocations of the same sign would be in a stable equilibrium. It should be noted that this is the arrangement of dislocations that coexist in low-angle grain (crystallite)

boundaries (see Section 2.2.3 in the preceding chapter). The situation when two parallel dislocations lay on two intersecting slip planes will be unstable, thence, the dislocations either will try to come together or will move apart from each other.

3.7.3 Dislocations' pile-up

The extensive study of the mechanisms leading to plastic deformation, strengthening, etc., showed that the dislocations tend to pile up on the slip planes, at obstacles such as grain boundaries, micro-, nano-sized inclusions, and precipitates (secondary-phase particles). It was found that the dislocations pile up densely together near the obstacle, i.e., at the head of the dislocations array and more widely spaced toward the source. It was evaluated [12-14] that the number of dislocations, N, occupying a distance l along the slip plane between the source and the obstacle is:

$$N = \frac{k\pi\tau D}{4Gb}. \qquad (17)$$

Where: τ is the average resolved shear stress in the slip plane and k is a factor close to unity.

For practical reasons, it could be considered the piled-up array of N dislocations as a giant dislocation with a Burgers vector equal to Nb. Thence, at large distances from the array the stress and the total slip produced by the array can be considered as produced by a single dislocation of strength Nb, located at the "center of gravity" of the pile-up; which is calculated to be at 3/4 of the distance l (see the references above). From the preceding, it could be presumed that the forces acting on the dislocations at the head of the pile-up should be very high and could be roughly equal to, $N\tau b$.

A detailed analysis of the stress distribution at the head of the dislocations array, made by Stroh [15] showed that the tensile stress behind the obstacle line is given by the relation:

$$\sigma = \frac{3\tau}{2} r^{-1/2} \sin\theta \cos\frac{\theta}{2}, \qquad (18)$$

where: θ is the angle between the line of the pile-up and a point at which the induced by the pile-up tensile stress is evaluated. The maximum value of the as-induced tensile stress σ, therefore, occurs at $\cos\theta = 1/3$ or $\theta = 70.5°$. The maximum is, thus, located on the line connecting the intersection of the pile-up line with the obstacle line and lies behind the obstacle line.

The number of dislocations that can be supported by an obstacle, therefore, will depend on the type of the barrier, the mutual orientation between the slip plane and the obstacle, the material's mechanical properties, the structure of the barrier, and its nearby environment, and the temperature. The overcoming of the obstacle from the dislocations can take place by several mechanisms including (i) a dislocation slip on a new plane, (ii) climbing of the dislocation(s) around the barrier, and (iii) generation of sufficiently high tensile stresses that exceed the fracture toughness of the material. As a result, cracks are generated, which relieve the excess stress. An extended version of the theory above is used in the explanation of the grain strengthening in materials, see Section 4.6, Ch. II-4.

3.8 Migration velocity of a dislocation

The velocity (more correctly the gliding velocity) with which the dislocations move depends on the applied shear stress, the purity of the crystal, the temperature, and the specific type of dislocation. It was evaluated, and subsequently experimentally confirmed, that the dislocation velocity could change over 12 orders of magnitude, depending on the conditions above. The experiments carried out on measuring the dislocation velocity, v, showed that it is exceptionally sensitive to the shear stress applied and that it fits very well the following power-law function:

$$v = A\tau^n . \tag{19}$$

Where: τ is the applied shear stress resolved in the glide plane, A is a material constant and n is an exponential factor. The n-factor varies significantly from one material to another and decreases with the increasing temperature; for instance, n is approximately a unity at 300 K in pure crystals, increases from 2 to 5 in alloys, and varies between, 4 to 12 at low temperatures [16-18].

Therefore from the equation above follows; the increase of the shear stress increases the dislocation velocity, while the increase of the temperature usually decreases it.

3.9 Study of the dislocations by transmission electron microscopy (TEM)

One of the powerful experimental tools extensively used in studying, detecting, and observing dislocations in materials is transmission electron

microscopy (TEM). Therefore, it seems reasonable in this chapter to briefly discuss some basic concepts of TEM.

The TEM study is performed on thin foils (samples) prepared from the tested material. The reason for this is to make the latter "transparent" to the electron beam of the microscope. TEM offers two methods of studying the specimen, observation in diffraction and image mode.

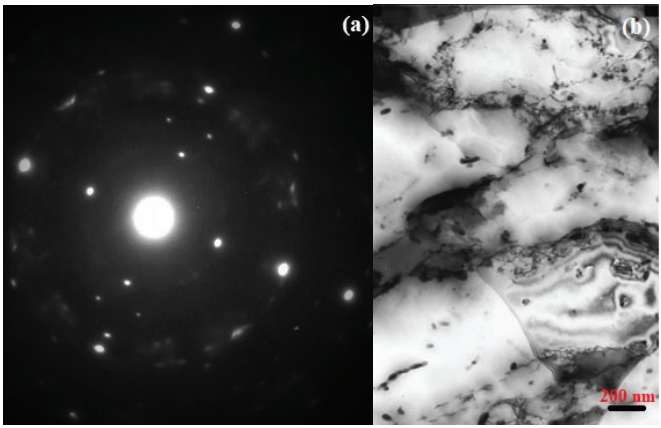

Figure II-3-5 (Fig. II-3-5a) A TEM-diffractogram taken from a rapidly quenched $(Al_{74}Cu_{19}Mg_{10})_{99}Zn_1$ alloy containing 29% crystalline fraction. The reflexes seen on the diffractogram are from the following crystalline phases Al, Al_2Cu, Al_2(Cu, Zn)Mg. The pale haloes linking some of the reflexes are a result of the electrons' diffraction on the amorphous phase, V. Dyakova [19]. (Fig. II-3-5b) A high contrast TEM image (bright field mode) showing the microstructure in an Al-based composite (Al-TiCN). On the micrograph are seen: (i) the Al-subgrains which are bounded by dislocation tangles, (ii) TiCN particles (reinforcement) embedded in the matrix (the larger black dots), and (iii) dislocation lines exiting the foil, which are visible owing to the extensive etching of the highly stressed matrix in the vicinity of the dislocations (the small black dots on the surface of the grains), V. Dyakova [20].

3.9.1 The diffraction mode

In the diffraction mode a diffraction pattern, obtained from the illuminated sample area, is projected on the TEM screen. The diffraction

pattern is entirely equivalent to that of the XRD (X-ray diffraction) but due to the considerable differences in the wavelengths, the electron's wavelengths are much shorter compared to those of the X-rays, the resolving capability of TEM is much higher. (Recall that the wavelength of the electrons in, e.g., 100k eV TEM is $\lambda = 0.037$ Å, while those used in XRD vary between 2 to 100 Å.) Depending on the microstructure of the studied material on the TEM-screen are produced, spots (single crystal specimen), rings (poly-crystals specimen), or diffuse haloes (amorphous specimen) patterns, see Fig. II-3-5a.

3.9.2 The image mode

The image mode produces an image of the illuminated sample area, as shown in Fig. II-3-4b. In that mode, the TEM is set to examine the information obtained from the transmitted signal which is directly related to the sample's microstructure. The different parts (grains, phases, etc.) of the TEM image are thus distinguishable if the difference in the electron densities at the image plane is sufficiently high. In the electron microscopy practice, that difference is termed *contrast* and is quantitatively defined as a difference in the intensities of two adjacent areas.

Two image-mode techniques are most frequently used in the study of dislocations by a conventional TEM; bright-field and dark-field microscopy. The difference between these two image modes is in the way of filtering in the back focal plane of the transmitted *e*-beam (the filtering is done by the TEM's objective diaphragm).

In *bright-field microscopy*, a small objective aperture is used, thus, all diffracted beams are blocked and only the non-diffracted electron beam is allowed to pass. Conversely, at the *dark-field* mode of the TEM, the unscattered *e*-beam is blocked.

The contrast observed in the bright-field image is due to scattering or absorption of the incident *e*-beam, which results from the thickness and/or compositional variations, or structural anomalies (e.g., grain boundaries, stacking faults, dislocations, etc.), see Fig. II-3-5b above. Thence, due to the factors listed, the regions in which the intensity of the incident *e*-beam is most effectively reduced, appear darker on the TEM image. In crystalline materials, dark areas are usually due to Bragg's wide-angle diffraction, hence the term *diffraction contrast*. Here, the intensity reduction is due to the coherent elastic scattered of the incident *e*-beam electrons which are then blocked by the objective aperture. Diffraction contrast is often observed in the vicinity of defects in the lattice as illustrated in Fig. II-3-6.

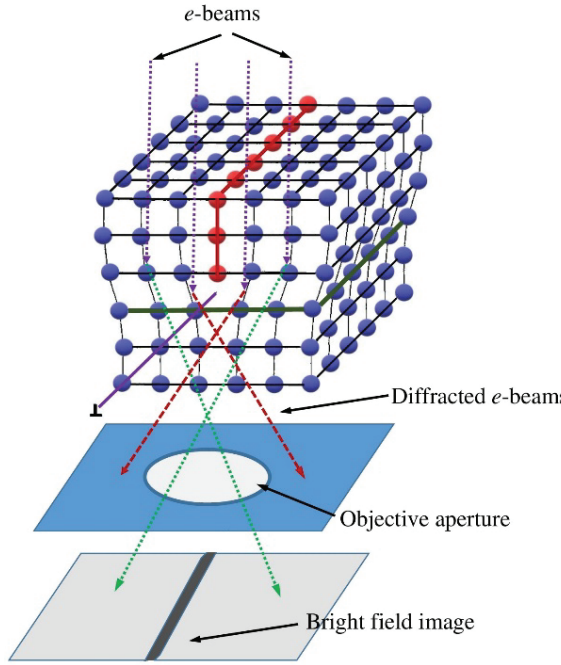

Figure II-3-6 Illustration of the image formation from a sample in which lattice is contained an edge dislocation (TEM working in bright field mode). When the crystal far from the dislocation obeys the Braggs condition then near the dislocation this condition is violated, thus resulting in stronger diffraction. These strongly diffracted electrons are stopped by the objective diaphragm, while those fulfilling the Braggs condition are allowed to pass through the objective aperture.

Consider an image formed from a lattice containing an edge dislocation (Fig. II-3-6). On the left and right sides of the dislocation, where the crystal planes are sufficiently well aligned with the incident *e*-beam direction, the transmitted electron's intensity would differ very slightly from that of the incident beam. Near the core of the edge dislocation, however, the lattice planes are distorted or bent to compensate for the strains associated with the atomic displacements at the dislocation core. The Bragg orientation of the planes near the core differs considerably, from that of the incident beam, and as a result, these are

strongly scattered and subsequently blocked by the objective diaphragm. The presence of the dislocation is, thus, made visible appearing on the image screen as a dark line across the bright-field image surrounded by highly intensive bright contrast resulting from the neighboring, undistorted crystalline material. The same dislocation, in dark-field TEM-mode, will appear as a bright line on a dark background, because the transmitted *e*-beam from the undistorted crystal lattice is blocked by the objective diaphragm, while the objective aperture is positioned in a way to transmit only the scattered electrons.

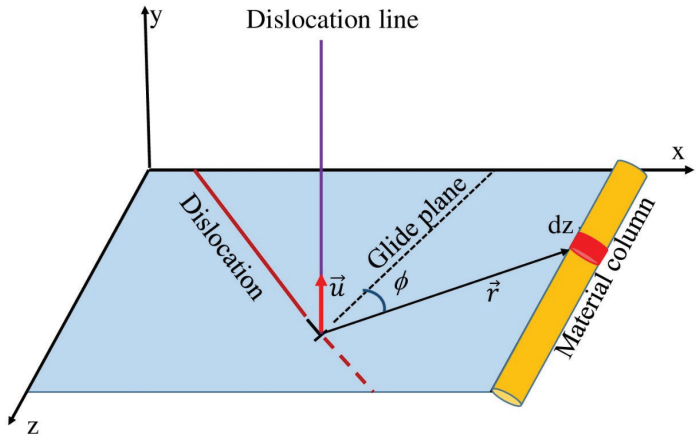

Figure II-3-7 Illustration of the contribution of a scattering unit cell at the calculation of the diffraction contrast. It is assumed that the displacement field $\vec{R}$ caused by the dislocation in the center of the picture affects the cell marked as dz in the material column.

3.9.3 The Diffraction Contrast and the Crystal Lattice Defects

The theory of the diffraction contrast in TEM is based on the waves' interference of those parts of the incident *e*-beam, scattered by the diffracting planes. In that theory is shown, that the amplitudes of those parts depend on the reciprocal lattice vectors, $\vec{g}$, of the diffracting planes (Kittel, 2005). By summing up the diffracted amplitudes from all of the unit cells that lie along the path of the diffracted beam, the resulting amplitude can be calculated, which when squared yields the scattered

beam intensity. A short overview of the basic ideas of that theory is given below.

Consider a column with a height equal to 2*d*, running from its top to the bottom of the sample, for the details see Fig. II-3-7. The phase difference Φ of the electrons diffracted by a unit cell positioned at a distance $\vec{r}$ from the origin of that column is, $\Phi = 2\pi\left(\vec{g}.\vec{r}\right)$. Therefore, the amplitude of the scattered beam is equal to, $e^{-i\Phi} = Ae^{-2\pi i\left(\vec{g}.\vec{r}\right)}$. Taking advantage of the fact, that the electron wavelength is much smaller than the lattice parameter, it could be assumed that each unit cell of the column scatters the electrons of the incident *e*-beam independently. Thus, as above, the overall amplitude scattered by the column cells is a vector sum of their amplitudes:

$$A_{total} \cong F\int_{-d}^{d} e^{-2\pi i\left(\vec{g}.\vec{r}\right)}dr \ . \qquad (21)$$

Where: *F* is the structure factor of the cells in a specific diffracting plane (a measure of the amplitude scattered by a unit cell of a crystal with a specific structure).

In the specific case here, when the structure of the "perfect" crystal is distorted due to some lattice defect, a displacement of the scattering elements equal, to a vector, say $\vec{R}$, is generated. The position of the scattering cell in the column will no longer be equal to $\vec{r}$ but will be a vector sum of $\vec{r}$ and $\vec{R}$, $\vec{r}+\vec{R}$. Therefore, after substituting $\vec{r}$ in Eq. 21 with $\vec{r}+\vec{R}$ and after performing the multiplication by the reciprocal lattice vector, $\vec{g}$, an extra phase shift due to the distortion of the perfect crystal lattice is generated $\vec{g}.\vec{R}$ which may either increase or decrease the Bragg condition, respectively, increase, or decrease, the total amplitude and the intensity of the produced contrast:

$$A_{total} \cong F\int_{-d}^{d} e^{-2\pi i\left(\vec{g}.\vec{r}+\vec{g}.\vec{R}\right)}dr \ , \qquad (22)$$

Diffraction contrast from a dislocation depends on its Burgers vector, since the strain field causing the displacement $\vec{R}$, is proportional to the value of $\left|\vec{b}\right|$ (see Eqs 6a and 6b). From Eq. 22 follows that at $\vec{g}.\vec{R}=0$, i.e., when the reciprocal lattice vector is perpendicular to the displacement, no contrast would be generated, and the dislocation is thus undetectable.

The displacement field $\vec{R}$ caused by a complex dislocation (see Section 3.1.4) in a unit cell of the column is mathematically expressed in cylindrical coordinates as:

$$\vec{R} = \frac{1}{8\pi(1-\nu)}\left\{4(1-\nu)\vec{b}\phi + \vec{b}\sin 2\phi + (\vec{b}\times\vec{u})\left[2(1-2\nu)\ln r + \cos 2\phi\right]\right\} \cdot \quad (23)$$

Where: r is the distance between the dislocation and the scattering cell, ϕ is the angle between the glide plane of the dislocation and the vector pointing from the dislocation core to the scattering cell, and $\vec{u}$ is a unit vector collinear with the dislocation line (see Fig. II-3-7). Notice, that the second member in Eq. 23, $\vec{b}\sin 2\phi$, is the edge component of the Burgers vector (see Section 3.1.4). By evaluating $\vec{R}$, with Eq. 23 and by substituting the obtained result in Eq. 22, it will be possible to calculate the phase shift contributed by every single cell of the column in the integral (Eq. 22). Respectively, the interference amplitude, as well as the resulting contrast could be also calculated.

For a screw dislocation, the edge component of the Burgers vector, and the vector product, $\vec{b}\times\vec{u}$, (the vectors $\vec{b}$ and $\vec{u}$ are collinear) are equal to zero. In that case, Eq. 23 reduces to $\vec{R} = \frac{\vec{b}\phi}{2\pi}$. From the preceding follows that the screw dislocation will be undetectable when $\vec{g}.\vec{R} = 0$ which is valid when, $\vec{g}.\vec{R} = \left(\vec{g}.\vec{b}\right)\frac{\phi}{2\pi} = 0$, i.e., when $\vec{g}.\vec{b} = 0$ or when $\phi = 0$. For an edge or mixed dislocation (i.e. dislocation containing edge and screw components) to be undetectable two conditions should be fulfilled simultaneously, $\vec{g}.\vec{b} = 0$, and $\vec{g}.\left(\vec{b}\times\vec{u}\right) = 0$. These two conditions are rarely fulfilled simultaneously, hence, in the reality, the edge dislocations, if present, are always visible on the TEM image. It was empirically established that: the dislocations are readily visible when, $\vec{g}.\vec{b} \geq 0.5$, they are invisible when, $\vec{g}.\vec{b} = 0$, the dislocation image is overlaid by additional optical effects when, $\vec{g}.\vec{b} \geq 2$ (Goodhew, Humphreys, Beanland, 2001; Williams, Carter, 2009).

Suggested additional reading to Ch. II-3

1. G. E. Dieter, Jr., Mechanical Metallurgy in Metallurgy and Metallurgical Engineering Series, edited by Robert F. Mehl and Michael B. Bever, McGraw-Hill Book Company, 1961.
2. R. E. Smallman and R. J. Bishop, Modern Physical Metallurgy and Materials Engineering, Sixth edition, Butterworth-Heinemann 1999, ISBN 0 7506 4564 4.
3. W. D. Callister, Jr., Fundamentals of Materials Science and Engineering, Fifth Edition, John Wiley & Sons, Inc. 2001, ISBN 0-471-39551-X.
4. G. Gottstein, Physical Foundations of Materials Science, Springer-Verlag Berlin Heidelberg GmbH 2004, ISBN 978-3-662-09291-0 (eBook).
5. R. Abbaschian, L. Abbaschian, R. E. Reed-Hill, Physical Metallurgy Principles, Cengage Learning 2009, ISBN-13: 978-0-495-08254-5.
6. W. F. Hosford, Mechanical Behavior of Materials, Cambridge University Press 2005.
7. M. Ohring, Engineering Materials Science, Academic Press, Inc. 1995, ISBN 0-12-524995-0.
8. R. A. Higgins, Engineering Metallurgy, Part I - Applied Physical Metallurgy, Sixth Edition, Arnold a member of the Hodder Headline Group 1999, ISBN 0 340 56830 5.
9. H. G. van Bueren, Imperfections in Crystals, North Holland, Amsterdam (1960).
10. M. Born and E. Wolf, Principles of Optics, Sixth Edition, Pergamon Press, 1980.
11. P. J. Goodhew, J. Humphreys, R. Beanland, Electron Microscopy and Analysis, Taylor and Francis 2001, ISBN 0 7484 0968 8.
12. D. B. Williams and C. B. Carter, Transmission Electron Microscopy: A Textbook for Materials Science, 2nd ed., Springer Science-Business Media, LLC, 2009.
13. D. Brandon, W. D. Kaplan, Microstructural Characterization of Materials, Second Edition, John Wiley & Sons Ltd. 2009, ISBN 978 0 470 02785 1.
14. A. H. Cottrell, Theory of Dislocations, in Progress in Metal Physics 4, B. Chalmers ed., Pergamon Press Ltd., London, 1953, pp. 205-264.
15. Ch. Kittel, Introduction to Solid State Physics, Eighth Edition, John Wiley & Sons Inc. 2005, ISBN 0-471-41526-X.

References to Ch. II-3

1. M. F. Ashby and D. R. H. Jones, Engineering materials. Vol.1 and 2, Butterworth-Heinemann (2002) ISBN 0 7506 3081 7.
2. V. Volterra “Sur l'équilibre des corps élastiques multiplement connexes”, Annales Scientifiques de l'École Normale Supérieure, Vol. 24, pp. 401–517 (1907).
3. G. I. Taylor “The Mechanism of Plastic Deformation of Crystals. Part I. Theoretical”. Proceedings of the Royal Society of London. Series A. 145 (855): 362–87 (1934).
4. J. Burgers, Some considerations on the fields of the stress connected with dislocations in a regular crystal lattice. I, II, Selected Papers of J. M. Burgers, Edited by F. T. M. Nieuwstadt and J. A. Steketee, Springer Science and Business Media, B.V. 1995, 335-390, ISBN 978-94-011-0195-0 (eBook).
5. Orowan, E. “Zur Kristallplastizität. III”. Zeitschrift für Physik. 89 (9–10): 634–659 (1934).
6. V. Dyakova, Dislocation Configurations in the Process of Microstructure Refinement by Plastic Deformation, Journal of Materials Science and Technology (ISSN 0861-9786), Vol. 18, No 2, pp 102-110 (2010).
7 J. S. Koehler, Imperfections in Nearly Perfect Crystals, John Wiley & Sons, Inc., New York, 1953.
8. J. S. Koehler, Phys. Review, 60 243 (1941).
9. W. T. Read, Jr., Dislocations in Crystals, McGraw-Hill Book Company, Inc., New York, 1953.
10. F. C. Frank and W. T. Read Jr., “Multiplication Processes for Slow Moving Dislocations”. Physical Review. 79 (4) 722–723 (1950).
11. A. H. Cottrell, “Dislocations and Plastic Flow in Crystals,” p. 48, Oxford University Press, New York, 1953.
12. J. D. Eshelby, F. C. Frank, and F. R. N. Nabarro, Phil. Mag., vol. 42, p. 351 (1951).
13. A. K. Head, Phil. Mag., vol. 4, pp. 295-302 (1959).
14. Meakin and Wilsdorf, cited by G. E. Dieter, Jr., see Suggested reading [1].
15. A. N. Stroh, Proc. Roy. Soc. (London), vol. 223, pp. 404-414 (1954).
16. Soboyejo, Wole. “7.3 Dislocation Velocity”. Mechanical properties of engineered materials. Marcel Dekker, 2003.
17. D. Hull and D. J. Bacon, Introduction to Dislocations, Fifth Edition, Butterworth-Heinemann, Amsterdam 2011, 18. Thomas H.

Courtney, Mechanical Behavior of Materials, Second Edition, Waveland Press, Inc. 2005, ISBN 1-57766-425-6.
19. V. Dyakova, G. Stefanov, I. Penkov, D. Kovacheva , N. Marinkov, Y. Mourdjeva, S. Gyurov, Influence of Zn on Glass Forming Ability and Crystallization Behaviour of Rapidly Solidified Al-Cu-Mg (Zn) Alloys, Journal of Chemical Technology and Metallurgy, 57(3) (2022) 622-630.
20. V. Dyakova, private communication (2017).
21. D. Kuhlmann-Wilsdorf, Dislocations in Physical Metallurgy, Edited by R. W. Cahn, North-Holland Publishing Company, Amsterdam, 1965.

CHAPTER II-4

STRENGTHENING MECHANISMS IN METALS AND ALLOYS

LUBOMIR A. ANESTIEV

In the middle of the last century, the progress in our knowledge of the structure of materials and the achievements of the experimental techniques of studying the material's structure led to the development of several theories that successfully explained the behavior of the materials under load. By introducing the concept of dislocations in crystals and their interaction with various defects of the crystal lattice, it was finally possible to explain, not only the plasticity in metals but also the strengthening due to the precipitation of stable phases in thermodynamically unstable alloys.

4.1 Precipitation: The formation of natural reinforcement particulates

Precipitation strengthening is a technique, used to increase the strength of the metals and their alloys, and which applies to most of the structural alloys used nowadays in the industry, e.g., those of aluminum, magnesium, nickel, titanium, and certain steels. In short, the precipitation strengthening technique uses the capability of certain dissolved elements in a phase system to form, at a specific temperature, finely dispersed phases which could subsequently serve as reinforcement of the matrix phase in which they have precipitated. Thence, by varying the temperature and the composition, which in this case are controllable parameters, it is possible, by using, say, the equilibrium phase diagram of a certain phase system of elements, to select composition and temperature, or a specific temperature regime, which would lead to the precipitation of the desired reinforcement phase.

During the research, carried out to synthesize new structural materials with improved mechanical properties, it was understood that the precipitation-

strengthening is a result of the interaction between the precipitated particles and the dislocations. Based on that knowledge, the mechanism of strengthening was readily explained; when the reinforced material (alloy, composite, etc.) is loaded the movement of the dislocations or the other defects, always present into the crystal's lattice, is impeded by these fine precipitates, see Ch. II-3. Yet it was confirmed that it is the dislocations, in the utmost, which are those accountable for the increase of, e.g., the yield strength of a material. Therefore, by taking the preceding into account, it was rationalized that by controlling the rate of the precipitation of the strengthening phase, it will be possible to produce precipitates with valuable, say, mechanical properties, thus, improving substantially these properties of the matrix. As shown below the precipitation rate is governed by the temperature and the composition of the incipient matrix (metal, alloy, etc.). Thence, controlling the precipitation rate would require studying the mechanisms behind the nucleation and the growth of new phases from a thermodynamically unstable matrix phase.

As above, the technique utilized in the precipitation strengthening is based on the supersaturation of one (or more) of the constituent element(s) in the matrix alloy, which occurs when the homogenized incipient matrix alloy is cooled below the solvus line. (Recall, that the solvus line is a curve on a temperature-composition binary diagram indicating the limits of solubility of a certain constituent element between two solid phases). The undercooled in that way matrix is said to be in a *metastable* condition. From a thermodynamic point of view, at that point, the Gibbs free energy of the undercooled matrix is higher than the free energy of the phases (products) that could be precipitated. From that moment onward the formation of precipitates is controlled by two kinetic processes, the nucleation, and the growth rate of the product phases. As above, the driving force behind these two processes is the difference between the free energies of the matrix and the product phases.

4.1.1 The precipitates nucleation

Two types of nucleation are distinguished depending on the mechanisms governing their kinetics: (i) the *heterogeneous nucleation*, as its name suggests, occurs on impurities, mechanical faults, on the surface of other phases present in the matrix, etc. All of those listed serve as a substrate on which the formation of the new phase(s) takes place. The rate of heterogeneous nucleation depends mainly on the surface tension between the nucleating phase and the substrate. When the surface tension is low, one should expect a very high rate of heterogeneous nucleation, for

obvious reasons; the energy required to form a nucleus is negligible. (ii) The homogeneous nucleation occurs within the matrix phase. The nucleation rate in this case is controlled by the fluctuations of the temperature, and the composition (the concentration of the components), and from there from the free energy. Due to the multiple factors controlling that type of nucleation, it is obvious that the naturally preferable kind of nucleation would be heterogeneous nucleation.

Regrettably, the rate of nucleation, *I*, could not be unambiguously determined. In the practice it is accounted for by the following expression, see e.g. [1]:

$$I = I_0 \exp\left(-\frac{\Delta G_n}{kT}\right) \text{ (in m}^{-3}\text{s}^{-1}\text{).} \quad (1)$$

Where: ΔG_n is the standard free energy change resulting from the transition of the matrix atoms to the nuclei of the new phase (the driving force), I_0 is a pre-exponential factor whose value varies depending on the nucleation mechanism and *k* is the Boltzmann constant.

As seen from Eq. 1 it is the preexponential factor that introduces ambiguity in determining the rate of nucleation. Despite the several attempts to derive a functional dependence linking I_0 with the factors controlling the nucleation process, the results obtained so far are not satisfactory [1]. For that reason, in the practice for I_0 and ΔG_n are used quasi-theoretical or empirical expressions. For instance, at the homogeneous nucleation, it is accepted that I_0 and ΔG_n, are equal to, $I_0 = 10^{36}$ m^{-3}s^{-1}, and $\Delta G_n = 69kT$, while at the most commonly encountered nonhomogeneous nucleation (e.g., the nucleation taking place on grain boundaries) these are, $I_0 = 10^{30}$ m^{-3}s^{-1} and $\Delta G_n = 57kT$.

Yet, for a specific alloy, an average rate of the nucleation could be obtained from the calorimetric data of the process studied, as described in a paper by Anestiev et al. [2].

4.1.2 The precipitation rate

The growth rate of the precipitate is again controlled by two separate processes: (i) attachment kinetics, which is the rate of transition of the matrix' atoms to the precipitating phases, (ii) the transport of the solute' atoms, required to the growth of these phases, from the matrix to the

precipitates interface. Keeping in mind that in the solids the dominant transport process is diffusion, two limiting mechanisms of precipitates' growth could be distinguished; kinetics and diffusion controlled. Therefore, depending on which of those two processes is slower, predetermines the precipitate formation and growth.

In mathematical terms, see [3,4], the growth rate of a precipitate is described by the following system of non-linear algebraic equations:

$$\mu_i^m - \mu_i^{ph} = -RT \ln\left(1 - \frac{v^{ph}}{v_0^{ph}}\right) + \frac{2\sigma V_m^{ph}}{r^{ph}} - \frac{v^{ph}}{v_0^{ph}} \sum_{k=0}^{n} \left(\mu_k^m - \mu_i^m\right) C_k^{ph} \cdot \quad (2)$$

Where the superscript letters (*m*) and (*ph*) indicate the matrix and the growing phase, the subscript in Eq. 2 denotes the *i*th component dissolved in the matrix, and the growing phase ($i \in \{0..n\}$, where $i = 0$, refers to the solvent, $i \in \{1..n\}$, to the dissolved components), T is the current temperature, μ_i^m and μ_i^{ph} are the chemical potentials of the *i*th component in the phases (*m*) and (*ph*), r^{ph} is the radius of the curvature of the growing phase, R is the universal gas constant and v^{ph} is the growth rate of the *ph*-phase. Here, v_0^{ph} is a complex parameter $v_0^{ph} = v_0^{Tph} \exp\left(-\frac{Q^{m-ph}}{RT}\right) \exp\left(-\frac{G^{ph}}{RT}\right)$ [3,4] that could be considered as the maximal growth rate attainable by the *ph*-phase (Notice that this maximal growth rate depends on the temperature, the activation energy Q^{m-ph} (which is different for each of the precipitating phases), and via the Gibbs energy of the *ph*-phase, G^{ph}, on the composition of the precipitating phase), v_0^{Tph} is a constant depending on the micro-scale characteristics of the phases involved in the growth, the vibrational frequency of the atoms, and the jump length, *a*, between the growing and the matrix phases (*a* is usually equal to 2 to 3 interatomic spacings of the *ph* lattice). It should be kept in mind that in the case of multiple phases, precipitating in the matrix, a similar system of equations should be solved for every growing phase, hence, the superscript index (*ph*) in Eqs 2. In contrast with the nucleation rate, the only unknown parameter in the equations above is the activation energy - Q^{m-ph}. However, this parameter can be determined from the

calorimetric data of the phase transformation ($m \rightarrow ph$), when the latter is subjected to an appropriate regression analysis [3].

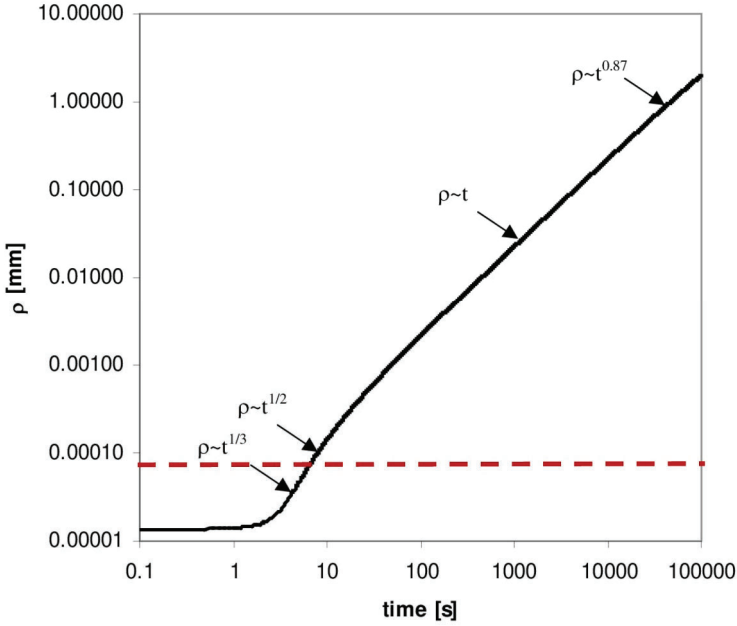

Figure II-4-1 Calculated with Eqs 2 precipitate radius as a function of the time. The precipitate is a solid solution of Si and Zn in fcc-Al, growing in an undercooled $Al_{68}Si_2Zn_{30}$ (at.%) melt. The arrows indicate the specific "growth laws" governing the process of growth at different stages of the precipitate's growth. Notice, how these laws change during the growth of the precipitate: in the beginning, the growth law is strongly influenced by the surface tension (melt-precipitate), at the end, however, the transport processes (the diffusion of Si and Zn) begin to dominate the growth kinetics.

A calculated with Eqs 2 precipitate radius (ρ) – time (t) dependence is shown in Fig. II-4-1 [5]. The growth takes place in a supersaturated, undercooled $Al_{68}Si_2Zn_{30}$ (at.%) melt with a temperature of 790 K. The precipitates are a solid solution of Si and Zn in fcc-Al (see the Al-corner of the Al-Si-Zn phase diagram in [6]. The calculations showed that the growth rate is not a constant but a quantity that varies with time.

Therefore, the growth law radii – time is not described by an invariable functional dependence but from time-dependent functions changing with time, as indicated by the arrows on the radii – time curve in Fig. II-4-1. At the beginning (left side of the graph) the growth rate is negligible up to a second after the nucleation. After that, however, it rapidly increases passing from cubic to parabolic law of growth. These are indicative of a strong influence of the surface tension on the growth kinetics. At the end of the growth (right side of the graph), the influence of the surface tension on the growth process is negligible. The precipitate radius is large enough and at that stage dominant are the transport processes – the growth law slowly changes from linear to a parabolic law. Recall, that the latter is typical for diffusion-controlled growth of flat surfaces (Khanna, 2012). Notice that the growth of the precipitate is rather fast (at the second minute its size is already above 1 μm), however, one should keep in mind that the growth takes place in a melt. In solid solutions, the precipitation curve r(t) would be quite different. The dashed line in Fig. II-4-1 (marked in red), indicates the upper limit of the practically useful nano-sized precipitates.

4.1.3 Evaluation of the precipitates' fraction

In case that the growth rate and the nucleation rate are known it is possible to evaluate the fraction of the precipitated strengthening phases as a function of the time, $f(t)$, by employing the Kolmogorov-Johnson-Mehl-Avrami (KJMA) equation. For non-isothermal conditions the latter reads:

$$f\left(t\right)=1-\exp\left(-\frac{4\pi}{3}\int_{0}^{t}I\left(\zeta\right)\left[\int_{\zeta}^{t}\dot{r}\left(\zeta'\right)d\zeta'\right]^{3}d\zeta\right). \tag{3}$$

Here $I\left(\zeta\right)$ and $\dot{r}$ are the nucleation and the growth rates. The growing particles are presumed to be spherical.

The simultaneous solution of the equation above together with the equations of nucleation and growth rates is a difficult mathematical task. It requires specific skills and knowledge from those who intend to employ them. However, the long period of studying the precipitation strengthening led to the formulation of the following useful empirical rules which are readily applicable in the practice: (i) precipitation strengthening is possible if the line of solid solubility slopes strongly toward the center of a phase diagram; (ii) when a large volume of precipitate particles is desired, the amount of the alloying element should be kept as low as possible; (iii) from the equations above follows that the lower initial temperatures

increase the driving force of nucleation, thus creating more nucleation sites, respectively, higher numbers of small precipitates at which the dislocations motion could be disrupted; (iv) the treatment of the alloy at higher temperatures promotes the precipitate's growth and coarsening, thus reducing the strengthening effect.

4.1.4 The precipitates' coarsening (see Fig. II-1-5 in Ch. II-1)

This is a process one should be aware of when designing the time-temperature processing regime when a precipitate strengthening is aimed. The precipitates coarsening as a rule is controlled by the differences in the surface energies between the smaller and the larger particles. Recall, that the excess surface energy of a spherical particle with radius R_p is $U_S = \frac{2\gamma}{r}$ (the Laplace law). Thence, if two particles are allowed to exchange material between each other, those of smaller radii will tend to dissolve, while the larger one will grow at their expense. The interested reader could find a description of the mechanisms involved in the precipitates coarsening and the equations governing the coarsening process, e.g., in [7].

4.2 The theory of precipitation strengthening

As from above, the primary cause of the precipitation strengthening is the second phase particles that precipitate during the heat/mechanical treatment of an alloy. The extensive research of the precipitation strengthening phenomena has shown that the strengthening effect is due to the impediment of the dislocations' mobility throughout the lattice caused by these particles. Indeed, a dislocation moving on a slip plane that contains statistically distributed precipitates (obstacles) may overcome them in three different ways, (i) shear through these particles, (ii) avoid them by moving out of the slip plane, or (iii) by bending between these obstacles, leaving, as a result, a dislocation ring around each precipitate. All of these processes require some work to be done, thence, a certain amount of energy must be expended. Which one of the preceding mechanisms would take place, however, depends on the applied stress and the nature of the precipitate (obstacle).

Physically, the factors that govern the strengthening process are the precipitates' size, their mechanical properties, the interfacial or surface energy at the precipitate-matrix interface, and the mechanical properties of the matrix, e.g., the Young modulus, the shear modulus, etc.

As a rule, when the precipitate particles differ, e.g., in specific volume, crystallographic structure, and lattice orientation from those of the matrix, their presence causes distortions in the matrix lattice. The size-effect of the precipitate on the stresses induced in the matrix could be summarized as follows; if the specific volume of the precipitate is smaller than that of the matrix, the precipitated particle causes tensile stress in the matrix lattice, while when the specific volume of the precipitate is larger, then compressive stresses are induced. Taking into account the fact that around, say, edge dislocation exists a stress field (recall that above the dislocation it is compressive, while below it is tensile) two different patterns of the interaction, dislocation-precipitate, could be distinguished (see for details Ch. II-3): (i) when the interaction energy between a dislocation and a precipitate is negative then the dislocation will be attracted to the precipitate, (ii) conversely, when the interaction energy between a dislocation and a precipitate is positive, the dislocation will be repulsed by the precipitate. Similarly, the precipitated particles tend to change the local stiffness of the matrix material that surrounds them. As a result, the dislocations are repulsed by these regions of higher stiffness and tend to pile up around them (see Chs II-6 and II-7).

Additionally, the mechanisms of interaction between the precipitates and the moving dislocations strongly depend on the type of the inter-phase (matrix-precipitate) boundary. Three types of inter-phase boundaries could be distinguished, respectively, three types of dislocations-precipitates interaction should be expected:

(i) *Coherent or ordered inter-phase boundary*. In this boundary type, the atoms of the matrix and the precipitate lattices match up, to a certain degree, along the boundary. Despite the mismatch between the lattices of the precipitate and the matrix, however, the chemical bonds between their constituent atoms are still preserved. That is why the differences in the parameters of the lattices, matrix-precipitate, although not considerable, still generate strain energy inside the matrix and the precipitate at their common boundary. It is the strain energy, associated with that stress field, that should be overcome by the moving dislocations and which eventually leads to the strengthening of the material.

(ii) *Fully disordered inter-phase boundary*. In this particular case, the lattices of the matrix and the precipitate are completely mismatched. That is, on the contact boundary between them there are no coherency-strains.

(iii) *Partially ordered (semicoherent) inter-phase boundary*. In this type of inter-phase boundary, the precipitate and the matrix lattices parameters are matching along with the one set of crystallographic directions, while, along with the other directions, dislocations are needed

to accommodate the large differences between the lattice parameters. Thence, the resulting incoherency strains are partially relieved from these dislocations formed at the boundary of the mismatching lattices.

Based on the preceding, a coherence criterion could be introduced to serve as a measure of the coherency between the lattices of the precipitate and the matrix:

$$\eta_{coh} = \frac{a_p - a_m}{a_m}. \quad (4)$$

Where: a_p and a_m are the lattice parameters of the precipitate (particle) and the matrix.

There are several ways by which the matrix could be strengthened by the precipitates. Yet, these could be summarized into two main groups, depending on the deformability of the precipitates, whence the terms used to identify these groups; deformable and non-deformable precipitates (particulates) strengthening. To all theories below the following conditions and assumptions apply: (i) the precipitates (particulates) are statistically distributed inside the matrix, (ii) the volume fraction of the particles, f, is constant and independent of particle radius, R_p, (iii) the increase of the resolved shear stress $\Delta\tau$, is defined as the increase in the shear stress caused by the presence of the particles, (iv) only one of the possible mechanisms of interaction between particles and the dislocations is active at the time of the interaction, and (v) the strengthening induced in the material is directly related to the resolved shear stress $\Delta\tau$ caused by the presence of the reinforcement (precipitates, introduced in the matrix particulates, etc.). From the preceding follows that (see Section 2.6 in Ch. II-2) the increase of the yield strength of the material, σ_Y, is m times the resolved shear stress $\Delta\tau$, $\sigma_Y = \Delta\tau / m$, where m is the Schmid factor. Thus, the main task of the strengthening theories discussed below could be formulated as; determine the resolved shear $\Delta\tau$, and by the Schmid formula, calculate the achieved strengthening of the material.

4.3 Precipitation strengthening: Deformable precipitates

In this case, the following strengthening mechanisms could be distinguished (Courtney, 2005; Soboyejo, 2003):

(i) Strengthening due to the differences in the lattice parameters at the particle-matrix interface. Its origin, therefore, stems from the lack of full coherency between the matrix and the precipitate lattices, hence, the term *coherency strengthening* to distinguish it from the other types of

strengthening. The coherency strengthening is due to the strains generated around the precipitate due to the differences in the lattices parameters of the precipitate and the matrix. The stress field associated with this strain could be considered as a barrier that should be overcome by the migrating dislocations when the material is under load. It is thus the load work, associated with the dislocations overcoming that barrier that leads to the increase of the yield strength of the material. The shear stress required by a dislocation to overcome the coherency-mismatch barrier was calculated to be:

$$\tau_{coh} = 7G\left|\eta_{coh}\right|^{3/2}\left(\frac{R_p f}{b}\right)^{1/2}. \qquad (5)$$

Where *b* is the Burgers' vector and $\frac{R_p f}{b}$ is the precipitate' concentration.

(ii) When a dislocation cuts through a precipitate whose shear modulus differs from that of the matrix another type of strengthening occurs, the *modulus strengthening*. This type of strengthening results from the energy change in the dislocation line tension when the dislocation cuts through the precipitate. Besides, the shearing of the precipitate the dislocation line could bend during the act of shearing, thus, increasing the length of the dislocation line affected by the shear-moduli difference. Keeping in mind that the force, required by a dislocation to shear through a particle with radius *r* is, $F = G_m b^2 \frac{G_p - G_m}{G_m} = G_m b^2 \left|\eta_G\right|$, it could be readily obtained that the shear stress, required by a dislocation to overcome the modulus-mismatch barrier, would be:

$$\tau_{\mathrm{mod}} = \frac{G_m b\left|\eta_G\right|}{L}. \qquad (6)$$

Where: *L* is the effective distance between the precipitate particles, $\eta_G = \frac{G_p - G_m}{G_m}$, and G_p and G_m are the shear modules of the precipitate and the matrix, respectively. By noticing that, $f = \frac{2R_p}{L}$ [8], Eq. 6 could be recast into new variables, R_p, and *f*, $\tau_{\mathrm{mod}} = G_m b\left|\eta_G\right|\frac{f}{2R_p}$. Eq. 6

above oversimplifies the process of modulus hardening. A more appropriate relation that combines the parameters involved reads [9]:

$$\tau_G = 0.01G\left|\eta_G\right|^{3/2}\left(\frac{R_p f}{b}\right)^{1/2}. \quad (7)$$

(iii) Along with the additional glide work, due to the differences in the shear moduli of the matrix and the precipitate an additional work is needed when the dislocation shears through a precipitate. This work is associated with the differences in the surface energies when the dislocation glide plane cuts through the precipitates laying at that plane. As above, the additional work required could be considered as an energy barrier on the dislocation path, thus leading to the increase of the yield strength of the material. This type of strengthening is known as *chemical strengthening*, and the force required to push the vacancy through this stress field equals, $F = \tau_{chem} Lb$. Taking into account that the force required to push the dislocation through a single particle is $F = \pi r \gamma_s$ [9] by replacing it in the preceding expression, $F = \tau_{chem} Lb$, we obtain the following simplified expression for τ_{chem}:

$$\tau_{chem} = \frac{\pi R_p \gamma_s}{bL}. \quad (8)$$

A more precise analysis, however, leads to the following expression:

$$\tau_{chem} = 2G\left(\frac{\gamma_s}{GR_p}\right)^{3/2}\left(\frac{R_p f}{b}\right)^{1/2} = 2G\left|\eta_{chem}\right|^{3/2}\left(\frac{R_p f}{b}\right)^{1/2}. \quad (9)$$

Here, γ_s stays for the particle-matrix interphase surface energy.

(iv) When edge dislocation shears through a precipitate composed of two or more sorts of atoms, that are ordered in a specific way (an ordered structure), a situation, quite similar to the case discussed above, occurs. Indeed, consider a structure of the precipitate composed of two sorts of atoms which are arranged in a sequence A-B-A-B- etc. When a dislocation shears through the precipitate the established order between the precipitate's atoms is breached and the already existing chemical bonds are severed and reordered anew. As a result, the existing A-A, A-B, and B-B bonds across the slip plane are rearranged in new combinations with different energies. The net difference in the energies of the initial and the final bond arrangements requires additional work to be done by the applied load to move the dislocations through the particles. The energy spent, associated with this process (units of Jm^{-2}), is called *antiphase*

boundary energy (APBE), denoted from here on as U_{APBE}, while the resulting strength increase is termed, *order strengthening*. Theoretically the problem is treated similarly to the preceding ones; the force required to move the dislocation through the precipitate (particle) is equated to the force required to overcome the stress barrier, caused by the breaking and reestablishing of the bonds between the different sorts of atoms. The more precise considerations of the problem, accounting for the increase in shear stress, due to order hardening in the early stages of precipitation, and the situation when the dislocations are widely separated, lead to the following expressions for the increased shear stress resulting from the order strengthening [9]:

$\tau_{ord} = 0.7G\left|\eta_{ord}\right|^{3/2}\left(\frac{R_p f}{b}\right)^{1/2}$ (valid for low η_{ord} at early stages of precipitation);

$\tau_{ord} = 0.7G\left|\eta_{ord}\right|^{3/2}\left(\frac{R_p f}{b}\right)^{1/2} - 0.5G\left|\eta_{ord}\right| f$ (valid for high η_{ord} at early stages of precipitation);

$\tau_{ord} = 0.44G\left|\eta_{ord}\right| f^{1/2}$ (valid for low η_{ord} at the late stage of precipitation) and

$\tau_{ord} = 0.44G\left|\eta_{ord}\right| f^{1/2} - 0.405G\left|\eta_{ord}\right| f$ (valid for high η_{ord} at the late stages of precipitation).

Here, η_{ord} denotes the relation, $\eta_{ord} = \frac{U_{APBE}}{Gb}$.

(v) *Strengthening due to short-range effects*: *Dislocations pairing*. (The mechanism is referred to as, the “super-dislocations” mechanism and was proposed by Gleiter and Hornbogen [10,11]). According to these authors, the short-range strengthening effects arise from the differences in the properties (mechanical, chemical, etc.) of the precipitate and the matrix. In reality, the mechanical properties of the precipitate or the physically introduced particulates excel over those of the matrix, thus for a dislocation, it is more difficult to shear the particle than to glide through the matrix. When the preceding condition is fulfilled, the differences, thus mentioned, lead to the formation of dislocation pairs. According to Gleiter-Hornbogen, the process of dislocation-pairs formation occurs in the following way; When a dislocation shears through a precipitate (particle) it experiences a force opposite to the direction of its motion due to the creation of an anti-phase boundary (A.Ph.B.) inside the particle.

When a second dislocation, generated from the same source as the first one, reaches the particle it removes the A.Ph.B., and as a result, it moves practically without experiencing any resistance to its motion. (The energy is gained from restoring the disrupted bonds between the atoms caused by the first dislocation.) The second dislocation would, therefore, move faster than the first one until starting to experience the repelling force by the dislocation that caused the A.Ph.B. In that way, due to the A.Ph.B. forces, these two dislocations are connected in a dislocation pair. According to the mechanism described it follows that the distance between the dislocations in the pair (if these are of a similar type) is obtainable by equating the attraction forces of the A.Ph.B. and the repulsive force between them.

At a particular particle size, the distance between the dislocations of the pair might be less than the particle's diameter, which means that the dislocation pair is running through the same particle at the same time. The two forces acting on the dislocations, the contractive force due to the A.Ph.B. and the repulsive force due to the stress fields of the dislocations would compensate each other in only small segments of their length. In reality, this is the difference between the segments that the particle cuts off from the lines of the dislocations pair. In that way, the pairs can cut through the larger particles at reduced critical resolved shear stress compared to a single dislocation. The reduction of the critical resolved shear stress with the increase of the precipitate (particulate) size means; the increase of the particles' size leads to a decrease of the strengthening effect. That is an argument in favor of using nano-sized instead of micron-sized reinforcement particulates.

The process described allows quantification by taking into account the following processes that contribute to the increase of the shear stress when the dislocation pairs cut through the particles. (a) The volume fraction and the energy of the A.Ph.B. increase with the particle size as $\Delta\tau_1 \cong \gamma_s^{3/2} f^{1/3}$; (b) With increasing inter-particles distance (R_p and f are kept constant) the dislocations are free to bow out more and more into the inter-particle space under the applied external shear stress. In the process, they come in contact with more and more particles. After the penetration of these, APhBs are generated, thus leading to an increase of the resistance to the dislocations' motion. (c) The formation of the dislocation pairs decreases $\Delta\tau$ with the increase of the particles' size by the mechanism described above. Based on the preceding assumptions (a-c) Gleiter and Hornbogen obtained the following equation:

$$\Delta\tau_{crss} = \frac{0.28\gamma_s^{3/2} f^{1/3}}{b^{3/2}} \left(\frac{R_p}{Gb}\right)^{1/2}, \quad (11)$$

that allows evaluating the increase in the critical shear stress for small particles.

(vi) *Shearaing of disordered precipitates (particulates)*. Subsections (iv) and (v) dealt with the shearing of precipitates (particulates) the atom's structure of which is arranged in a specific ordered way. The shearing of disordered particles by a dislocation occurs by the formation of ledges on the particle's surface, thus, resulting in shifts equal to the Burgers vector at the places of entry and the exit of the dislocation. For the specific cases of particles that have similar crystal structures with the matrix (sufficiently good coherency, $\eta_{coh} \to 0$), it can be shown [12] that the shear strengthening generated by the shearing of a disordered precipitate is:

$$\Delta\tau_{drdr-ch} = \frac{3\overline{g}\left(b_p - b_m\right)}{\overline{b}} \frac{R_p}{d}, \quad (12)$$

where $\overline{g}$ is the average shear modulus, b_p and b_m are the Burgers vectors of the dislocation into the particle and the matrix, $\overline{b}$ is the average Burgers vector, and d is the distance passed by the dislocation along with the particle.

(vii) *Strengthening due to long-range effects*. The long-range strengthening effects of the particulates (precipitates) embedded in a metal matrix are characterized with: (a) they are independent of the particle-dislocation distance and (b) they are usually caused by a long-range stress field, generated by a difference in the specific volumes of the particle and the matrix. In this case, the lattice mismatch between the matrix and the reinforcement particle is significant ($\eta_{coh} \neq 0$), and the overall strengthening generated equals the stress required to move the dislocations through the stress/strain fields at the particle-matrix boundaries. The shear strengthening is then given by the equation [13-15]:

$$\Delta\tau_{long-range} \cong 3\left(\frac{\varepsilon_{nch} E}{1+\nu}\right)^{3/2} \left(\frac{bR_p}{T}\right)^{1/2} f^{5/6}. \quad (13)$$

Where: ε_{nch} is the misfit strain equal to, $\varepsilon_{nch} = \dfrac{3K\eta_{coh}}{3K+4G}$, T is the line energy of the dislocation (see Ch. II-3), and the other parameters have their usual meanings.

Eq. 13 may be used generally in strengthening due to any type of misfit strain in which case ε_{nch} represents the misfit strains corresponding to the mean expansion mismatch.

The equations above are valid for edge dislocations, the similar calculations carried out for screw dislocations showed that the force to push a screw dislocation through the same stress field would be about seven times smaller than that required to push an edge dislocation. Therefore, it follows that the screw dislocations in alloys containing particles are much more mobile than edge dislocations, respectively, the expected strengthening effect contributed by that type of dislocations would be approximately an order of magnitude smaller.

(viii) *The effect of the coarsening on the strengthening*. Concluding this section, dedicated to the strengthening induced by deformable particles, it should be noted that at a certain f and R_p the shearing mechanism stops being energetically effective any longer. The explanation is that the coarsening process, which as a rule takes place after the end of the precipitation (see Section 4.1.4 and Fig. II-4-5 in Section 1.2.3 above). At this stage, after precipitation is complete, the particle size continues to increase due to the particles' coarsening while f is fixed. As a result, the distance between these (now larger) particles becomes larger. At a certain particle separation, for the dislocations will be more energetically favorable to bow between the particles, rather than cutting them; the bowing in those conditions is more energy cost-effective even in comparison to the dislocation-pair formation mechanism of Hornbogen and Gleiter. Typical particle sizes at which this transition occurs are in the range of tens of nanometers (see below).

4.4 Non-deformable precipitates: The bowing (looping) mechanism

The second mechanism, by which a dislocation could overcome an obstacle is by bowing around it (this mechanism was proposed by Orowan [16-18] and is frequently referred to as Orowan's mechanism or Orowan's bowing). According to Orowan, when a linear dislocation encounters an obstacle(s) it deforms and protrudes through the inter-particle spaces between the obstacles, and eventually, by making a loop around the obstacle, it restores its linear form and proceeds further on. (Recall, that the linear form is most energetically favorable.) The process is illustrated in Fig. II-4-2.

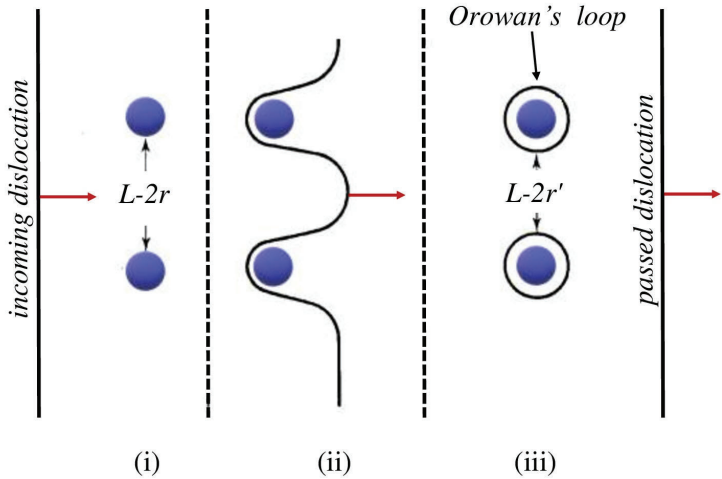

Figure II-4-2. A view of a slip plane of a dislocation approaching a pair of non-deformable particles (i). The dislocation bows around the particles (ii). The stress required to effectively bypassing of the obstacles is inversely proportional to the interparticle spacing *(L - 2r),* where, *r* is the slip plane particle radii. Dislocation loops encircle the particles after the bypass operation (iii). The subsequent dislocations would have to be pushed between the loops. Thus, the effective particle spacing for the second dislocation is reduced to *(L - 2r'),* and the bypassing stress for this dislocation will be greater than for the first one.

The dislocation bowing, however, could occur only in the cases when the following limitations are fulfilled: (i) the spacing between the particles should exceed a certain length, (ii) when the shearing mechanisms, discussed in the preceding section, do not apply. In other words, the particle is "hard" enough that bowing, rather than cutting, is the preferred slip mechanism, and (iii) the particle size should be above some critical value, beyond which it is energetically favorable for the incoming dislocation to bow around the particle, rather cutting through it. Remember, that bowing around an obstacle is also an energy-consuming process.

4.5 The interactions of the dislocations with non-deformable obstacles

Consider a moving dislocation in a medium that contains an array of obstacles of a different kind, e.g., solutes/interstitials, vacancies, artificial particles or precipitates, etc. If the conditions (i-iii) above are applicable then the dislocation by encountering such an array of obstacles, would bow and eventually would form loops around them. According to Nabarro [19], two kinds of obstacles could be distinguished depending on the way of interaction between the obstacle and the dislocation: (i) *Localized obstacles* (illustrated in Fig. II-4-3). Localized obstacles are those that interact with the dislocations only when they are in direct physical contact with each other [12], (ii) *Diffuse obstacles*. Diffuse obstacles are those that interact with the dislocations at a distance (e.g., via some energy field formed around the particle, as illustrated in Fig. II-4-4). These are characterized by an interaction range, ω, and interaction energy, U_{diff}. When $U_{diff} > 0$ the diffuse obstacles are repulsive and at $U_{diff} < 0$ they are attractive [20]. Common for both types of obstacle-dislocation interaction is the way by which they overcome the obstacle. Initially, when the dislocation bows out around the obstacle it sustains a gradual mounting of the resistance directed opposite to the direction of its motion, which is due to the increase in the dislocation length. After that, however, when some critical length of the bow is reached, the dislocation breaks free and moves until it encounters a new obstacle. Ashby and Jones gave in their book [21] a very illustrative explanation of the process described above:

> "It is like blowing up a balloon in a birdcage: a very large pressure is needed to bulge the balloon between the bars, though once a large enough bulge is formed, it can easily expand further."

Localized Obstacles

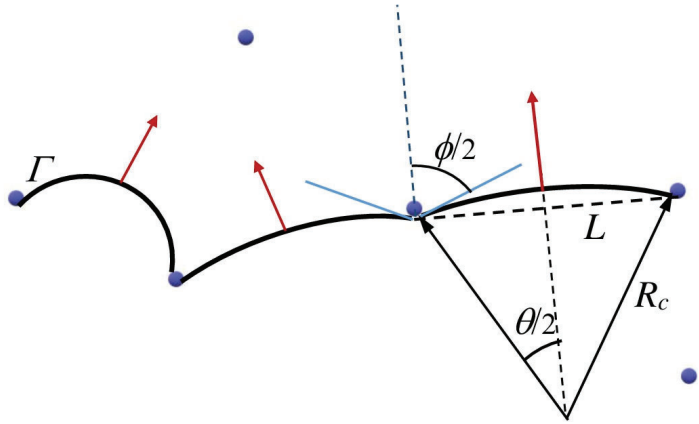

Figure II-4-3 Illustration of the interaction mechanism between a dislocation and localized obstacles.

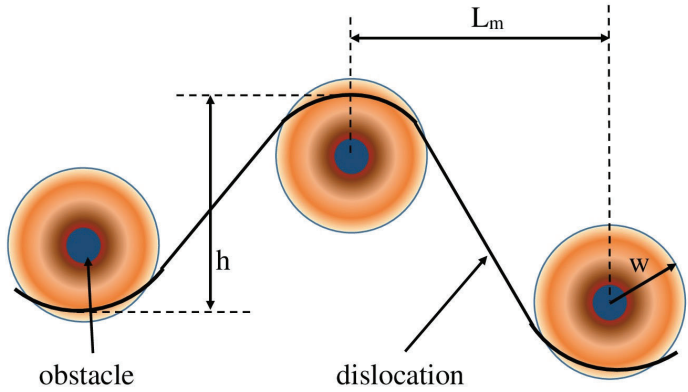

Figure II-4-4 Illustration of the interaction mechanism between dislocation and diffuse obstacles. The colored halos around the particles indicate the stress-energy field.

The critical length of the dislocation bow (see Fig. II-4-3) is determined by the angle, say ϕ, between the tangents to the dislocation line drawn at both sides of the obstacle. As seen from Fig. II-4-3 that angle

varies within the range limit, $0 < \phi < 180^{o}$, and its value is used as a measure of the strength of the obstacle; weak obstacles have ϕ close to 180^{o}, while the strong obstacles have $\phi \sim 0^{o}$.

In the practice, however, instead of ϕ is used the half of the angle subtended between two adjacent obstacles, $\theta/2$, as shown in Fig. II-4-3. Notice that, $\phi = \pi - \theta$. It could be shown that the angle θ is directly related to the critical stress, τ_{crit}, required by the dislocation to break free of the obstacle [22]. For localized obstacles, the following relation was found between, τ_{crit}, the effective obstacle spacing L, and a parameter β_c, defined as, $\beta_c = \sin\left(\frac{\theta_{crit}}{2}\right)$:

$$\tau_{crit} = \frac{2T}{bL}\sin\left(\frac{\theta_{crit}}{2}\right) = \frac{2T}{bL}\beta_c . \quad (14)$$

The equation above does not take into account how L depends upon the applied stress. It was found that this dependency is, $L = \frac{L_s}{\beta_c^{1/2}}$, thence, the expression above transforms to:

$$\tau_{crit} = \frac{2T}{bL_s}\beta_c^{3/2} . \quad (15)$$

Here L_s is the center-to-center distance between the obstacles.

A more accurate evaluation of the relation between L and L_s, based on experimental results and numerical modeling, that is valid within nearly all range of β_c, however, shows that the critical stress, τ_{crit}, required by a dislocation to break free of an obstacle is [23,24]:

$$\tau_{crit} = \frac{1.93T}{bL_s}\beta_c^{3/2}\left(1 - \frac{\beta_c^2}{8}\right) . \quad (16)$$

Similarly, the critical stress, τ_{crit}, for diffuse obstacles, i.e. the counterpart of the equation above, was determined by [20] to be equal to:

$$\tau_{crit} = \frac{2T\omega^{1/3}}{bL_s^{4/3}}\beta_c^{4/3} . \quad (17)$$

Below, to account for the strengthening, a different approach from that in Eqs 15 to 17 will be followed; a modified version based on Orwan's original equation will be developed, which takes into account some later

results concerning the strengthening due to the bowing of the dislocations around the obstacles.

Historically, it was Orowan who first attempted to evaluate τ_{crit} [16,25]. In his approach he used as a starting point Eq. 14 in which he replaced the line tension force by Gb^2, thus, obtaining a relation combining τ_{crit}, L_s, β_c, and the Burgers vector, b:

$$\tau_{crit} = \frac{Gb}{L_s}\beta_c . \tag{18}$$

In his original theory, Orowan assumed $\beta_c \approx 1$ (strong obstacles), thence, the original Orowan's formula reads:

$$\tau_{crit} = \frac{Gb}{L} . \tag{18a}$$

Since the publication of Orowan's theory, many researchers have confirmed its significance and, by making several additions and improvements, have considerably expanded its applicability (for instance Eqs 15 to 17 above).

One of the first modifications of Orowan's version of the theory was the accounting of the fact that the actual distance between the obstacles is not L_s but $L_s - 2R_p$ (see Fig. II-4-2). Thence:

$$\tau_{crit} = \frac{Gb}{L_s - 2R_p} . \tag{19}$$

As above Eq. 19 does not account for the increase in the length of the dislocation during overcoming the obstacle. By taking into account this circumstance, for a dislocation bowing between two pinning obstacles, it was found that the critical stress, τ_{crit}, should obey the following relation:

$$\tau_{crit} = A(\theta)\frac{Gb}{2\pi\left(L - 2R_p\right)}\ln\left(\frac{L - 2R_p}{R_p} + B(\theta)\right), \tag{20}$$

where, $A(\theta)$ and $B(\theta)$ are some functions of θ, and θ is the angle between the dislocation line and the Burgers vector. Weeks et al. [26] simplified the expression above showing that at the initial stage of the bowing the function $A(\theta) = 1$ for an edge dislocation and $A(\theta) = \frac{1}{1-\nu}$,

for a screw dislocation segment, and that, $B(\theta)=0$. Thence, for this special case, the equation above reduces to:

$$\tau_{crit} = A(\theta)\frac{Gb}{2\pi\left(L-2R_p\right)}\ln\left(\frac{L-2R_p}{R_p}\right). \qquad (21)$$

The averaged values of $A(\theta)$ and $B(\theta)$ have been calculated for different combinations of the dislocations types and different values of θ. The interested reader could find details about the conditions used and the methods applied in the original papers of Foreman [27] and Brown and Ham [28].

Notice the crucial difference between the original Orowan equation, Eq. 19, and Eq. 21. At $2R_p \to 0$, the shear stress evaluated by Eq. 19 tends to, $\tau_{crit} \to \frac{Gb}{L}$, while at $2R_p \to L$ it tends to infinity, $\tau_{crit} \to \infty$, results that contradicted the experimental findings. On the contrary, Eq. 21 predicts that at $2R_p \to 0$, the shear stress is, $\tau_{crit} \to 0$, while at $2R_p \to L$ it tends to, $\tau_{crit} \to \infty$, which is in agreement with the experiment (pushing a dislocation between two obstacles which are in contact with each other would require infinitely large force, recall the cited above analogy, used by Ashby and Jones [21], to explain Orowan's bowing mechanism).

Further improvement of Orowan's equation was made by Melander [29] who obtained the following equation:

$$\tau_{crit} = \frac{0.84Gb}{2\pi\left(1-\nu\right)^{1/2}}\frac{\ln\left(\Lambda/r_0\right)}{L_s-2\langle r_s\rangle}. \qquad (22)$$

Where: $\langle r_s \rangle$ is the mean radius of a circular cross-section in a random plane for a spherical reinforcement particle with mean radius $\langle r_s \rangle$, L_s in Melander's version represents not the distance between the particles but the distance between obstacles on the glide plane (the obstacles could be also segments of the particles cut by the glide plane), Λ and r_0 are outer and inner cutoff distances used to calculate the line energy of a dislocation. Following Melander, from here on will be taken into account the fact that the radii of the reinforcement particulates are not equal, but

distributed around some average value. Thence, in the theory henceforth instead of R_p will be used the more correct denotation, $\langle r_p \rangle$. (Remember that in mathematics the angle brackets are used to denote the average value of a variable.) In a review paper [22], Ardell made a further improvement in Orowan's theory by calculating the functional dependencies between, $\langle r_p \rangle$, $\langle r_s \rangle$, f and L_s:

$$L_s = \left(\frac{32}{3\pi f} \right)^{1/2} \langle r_s \rangle = \left(\frac{2\pi}{3f} \right)^{1/2} \langle r_p \rangle . \tag{23}$$

Thence according to Ardell:

$$\langle r_s \rangle = \frac{\pi}{4} \langle r_p \rangle , \tag{23a}$$

or with a good approximation it can be accepted:

$$\langle r_s \rangle \approx \langle r_p \rangle . \tag{23b}$$

By substituting Eq. 23 into Mellander's version of the Orowan equation it is obtained:

$$\tau_{crit}(f) = \frac{0.84Gb \ln(\Lambda/r_0)}{2\pi(1-\nu)^{1/2} \langle r_p \rangle} \frac{1}{\left(\frac{2\pi}{3f} \right)^{1/2} - 2} = \frac{0.134Gb \ln(\Lambda/r_0)}{(1-\nu)^{1/2} \langle r_p \rangle} \frac{1}{2.094 f^{-1/2} - 2} . \tag{24}$$

In an unjustly forgotten paper, Fisher, Hart, and Pry (FHP) [30] were first to point out that the number of the loops around a single particle could exceed one and that the stress exerted by those loops in the matrix serves as a brake to the dislocation mobility [30,31]. Their hypothesis was later confirmed by the experimental works of Hirsch, Humphreys, and Hazzledine [32,33].

The additional strengthening in the case of multiple loops around the obstacle, therefore, should be a result of two factors, not considered in the theories discussed up to here: (i) The reduction of the effective distance between the particles after every dislocation loop is formed (not to be confused with the geometric distance between the particles), (ii) The interaction of the incoming dislocations with the loops already formed around the reinforcement particles; any subsequent dislocation coming in

the vicinity of the obstacle (precipitate, particle, etc.) will require a stronger force to overcome the steadily mounting resistance caused by the dislocation loops which were left by the dislocations that have already overcome the obstacle [30, 31, 34]. Thence, after every act of dislocation bowing, the stress in the matrix around the reinforcement particles will increase. Fisher, Hart, and Pry evaluated the increase in the stress around the particle that results from the increment of the number of loops formed. Using an analogy between the magnetic field and the stress field generated by the loops around the obstacles, they showed that the increment of the resolved shear stress, due to the loops, should be proportional to:

$$\Delta\tau_{FHP} \cong \sigma_{cr}^{m} f^{3/2}. \tag{25}$$

Where: σ_{cr}^{m} is a proportionality term. By Anestiev in (Anestiev et al, 2021) and in Ch. II-6 of this part of the book is shown that σ_{cr}^{m} could be associated with the stress relieved by the formation of cracks in the matrix. Thence, Eq. 25 could be used to account for the absorption of the accumulated stress-energy in the matrix of the composite.

By assuming the FHP theory for the multiplicity of the loops formed around an obstacle correct, the Melander and Ardell version of Orowan's equation (MAO) could be further improved:

$$\Delta\tau\left(f\right) = \frac{0.134NGb\ln\left(\Lambda/r_0\right)}{\left(1-\nu\right)^{1/2}\left\langle r_p\right\rangle}\frac{1}{2.094f^{-1/2}-2}. \tag{26}$$

Here, N stays for the number of dislocation loops formed around the reinforcement particles.

Recall, that by dividing $\Delta\tau$ above on the Schmidt factor, m, we could estimate the increase in the yield strength of the matrix, achieved by precipitation or adding particulates in it.

The change in the mechanism by which the dislocations overcome the obstacles obviously should reflect, in some way, on the strengthening achieved. Therefore, it is worth discussing the influence of the reinforcing particle size on the composite's strengthening. The overview of the theories in the preceding and the present sections follows that some critical value of the reinforcement's radius $\left\langle r_p\right\rangle_{crit}$ exists at which both mechanisms of strengthening, shearing, and bowing transit from one into the other.

4.6 The strengthening mechanism selection

The research carried out until now showed that the selection mechanism between the shearing and bowing mechanisms, by which a dislocation overcomes an obstacle (when the composite is loaded), depends largely on the size of the reinforcement. Additionally, it could depend on the matrix-obstacle (precipitate) boundary coherence, the volume fraction (VF) of the reinforcement, and the spatial distribution of the obstacles (i.e., is there an agglomeration(s) of particles in the body of the composite or not). The critical radius of the obstacle at which the transition from shearing to bowing mechanism occurs could be determined by equating the stresses that govern both mechanisms (i.e., all of the outstanding parameters except the radius are kept constant). The transition, therefore, would occur when the difference between the shearing $\Delta\tau_{shearing}$ and the Orowan's $\Delta\tau_{Orowan}$ stresses, $\Delta\tau$, is equal to zero, i.e., $\Delta\tau = \Delta\tau_{shearing} - \Delta\tau_{Orowan} = 0$. In the case when several shearing mechanisms are operative (see Section 3 of this chapter) the shearing is controlled by the one with minimal $\Delta\tau_{shearing}$. For illustration purposes, let assume that the order strengthening mechanism (valid for low η_{ord} at early stages of precipitation) is controlling the shearing process. Recall that the resolving shear stress for that mechanism is, $\tau_{ord} = 0.7G\left|\eta_{ord}\right|^{3/2}\left(\frac{R_p f}{b}\right)^{1/2}$. By taking the preceding into account, after equating τ_{ord} with Eq. 22,

$$\tau_{Orowan} = \frac{0.84Gb}{2\pi\left(1-\nu\right)^{1/2}}\frac{\ln\left(\Lambda/r_0\right)}{L_s - 2\left\langle r_p\right\rangle}, \text{ for } \Delta\tau = \Delta\tau_{shearing} - \Delta\tau_{Orowan} = 0$$

is obtained:

$$\left(L_s - 2\left\langle r_p\right\rangle\right)\left\langle r_p\right\rangle^{1/2} = \frac{b^{3/2}\ln\left(\Lambda/r_0\right)}{2\pi\left(1-\nu\right)^{1/2}\left|\eta_{ord}\right|^{3/2} f^{1/2}}, \qquad (27)$$

i.e., a cubic algebraic equation with $\left\langle r_p\right\rangle$ as unknown.

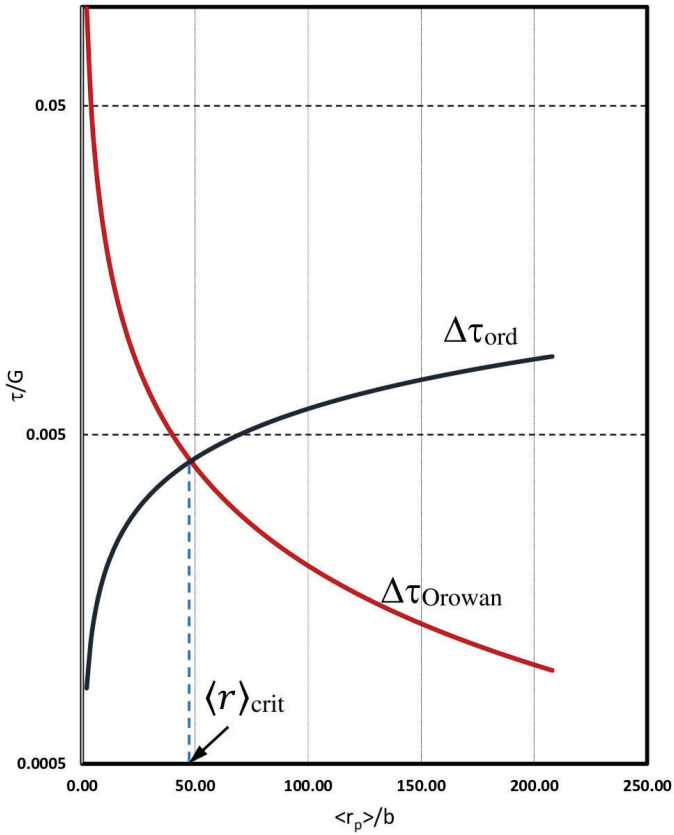

Figure II-4-5 Plots of the right and the left sides of Eq. 27 in τ / G *vs.* $\langle r_p \rangle / b$ coordinates, showing the competition between cutting and bowing mechanisms. The calculations were carried out for; $|\eta_{ord}| << 1$ (fully incoherent lattices of the matrix and reinforcement) and VF, f = 0.1.

However, by making use of Ardell's relation between L_s and $\langle r_p \rangle$ (see Eq. 23) the Eq. 27 reduces to a simple algebraic relation which could be readily solved, thus, yielding for $\langle r_p \rangle_{crit}$:

$$\left\langle r_p \right\rangle_{crit} = \frac{b\left[\ln\left(\Lambda/r_0\right)\right]^{2/3}}{5.41\left(1-\nu\right)^{1/3}\left|\eta_{ord}\right|\left(0.84-f^{1/2}\right)^{2/3}}. \qquad (28)$$

The analysis of the results plotted in Fig. II-4-5 shows that maximal strength is achieved at $\left\langle r_p \right\rangle_{crit} \approx 48b$. The evaluations carried out by some authors showed that for most of the precipitates (particulates) encountered in the reality the value of, $\left\langle r_p \right\rangle_{crit}$, is around 20-40 nm which correlates favorably with the result obtained by using Eq. 28. The increase or the reduction of some of the parameters at the right-hand side of the equation, or L_s, would, thus, lead to a shift of the $\left\langle r_p \right\rangle_{crit}$ to left or right along the *r*-axis. Thence, by varying VF and the radii of the reinforcement particles, a limited potential exists to optimize the mechanical strength of the composite.

4.7 The Hall-Petch strengthening mechanism

Thus far, the mechanical properties of crystalline metals have been discussed by taking into account only the interaction of the defects of the crystal lattice, particulates embedded in the matrix, dissolved chemical elements, etc., with the migrating dislocations. In reality, however, the metals (alloys) are comprised of many grains (see Section 2.2.4 and Fig. II-2-5 in Ch. II-2). That is why, the mechanical properties of these materials, such as yield strength and ductility (i.e., elongation to fracture) should also be strongly dependent on the grains microstructure. Once again, the influence of the grain structure could be rationalized by considering; how a moving dislocation interacts with such obstacles as the grain walls (boundaries). As repeatedly discussed, the strength of a metal (alloy) is related to the ease, or conversely the difficulty, in the dislocation movements. If the dislocation migrations are unrestricted (i.e., dislocation migration is easily initiated and continued without hindrance), the strength will be low, and relatively little strengthening in the material will occur. Conversely, the presence of obstacles, or barriers, within the microstructure hinders the dislocation migrations, due to the dislocation-dislocation, and/or dislocation-obstacles interaction, and eventually leads to an increase in the material's strength. Together with the obstacles discussed so far, the grain boundaries also serve as obstacles to the

dislocation's motion. It could thus be assumed that; when the moving dislocations encounter a grain boundary they will pile up as described in Section 3.7.3 of Ch. II-3. The concept of the dislocations pile-up was adopted by Hall and Petch in the development of their celebrated theory, which binds together the yield strength of a polycrystalline material with the grain size of the latter. In their analysis, Hall and Petch (HP) assumed that the dislocations are generated by a source that is located in the grain center (grain's diameter D). Under the applied load the as-generated dislocations move along their slip plane until encountering the grain walls which, as discussed above, serve as obstacles to their movement. The restrictions in the dislocation's mobility would lead to their pile-up along the grain walls. The pile-up of the dislocations with equal signs along a single slip plane has been studied by Eshelby, Frank, and Nabarro [34]. The number of such dislocations in the pile-up, according to these authors, is given by the relation:

$$N_d = \frac{k\pi\tau D}{4Gb}, \tag{29}$$

where: τ is the average resolved shear stress in the slip plane, k is a factor varying with the type of the dislocation, $k = \left.\begin{cases} 1-\nu & for\ edge \\ \cong 1 & for\ screw \end{cases}\right\} dislocation$, and the rest of the parameters have their usual meaning.

The number of dislocations in the pile-up, which could be supported by an obstacle, depends on the type of the barrier, the orientation of the slip plane toward the structural features at the barrier, the material, and the temperature. Breakdown through a barrier could occur by a slip on a new glide plane, by a climb of the dislocations around the obstacle, or by the generation of very high tensile stresses which would produce cracks in the material (see Sections 3.5 and 2.8). Hall and Petch's equation that relates the dependence of yield stress with the grain size can be readily worked out by employing the concepts discussed above: (i) the yielding occurs when a critical shear stress τ_c, is reached at the head of the pile-up, and (ii) the critical shear stress is independent of the grain size. Thence, from Eq. 29 one gets:

$$\tau_c = N_d\tau = \frac{(1-\nu)\pi\tau^2 D}{4Gb}\ . \tag{30}$$

In their analysis, HP assumed that the resolved shear stress should be equal to the applied stress, which in terms of tensile yield strength is σ_Y,

minus the average internal stress required to overcome the resistance to the dislocation migration, σ_i. Keeping in mind that the shear stresses could be converted to uniaxial tensile stresses, e.g., $\tau_c = \frac{\sigma_c}{2}$, the Eq. 30 transforms to:

$$\sigma_c = \frac{\pi(1-\nu)(\sigma_Y - \sigma_i)^2 D}{8Gb} \quad , \tag{31}$$

which, when solved to σ_0, reduces to the Hall-Petch equation [35, 36]:

$$\sigma_Y = \sigma_i + \sqrt{\frac{8Gb\sigma_c}{\pi(1-\nu)}\frac{1}{D}} = \sigma_i + K_{HP}D^{-1/2} \quad . \tag{32}$$

The proportionality factor, $K_{HP} = \sqrt{\frac{8Gb\sigma_c}{\pi(1-\nu)}}$, evidently depends on the material's properties, thence, together with the grain size D it also could contribute to some extent to the increasing of the material's strength (for instance, by selecting materials with higher shear modulus).

The equation above shows that the yield strength σ_Y of the metal would increase when the grain size is decreased. At smaller grain sizes, there is a larger probability of dislocation-dislocation interactions (dislocation "pile-up" at the grain boundaries), leading to a larger resistance to the dislocation mobility. As the grain size increases, the opposition to the dislocation mobility, due to back stresses associated with dislocation tangles at grain boundaries lessens, because of the larger distances between grain boundaries. Therefore, the lower strength of a large-grained metal when compared to a small-grained metal can be rationalized by a decrease in the resistance to the dislocation mobility.

4.8 Other types of strengthening mechanisms

In addition to the mechanisms discussed above, there exist others, which strengthening effect is also due to the impediment of the dislocations' migration. These relevant to the topics studied in the present part of this book are given a short overview below.

4.8.1 Solid solution strengthening

The solid solution strengthening occurs when in the matrix lattice are embedded foreign atoms. The types of microstructures, which include the presence of foreign atoms, are typical to the solid solutions, hence, the definition "solid solution strengthening". Historically this is one of the oldest methods of increasing the metals' strength, e.g., the alloying of Cu with Sn (bronzes) or Zn (brasses). Depending on the sizes of the dissolved atoms, in comparison with those of the matrix, the foreign atoms may be integrated into the matrix lattice, i.e., forming a substitutional solution, or they could be located in the interstitial sites of the matrix lattice. The rules governing the formation of solid solutions were first formulated by Hume–Rothery (H-R) [37]. The H-R rules state that stable solid solutions form preferably between atoms with similar radii, valence, electronegativity, and type of chemical bonding.

Since the dissolved atoms interact differently with the matrix atoms surrounding them and as a rule, their ionic radii differ from that of the atoms of the matrix; the energy fields formed around the solute atoms differ from those of the surrounding lattice. When a moving dislocation glides in a plane with embedded "foreign" atoms it interacts with the energy fields of these atoms. The overall effect of that interaction is a restriction of the dislocation migration. Thence, an additional driving force should be applied to the dislocations to enable them in overcoming these energy fields. These additional driving forces are induced by the stresses which are generated into the matrix at the loading of the material. Therefore, to keep dislocations moving further in the material, i.e., to overcome the resistance of the energy fields in question, the applied load should be steadily increased. That increased load, which is experimentally registered at the testing of the material, is a measure of the increased strength of the material and is termed - *solid solution strengthening*.

The dislocation-solute atom interaction is elastic by nature and is a synergy between two factors: (i) the size of the solute atoms (actually the ions of the solute) and (ii) the increase/decrease of the shear modulus of the alloy as a function of the solute concentration, $\varepsilon_G = \frac{1}{G}\frac{\partial G}{\partial C}$. (Recall, that the self-energy of the dislocation is proportional to the shear modulus.)

Depending on the distortion, caused by the solute atom, the ion-size effect on the induced stress field is twofold; (i) spherical dilation in the surrounding matrix, all displacements are equal (all positive, or all negative, i.e., the geometry of the distortion is a sphere), or (ii) tetragonal

distortions, some of the displacements are positive, while others are negative (the geometry of the distortion resembles an ellipsoid).

The effect of the solute on the shear modulus is also twofold. The substitutional atoms could contribute to the interaction force dislocation-solute atom by (i) increasing the attraction force between the dislocation and the dissolved atoms, which would lead to a reduction of the resistance opposing the dislocation motion, aka "*softening*" of the matrix, or (ii) increasing the repulsive forces between the dislocation and the solute atoms, i.e., to "*strengthening*" of the matrix.

Once the mechanism, leading to the strengthening of the material, has been clarified, it is possible to give a quantitative description of the solid solution strengthening [9]. Recall, that the yielding of the material occurs when the force applied to the dislocations, $\tau bL = f_Y$ exceeds the resistance force that opposes their motion. Here L is the effective obstacle spacing. It is apparent, that the resistance force should depend on the type of obstacle; the estimates showed that for hard obstacles with spherical symmetry, f_r is on the order of $f_r = Gb^2$, while for hard obstacles causing tetragonal distortions it varies between, $f_r \approx \frac{Gb^2}{5}$ and $f_r \approx \frac{Gb^2}{10}$. In contrast, f_r, for soft obstacles with spherically symmetric distortions, which is the case with most substitutional solutes, is $f_r \approx \frac{Gb^2}{120}$. The effective spacing, L, is also related to the obstacle strength. For tetragonal distortions, the mean free path between the solute atoms, associated with the slip plane, is $L \approx \frac{b}{2C}$, while for the "soft" obstacles it is much greater, $L \approx \frac{b}{\left[C\left(\pi - \phi\right)\right]^{1/2}}$, where C is the solute concentration and ϕ is the angle between the tangents to the dislocation line drawn at both sides of the obstacle (see Fig. II-4-3 in Section 4.4, Ch. 4). In the case here, $\pi - \phi$, is on the order of 1°.

Taking into account the preceding, for tetragonal defects (hard obstacles) the solid solution strengthening is given as:

$$\tau_{ss} = k_{ss} G C^{1/2}, \tag{33}$$

where: k_{ss} is a proportionality strengthening constant, specific for each solid solution.

Similar estimates, valid for the flow stress induced by spherical distortions, showed that in this case, the strengthening effect will be much smaller, but yet proportional to $C^{1/2}$:

$$\tau_{ss} = \frac{G\varepsilon_s^{3/2} C^{1/2}}{700}, \tag{34}$$

where: $\varepsilon_s = \left| \frac{\frac{\partial G}{\partial C}}{G + \frac{1}{2}\left|\frac{\partial G}{\partial C}\right|} - \delta \frac{1}{a}\frac{\partial G}{\partial C} \right|$ and δ is a parameter.

Summing up the results above it could be stated that the scale of solid solution strengthening depends on the solute-solvent ion size mismatch and is a function of (i) the essential characteristics of the foreign atom (interstitial or solute), (ii) the surrounding stress field that it induces inside the matrix and (iii) of the interaction between the stress fields of the solute atom and the dislocation. The predictions of Eqs 33 and 34 provide a useful approximation of the solid solution strengthening in materials. In some solid solutions, however, $\tau_{ss} \cong C^n$ rather to $C^{1/2}$, where $\frac{1}{3} < n < 1$, which suggests that not all of the possible mechanisms, that govern the solute strengthening, are accounted for in the theory discussed above. Yet, one should keep in mind that many of the mechanisms causing the solute strengthening are difficult to be quantified accurately.

4.8.2 Dislocation strengthening

This type of strengthening is a result of dislocation-dislocation interactions (see Section 3.7.2, Ch. II-3). These may be interactions between individual dislocations or dislocation tangles that also could impede the dislocation motion. The estimates of the dislocation strengthening are obtained by evaluating the effects of the overall dislocation density, ρ_{disl}. The average separation, $\overline{l}$, between the dislocations is related to the density as:

$$\overline{l} = \rho_{disl}^{-1/2}. \tag{35}$$

Recalling that the shear strengthening, $\Delta\tau_{G-disl}$, with pinned dislocation segments is proportional to, $\frac{Gb}{\bar{l}}$, for the shear strengthening due to dislocation interactions is valid:

$$\Delta\tau_{G-disl} = k_{G-disl} Gb\rho_{disl}^{1/2} \quad (36a), \text{ or } \Delta\sigma_{G-disl} = \frac{k_{G-disl} Gb\rho_{disl}^{1/2}}{m} \quad (36b),$$

where k_{G-disl} is a proportionality constant and *m* is the Schmidt factor (see Section 2.6, Ch. II-2). Some restrictions apply to the application of the above equations. The interested reader could find these in, e.g., Courtney [9].

4.9 Work – strengthening

The crystal's yielding is associated with the dislocation migration along certain slip planes (however, there could be several slip planes in a single type of crystal along which the dislocation could move, see e.g. Ashby and Jones [21]). It is understandable that when the dislocations move along these intersecting planes they are interacting with each other, see Section 3.7.2, thus obstructing each other in their movement. As a result, these dislocations are accumulated in the material, eventually leading to an increase in the material's strength. The result is known as *work-strengthening* (or *work-hardening*). The work-strengthening is readily distinguished on the stress-strain curve, immediately after yield point, by the steep increase of the stress with the strain increase, see Fig. II-4-10 in Chapter 2. All metals and ceramics do work-strengthen when loaded above the yield point, thus, the work-strengthening could be considered a useful and powerful strengthening method, which could be combined with the other methods above to produce much stronger materials.

4.10 The coefficients of thermal expansion mismatch strengthening

This type of strengthening is limited to composites in which particulates or wires, with thermo-mechanical properties different from that of the matrix, are used as reinforcement. In essence, the coefficients of thermal expansion (CTE) mismatch strengthening mechanism in composites presumes that; during heating or cooling, due to the differences in the

thermal expansion coefficients of the reinforcement and the matrix in the latter are induced thermal deformations, which are balanced by the generation of dislocations around the reinforcement particles. When the composite is loaded these stationary dislocations obstruct the movement of those generated by the loading, thus leading to a strengthening of the composite. Notice, that according to that theory, the strengthening of the composite should take place only when the CTE mismatch $\Delta\alpha$, i.e., the difference between the thermal expansion coefficients of the matrix α_{mrx} and the reinforcement α_{ref} is positive, $\Delta\alpha = \alpha_{mrx} - \alpha_{ref} > 0$. According to the theory, see e.g. [38, 39], in that specific case the dislocation density around a reinforcement particle, ρ_{CTE}, should be, $\rho_{CTE} = \frac{6\Delta\alpha\Delta Tf}{b\langle r_p \rangle(1-f)}$ [m^{-2}], where, ΔT is the temperature difference (remember that $\langle r_p \rangle$ is the mean radius of the reinforcement). For $\Delta\alpha \approx 10^{-6}$ K^{-1}, $\langle r_p \rangle = 50$ nm, and ΔT=500 K an evaluation of ρ_{CTE}, with the above dependence, yields ρ_{CTE}~60 dislocations per μm^{-2}. The result obtained suggests that a dense tangle of dislocations should be visible around the reinforcement particles, similar to those observed on the TEM micrographs of specimens subjected to tensile loading. The study of specimens obtained by hot extrusion, however, doesn't show such high dislocation density around the reinforcement particles. On the contrary, not a single dislocation is visible around them as seen from the TEM micrographs shown in Fig. II-4-6a. For comparison in Fig. II-4-6b is shown the microstructure of the same specimen but after a tensile loading. The difference between these two micrographs is noticeable; the well-developed dislocation tangle around the reinforcement particles in Fig. II-4-6b (seen at the upper left corner) and the total lack of dislocations in Fig. II-4-6a.

To test that this is not some specific case where all dislocation's planes are parallel to the *e*-beam (see Section 3.9.2), thus, not diffracting, the specimen in Fig. II-4-6a was tilted (inclined) at 8° in both directions, but the images obtained did not differ significantly from that already obtained. This result was also confirmed by switching from bright to dark field mode. Therefore, the only option left was to conclude that the CTE mismatch effect is missing or is so weak that it fails to produce sufficiently high dislocation density which could be detected on the TEM image.

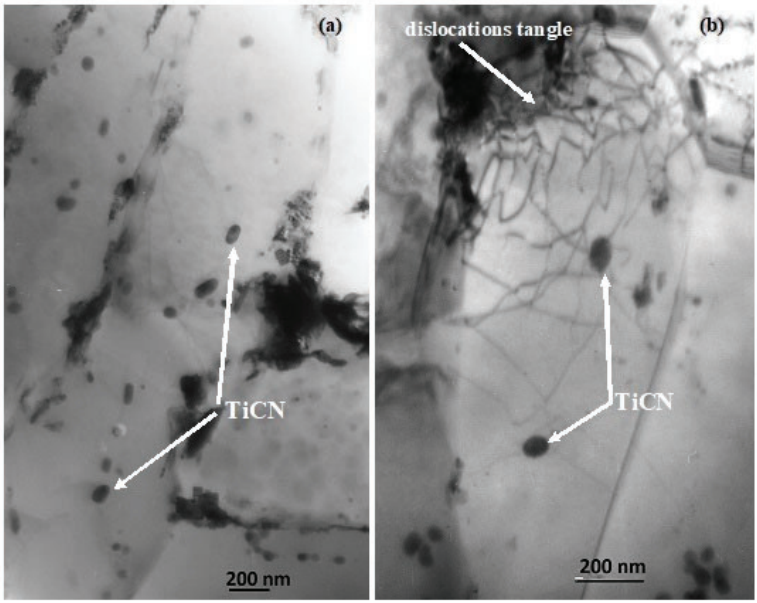

Figure II-4-6 TEM micrographs of two specimens reinforced with 10 wt.% TiCN. (Fig. II-4- 6a) a reference specimen, (Fig. II-4- 6b) specimen after a tensile stress test. In the upper left corner of Fig. II-4- 6b is seen dislocations tangle formed around a group of reinforcement particles. Two randomly selected TiCN particles are shown for demonstration purposes V. Dyakova [40].

The results above provoked the present author to launch a thorough study of the problem. The goal was to answer the question; why the CTE-mismatch mechanism fails to produce the dislocation density predicted by the theory. At first, an SEM micrograph of one of the TEM-foils shown in Fig. II-4-6 (prepared from, Al + 10 wt. % TiCN) was made. The resulting micrograph is shown in Fig. II-4-7. Two items on the micrograph are of special interest: (i) The micron-sized “hole” seen at the center of the micrograph and (ii) The two marked TiCN-particles in the upper right corner.

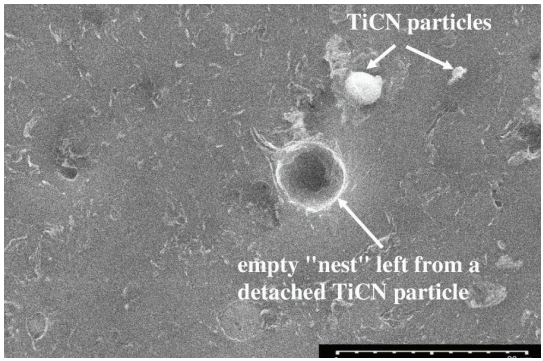

Figure II-4-7 A SEM image of a TEM-foil made from a reference specimen (V. Dyakova, [41]).

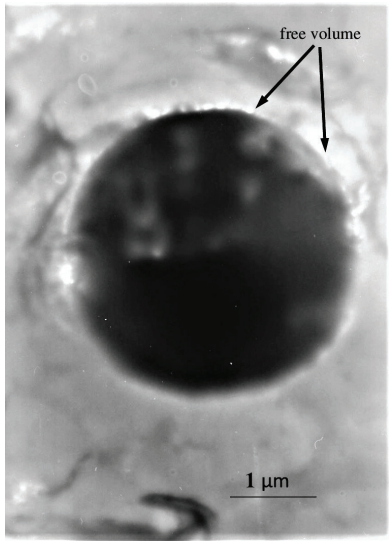

Figure II-4-8 TEM micrograph showing the microstructure of the matrix around an Al-based composite reinforced with 5 wt. % TiCN, V. Dyakova [42]. The micrograph is taken from an as-produced sample. Notice the bright parts in the Al -matrix, close to the reinforcement particle due to the broadening of the "free volume" around the reinforcement during the etching of the sample. The bright spots in the center of the reinforcement particle aren't cracks, but volume defects that occurred during the production of the TiCN nano-particles.

It could be readily figured out, that the "cavity" in the center is left by a micron-sized particle, which has separated, presumably, at the preparation of the TEM folio. The examination of the "nest", left by that particle, shows a rough contact surface, which suggests a partially bonded contact zone. As the specimen studied was not tensionally loaded, the partial bonding should have formed during the cooling of the specimen. Two possibilities exist: (i) for some reason, the reinforcement particle has shrunk more than the matrix and as a result, has separated from the surrounding matrix, which is contradicted by the fact that $\Delta\alpha > 0$ (the matrix shrinks more than the reinforcement), or (ii) during the cooling of the specimen the CTE-mismatch generated dislocations has moved toward the particle and annihilated in the reinforcement-matrix contact zone. If that is true, the specific volume of the matrix around the reinforcement will reduce proportionally to the number of the dislocations that are annihilated in the reinforcement-matrix contact zone, or by $n \approx 4\pi\rho_{CTE}\left(L_s^2 - \left\langle r_p \right\rangle^2\right) = 4\pi\rho_{CTE}\left(\frac{2\pi}{3f} - 1\right)\left\langle r_p \right\rangle^2$. Recall that ρ_{CTE} is measured as m^{-2} and that, $L_s \cong \left(\frac{2\pi}{3f}\right)^{1/2}\left\langle r_p \right\rangle$. The volume reduction of the matrix surrounding the reinforcement, for say, f = 0.1, therefore, will be; $\Delta\upsilon \cong 4\pi\left\langle r_p \right\rangle^2\left(\frac{2\pi}{3f} - 1\right)\rho_{CTE}\overline{\upsilon}_d$, where $\overline{\upsilon}_d$ is the mean volume carried out by a dislocation to the interstice reinforcement-matrix. The net result of the process, therefore, would be a reduction of the expected shrinking of the matrix surrounding the reinforcement which should be equal to $\Delta\upsilon$. The mean distance, $\overline{\delta}$, between the reinforcement and the matrix, is then readily obtained by dividing $\Delta\upsilon$ on the $4\pi\left\langle r_p \right\rangle^2$. By taking into account that the volume of a thin spherical shell equals, $4\pi\overline{\delta}\left\langle r_p \right\rangle^2$, for $\overline{\delta}$ is obtained, $\overline{\delta} \cong \left(\frac{2\pi}{3f} - 1\right)\rho_{CTE}\overline{\upsilon}_d$. By taking into account that $\rho_{CTE} \sim 10^{14}$ m^{-2} (see above) and that $\overline{\upsilon}_d \approx 5.10^{-24}$ m^3 for $\overline{\delta}$ is readily obtained $\overline{\delta} \approx 10$ nm.

At the same time, the change of the distance between the reinforcement particle and the matrix due to CTE-mismatch is $\left|\delta_{CTE}\right| \approx \left\langle r_p \right\rangle \Delta\alpha\Delta T$, which, using the same values for $\Delta\alpha$ and ΔT as above yields $\left|\Delta\delta_{CTE}\right| \approx 0.5$ nm. Remember that $\Delta\delta_{CTE}$ and $\overline{\delta}$, when treated as vectors, have opposite directions. Thence the gap between the particle surface and the inner radius of the cavity should be $\overline{\delta} - \left|\Delta\delta_{CTE}\right| \approx$9 nm! Therefore it could be reasonably assumed that the CTE mismatch is fully compensated by the annihilation of the dislocations in the contact zone reinforcement - matrix.

This result is valid for micron-sized particulates. Recall that ρ_{CTE} depends on the reinforcement size, being smaller around the smaller particles. Respectively, $\overline{\delta}$ will be less, compared to that estimated, for the particles with smaller size. This conclusion is confirmed by the images of the two particles located in the upper right corner in Fig. II-4-7. From the micrograph is seen that the contact zone between these particles and the matrix is also loose, which is readily deduced by the dark gray fringe that follows the periphery of these particles. (Recall, that dark parts on an SEM-micrograph are formed when the incident electrons are scattered at an obtuse angle (i.e., away from the SE-detectors) or trapped into cavities.) However, $\overline{\delta}$ is not large enough to lead to a full disruption of the bonds between these particles and the matrix.

If the evaluations carried out above are correct, then a free volume, around the micron-sized particles, should be readily detectable (see discussion at the beginning of this subsection). The TEM micrograph in Fig. II-4-8 shows that this is actually the case; the free volume is readily detected as very bright spots on the particles' periphery (in the figure these are marked with black arrows). This result complements those shown in Fig. II-4-7. Note: In the micrograph, the "free volume" zones are slightly larger than those predicted by the theory. The broadening observed is due to the etching applied in the preparation of the TEM foils.

The results which were shown in the micrographs, Fig. II-4-6 to II-4-8 unambiguously support the conclusion that the stress, generated in the matrix by the CTE mismatch, $\Delta\sigma_{CTE}$, is far less of that evaluated by the dependence:

$$\Delta\sigma_{CTE} \approx \left(\alpha_{mrx} - \alpha_{ref}\right)\Delta T E_{mrx}. \qquad (37)$$

Listed below are other factors that would also contribute to the reduction or even non-existence of the CTE mismatch strengthening:

(i) The temperature dependence of the Young modulus is usually not taken into account, thus, the mobility of the dislocations in the matrix is seriously underestimated. Indeed, in a recent paper, Y. Zhang et al. [43] found that at 400 °C the Young modulus of the Al is only 5% of that at 0 °C! By recalling that the elastic energy stored in the dislocation is proportional to the shear modulus of the matrix it could be argued that; at higher temperatures, the dislocations' gliding through the matrix is much easier due to the reduced resistance opposing their mobility. Therefore, the generated by the CTE-mismatch dislocations would move faster, thus, reaching the annihilation sinks for a time comparable or less than that required for achieving a considerable temperature change in the composite. Hence, in this way, the dislocations' pile-up at the obstacles' walls is avoided and the strengthening does not take place. Summing up the discussion above the following factors, facilitating the process of the dislocations' annihilation could be indicated: (a) the dislocation mobility is a thermally activated process [44], thus, at higher temperatures, the transfer rate of the dislocations through the matrix would be higher; (b) the "friction exerted by the matrix on a moving dislocation" is proportional to the Young modulus which, as discussed above, would lead to a considerable increase of the dislocations' transfer rate; (c) the distance that the dislocation overcomes to the nearest sink is short, $L_s \cong \left(\frac{2\pi}{3f}\right)^{1/2} \left\langle r_p \right\rangle$; it could be presumed that a considerable part of the dislocations, generated during cooling would annihilate, thus, reducing ρ_{CTE}, respectively, the stress generated;

(ii) The estimates of the CTE mismatch do not take into account the fact that the introduction of the reinforcement creates internal walls (boundaries) inside the matrix that redirect the stresses in the composite arising at loading, cooling, etc. Keeping in mind that the local deformations in the matrix are determined by the local stresses, it is obvious that at, say, cooling the matrix would deform in a very complex way, which is not taken into account by Eq. 36 (Remember that it is valid for homogeneous solid materials only.).

(iii) The estimates of the CTE carried so far do not take into account the size of the reinforcement. It is well known that the normal and the shear stresses, induced by introducing a spherical particle in an elastic

medium, drop as $\cong \left(\frac{\langle r_p \rangle}{r} \right)^3$ [45], where r denotes the distance from the center of the particle. For a point in the matrix distanced at only one particle radius from the particle's surface, i.e., $r = 2\langle r_p \rangle$ the stress in the matrix drops approximately 10 times! Thus, ρ_{CTE} will be considerably high only in a very thin shell around the reinforcement particle. As a result, the distance to the annihilation sinks that should be overcome of these dislocations is very short, thus allowing a considerable reduction of the dislocation density around the reinforcement during the cooling of the composite. Respectively, that will lead to a reduction of the strength induced.

The list above is not considered exhaustive, but only the most possible. All of these point to the fact that the stress caused by the CTE mismatch, if any, should be insufficient to generate a considerably high dislocation density, hence, the strength generated would be also insignificant. The considerations above, together with the experimental evidence, allows concluding that the effect of the CTE mismatch should be considerably lower than expected. For these reasons, in the author's opinion, one should be very cautious when using the CTE-mismatch mechanism in explaining the strengthening in particulate-reinforced composites.

Suggested additional reading to Ch. II-4

1. R. W. K. Honeycombe, *The plastic deformation of metals*, Edward Arnolds Publ. ltd, 1968.
2. A. H. Cottrell, *Theory of Dislocations*, in *Progress in Metal Physics 4*, B. Chalmers ed., Pergamon Press Ltd., London, 1953, pp. 205-264.
3. R. Ebeling and M. F. Ashby, *On the determination of the number, size, spacing, and volume fraction of spherical second-phase particles from extraction replicas*, Trans. AIME 236 (1966), pp. 1396 - 1404.
4. L. Anestiev, R. Lazarova, P. Petrov, V. Dyakova, L. Stanev On the strengthening and the strength reducing mechanisms at aluminum matrix composites reinforced with nano-sized TiCN particulates, Philosophical Magazine, 101:2, 129-153, (2021) DOI: 10.1080/14786435.2020.1821114.

5. A. S. Khanna, in Handbook of Environmental Degradation of Materials (Second Edition), 2012.
6. W. Soboyejo, Mechanical properties of engineered materials. Marcel Dekker, 2003.

References to Ch. II-4

1. J. W. Christian, The theory of transformations in metals and alloys, Pergamon, An Imprint of Elsevier Science, ch. 10 Classical theory of nucleation, (2002).
2. L. A. Anestiev, D. Malakhov, and G.R. Purdy, (2004) On the determination of the nucleation and growth activation energies using calorimetric data, Proc. Int. Symp. on Light Metals and MMC (edited by D. Gallienne and R. Ghomashchi), August 22-25, 2004, Hamilton, Ontario, p.227-237.
3. L. A. Anestiev On the solute redistribution at thermally activated phase transition processes I. Theory, J. Crystal Growth 140, p.167-174 (1994).
4. L. A. Anestiev and D. Malakhov, Growth rate at first-order phase transformation processes in multi-component systems J. Crystal Growth 276, p.643-651 (2005).
5. L. A. Anestiev, Precipitate growth from multi-component super-saturated solutions, Journal of Materials Science and Technology (ISSN 0861 – 9786) v.16, (1) pp. 40-64 (2008).
6. M. H. G. Jacobs and P. J. Spencer, A critical thermodynamic evaluation of the systems Si-Zn and Al-Si-Zn, Calphad 20 (1996) 307.
7. L. A. Anestiev and L. Froyen, On the processes of microstructure coarsening at liquid phase sintering (LPS), Physical Review E 61, p. 6721 (2000).
8. A. Kelly: Strong Solids, Clarendon Press, Oxford, (1966).
9. T. H. Courtney, Mechanical Behavior of Materials, 2nd ed. Waveland Press, Inc., pp. 198-205 (2005).
10. H. Gleiter and E. Hornbogen, Phys. Status Solidi, 12 251 (1965).
11. H. Gleiter and E. Hornbogen, Phys. Status Solidi, 22 235 (1965).
12. H. Gleiter and Hornbogen, Precipitation Hardening by Coherent Particles, Materials Science and Engineering, Review paper, 285 (1967).
13. H. Gleiter, Acta Met., 16 (1968).
14. H. Gleiter, Z. Angew. Physik, 23 108 (1967).
15. H. Gleiter, Z. Metallkunde, 58 99 (1967).

16. E. Orowan, Discussion on internal stresses, Symposium: Internal Stresses in Metals and Alloys, The Inst. of Metals, London, 1948, pp. 451-453.
17. E. Orowan, Mechanische Festigkeitseigenschaften und die Realstruktur der Kristalle, Zeitschrift für Kristallographie 89 (1934), pp. 327–343.
18. R. Ebeling and M. F. Ashby, Dispersion hardening of copper single crystals, Philosophical Magazine 13 pp. 805 – 834 (1966).
19. F. R. N. Nabarro: J. Less-Common Metals, vol. 28, p. 257 (1972).
20. N. F. Mott: Imperfections in Nearly Perfect Crystals, W. Shockley, J. H. Hollomon, R. Maurer, and E. Seitz, eds., John Wiley & Sons, New York, NY, 1952, p. 173.
21. M. F. Ashby and D. R. H. Jones, Engineering Materials 1, An Introduction to their Properties and Applications, Second Edition, Butterworth-Heinemann, an imprint of Elsevier Science (2002).
22. A. J. Ardell, Precipitation hardening, Metall. Trans. A16, pp. 2131-2165 (1985).
23. J. W. Morris, Jr. and D. H. Klahn, J. Appl. Phys., vol. 45, p. 2027 (1974).
24. K. Hanson and J.W. Morris, Jr.: J. Appl. Phys., vol. 46, p. 983 (1975).
25. E. Orowan, Z. Phys., vol. 89, p. 634 (1934).
26. R. W. Weeks, S. R. Pati, M. J. Ashby, and P. Barrand, Acta Metall. vol. 17, p.1403 (1969).
27. A.J.E. Foreman, Phil Mag. vol. 15, p 1011, (1967).
28. L. M. Brown, and R. K. Ham, Dislocation–particle interactions. In: A. Kelly and R. B. Nicholson, eds. Strengthening Methods in Crystals. Applied Science, London, pp 9–135, (1967).
29. A. Melander, The critical resolved shear stress of dispersion strengthened alloys, Scand. J. Metall. 7, p. 109 (1978).
30. J. C. Fisher, E. W. Hart, and R. H. Pry, The hardening of metal crystals by precipitate particles, Acta Metall. 1, pp. 336-339 (1953).
31. R. H. Jones, Predicting the stress-strain behavior of polycrystalline α-iron-containing hard spherical particles, U. S. Atomic Energy Commission, W-7405-ENG-48, Lawrence Berkeley National Laboratory, USA, 1973; https://escholarship.org/uc/item/0gj769z4.
32. J. Humphreys and P. B. Hirsch, The deformation of single crystals of copper and copper-zinc alloys containing alumina particles II. Microstructure and dislocation-particle interactions, Proceedings of the Royal Society (London) A. 318, pp. 73-92 (1970).

33. P. M. Hazzledine and P. B. Hirsch, A Coplanar Orowan Loops Model for Dispersion Hardening, Philosophical Magazine 30, pp. 1331-1351 (1974).
33. E. W. Hart, Theory of dispersion hardening in metals, Acta Metall. 20, pp. 275-289 (1972).
34. J. D. Eshelby, F. C. Frank, and F. R. N. Nabarro, Phil. Mag., vol. 42, p. 351, (1951).
35. E. O. Hall, "The Deformation and Ageing of Mild Steel: III Discussion of Results". Proc. Phys. Soc. Lond. 64 (9): 747–753 (1951).
36. N. J. Petch, "The Cleavage Strength of Polycrystals". J. Iron Steel Inst. London. 173: 25–28 (1953).
37. W. Hume-Rothery, R. W. Smallman and C. W. Haworth, The Structure of Metals and Alloys, The Institute of Metals, London, 1969.
38. M. Taya and R.J. Arsenault, Metal Matrix Composites – Thermo-mechanical behavior, Pergamon press 1989.
39. D.C. Dunand and A. Mortensen, Thermal mismatch dislocations produced by large particles in strain hardening matrix, in Metal Matrix Composites 1st ed., vol. 15, G. Chadwick and L. Froyen eds., North-Holland, Amsterdam, 1991, pp 179-185.
40. V. Dyakova, private communication (2018)
41. V. Dyakova, private communication (2019)
42. V. Dyakova, private communication (2016)
43. Y. Zhang, Y. Yi, Sh. Huang, H. He, Influence of Temperature-Dependent Properties of Aluminum Alloy on Evolution of Plastic Strain and Residual Stress during Quenching Process, Metals 7, p. 228 (2017), doi:10.3390/met7060228.
44. J. P. Hirth, Dislocations, in Physical metallurgy, 4th ed., vol. 3, R. W. Cahn and P. Haasen eds., North-Holland, Amsterdam, 1996, Ch. 20.
45. L. D. Landau, E. M. Lifshitz, Theory of elasticity, Pergamon press 1989.

CHAPTER II-5

A REVIEW AND ANALYSIS OF THE RESULTS IN REINFORCING WITH NANO-SIZED PARTICULATES

LUBOMIR A. ANESTIEV

The understanding of the mechanisms leading to usable mechanical properties of a material is essential for their employment in the practice. As above (see the preceding chapter) the mechanical properties of a composite could depend on many factors such as the type of reinforcement, its volume fraction, geometrical shape, size, homogeneity of the distribution, the isotropy of the system, etc.

In this chapter, a retrospective review of the results published so far by different authors is made. The production methods used by these authors and their evaluation of the strong and the weak sides of the methods used by them are also discussed.

Tee et al. [1] studied the mechanical properties of an Al-TiB_2 composite produced by *in situ* stir casting. They found that the tensile and the yield strengths of the as-produced composite are about twice that of the unreinforced matrix. However, these authors reported that this remarkable improvement was achieved at the expense of deterioration of the ductility of the composite.

The mechanical and wear properties of a stir cast composite based on Al-Si-Cu-Ni reinforced with Al_2O_3 were studied by Azim et al. [2]. The authors found that the composite containing 2% by weight of Al_2O_3 exceeds the tensile strength and the hardness of the unreinforced matrix alloy by 505 MPa and 123 Hv, respectively. They also observed an increase in the wear resistance and an increase in the hardness compared to that of the unreinforced alloy. According to them, a significant increase in hardness of the alloy matrix could be achieved by varying the shape of the reinforcement, e.g., by the addition of alumina fibers instead of spherically-shaped particulates. They attributed the increase of the hardness to the

relatively high hardness of alumina fibers and the refinement of the eutectic and the precipitated in the matrix alloy silicon particulates. An important result of their study was the establishment of the fact that the 0.2% proof strength and ultimate tensile strength of the composite samples increases with the increase of the weight fraction of the alumina fibers, used as reinforcement when the latter was kept within the range of 2 to 6 wt.%. However, they found that the ductility decreased reciprocally with the increase of the weight percent of alumina fibers. The authors explained the results obtained by them with the increase of the dislocation density inside the matrix with the increase of the weight percentage of the alumina fibers.

Kang and Chan [3] used a traditional powder metallurgy technique, to introduce nanometric particulates into the aluminum matrix. They found that: (i) the nanometric particulates improve the mechanical properties of the monolithic composite system, (ii) the increase of the reinforcement volume fraction, however, leads to an increase of the agglomeration of the reinforcement particulates. These authors established that the composites with nanometric particulates exhibit much higher yield and tensile strengths than that of the monolithic aluminum. They also reported that the tensile strength of the 1 vol.% Al_2O_3-Al composite was similar to that of the 10 vol.% SiC-Al composite, and that the yield strength of the former was higher than that of the latter. By analyzing their results, they concluded that the strength of the composite increases with the increase of the volume fraction of the nano-sized reinforcement. Yet, once the volume fraction of the nano-particulates in the composites studied by them exceeded the 4% barrier, the strength of composites showed no further improvement. Concerning the ductility of the composite, the authors found that it gradually reduces with the increase of the volume fraction of reinforcements in the composite. The study of the dislocation substructure developed during tensile testing showed that the dislocation density was higher near the particles; tangled dislocations were observed around the agglomerations of the nano-sized particles. According to Kang and Chan that suggests that the reinforcement agglomerations could also contribute to the reinforcement of the aluminum matrix. The authors explained the increase of the yield strength observed in their study by the following strengthening mechanisms: quenching effect (probably they meant thermal expansion coefficients mismatch), grain size (Hall-Petch effect), the sub-structure, and the Orowan bowing. However, based on the conditions at which their experiments were carried out, Kang and Chan argued that all specimens have been fully annealed and that there was no detectable variation in the sub-grain size. Therefore, according to them, the quench

and the sub-structure strengthening mechanisms should have to be excluded. They evaluated that the increase of the yield strength, due to the grain strengthening - the Hall-Petch effect, would show an increase from 29 to 40 MPa when the volume fraction of the nano-sized Al_2O_3 reinforcement is increased between 0 to 7%. Based on their evaluations they concluded that the grain boundary strengthening alone does not suffice to explain the very high increase in yield strength in composites. Thence, they concluded that the major strength mechanism should be the Orowan strengthening (see Section 4.3 in Ch. II-4) induced by the nano-sized particulates. Kang and Chan also reported that; when the nano-particle content in the composites exceeds 4 vol.%, the agglomerations lead to a reduction of the amount of 'effective' nano- particulates available, hence, the particle strengthening effect reduction. The calculations estimating the yield strength, however, exceeded considerably those measured in the experiment. This discrepancy with the experimental evidence was explained by these authors with the fact that in their experiments the nano-reinforcements were never uniformly dispersed. According to them, the inhomogeneous distribution of the reinforcement (quite possibly a size-liquation-based agglomeration of the reinforcement particulates, see for details in the next chapter) reduces the effective amount of particulates available for strengthening. Thence, the effective yield strength is significantly lower than that calculated. Kang and Chan considered three factors that could lead to an explanation of the observed results: (i) the increase in the volume fraction of the reinforcement beyond 4% do not bring any further grain-refinement; (ii) grain boundary aggregated nano-particulates, weaken the strength and ductility of materials; (iii) the 'effective' nano-particulate content is effectively reduced due to the agglomeration.

Kok [4] produced a composite using 2024 Al-alloy as matrix and Al_2O_3 as reinforcement and studied its mechanical properties. The author reported that the hardness and the tensile strength of the composite improve with increasing the weight percentage of the reinforcement.

Zh. Ren [5] studied the microstructure of nanocomposites fabricated by powder metallurgy and hot extrusion. He found that the distribution of the nanometric particulates in the aluminum matrix is inhomogeneous; in his experiments, most of the reinforcements concentrated along the grain boundaries. The particulates clustered in aggregates which density tended to increase with increasing particulates content. Ren found that a composite with a 1% volume fraction of SiC dispersed in Al7075 exhibits the highest yield and ultimate strength compared to all composites that he studied in his work. He argued that the strengthening effect obtained by

the introduction of the nanometric particulates into the matrix is due to Orowan strengthening. However, he found that the improvement of the mechanical properties was not so notable when comparing these results with those measured at composites reinforced by micro-sized particulates. He explained his findings with the unfavorable tendency, typical to the nano-sized particulates, to cluster in aggregates.

Kumar et al. [6] studied the mechanical properties and the wear resistance behavior of an *in situ* synthesized composite, Al-7Si alloy reinforced with TiB_2. The authors established that the increase of the weight percentage of TiB_2 leads to an improvement (increase) of the hardness, the Young modulus, the yield, and the ultimate tensile strength. They also found that the coefficient of friction decreased with the increase of the fraction of the reinforcer.

In a paper, Jinfeng et al. [7] studied the machinability of a composite produced by reinforcing with pure Al with SiC and Graphite. They found that the tensile strength and elastic modulus of the composite are higher, compared to those of the pure matrix. They noted that the increase of the volume fraction of graphite favors the improvement of the mechanical properties listed above.

Yar et al. [8] produced Al (A356.1) studied an aluminum matrix composite reinforced with nano-particulate MgO. The authors reported that the hardness and compressive strength of the composite is higher compared to that of the matrix alloy.

Mazaheri et al. [9] studied an aluminum base matrix composite (AMC) (An A356 Al-alloy was used as a matrix while for reinforcement were used nano-sized Al_2O_3 particulates). The reinforcement was incorporated into the aluminum matrix by mixing the reinforcement phase with micro-sized Al-alloy particles and subsequent melting of the green powder mixture in a stir furnace. The SEM micrographs of the as-prepared composite indicated that the nano-sized Al_2O_3 particles are homogeneously dispersed throughout the composites' samples. Yet, despite the measures taken by the authors, some zones of agglomeration have been detected inside the composite. The authors reported that the values of the ductility, the yield, and the ultimate tensile strength of the composite increased with the increase of the volume fraction of the nano-particles. They argued that the considerable enhancement in the observed values of UTS is due to (i) the reinforcer size, (ii) the homogeneous distribution of the nano- Al_2O_3 particles, (iii) the effective transfer of applied tensile load to the nano-sized Al_2O_3 particulates, and (iv) the grain refinement of the aluminum matrix. These authors also found that the hardness of the MMCs increases with the volume fraction of the particulates which was also attributed to

the increase of the ceramic phase in the matrix alloy. They argue that the higher hardness of the composites could be explained by the fact that the nano- Al_2O_3 particles act as obstacles to the dislocations' migration. They reported that the maximal hardness was observed in composites with 2.5 vol.% Al_2O_3 cast at 800 °C.

Ling et al. [10] fabricated an AMC reinforced with $Al_9(Co, Ni)_2$ particles. They observed that the ultimate tensile strength and the yield strength of the composites studied increased with the increase of the volume fraction of the reinforcement. The authors noticed that the elongation fracture first increased, but beyond some critical value of the reinforcement's volume fraction, it started to decrease despite the increase of the volume fraction of the reinforcer.

Amirkhanlou et al. [11] evaluated the hardness and impact energy adsorbed by an Al-alloy (A356) reinforced with a nano-sized SiC composite. They reported that both the hardness and the impact energy absorbed by the composite are higher compared to that of the pure alloy.

In research, carried out by M. Khorshid et al. [12], aluminum matrix composites reinforced by alumina particles with mixed sizes (nano and submicron) have been studied. The method of production used by the authors was; wet attrition milling with a subsequent hot forward extrusion. It was found that by increasing the ratio of the nano- to submicron-sized particulates, the relative density of the composite first increases and then decreases. Respectively, the micro-hardness and the strengths of the composites studied first increased and then decreases with the increasing of the fraction of the nano-sized particles. The observed improvement of the mechanical properties was explained with Orowan's bowing mechanism and thermal expansion coefficients mismatch between the matrix and reinforcement particles. The deterioration of mechanical properties of the samples with the increase of the volume fraction (VF) of the reinforcer above 4 wt.%, was attributed to the agglomeration of the nanoparticles and the formation of a continuous chain of brittle phases along grain boundaries. The authors noticed that the dimension of dimples formed in the fractured surfaces decreases with the increasing of the VF of the nano-sized particulates.

Sajjadi et al. [13] studied the mechanical properties of a stir cast Al-alloy (A356) - Al_2O_3 composite. The authors reported that the hardness and compressive strength of the composite increases: (i) by the increase of the weight percentage of Al_2O_3 and (ii) by the decrease of the reinforcer's particle size.

Kalaiselvan et al. [14] studied an AMC produced from an Al alloy (6061-T6), reinforced with B_4C, and investigated the mechanical properties

of the as-produced composite. They found that the hardness and the tensile strength of the composite increase linearly with the increase of the weight fraction of the reinforcer, B_4C.

Prasad et al. [15] produced by the stir casting method an AMC using as matrix the Al alloy, A356.2, and as a reinforcer - rice hush ash (RHA). The authors found that the hardness and ultimate tensile strength of the composite are higher compared to those of the incipient A356.2 alloy.

In a paper, A. Chennakesava [16] studied the tensile and bending properties of an AMC reinforced with Al_2O_3. The authors found that the produced composite exhibits maximal strength when the volume fraction of the alumina is 20%. They also found that the flexural fracture, and the yield strengths, of the composite decrease with the increase of the reinforcer when the volume fraction exceeds 20%. In a discussion of the reported results, the authors attributed the observed strain hardening to the changes in the grain size of the matrix which, according to them, is induced by the introduction of the reinforcer. They also have noticed an increase in the hardness with the increase of the alumina addition, however, according to them this positive effect was achieved at expense of a decrease in the ductility of the composite. The clustering (agglomeration of alumina particulates) was observed in some of the tensile test specimens. By implementing an X-ray analysis the authors established that the strengthening could be partially due to the precipitation of different intermetallic phases (i.e., to the precipitation strengthening mechanism): (i) $MgZn_2$ phase along the grain boundaries, (ii) $Mg_{17}Al_{12}$ at the grain boundary junctions, and (iii) Al_7Cu_2Fe, that clustered in bands in the composite. According to the authors, the tensile fracture is governed by (i) the ductile-brittle behavior of the phases that nucleate at the reinforcement-matrix interfaces, (ii) de-cohesion of the particles from the matrix, and (iii) particle (cluster) cracking.

Kumar et al. [17] investigated the mechanical properties of a stir cast Al-alloy (6061) matrix composite reinforced with AlN particles. They concluded that the ultimate tensile, and the yield strength of the composite is improved as a result of the introduction of the AlN particles. The authors found that the microhardness of the produced composites increases with the increase of the fraction of the AlN particulates in the alloy matrix.

Atuanya et al. [18] produced by the stir casting technique a composite based on an Al-Si-Fe alloy using as a reinforcer the breadfruit seed hull ash. The authors report an increase in the composite's tensile strength and hardness and a decrease in the impact strength.

Hai Su with collaborators [19], studied the elongation, the yield, and the ultimate tensile strengths of as-cast composites, based on 2024 Al-

alloy, that were reinforced with nano-sized Al_2O_3. They found that the yield and the ultimate tensile strengths of the composite are simultaneously enhanced, compared to the same parameters in the 2024 alloy. The results obtained were attributed to the coupled effects of an increase in the grain boundary area, due to grain refinement and the strong thermal stresses induced by the large differences in the thermal expansion coefficients of the matrix and the reinforcement. According to these authors, the optimal mechanical properties of the studied composite are achieved at 1 wt.% of the reinforcer, Al_2O_3. The reported by Hai Su et al enhancement of the ultimate tensile and yield strengths is 37% and 81%, respectively. Yet, they report that with the increase of the nanoparticles' weight fraction, the tensile strength of the composites decreases. The latter result was attributed by the authors to the fact that the increase of the reinforcer increases the possibility of the particulates' agglomeration. They also found that the elongation at fracture decreased gradually with increasing the nanoparticles' mass fraction, which again was explained by the increased clustering of the latter. Hai Su et al. also argued that the increased mass fraction of nanoparticles would decrease the effective slip distance of dislocations during loading, which would lead to a decrease of the elongation.

Mazaheri et al [20] conducted a comparative study of the mechanical properties of the composites Al-TiC, Al-B_4C, and a hybrid composite, Al-TiC-B_4C. The authors found that the hybrid composite possesses the highest hardness compared to the other composites studied by them. The highest yield strength and tensile strength were reported for the Al- B_4C composite, while maximum elongation at fracture was achieved by the composite Al-TiC.

Alaneme et al. [21] studied the mechanical and corrosion resistance properties of a hybrid composite based on an Al-Mg-Si alloy which was reinforced with SiC and bamboo ash. The authors report that the values of the hardness, the yield, and the ultimate tensile strengths of the composite decreased with the increase of the weight fraction of the bamboo leaf ash. At the same time, the fracture toughness of the hybrid composite excelled.

Kumar et al. [22] fabricated via the electromagnetic stir casting method an A359-alloy based AMC reinforced with Al_2O_3. These authors measured the hardness and the tensile strength of the as-produced composite and found that its hardness values increased from 46 HRC, (that of the matrix alloy), to 72.8 HRC (of the composite). The tensile strength of the composite increased accordingly from 103.7 N mm^{-2} to 148.7 N mm^{-2}.

Akbari et al. [23] produced a composite based on the Al (A356) alloy using as reinforcement mixtures of milled nano-sized Al_2O_3, Al particles,

and nano-sized Al_2O_3 and Cu particles. The authors reported that the ultimate tensile strength and the compressive strength of the composite are higher than that of the pure alloy.

Baradeswarn et al. [24] studied the mechanical properties of a composite based on an A-7075 alloy reinforced with B_4C. The authors reported that the composite's hardness, compressive, and ultimate tensile strength increase linearly with the increase of the volume fraction of the reinforcement, B_4C.

Selvam et al. [25] studied the mechanical properties of a stir cast hybrid composite based on the Al alloy (6061) reinforced with SiC and fly ash. The authors reported an increase in the macro hardness and the tensile strength of the composite with the increase of the weight fraction of the nano-sized SiC.

Boopathi et al. [26] produced a hybrid metal matrix composites from the Al-alloy Aluminium-2024, used as a matrix, while as reinforcement they used a mixture of silicon carbide and fly ash (a coal combustion product). The authors reported an increase in the values of the mechanical parameters of the composite, such as the tensile strength, the yield strength, and the hardness compared to those of the matrix alloy. They found that: (i) the density of the composites decreased with the increase of the reinforcement's fraction, (ii) the tensile and yield strengths, and the hardness increased with the increase of the VF of the reinforcement, (iii) the addition of the SiC and fly ash led to a significant decrease of the rate of elongation, (iv) the addition of the reinforcement did not affect the amount of the constituent phases in the matrix.

Saravanakumar et al. [27] investigated hybrid AMCs manufactured by the stir casting method. By varying the volume fractions of the constituents in the complex reinforcement, which was a combination of alumina and graphite, they succeeded to obtain composites with diverse properties. Employing scanning electron microscopy the authors studied the effect of the reinforcement on the matrix grain size, the distribution of reinforcement, and the clustering of reinforcement inside the matrix. They found that the increase of the reinforcement up to 6% leads to an improvement of the hardness, the compressive, the impact strengths, and the flexural strength of the composite. The authors attributed the improvement of these parameters to the uniform distribution of the reinforcement within the composite. The further increase of the reinforcement, beyond 6%, however, led to a deterioration of the mechanical properties, which was attributed to the clustering of the reinforcement particles.

D. Markó et al. [28] used the powder metallurgy technique to produce MMCs consisting of an Al-alloy (A2024) based matrix, reinforced with different volume fractions of gas-atomized $Fe_{49.9}Co_{35.1}Nb_{7.7}B_{4.5}Si_{2.8}$. The mechanical properties of the as-produced composites were then studied under tensile loading. The tensile tests at room temperature revealed a significant improvement in the mechanical properties of the composites compared to those of the unreinforced 2024 matrix. For instance, the yield and tensile strength of the composite reinforced with 40 vol.% of glassy particles increased, from 180 and 300 Mpa (of the pure 2024 alloy) to about 230 and 360 Mpa, respectively. The authors noticed an appreciable rise in the tensile ductility which ranged between 5% and 10%. Based on the results obtained they concluded that the glassy particles are not only effective reinforcements under compression but also under tensile loading.

The effect of the particle size and the weight fraction of the reinforcement on the compressive strength was studied by El-Kady and Fathy [29]. For that purpose, a SiC-reinforced composite was used. The authors found a considerable difference between the strength of the pure aluminum and that of the composite. They reported that the samples containing 10 wt.% SiC have generally better strength than those with 5 wt.% SiC and the pure aluminum samples. This finding was attributed to the changes in the particle size of SiC. According to El-Kady and Fathy's experiments, the composites containing 70 nm SiC particles show exceptionally good mechanical properties. They found that the additions of up to 10 wt.% SiC to the aluminum powder increased the compressive strength. The obtained results were explained by the fact that SiC particles prevent the movement of dislocations in the aluminum matrix. Moreover, according to El-Kady and Fathy, the increase of the amount of SiC leads to a decrease in the distance between the SiC particles, which increases the required tension for pushing the dislocations between the SiC particles, hence, to an increase of the material strength. The obtained by these authors results could be summarized as: (i) The increase of the amount of the SiC particles deteriorates the composite's densification, while the increase of the reinforcement size increases densification. (ii) When the size of the SiC particles is decreased, the grain size and the distribution of reinforcement also decrease. With the decrease of the reinforcement fraction the grain size and SiC particle distribution homogeneity increases. (iii) Increasing the amount of SiC and/or decreasing the particle size of SiC favors achieving a higher hardness in the composite produced. The highest hardness of 72 HV was measured by these authors in the composites containing 10 wt.% of SiC with 70 nm particle size. (iv) The reduction of the reinforcer particles' size leads to considerable

improvement of the compressive strength. The increase of the VF of the SiC led also to an improvement of the compressive strength of the composite. The highest strength measured, according to the authors, was 601 MPa, for a composite produced from reinforcer with 70 nm size and containing 10 wt. % SiC.

Das et al. [30] studied series of aluminum-based matrix composites produced by the stir casting method. They reported that obtaining a perfectly homogeneous distribution of reinforced particles in the matrix phase was difficult. The authors found that the increase of the reinforcement fraction increases the density of the composite. They observed that the aluminum matrix hardness improves when the reinforcement fraction is increased or when the size of reinforcement is reduced. Based on their experiments Das et al. concluded that the hardness of the ceramic-reinforced composites can be improved by carefully selecting the heat treatment, the aging temperature, and the aging time. The authors found that the breaking (fracture) stress, Young's modulus, yield, and ultimate tensile strengths of the ceramic-reinforced aluminum matrix composites are higher than those of the monolithic alloys. The increase of the fraction of the reinforcement, however, reduced the ductility (the percent elongation) of the composites. The fractography studies, carried by the authors, revealed that the mechanism and mode of failure of the aluminum matrix composites during tensile testing might be due to a generation and growth of fine microcracks which lead to macroscopic failure. The compressive strength of ceramic-reinforced AMCs was found to increase with the increase of the reinforcement fraction and with the increase of the strain rate during compression. The flexural strength (bending strength) of ceramic reinforced aluminum matrix composites increased until a certain percentage of reinforcement was reached, beyond that critical percentage the flexural strength reduces. The authors found that the toughness (impact strength) of the aluminum matrix composites reinforced with ceramics could be increased by an increase of the reinforcement fraction or by applying an aging treatment.

In a review, Pramod et al [31] summarized the results obtained by utilizing the *in situ* casting method at the production of Al-based composites utilizing different reinforcements. They considered the influence of various process parameters on the composite properties such as the nature, size, and morphology of the reinforcement particles. They found that many of the *in situ* produced composites show excellent mechanical and wear properties when the reinforcement content is increased. Yet, while the tensile and yield strength show a significant increase with the increase of the reinforcement fraction, it was noticed that the ductility reduces. The

analysis carried out by the authors led to the conclusion that using reinforcement particles with sub-micron sizes improves the combination of strength and ductility. Additionally, the authors of the review discussed the influence of secondary mechanical processing. Recall that such procedure is usually carried out after the synthesis of the cast composites and it intends to improve the particle distribution and strength, to enhance the results from the heat treatments, etc. Based on the research carried out Pramod et al. concluded that TiB_2 and Mg_2Si reinforcements attract the attention of most of the researchers because of their easiness to fabricate and cost-effectiveness. The issues as; the coarseness of the primary Mg_2Si phase, the effect of the TiB_2, TiC, and ZrB_2 particles on the grain refinement of the Al matrix were also addressed in their review.

Park et al [32] investigated the strengthening mechanisms in CNT (carbon nanotubes) reinforced Al-composites. They found that the preprocessing of the reinforcement is critical for the formation of effective covalent bonds between the Al matrix and the CNTs, respectively, for the quality of the produced composite. It was established that the formed Al-C covalent bonds play an important role in the load transfer from the Al matrix to the CNTs. The authors reported that the addition of 0.2 wt. % CNTs led to an increase in the values of the yield and tensile strengths of the Al-CNT composite by 60% and 23%, respectively. The improvement in strength was well corroborated with the values predicted by the following strengthening mechanisms; load transfer, the generation of dislocations, thermal mismatch, and Orowan's bowing mechanism. According to the authors of the research, the load transfer mechanism is dominant, contributing to more than 50% of the increase of the yield and tensile strengths.

Pan Ma et al. [33] studied a composite synthesized from an Al-12Si alloy which was reinforced with nano-sized Al_2O_3. The method of production utilized was hot extrusion. The authors reported a considerable agglomeration of the reinforcement in the composite when the weight fraction of the reinforcement exceeded 10 wt. %. They found that a further increase in the weight percentage of Al_2O_3 nanoparticles, i.e. above 10 wt. % led to a decrease in the measured hardness values. The decrease was attributed to the porosity and irregularities generated by the agglomerated nanoparticles. The results obtained by Pan Ma et al could be summarized as (i) The composites reinforced with 2 to 5 wt. % Al_2O_3 nanoparticles exhibited relatively homogeneous distribution, while the microstructure of the composites with 10 wt. % reinforcement exhibited agglomeration of the Al_2O_3 particles in the matrix. (ii) The hardness of the composites increased when the weight fraction of the reinforcement was between 2

and 5 wt. %, after that, however, it decreased (the transition between the increase and decrease of the hardness, according to the authors, was observed at 10 wt. % of the reinforcement). The strength of the composites displayed similar trends to that of the hardness. The maximum values of the strength were observed for the composites with 5 wt. % Al_2O_3. The measured elongation, yield, and ultimate tensile strengths at 5 wt. % Al_2O_3 was, ~30%, 244 MPa, and 286 MP, respectively. Pan Ma et al. carried out an analysis of the strengthening mechanisms that could be involved in the observed strengthening of the composites studied. According to their analysis, the increase of the yield strength of a composite is largely due to the thermal mismatch enhancement mechanism, while the Hall-Petch's and the Orowan's mechanisms play a secondary role in the composite's strengthening.

K. Kallip et al. [34] used a simple one-step process to produce series of composites based on the commercial 5xxx Al-alloys reinforced with nano-sized Al_2O_3. According to these authors, the process used by them, cube milling and uniaxial hot pressing, enables producing, without the need for secondary operations, net-shape products which possess high strength and good ductility. The authors found that the mechanical properties of the composites produced exceeded those of the commercial 5xxx alloys both in strength and ductility. The results obtained showed that the UTS raised to, 562 MPa and the yield strength to, 527 MPa. The elongation at rupture achieved was 4% at composites with 1 vol. % of the reinforcer. The authors succeeded in tailoring an optimal strength-ductility combination of the composites by varying the VF content of the reinforcer between 0.3 and 1 vol.%. The solid solution strengthening, the Orowan strengthening, and grain boundary strengthening are presumed to be the main mechanisms contributing to the achieved high strength, while the bimodal grain structure together with the LAGBs (Low Angle Grain Boundary) is believed to be the main source of retained ductility.

In his Ph.D. thesis, M. Khorshid [35] studied the effect of reinforcement properties and concentration on the mechanical behavior of composites produced from Al and reinforced with, Al_2O_3, nano-carbon, and graphene nanoparticles (GNP). He reported that changing the type of reinforcement changes the compressibility of the composite. The author also found that the Graphene nano-platelets improve the compressibility of the composite powders. The measured relative density of a composite reinforced with graphene was close to the theoretical limit. According to the author, the grain boundary strengthening (the Hall-Petch effect) appears to be the predominant strengthening mechanism. The strengthening was primarily attributed, by the author, to the indirect effect of the

reinforcement “grain boundary pinning” which occurred during the processing of the composites. Based on the experimental findings the author argued that controlling the grain size would be the major factor for increasing the strength and the hardness of the Al - Al_2O_3 composites. The Al - GNP composites showed in general higher grain size in comparison to the Al - Al_2O_3 ones. Solid solution strengthening from impurities in the GNP and CTE mismatch strengthening were also considered. The conclusion was drawn that the grain size is the major factor controlling the hardness/ strength of the Al-based nano-composites reinforced by GNPs.

In a review paper dedicated to the AMCs and their properties, R. Sharma et al. [36] made an overview of the best combination of the individual parameters that lead to high-quality composites. The conclusions drawn by them could be summarized as follows: (i) For composites reinforced with silicon carbide optimal hardness results are achieved at 25% weight percent of the reinforcer. (ii) Hardness increases with the increase of the fraction of the silicon carbide but decreases when a second reinforcer, e.g., graphite, is added. Thence, optimal hardness could be obtained by varying the proportions of both reinforcement additions. (iii) Several reinforcement materials such as graphite, fly ash, red mud, and alumina show better results compared to the tensile strength induced by the nano-sized SiC. (iv) Improvement of the compressive strength is achieved by utilizing as reinforcement, fly ash particulates. (v) The ductility of the composite tends to decrease with increasing the fraction of the reinforcement. Yet, according to the authors, fly ash would be the worst choice in improving that property. (vi) Combined reinforcing with SiC and graphite results in no pores if the mixing is done well. (vii) Various organic materials, used as reinforcements, such as rice husk ash and cow dung could also play a significant role in the improvement of the mechanical properties and are in trend, due to their economic value. (viii) The reinforcing of the Al-matrix with SiC increases the wear resistance. (ix) The uniform distribution is improved, when using graphite, instead of SiC, as reinforcement. (x) Additions of graphite result in a decrease in the thermal expansion of the composite.

A. Bishta et al. [37] produced by spark plasma sintering (SPS) route an Al-GNP composite, with high strength and hardness. They argued that SPS yields good compaction and high relative density to the structures, without affecting the microstructure of the GNPs. A dense and clear interface between GNP and Al, without significant precipitation of GNP - Al reaction products, was also reported. The presence of the GNP in the Al matrix was confirmed by XRD analysis, scanning, and transmission electron microscopy. The grain size homogenization, which followed after

the GNP introduction in the Al-matrix, was verified by optical microscopy. The improvement in hardness was confirmed by the nano-indentation technique. The results, obtained for the 1 wt% GNP weight fraction of the reinforcement, show 84.5% and 54.8% improvement in the yield and ultimate tensile strengths, respectively. The improvements in the mechanical properties of the composite are attributed to the proper dispersion of the reinforcement inside the matrix and the strong interaction of the GNP with the Al. By comparing the theoretical and experimental data the authors concluded that Orowan's bowing mechanism is the principal strengthening mechanism in the studied Al-GNP composites. Yet, the composites did not perform up to the expectations of the authors mostly due to the agglomeration of the reinforcement phase.

Ajagol et al. [38] studied aluminum-based composites reinforced with different weight fractions of SiC all of which have been produced by the stir casting method. Their results could be summarized as follows: (i) the adoption of the stir casting technique was successful because it allowed the fabrication of quality aluminum-silicon carbide composites, (ii) with the increase of the SiC content in the aluminum matrix was observed clustering of the reinforcement and increased level of porosity, (iii) the addition of the SiC particles led to a significant improvement of the tensile strength and hardness compared to these of the unreinforced composites, (iv) it was found that the improvement in the mechanical properties of the composite is proportional to the wt % of the added SiC particulates. The authors reported that the best results are obtained when the reinforcement is 15% by weight. The maximal hardness measured was 47 HV, while the maximal ultimate tensile strength was 130 MPa. The obtained in their research favorable results, Ajagol et al. explained by the high amount of dislocations that were generated in the composite. According to them the dislocations were generated during the cooling of the composite and are due to the differences in the thermal expansion coefficients of the matrix and the reinforcement. The authors argued that the dislocation to dislocation interaction, dislocation density, and the constrained plastic flow, due to the resistance rendered by the SiC particles, are the factors that led to the observed strengthening of their composites.

In two papers Wang et al. [39,40] studied fabricated via ultrasonic stir casting technique composites, based on Al-11Si that were reinforced with TiCN nano-particulates. Microstructural analysis, carried out by these authors, revealed that a large proportion of the TiCN particles are distributed along grain boundaries or the Si-phase of the eutectic, i.e., distributed in an intergranular fashion. A small proportion of the nano-particles were dispersed within the interior of the α-Al dendrites, i.e.,

distributed in an intragranular fashion. It was presumed by these authors that during the solidification, a large population of the nano-particles are pushed to the grain boundaries and then to the eutectic interfaces, thus leading to refined cast microstructures. Overall, the as-produced TiCN - Al11Si composites exhibited superior mechanical properties over the matrix Al alloy at various levels of the reinforcement. It was found by the authors that the composite with 2 vol.% of TiCN exhibits excellent mechanical properties with hardness, ultimate tensile strength, yield strength, and elongation that are higher, compared to those of the matrix alloy, by 45%, 22%, 16%, and 108%, respectively. The significant improvement in the mechanical properties, particularly the ductility, of the composites was attributed to the microstructure refinement and the positive effect of the reinforcing particles, which, according to the authors, is due to the absence of brittle intermetallics precipitated at the reinforcement-matrix interface.

Summary of the results reported in the reviewed papers

(1) Most popular reinforcements used so far are alumina and SiC. Yet, some reinforcement materials, e.g., fly ash or even rice ash were also tested. The general conclusion is that carbides are considered to be the most appropriate reinforcement material;

(2) Up to the present the preferred method of composites' production is stir casting. However, the PM techniques e.g. hot extrusion is nowadays also gaining strength and favor among the researchers and the producers of composites reinforced with nano-particulates;

(3) Without exception all of the researchers report an increase in the yield and ultimate tensile strengths of the composites with the increase of the volume fraction of the reinforcement, no matter what method and/or reinforcement were used at their production;

(4) However, the increase of the yield and the ultimate tensile strengths, with the increase of the volume fraction of the reinforcement, is achieved at the cost of a decrease of the composite's ductility;

(5) Up to now, the attention of the researchers is focused mostly on the mechanical properties of the composite. Yet, some papers dealing with the corrosion resistance of the composites or some physical properties as heat conduction could also be found in the specialized literature;

(6) According to the authors of the reviewed papers, the possible mechanisms explaining the strengthening effect of the added to the matrix nano-particulates are, (i) the increased dislocation density induced by the nano-sized particulates, (ii) the Hall-Petch grain effect strengthening, (iii)

the thermal expansion coefficients mismatch and (iv) the Orowan's bowing mechanism. It should be noted that Orowan's bowing mechanism is the most favored among the reviewed authors when it comes to explaining the increase of the composites' strength. In the last chapter of this part of the book it will be shown that the Orowan bowing mechanism indeed plays a crucial role in AMC's strengthening;

(7) Most of the authors report that the strengthening effect of the nano-sized particulates used as reinforcement is not limitless. It was found that beyond a certain VF of the reinforcement instead of improving the mechanical properties of the composite deteriorate;

(8) The possible causes of the strength reduction observed by almost all of the reviewed authors are not discussed or studied systematically. Most of the researchers are inclined to attribute the observed reduction of the mechanical properties to the clustering and the agglomeration of the reinforcement particles. In the last two chapters of this part of the book will be illustrated that the clustering and the agglomeration indeed reduce the strength of the composite. Yet, it will be also shown that the strength reduction, observed in the composites reinforced with nano-particulates, has its roots in the formation within the matrix of micro(nano)cracks, located at the vicinity of the reinforcement particulates.

References to Ch. II-5

1. K.L. Tee, L. Lu, M.O. Lai, 1999, Synthesis of in situ Al-TiB_2 composites using stir cast route, Composite Structures 47, 589-593 (1999).
2. A.N. Abd El-Azim, M.A. Kassem, Z.M. El-Baradie, M. Waly, Structure and properties of short alumina fiber reinforced AlSi18CuNi produced by stir casting, Materials Letters 56, pp. 963 – 969 (2002).
3. Yung-Chang Kang, Sammy Lap-Ip Chan Tensile properties of nanometric Al_2O_3 particulate-reinforced aluminum matrix composites Materials Chemistry and Physics 85 438–443 (2004).
4. M. Kok, Production and mechanical properties of Al_2O_3 particle-reinforced 2024 aluminum alloy composites, Journal of Materials Processing Technology 161, 381–387, (2005).
5. Zh. Ren, Mechanical Properties of 7075 Aluminium Matrix Composites Reinforced by Nanometric Silicon Carbide Particulates, Master of Engineering thesis School of Materials Science and Engineering Faculty of Science University of New South Wales 2007.

6. S. Kumar, M. Chakraborty, V. Subramanya Sarma, B.S. Murty, Tensile and wear behavior of in situ Al–7Si/ TiB_2 particulate composites, Wear 265, 134–142 (2008).
7. Jinfeng Leng, Lontan Jiang, Qiang Zhang, GaohuiWu, Donli Sun, Qingbo Zhou, 2008, Study of machinable Sic/Gr/Al Composite, J Mater Sci. 43, pp. 6495-6499 (2008).
8. Yar A. Ansary, M. Montazerian, H. Abdizadeh, H.R. Baharvandi, Microstructure and mechanical properties of aluminum alloy matrix composite reinforced with nano-particle MgO, Journal of Alloys and Compounds 484, 400–404 (2009).
9. H. Mazahery, H.R. Abdizadeh, Baharvandi, Development of high-performance A356/nano- Al_2O_3 composites, Materials Science and Engineering A 518, 61–64 (2009).
10. Cheng Su-ling, Yang Gen-Cang, Zhu Man, Wang Jin-cheng, Zhou Yao-he, Mechanical properties and fracture mechanisms of aluminum matrix composites reinforced by $Al_9(Co, Ni)_2$ intermetallics, Trans. Nonferrous Met. Soc. China 20, 572-576 (2010).
11. S. Amirkhanlou, B. Niroumand, Synthesis and characterization of 356-SiCp composites by stir casting and compo-casting methods, Trans. Nonferrous Met. Soc. China 20, s788-s793, (2010).
12. M. T. Khorshid, S.A. Jenabali Jahromi, M.M. Moshksar, Mechanical properties of tri-modal Al matrix composites reinforced by nano- and submicron-sized Al_2O_3 particulates developed by wet attrition milling and hot extrusion. Materials and Design 31 3880–3884 (2010).
13. S.A. Sajjadi, H.R. Ezatpour, H. Beygi, Microstructure and mechanical properties of Al – Al_2O_3 micro and nanocomposites fabricated by stir casting, Materials Science and Engineering A 528, 8765– 8771, (2011).
14. K. Kalaiselvan, N. Murugan, Siva Parameswaran, 2011, Production and characterization of AA6061–B4C stir cast composite, Materials and Design 32, 4004–4009.
15. S. Prasad, A. R. Krishna, Production and Mechanical Properties of A356.2 /RHA Composites, International Journal of Advanced Science and Technology Vol. 33, August 2011.
16. A. Ch. Reddy, E. Zitoun, Strengthening mechanisms and fracture behavior of 7072al/ Al_2O_3 metal matrix composites, International Journal of Engineering Science and Technology (IJEST) Vol. 3 No. 7 July 2011.

17. B. Ashok, Kumar, N. Murugan, Metallurgical and mechanical characterization of stir cast AA6061-T6–AlNp composite Materials and Design 40 52–58 (2012).
18. C. U. Atuanya, A. O. A. Ibhadode, I. M. Dagwa, Effects of breadfruit seed hull ash on the microstructures and properties of Al-Si–Fe alloy/breadfruit seed hull ash particulate composites, Results in Physics 2, 142–149 (2012).
19. Hai Su, Wenli Gao, Zhaohui Feng, Zheng Lu, Processing, microstructure and tensile properties of nano-sized Al_2O_3 particle reinforced aluminum matrix composites Materials and Design 36 590–596 (2012).
20. Y. Mazaherin, M. Meratian, R. Emadi, A. R. Najarian, Comparison of microstructural and mechanical properties of Al–TiC, Al–B_4C, and Al–TiC-B_4C composites prepared by casting techniques, Materials Science & Engineering A 560, 278–287 (2013).
21. K. K. Alaneme, B. O. Ademilua, M. O. Bodunrin, Mechanical Properties and Corrosion Behaviour of Aluminium Hybrid Composites Reinforced with Silicon Carbide and Bamboo Leaf Ash, Vol. 35, No. 1 25-352013 (2013).
22. S. Kumar, R. S. Panwar, O. P. Pandey, Effect of dual reinforced ceramic particles on high-temperature tribological properties of aluminum composites, Ceramics International 39, 6333–6342 (2013).
23. M. Karbalaei Akbari, H. R. Baharvandi, O. Mirzaee, Fabrication of nano-sized Al_2O_3 reinforced casting aluminum composite focusing on preparation process of reinforcement powders and evaluation of its properties, Composites: Part B 55, 426–432, (2013).
24. A. Baradeswaran, A. Elaya Perumal, Influence of B_4C on the tribological and mechanical properties of Al 7075–B_4C composites, Composites: Part B 54, 146–152, (2013).
25. D. R. Selvam, J. R. Smart, D. S. Dinaharan, Synthesis and characterization of Al6061-Fly ASHP-SiCp composites by stir casting and compo-casting methods, Energy Procedia 34, 637 – 646, (2013).
26. M. Boopathi, K. P. Arulshri, N. Iyandurai, Evaluation of mechanical properties of aluminum alloy 2024 reinforced with silicon carbide and fly ash hybrid metal matrix composites, American Journal of Applied Sciences, 10 (3): 219-229 (2013).
27. A. Saravanakumar, P. Sasikumar, and S. Sivasankaran, Synthesis and mechanical behavior of AA 6063-x wt. % Al_2O_3-1% Gr (x = 3,

6, 9 and 12 wt. %) hybrid composites, Procedia Engineering, Vol. 97, 951-960 (2014).

28. D. Markó, K.G. Prashanth, S. Scudino, Z. Wanga, N. Ellendt, V. Uhlenwinkel, J. Eckert, Al-based metal matrix composites reinforced with Fe49.9Co35.1Nb7.7B4.5Si2.8 glassy powder: Mechanical behavior under tensile loading, Journal of Alloys and Compounds 615 S382–S385 (2014).
29. O. El-Kady, A. Fathy, Effect of SiC particle size on the physical and mechanical properties of extruded Al matrix nanocomposites, Materials and Design 54 348–353 (2014).
30. D. K. Das, P. Ch. Mishra, S. Singh, and R. K. Thakur, Properties of ceramic-reinforced aluminum matrix composites - a review, International Journal of Mechanical and Materials Engineering 1-12 (2014) http://www.springer.com/40712/content/1/1/12.
31. S. L. Pramod, S. R. Bakshi, and B. S. Murty, Aluminum-Based Cast In Situ Composites: (2015) A Review, Journal of Materials Engineering and Performance, ASM International DOI: 10.1007/s11665-015-1424-2
32. Jong Gil Park, Dong Hoon Keum, Young Hee Lee, Strengthening mechanisms in carbon nanotube-reinforced aluminum composites, Carbon 95 690-698 (2015).
33. Pan Ma, Yandong Jia, P. K. Gokuldoss, Zhishui Yu, Shanglei Yang, Jian Zhao and Chonggui Li, Effect of Al_2O_3 Nanoparticles as Reinforcement on the Tensile Behavior of Al-12Si Composites Metals, 7, 359 (2017); doi:10.3390/met7090359.
34. K. Kallip, High Strength Ductile Aluminium Matrix Composite, Ph.D. thesis 2017; K. Kallip, N. K. Babu, Kh. A. Al-Ogab, L. Kollo, X. Maeder, M. Leparoux, Y. Arroyo, Microstructure and mechanical properties of near net-shaped aluminum/alumina nanocomposites fabricated by powder metallurgy, Journal of Alloys and Compounds 714 133-143 (2017).
35. M. T. Khorshid, Nano-Crystalline Metal Matrix Nano-Composites Reinforced by Graphene and Alumina: Effect of Reinforcement Properties and Concentration on Mechanical Behavior Ph.D. thesis, University of Wisconsin-Milwaukee 2017.
36. R. Sharma, S. Jha, Kh. Kakkar, K. Kamboj, P. Sharma, A Review of the Aluminium Metal Matrix Composite and its Properties, International Research Journal of Engineering and Technology (IRJET) Volume: 04 Issue: 02 Feb. 2017.
37. A. Bisht, M. Srivastav, R. M. Kumar, I. Lahiri, D. Lahiri, Strengthening mechanism in graphene nano-platelets reinforced

aluminum composite fabricated through spark plasma sintering, Materials Science and Engineering A 695 20–28 (2017).

38. P. Ajagol, B. N. Anjan, N. Rajaneesh, Marigoudar, Preetham, G V Kumar, Effect of SiC Reinforcement on Microstructure and Mechanical Properties of Aluminum Metal Matrix Composite, IOP Conf. Series: Materials Science and Engineering 376 (2018) 012057 doi:10.1088/1757-899X/376/1/012057.
39. K. Wang, H. Y. Jiang, Y. X. Wang, Q. D. Wang, B. Ye, W. J. Ding, Microstructure and mechanical properties of hypo-eutectic Al-Si composite reinforced with TiCN nanoparticles, Materials and Design 95 545–554 (2016).
40. K. Wang, G. P. Xu, H. Y. Jiang, Q. D. Wang, B. Ye, W.J. Ding, Development of Al-TiCN nanocomposites via ultrasonic-assisted casting route, Ultrasonics - Sonochemistry 58 104626 (2019).

CHAPTER II-6

STRENGTH REDUCTION IN COMPOSITES REINFORCED WITH NANO-SIZED PARTICULATES

LUBOMIR A. ANESTIEV

In a previous chapter, Ch. II-4, we discussed the most important mechanisms that govern the mechanical strengthening of a composite material. From these theories, it could be deduced that the increase of the volume fraction of the reinforcement would lead to an increase in the strength of the composite, whatever the volume fraction (VF) of the reinforcement. The experimental evidence, however, shows that the increase of the composite's strength is limited, i.e., not incessant growth of the strength is achieved by the increase of the reinforcement fraction (see Ch. II-5). As reported by many investigators, a limit in the VF of the reinforcement exists, $f_{\max}$, beyond which the strength begins to decrease. The present chapter aims to distinguish the mechanisms behind the strength reduction observed and to point out the factors that govern these mechanisms. Unfortunately, so far no sufficient attention has been paid or attempts made to explain the decrease of the composite' strength that occurs when VF exceeds $f_{\max}$.

In the present author's opinion, the factors governing the strength reduction could be divided into three major groups: (i) Factors depending on the mechanical properties of the matrix and the reinforcement; (ii) Factors depending on the specific properties of the reinforcement, such as the specific weight. The latter governs one of the most frequently quoted reasons for the decrease in strength of the composites reinforced with nano-sized particulates, the agglomeration; (iii) The combined influence of the geometry of the reinforcement and the mechanical properties of the matrix.

The first two groups of factors are directly dependent on the volume fraction of the reinforcement. Although the third is seemingly independent of the VF as it will be shown below, an implicit connection between the shape of the reinforcement and the mechanical properties of the composite exists.

6.1 Strength reduction due to the mechanical properties

In the practice, the value of the materials intended for use in structural constructions is their ability to sustain considerable loads without yielding. From that point of view, therefore, the most important mechanical property for a structural engineer is the yield strength of a material [1]. Moreover, the yield strength is the most representative mechanical characteristic of the material, when the effects of the strengthening and strength reduction mechanisms are to be studied [2,3]. Therefore, it is desirable to focus on that mechanical property when studying the strength reduction mechanisms in particulate-reinforced composite materials. In the approach, adopted here, the mechanisms of strength reduction will be studied in conjunction with those of strengthening. In that way, it will be possible to use the accumulated so far experimental data of the effect of the volume fraction of the reinforcement on the strengthening and strength reduction in composites reinforced with nano-sized particulates.

As it was repeatedly mentioned, it is well established experimental fact that the yield strength of a composite, reinforced with nano-sized particulates, is strongly dependent on the volume fraction of the reinforcement, *f*, thence, $\sigma_Y = \sigma_Y(f)$. It was also established that the function $\sigma_Y(f)$ passes through a maximum. This experimental fact suggests that at least two mechanisms, acting in opposite directions and dependent on the VF of the reinforcement, contribute to the yield strength of the composite. Taking into account the mechanisms contributing to the strength of a material, for the yield strength of the composite, $\sigma_Y(f)$, could be readily written:

$$\sigma_Y(f) = \sigma_{str}(f) - \sigma_{sr}(f). \quad (1)$$

In the expression above $\sigma_{str}(f)$ is the cumulative strengthening contributed by all or some of the strengthening mechanisms discussed in Ch. II-4, while $\sigma_{sr}(f)$ is the strength reduction generated by mechanism(s) which is yet to be determined. (Obviously, the number of

active strengthening mechanisms will vary depending on the structure and the composition of the reinforcement and the matrix, the temperature, the loads applied, etc.). For the $\sigma_{str}(f)$ is thus valid, $\sigma_{str}(f) = \frac{\sum_i \Delta\tau_i(f)}{m}$, where $\Delta\tau_i$ is the contribution of the *i*th strengthening mechanism to the resolved in the glide plane shear stress and *m* is the Schmid factor. Thus, our objective here is to determine, $\sigma_{sr}(f)$, since the strengthening mechanisms are well established and generally known (see Ch. II-4).

In a preceding chapter, Ch. II-4, it was repeatedly stressed that the strengthening of a composite (natural or artificial) is a consequence of the stresses generated in the matrix due to the impediment of the dislocation mobility by different obstacles. The obvious way to explain the strength reduction in a composite, therefore, should be sought in the factors leading to the reduction of these stresses. Two possibilities exist: (i) Making the obstacles penetrable to the moving dislocations; (ii) Absorbing the stress-energy accumulated around the obstacles.

(i) *Penetrable by the dislocation obstacles*. In Ch. II-4, see Section 4.2.1, was shown that at certain conditions the dislocations could overcome the obstacles by shearing through the reinforcement particles. The condition that should be fulfilled, so that this mechanism to be active, is the reduction of the reinforcement particles size. Indeed, according to the theory, when the radius of the reinforcement particle is below some critical value, a possibility exists that the accumulated stress energy will exceed the energy required for disrupting the bonds acting between the atoms of the reinforcement. However, when the reinforcement particles' size is above that critical value another mechanism is activated, the Orowan's bowing mechanism. The latter implies that the stress around the obstacle should decrease with the increase of the reinforcement particles' size, see Eq. 24 and Fig. II-4-5 in Ch. II-4. This is valid, however, only if the stress accumulated in the dislocations loop(s), left after the passage of the dislocations, is neglected, or as assumed in Orowan's theory, if a single residual loop is left after the dislocation passage. As pointed out by Fisher, Hart, and Pry (FHP) [4], however, there could be more than one residual loop formed around the obstacle; the number of the loops should match the number of dislocations that passed it. Therefore, based on the preceding arguments it is not quite clear how far the decrease of the accumulated stress will continue with the increase of the reinforcement size. Moreover, at nano-sized composites, the size of the reinforcement particulates is limited within the range, 20-100 nm, thus it is difficult to

accept that the experimentally observed reduction is due to reinforcement size alone.

Because of the reasoning above, in the present author's opinion, the reported by many authors reduction in the composite strength should be sought in a mechanism based on the absorption of the accumulated stress-energy which takes place inside the matrix surrounding the reinforcement.

(ii) *Strength reducing mechanism based on stress-energy absorption.* In a study carried out in a recent paper [5], the present authors argued that the strength reduction of the composite could be due to the formation of cracks in the matrix (see also the discussion in Appendix II-A). The following considerations were brought in support of this hypothesis: (a) Due to the impediment of the mobility of the dislocations a considerable amount of stress-energy could be accumulated around the obstacles. Recall, that according to FHP theory, any dislocation that has bypassed the obstacle leaves a dislocation loop around it. See also the results from the case study in Ch. II-7; (b) Ultimately, this is the Orowan's mechanism by which, in most of the cases, the dislocations overcome the obstacles (the used in the practice sizes of the reinforcement are usually above $\left\langle r_p \right\rangle_{crit}$). (c) The increasing mechanical stress that accumulates in the matrix after each dislocation passage cannot be infinite. Apparently, after the formation of several dislocation loops, the stress accumulated in the matrix near the reinforcement would exceed the matrix strength limit, σ_b. This accumulated stress should be somehow relieved. (d) On the micro/nano-size level the only way to reduce stress is by the formation of cracks. The act of the cracks' formation is an effective way to absorb the accumulated energy [6]. By Orowan's theory, the most stressed parts of the matrix are those near the reinforcement, therefore, if the assumption above is correct, the cracks should be localized in the vicinity of the reinforcement. The result from the TEM study of an Al-TiCN composite, shown in Fig. II-6-1, proves that assumption correct. It is readily noticed that the cracks and their branching are located near the reinforcement particles. (e) According to Orowan's theory, cracking of the matrix should lead to a reduction in the accumulated stress, and to a reduction in the force required to push the dislocations between the reinforcement particles. As a consequence, this would reduce the strength of the composite, which is in fact observed experimentally (see Fig. II-7-3 in Ch. II-7).

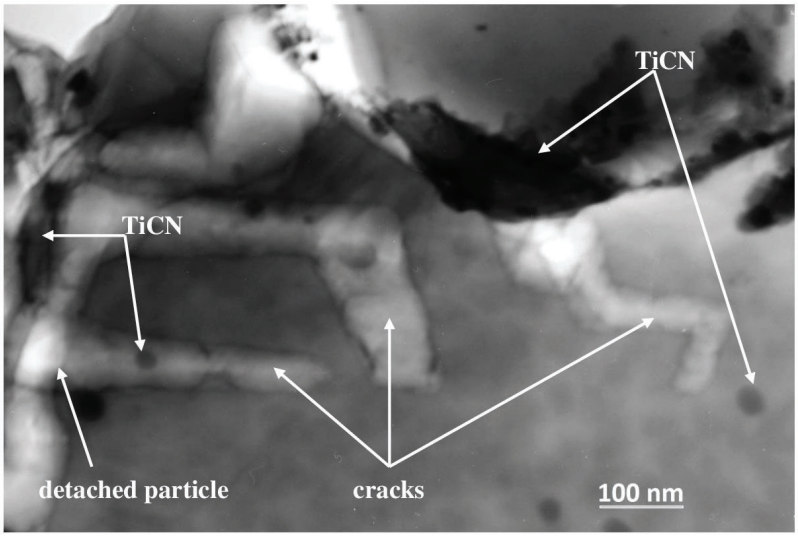

Figure II-6-1 TEM micrograph showing several cracks formed in the Al-matrix in an Al-TiCN composite. The micrograph shows that the breadth of the cracks is not constant, which is deduced by the brightness of the cracks' traces. The bright spot (left), from which multiple cracks have grown, is a void left by a reinforcement particle (~50 nm in diameter) that has detached during the specimen preparation (Note: this micrograph is a copy of Fig. II-2-12 in Section 2.8, Ch. II-2).

In their theory, FHP-authors calculated that the maximal stress accumulated in the matrix depends on the VF of the reinforcement and that it should be equal to, $\sigma_{cr} f^{3/2}$, see Section 4.4 in Ch. II-4. Originally FHP associated the proportionality constant, σ_{cr}, with the fracture stress limit of the reinforcement or the matrix. However, in the practice, the reinforcement material is selected in a way to possess a strength limit much higher compared to that of the matrix, σ_{cr}^{m}. Therefore, it is reasonable to accept that the cracking occurs only in the matrix. It should be noted that this assumption is confirmed by the results shown in Fig. II-7-1 and Fig. II-7-3 in Ch. II-7. By adopting the results of FHP and bearing in mind the strength-reducing factor above, it could be argued that: (a)

$\sigma_{sr}(f) \propto \sigma_{cr}^{m} f^{\frac{3}{2}}$; (b) the proportionality term, σ_{cr}^{m} is associated with the stress relieved by the formation of cracks in the matrix. By making use of the Griffiths equation, see Eq. 19 in Section 2.8 of Ch. II-2, for the stress absorbed by the formation of a crack, is readily obtained; $\sigma_{cr}^{m} = \frac{K_I}{\sqrt{\pi l}}$. As in Section 2.8 in Ch. II-2, *l*, is the crack's length, and K_I [Nm$^{-3/2}$] is the fracture toughness of the matrix material in the case that the crack grows in a plane perpendicular to the applied load (as shown in Fig. II-7-1 and Fig. II-7-3 in Ch. II-7). Thence, when several cracks are formed in the matrix, each of length l_i, the cumulative stress relieved, σ_{cr}^{m}, should be:

$$\sigma_{cr}^{m} = \frac{K_I}{\sqrt{\pi}} \sum_{i}^{n} \frac{1}{\sqrt{l_i}} = \frac{K_I}{\sqrt{\pi}} S . \qquad (2)$$

Where: $S = \sum_{i}^{n} \frac{1}{\sqrt{l_i}}$ [m$^{-1/2}$] and *n* is the average number of cracks per reinforcement particle. Thus, for $\sigma_{sr}(f)$ should be valid:

$$\sigma_{sr}(f) = \frac{K_I S}{\sqrt{\pi}} f^{\frac{3}{2}} H_V(\sigma_{cr}, \sigma_{sr}) \qquad \text{[Pa]}. \qquad (3)$$

Here, $H_V(\sigma_b, \sigma_{sr}) = \begin{cases} 1, & \sigma_{sr} > \sigma_b \\ 0, & \sigma_{sr} \le \sigma_b \end{cases}$ is the Heavyside step function which accounts for the fact that the cracking occurs when the strength limit of the matrix, σ_b, is exceeded.

6.1.1 Evaluation of the yield strength of a composite

As of above, the yield strength of a composite should be a difference between $\sigma_{str}(f)$ and $\sigma_{sr}(f)$. By assuming, according to the clauses of the hypothesis above, that Orowan's strengthening mechanism is dominant when the reinforcement size exceeds $\langle r_s \rangle_{crit}$, it is possible to evaluate the increase of the yield strength of the composite, compared to that of the

matrix. Indeed, replacing in Eq. 1 $\sigma_{str}\left(f\right)$ with MAO (Eq. 26 from Section 4.4 of Ch. II-4) and $\sigma_{sr}\left(f\right)$, with its equal from Eq. 3, and taking into account that, $G=\frac{E}{2\left(1+\nu\right)}$, for the relative yield strength increase of the composite as a function of VF is obtained:

$$\Delta\sigma_{Y}\left(f\right)= \\ =\frac{0.067NEb\ln\left(\Lambda/r_{0}\right)}{\left(1+\nu\right)\left(1-\nu\right)^{1/2}\left\langle r_{p}\right\rangle}\frac{1}{2.094f^{-1/2}-2}-\frac{K_{I}S}{\sqrt{\pi}}f^{\frac{3}{2}}H_{V}\left(\sigma_{cr},\sigma_{sr}\right). \quad (4)$$

Although the addition of the Heavyside's step function could prove in some cases indispensable, the estimates carried out for AMCs showed that for, $f\geq 0.005$, $H_{V}\left(\sigma_{cr},\sigma_{sr}\right)$ could be readily replaced with 1. Therefore, it is up to the user of Eq. 4 to decide, by checking the conditions of applicability of the Heavyside's step function, which value the Heavyside function takes in its experiment. From here on it will be assumed that $H\left(\sigma_{cr},\sigma_{str}\right)=1$. Thence, Eq. 4 could be rewritten as:

$$\Delta\sigma_{Y}\left(f\right)= \\ =\frac{0.067NEb\ln\left(\Lambda/r_{0}\right)}{\left(1+\nu\right)\left(1-\nu\right)^{1/2}\left\langle r_{p}\right\rangle}\frac{1}{2.094f^{-1/2}-2}-\frac{K_{I}S}{\sqrt{\pi}}f^{\frac{3}{2}}. \quad (5)$$

Eq. 5 allows (i) evaluation of the relative yield strength of composites reinforced with nano-scale particulates at different VF, provided that the values of all of the involved parameters are known or (ii) evaluation of the parameters, $\frac{0.067NEb\ln\left(\Lambda/r_{0}\right)}{\left(1+\nu\right)\left(1-\nu\right)^{1/2}\left\langle r_{p}\right\rangle}$ and $\frac{K_{I}S}{\sqrt{\pi}}$, from the experimental data, thus, obtaining valuable information about the mechanisms governing the mechanical strengthening of the composite. For practical application of equation 5 to the study of a particular composite, see ch. II-7.

The evaluation of the parameters involved could be done in two ways: (i) Directly, by nonlinear regression. This approach, however, requires a

considerable amount of experimental data points, which are not always available. (ii) Graphically, by plotting $\Delta\sigma_Y = \Delta\sigma_Y(f)$ in a set of coordinates that render Eq. 5 linear.

A linearization procedure is shown in Appendix II-B, where the linearization of Eq. 5 is achieved by recasting the latter in a new set of variables, $\Delta\sigma_Y$ and $\xi = \dfrac{\left(2.094 - 2f_{\max}^{1/2}\right)^2 f_{\max}}{0.698\left(2.094 f^{-1/2} - 2\right)} - f^{\frac{3}{2}}$. Thence:

$$\Delta\sigma_Y = \frac{K_I S}{\sqrt{\pi}}\left(\frac{\left(2.094 - 2f_{\max}^{1/2}\right)^2 f_{\max}}{0.698\left(2.094 f^{-1/2} - 2\right)} - f^{\frac{3}{2}}\right) = \frac{K_I S}{\sqrt{\pi}}\xi. \quad (6)$$

In Eq. 6, with $f_{\max}$ is denoted the value of f, at which $\Delta\sigma_Y$ passes through a maximum. Therefore, plotting the experimental data in $\Delta\sigma_Y - \xi$ coordinates allows determining from the slope of the plot, $\dfrac{K_I S}{\sqrt{\pi}}$. By solving Eq. II-B-2.2 in Appendix II-B, the term, $\dfrac{0.067 NEb \ln\left(\Lambda / r_0\right)}{\left(1+\nu\right)\left(1-\nu\right)^{1/2}\left\langle r_p \right\rangle}$, is evaluated.

Our experience with employing the graphical method shows that the latter is very sensitive to the accuracy with which is determined, $f_{\max}$. Thus, if a sufficient number of experimental points are available, it is advisable to use nonlinear regression methods for determining the parameters $f_{\max}$, *N,* and *S*. Yet, the graphical method is very convenient when the number of the experimental points is limited.

It is understandable, that the increase of the volume fraction of the nano-sized additive beyond some limit would eventually lead to problems with the physical integrity of the composite. It is therefore of academic interest to test the developed above theory beyond the limits of the VF which are usually employed in the practice. The objective of such a study is to find the value of, *f*, at which the composite will disintegrate. It is reasonable to assume that this will take place when the predicted yield strength of the composite is zero, $\sigma_Y(f) = 0$. Replacing in Eq. 5 the parameters involved with those determined in the next chapter; $\Delta\sigma_Y = \sigma_Y$

- 74 MPa, (see Table 2, Ch. II-7), $\frac{0.067\,NEb\ln\left(\Lambda/r_0\right)}{\left(1+\nu\right)\left(1-\nu\right)^{1/2}\left\langle r_p\right\rangle}=393$ MPa and $\frac{K_I}{\sqrt{\pi\lambda}}=2230$ MPa, for the yield strength as a function of f is obtained:

$$\sigma_Y=74+\frac{393}{2.094f^{-1/2}-2}-2230f^{\frac{3}{2}}\ \text{(MPa)}. \qquad (7)$$

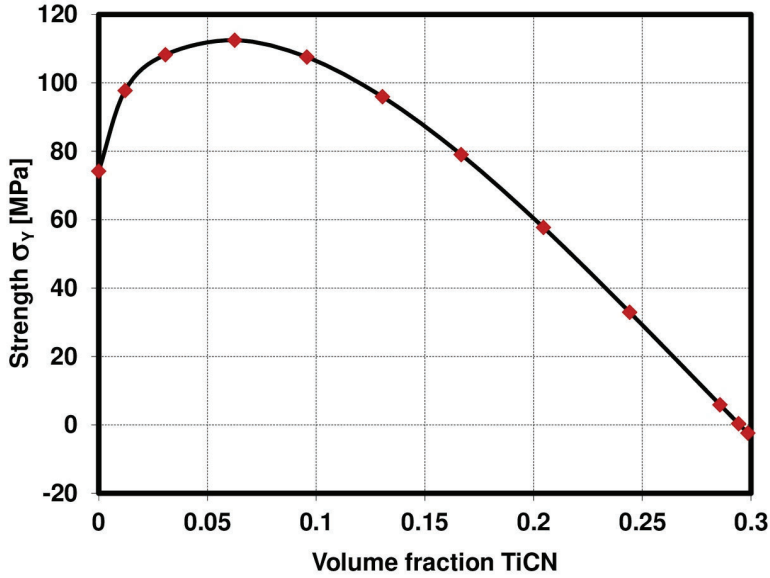

Figure II-6-2 Plot of Eq. 7 in $\Delta\sigma_Y-f$ coordinates, showing the predicted by that equation yield strength as a function of the volume fraction of the reinforcement. Notice that at $f\sim 30$ % the strength of the composite is already negative, which practically means that at that value for f the composite will physically disintegrate.

By equating Eq. 7 to zero a non-linear equation is obtained whose solution, with respect to f, predicts that the disintegration of the composite (in the case of Al-TiCN) will take place at $f\approx 0.294$ ($w\approx 41$ wt. %), i.e.,

far below VF = 1 (see Fig. II-6-2). Our experiments, see the next chapter, confirmed this result; our attempt to produce a composite with w = 25 wt. % TiCN ($f \approx 17\%$) failed because the composite disintegrated during the stage of the hot extrusion (see the processing chart-flow shown in Fig. II-1-1, Ch. II-1). It could be, thus inferred that the theory described is valid up to, $f \approx 30\%$. Yet, without hard experimental data to support the preceding speculative conclusion, the results obtained from the solution of Eq. 7 may be due simply to pure coincidence.

A test of the theory developed and how it correlates with the experimental results obtained so far is shown in the next chapter.

In the authors' opinion, Eq. 5 is inapplicable to composites reinforced with CNT, because the latter lacks the strength to withstand the stresses involved (see the discussion in Appendix II-A).

6.2 Agglomeration

One of the serious problems encountered in the production of composites is the agglomeration of the reinforcement particles. The problem typically appears (see Ch. II-1 and Ch. II-5) when the composite is prepared by stir casting. However, cases have been reported where the hot extrusion method has been used. As a rule, the agglomeration leads to deterioration of the mechanical properties of the composite. This section gives a qualitative explanation, based on the theory above, why the agglomeration leads to the deterioration of the mechanical properties of the composite.

6.2.1 Factors leading to agglomeration at the composites' production

It is sometimes erroneously believed that the cause of the agglomeration is Van der Waals forces acting between the particles. This could be true, but only before adding the reinforcement to the melt. However, when the reinforcement comes in the contact with the liquid metal, the situation changes dramatically because in a melt the Van der Waals forces should be equal to zero. That difference in inter-particle interaction behavior, inside and outside of the melt, follows from the nature of the Van der Waals forces. Recall that the Van der Waals forces are a result of permanent, or dynamic, unevenness in the distribution of electric charges, which for the case discussed here means uneven distribution of these charges on the reinforcement particle’s surface. As a result, depending on the geometry of the reinforcement particle, permanent

or temporary multipoles, e.g., dipoles, quadrupoles, etc., are generated by these free electric charges. Keeping in mind that liquid metals are good conductors, it is obvious, that inside the melt, whatever the distribution of electric charges, it could not be supported; at the first contact with the melt, these will be neutralized and conducted, via the melt, to the ground. Thence, the local uneven distribution of the electric charges, which is the cause of the existence of the Van der Waals forces, will cease to exist. The causes for the agglomeration, therefore, should be sought elsewhere.

By analyzing the possible factors that could lead to an agglomeration the most probable one seems to be the liquation, caused by the difference between the specific weights of the reinforcement and the melt (usually it is 2:1). Suppose that the process of composite production is the stir-casting, two types of forces acting on the reinforcement particles, which could lead to agglomeration, are distinguishable; (i) the gravity forces and (ii) the centrifugal forces. Recall that both of these depend linearly on the specific weight of the reinforcing material. It should be noted, however, that each of these forces will be dominant at different stages of the stir-casting process.

In a broad sense, the agglomeration of the particles introduced into the melt could be characterized by the time it takes for a particle, with radius R_p, to reach the wall of the stir-furnace or the bottom of the crucible, i.e., the sedimentation time, t_{sed} .

Before starting the analysis of the factors of the sedimentation, however, it is appropriate to discuss the flow regime induced by the impeller. In other words what kind of flow do we have in the stir furnace, laminar or turbulent.

The transition from laminar to turbulent flow during stirring is determined by the Reynolds number of the melt in the stir-furnace. For an impeller-driven flow, the Reynolds number, **Re**, is given from the formula, $\mathrm{Re} = \frac{\omega D_{impeler}^2}{\nu}$ (Perry et al, 1999), where $D_{impeler}$ is the diameter of the impeller, ω is the angular velocity of the melt (induced by the impeller), and ν is the melt's kinematic viscosity. The evaluation of **Re** by replacing $D_{impeler}$= 0.2 m, $\omega \approx 4$ s^{-1}, and $\nu \approx 10^{-7}$ m^{2}s^{-1} (data for Al at the melting point [8]) yields Re≈2. 10^6 which is well above the critical **Re** number for the transition from laminar to turbulent flow (**Re**≈10^4). This fact makes the analysis of the melt and the particles' motion in the stir furnace very complicated. However, a computer simulation of the stirring process revealed that the time-averaged melt velocities, with a good approximation, could be assumed to be laminar (see Fig. 18.36 in Perry et

al, 1999). Therefore, the results that will be obtained further on could be assumed, in general, correct and used in the evaluation of the sedimentation time of the reinforcement particles in the stir-furnace. (In support of the preceding assumption one could consider the water flow under gravity in a river or a channel. As a rule, those flows are turbulent. However, the water in the river maintains a general flow direction and maintains an average velocity in that flow direction, despite local fluctuations in velocity directions due to turbulence.) Thence, in the analyses below, the melt flow in the stir-furnace could be considered quasi-laminar, thus neglecting the rapid changes in the velocity directions due to local turbulences.

(i) *Sedimentation due to the centrifugal force*. The centrifugal forces are dominant during the stage of stirring. Thence, the effect of the gravitational force could be neglected in the analysis below. From the course of mechanics is known, see e.g. [7], that the centrifugal force acting on a particle suspended in melt should be equal to, $F_{cf} = m_p r\omega^2$. Here m_p is the mass of the reinforcement particle and r is the distance of the particle from the propeller axis. Due to the action of, F_{cf}, the reinforcement particles will be pushed, together with the melt in which they are suspended, toward the wall of the furnace. Therefore, given sufficient time of stirring, all of the introduced particles would reach the furnace wall, leaving the main melt body depleted of reinforcement particles. Near the furnace wall, because of the friction between the melt and the furnace wall the tangential velocity of the melt drops to zero (due to the boundary layer effect, see e.g., L. Prandtl and G. Tietjens, 1934), and the gravitational force becomes dominant. To avoid that scenario, it is important to evaluate the time for which the particle will reach the furnace wall (for convenience below that time is referred to as sedimentation time). Assuming that the friction forces between the melt and the particle are governed by the Stokes-Einstein law, for the sedimentation time, t_{sed}, required by a particle with a mean particle's radius $\langle r_p \rangle$ to reach the wall of the stir-furnace is valid:

$$t_{sed} = \frac{\ln\left(\frac{H_{sf}}{r_0}\right)}{\frac{9\nu}{2\left\langle r_p \right\rangle^2}\left(\sqrt{1+\frac{16}{81}\left(\frac{\omega\left\langle r_p \right\rangle^2}{\nu}\right)^2}-1\right)} \approx \frac{9\nu \ln\left(\frac{H_{sf}}{r_0}\right)}{4\omega^2\left\langle r_p \right\rangle^2}. \quad (8)$$

Where: r_0 is the initial distance of the particle from the impeller axis, and H_{sf} is the internal radius of the stir-furnace (the distance between the impeller axis and the inner wall). In the last term at the right-hand side of Eq. 8, is accounted that in the case studied, $\frac{16}{81}\left(\frac{\omega\left\langle r_p \right\rangle^2}{\nu}\right)^2 << 1$.

As seen the sedimentation time is inversely proportional to the squares of the particle's radius and proportional to the angular velocity of the melt Keeping in mind that the latter is induced by the impeller follows that; the higher the angular velocity of the melt the less is the sedimentation time. Thence, a conclusion could be drawn that the vigorous stirring of the melt-particles mixture should be avoided. The evaluation of the sedimentation time by Eq. 8 for, say; $\frac{H_{sf}}{r_0} \approx 10$, $\left\langle r_p \right\rangle \approx 40$ nm, $\omega \approx 4$ s^{-1}, and $\nu \approx 10^{-7}$ m^{2}s^{-1} yields $t_{sed} \sim 2.10^7$ s, which is several thousand hours. Therefore, if it were possible to introduce the particles into the melt without being agglutinated, then the stirring stage would readily reach its goal. Regrettably, as we will see in the discussion below, this could not be easily achieved.

(ii) *Sedimentation due to the gravitational force.* The gravitational force becomes dominant at two of the stages of the stir-casting process; (a) when the dissolved reinforcement particles reach the furnace wall (as described in the preceding Subsection (i)), and (b) at the casting stage when the sedimentation time (here that is the time required by the particles to reach the bottom of the crucible) is less than the time for the solidification of the melted matrix. It could be shown that the time, required by a particle to sink to the bottom of the crucible, is a solution of the following non-linear algebraic equation:

$$\frac{2\left[1-\left(\rho^L/\rho^S\right)\right]g\left\langle r_p\right\rangle^2}{9\nu\left(\rho^L/\rho^S\right)}t_{sed}+ \\ +\frac{4\left[1-\left(\rho^L/\rho^S\right)\right]g\left\langle r_p\right\rangle^4}{81\nu^2\left(\rho^L/\rho^S\right)^2}\left[\exp\left(-\frac{9\nu\left(\rho^L/\rho^S\right)}{2\left\langle r_p\right\rangle^2}t_{sed}\right)-1\right]=H \tag{9}$$

Where: H is the depth of the crucible, ρ^S and ρ^L are the specific weights of the reinforcement of the melt, and g is the gravitational constant. In Eq. 9 the friction force is again evaluated by the Stokes-Einstein law.

The equation above could be solved only numerically. However, presuming a steady-state rate of sinking of the reinforcement particles into the melt, vanishes the second member in the left-hand side of the equation, thus yielding for the time of sedimentation, t_{sed} :

$$t_{sed}=\frac{9\nu\left(\rho^L/\rho^S\right)H}{2\left[1-\left(\rho^L/\rho^S\right)\right]g\left\langle r_p\right\rangle^2}. \tag{10}$$

It is noticed that the sedimentation time is again inversely dependent on the squared particle radius. Thus, the smaller the particle the longer is the time of sedimentation. Thence, the small size of the nano-particles should be in favor of an even distribution of the reinforcement within the melt. Indeed, the evaluation of the sedimentation time by Eq. 10 for, say; $\rho^L/\rho^S\approx 0.5$, $\left\langle r_p\right\rangle \approx$ 40 nm and H=30 cm yields $t_{sed}\sim 5.\ 10^5$ s, i.e., t_{sed} would be above a hundred hours. Again, the preceding evaluation is valid only if the reinforcement particles are added individually, as single particles, into the melt. Regrettably, at the stir casting the particles are added to the melt as bulk agglutinated chunks; it is expected that the stirring would crush these chunks into smaller pieces. As it will be shown in the next subsection, this is not the case.

6.2.2 Causes of the agglomeration

As shown above, when the armament is added individually into the stir furnace, the purpose of the stir casting will be fulfilled seamlessly. However, the presence of agglomerates in the final product suggests that something is amiss. Keeping in mind the preceding considerations it should be thus reasonable to seek the cause of the agglomeration at stir

casting in the innate agglutination of the reinforcement particles when these are added to the melt. If the crushing of the agglutinates fails, the gravitational and centrifugal sedimentation times would change dramatically. Regrettably, the experience gained so far shows that it is difficult to avoid the agglutination of the reinforcement particles when these are added to the melt. Therefore, in the discussion below, it can be firmly assumed that the reinforcement enters the melt in the form of agglomerates of different sizes that, despite the action of the impeller, succeed in, more or less, keeping their initial size. As of above, it is not the Van der Waals forces that keep particles agglutinated together inside the melt, rather it is the surface tension. Indeed, together with the particles in the melt is introduced also the gas in which these particles have been stored before entering into the feeder. It is the surface tension between the melt and the as-introduced gas that keeps the particles together, as pointed out by A. Sommerfeld in [7] as in an "elastic coating". Due to the surface tension, it is very difficult for the molten metal to penetrate inside these gas-particles 'containers" and to wet the reinforcement particles. The preceding is true even at a vigorous stirring of the as-formed slurry – melt-gas-powder. The following considerations support this argument. Let the distance between the reinforcement particles in the gas-particles agglomerate be proportional to $\langle r_p \rangle$ (which means not densely packed particles). As a rule, the reinforcements used are unwettable by the melt (see as a confirmation of this statement Fig. II-3-5b). Thence, by the virtue of the Laplace formula, for the pressure which is necessary to separate the particles apart is valid, $p = \frac{2\sigma}{\langle r_p \rangle}$. Here σ is the surface tension on the melt-gas surface. By substituting in the latter expression, say; $\langle r_p \rangle \approx 40$ nm and $\sigma \approx 1$ Nm^{-1} for p is obtained, $p \approx 5.10^8$ Pa or 5. 10^3 bars! Yet, even if the forced stirring of the melt succeeds in crushing the sizes of these gas-particles containers, say, to 4 micrometers both sedimentation times (the gravitational as well as the centrifugal) will be, as already pointed out above, reduced dramatically (by a factor of 10^4 each) which is to a minute and half an hour for the gravitational and centrifugal sedimentation. Given the estimates obtained above, however, breaking up the incoming from the feeder agglutinates, into such small agglutinates, would be a very difficult task (see required pressure). Thence, even a very intensive stirring would not help in avoiding the agglomeration. Moreover, recall that an intensive stirring will force the reinforcement particles in the direction of the wall of

the crucible, where, due to the friction with the wall of the stir-furnace, these will sediment gravitationally, i.e., much faster than estimated. Based on the results so far it could be predicted that a part of the introduced into the melt reinforcement particles, will be sedimented along the bottom periphery of the stir-furnace. The preceding explains, why the cases of agglomeration are more frequently reported at increased VFs of the reinforcement.

6.2.3 Factors leading to agglomeration in the other methods of composites' production

The other methods of composites' production, used in the practice, are also not without deficiencies. Agglomeration of the reinforcement particles was also reported by employing one of the most prospective methods of composites production, the hot extrusion. Here again, the agglomeration is due to the liquation, caused by differences in the specific weights of the reinforcement and the matrix. Indeed, when working with powder mixtures the liquation could arise because of (see Section 1.1.1): (i) Differences in the specific weight of the powders in the mixture (the "classical" cause of the liquation) and (ii) Differences in the sizes of the powder particles in the mixture, i.e. by the size-liquation. When in a powder mixture the particle sizes differ considerably (as in the case of mixtures of nano-sized and micron-sized powders) the smaller particles literally "ooze" (due to the gravity, vibrations during handling, etc.) through the interstices formed between the larger powder particles. In the case of using nano-sized reinforcements, the ratio between the powder sizes of the reinforcement (smaller particles) and the basic (larger particles) is ~1:1000. Thus, without taking special measures to avoid the size-liquation the latter would lead to agglomerations inside the powder mixture which later will be transferred to the extrudate. Hence, the cases of agglomeration in hot extruded composites, reported by some authors. The size-liquation, however, could be avoided by a simple but very effective procedure, Mix & Mill (M&M), which should precede the compaction of the powders and the hot extrusion. At the M&M procedure, the liquation (respectively, the accompanying agglomeration) is prevented by embedding the reinforcement particles onto the base-powder surface. Ensuring in that way easy handling of the green powder mixture during the processing of the composite and subsequently a homogeneous distribution of the reinforcement throughout the composite. (Notice that the M&M procedure is applicable only if differences in the ductility of the matrix and the reinforcement powders exist, e.g. ductile base powder

(matrix) and rigid (unyielding) reinforcement.) As suggested by the name the M&M procedure is carried out in a ball mill, usually for a time lasting from 30 min to an hour.

Regrettably, within the limited volume of this part of the book, it is impossible to discuss all factors leading to agglomeration at the production of composites, thus restricting ourselves to those few discussed so far.

6.2.4 Agglomeration and the mechanical properties of the composite

The theory of strength reduction, developed in Section 6.1, allows a qualitative explanation of how the agglomeration affects the mechanical properties (more accurately how it reduces the strength) of the composite, say, its yield strength.

When an agglomeration is present, within the composite are formed regions that are enriched and depleted of reinforcement particles. Let; f_{in} to be the VF of the reinforcement particles introduced in the composite, see Fig. II-6-3. In case that the reinforcement particles are homogeneously distributed the expected increase of the yield strength, according to Eq. 5, should be $\Delta\sigma_{Yex}$. Let the VFs of the reinforcement in the enriched and depleted regions be as shown in the figure. According to Eq. 5, the actual strengthening effect achieved in enriched and depleted regions would be, $\Delta\sigma_{Yenr}$, and $\Delta\sigma_{Yd}$, instead of $\Delta\sigma_{Yex}$, as indicated in Fig. II-6-3. Under load, the measured strength of the composite will be the least of, $\Delta\sigma_{Yenr}$, or $\Delta\sigma_{Yd}$, in the hypothetical case shown in Fig. II-6-3 that is $\Delta\sigma_{Yd}$. As seen the achieved strengthening will differ from that expected, which is $\Delta\sigma_{Yex}$, thus explaining the reported by many researchers decrease of the composite strength, when an agglomeration is present.

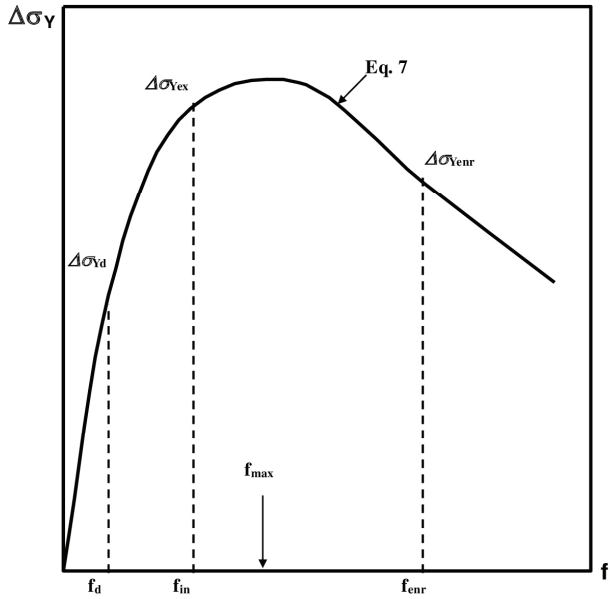

Figure II-6-3 Graph illustrating the effect of the reinforcement's agglomeration on the yield strength of the composite. f_{in} is the introduced VF of the reinforcement. f_d and f_{enr} are the VFs of the reinforcement in the depleted, and the enriched regions in the composite. $\Delta\sigma_{Yex}$, $\Delta\sigma_{Yd}$, and $\Delta\sigma_{Yenr}$ are the expected and the actual increase of the yield strengths in the depleted and the enriched regions.

Based on the preceding considerations it could be argued that Eq. 5 could be used as a qualitative test for the presence or absence of agglomeration in the composite. That will be illustrated in the next chapter by applying the theory developed to experimental data of authors who reported agglomeration of the reinforcement in their experiments.

6.3 Effect of reinforcement shape irregularities on the mechanical properties of the composite

Another factor leading to strength reduction in composites is the shape irregularities of the reinforcement particles. From the structural mechanics is well known that the discontinuities in the material, such as inclusions, voids, or variations in the strength and stiffness, serve as a concentrator of stresses in the material when the latter is under, e.g., tensile load. Usually, in the specialized literature, the discontinuities in the material, like those listed above, are referred to as *stress concentration factors*. The effect of the shape irregularities of the reinforcement particles on the strengthening could be readily accounted for by using the tabulated results obtained in the mechanics of the materials, see e.g. [9 -11].

From the preceding, it could thus be deduced that the irregularities in the shape of the reinforcement particle would also serve as stress concentrators. The effect of these on the composite strength is not straightforward. When the composite is loaded, due to the irregularities of the reinforcement particles, the dislocation density in the matrix in the interparticle space would be higher. According to the theories discussed in Ch. II-4, this could lead to a sharp increase of the strengthening effect even at small loads. The as-generated high density of dislocations, however, would also lead to higher stresses in these parts of the matrix, and eventually to cracking and fracturing of the latter when the fracturing strength of the latter is exceeded. There are, however, advantages of using irregularly shaped reinforcement particulates. These could be sought in: (i) the desired strengthening effect could be achieved by using small VF of the reinforcement; (ii) at lower VFs the fracture ductility of the composite would be higher, thus, facilitating the machinability of the composite. A disadvantage is the fracturing and eventual destruction of the composite at relatively lesser loads, compared to those which will be achieved by a composite reinforced with regular-shaped particles.

Appendix II-A

In this Appendix are selected some topics on the composite strengthening which have not been discussed so far in this part of the book. In their paper, FHP argued that the breaking could occur, both, in the matrix and the reinforcement. Their point of view, however, is not supported by other authors, e.g., Ansell and Lenel, [12], who argued that the breaking should occur predominantly in the precipitates (reinforcement). It should be noted, however, that the papers cited are discussing precipitation hardening, i.e., they have been published 10-20 years before the first attempts of increasing the material strength by introducing "foreign" particulates in the metal matrix. In the specific case of the precipitation hardening, the theories proposed and the conclusions drawn are still valid today. The inference made is supported by the fact that the fracture toughness of most of the precipitates encountered in the practice does not exceed that of the maternal phase. For instance, the fracture toughness of $FeAl_3$ is 4.92 [$MNm^{-3/2}$] [13], i.e., comparable to that of the pure Al, which is ~5 [$MNm^{-3/2}$] [14].

The theory discussed in this chapter is based on the experimental fact that the fracture toughness of the reinforcement is much higher than that of the matrix. For instance, a cermet based on TiCN (TiCN with 5 wt.% Mo_2C) has a fracture toughness of 18.4 [$MNm^{-3/2}$] [15], i.e., its toughness exceeds that of the Al several times. Keeping in mind that in the metal matrix composites the load stress is transmitted from the matrix to the reinforcement it should be readily concluded that the first to crack under load will be the matrix, which could be deduced by simply comparing the values of the fracture toughnesses above.

That inference is supported by the results obtained from our experiments carried out on an Al-composite reinforced with TiCN. Fig. II-6-.4 shows a TEM micrograph of the matrix (Al) microstructure around a reinforcement particle after a tensile loading. The bright spots in the center of the particle aren't cracks, but a defect that occurred during the reinforcement production. Remarkably, despite the presence of those defects, the particle sustained extensive loading without cracking.

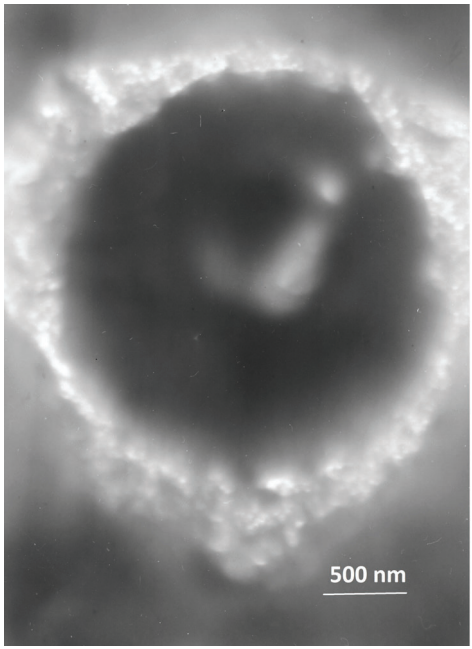

Figure II-6-4 TEM micrographs showing the microstructure of an Al-composite reinforced with TiCN. The bright halo surrounding the reinforcement particles (the dark spherical object in the center) is a result of the etching (for an explanation of that effect see the next chapter). The bright spots in the center of the particle aren't cracks, but defects that occurred during the production of the TiCN nano-particles. V. Dyakova [16].

Another topic worth discussing is; whether the cracking of the reinforcement would lead to a decrease in the stress accumulated in the matrix. (Recall that Ansell and Lenel supported the idea that the breaking should occur predominantly in the precipitates/particulates.) It seems that the answer to this question is negative. Indeed, even in the case that the reinforcement cracks its fragments will stay encapsulated inside the same cavity where the reinforcement particle did reside, which follows from the fact that these have nowhere to go. The reduction of the stress in the matrix can occur, hypothetically, only if the cracking leads to a reduction in the volume of the reinforcement fragments. In that case, the matrix will expand within the cavity occupied by the fragments, thus, relieving some

of the stress accumulated in it. An analysis, based on the theory of dislocations (see Ch. II-3), does not support this point of view. Indeed, the reduction of the stress accumulated would occur if the movement of the dislocations, around, or through the inclusions, is somehow facilitated. The fragmentation of the reinforcement particle will produce new surfaces which from the point of view of the dislocation theory could be considered as plane defects, similar to, e.g., the grain walls. As a result, the incoming dislocations will pile up around the fractured reinforcement, thus increasing, instead of decreasing, the stress accumulated in the matrix.

Appendix II-B

The linearization of Eq. 5 is done by employing the experimental fact that the function, $\Delta\sigma_Y = \Delta\sigma_Y(f)$, passes through a maximum at, $f_{\max}$. Thence for $\frac{d\Delta\sigma_Y}{df}$ at $f_{\max}$ is valid, $\left.\frac{d\Delta\sigma_Y}{df}\right|_{f_{\max}} = 0$. Thus, taking a derivative of both sides of Eq. 5, with respect to *f*, it is obtained:

$$\frac{0.067\,NEb\ln(\Lambda/r_0)}{(1+\nu)(1-\nu)^{1/2}\langle r_p\rangle} = \frac{\left(2.094-2f_{\max}^{1/2}\right)^2 f_{\max}}{0{,}698}\frac{K_I S}{\sqrt{\pi}} \text{ .(II-B-2.1)}$$

Replacing, $\frac{0.067\,NEb\ln(\Lambda/r_0)}{(1+\nu)(1-\nu)^{1/2}\langle r_p\rangle}$ in Eq. 5 with that from Eq. II-B-2.1 yields:

$$\Delta\sigma_Y = \frac{K_I S}{\sqrt{\pi}}\left(\frac{\left(2.094-2f_{\max}^{1/2}\right)^2 f_{\max}}{0.698\left(2.094f^{-1/2}-2\right)} - f^{\frac{3}{2}}\right) = \frac{K_I S}{\sqrt{\pi}}\xi \text{ .(II-B-2.2)}$$

The Eq. A-II-2.2 is linear relative to, $\frac{\left(2.094-2f_{\max}^{1/2}\right)^2 f_{\max}}{0.698\left(2.094f^{-1/2}-2\right)} - f^{\frac{3}{2}}$. Thence, by plotting the experimental data in $\Delta\sigma_Y - \xi$ coordinates from the graph's slope is determined, $\frac{K_I S}{\sqrt{\pi}}$ which, when substituted in Eq. II-B-2.1 determines $\frac{0.067\,NEb\ln(\Lambda/r_0)}{(1+\nu)(1-\nu)^{1/2}\langle r_p\rangle}$.

Suggested additional reading to Ch. II-6

1. W. D. Callister, Jr., Fundamentals of Materials Science and Engineering, Fifth Edition, John Wiley & Sons, Inc. 2001, ISBN 0-471-39551-X.
2. G. Gottstein, Physical Foundations of Materials Science, Springer-Verlag Berlin Heidelberg GmbH 2004, ISBN 978-3-662-09291-0 (eBook).
3. N. E. Dowling, Mechanical Behavior of Materials Engineering: Methods for Deformation, Fracture, and Fatigue, Fourth Edition, Pearson Education Limited 2013, ISBN 10: 0-273-76455-1.
4. Th. H. Courtney, Mechanical Behavior of Materials, Second Edition, Waveland Press, Inc. 2005, ISBN 1-57766-425-6.
5. S. P. Timoshenko and J. N. Goodier, Theory of Elasticity, Third Edition, McGraw-Hill, New York, 1970.
6. Perry's chemical engineers' handbook: Liquid-Solid Operations and Equipment, Robert H. Perry†, Don W. Green, and James O. Maloney Editors, Seventh Edition, McGraw-Hill Companies 1999, ISBN 0-07-049841-5
7. G. E. Dieter, Jr., Mechanical Metallurgy, in Metallurgy and Metallurgical Engineering Series, edited by Robert F. Mehl and Michael B. Bever, McGraw-Hill Book Company, 1961.
8. L. Prandtl and G. Tietjens, Applied Hydro·and Aeromechanics (based on lectures of L. Prandtl) Mcgraw-Hill Book Company, Inc. New York and London, 1934.

References to Ch. II-6

1. M. F. Ashby and D. R. H. Jones, Engineering Materials I, Third Edition, Elsevier Butterworth-Heinemann, Oxford, 2005, part C, Yield strength, tensile strength, and ductility.
2. P. Ma, Y. Jia, P. K. Gokuldoss, Zh. Yu, S. Yang, J. Zhao, and Ch. Li, Effect of Al_2O_3 nanoparticles as reinforcement on the tensile behavior of Al-12Si composites, Metals 7, pp. 359-370 (2017).
3. D. Zhang and Z. Zhan, Preparation of graphene nanoplatelets-copper composites by a modified semi-powder method and their mechanical properties, J. Alloys Compd. 654, pp. 226–233 (2016).
4. J. C. Fisher, E. W. Hart, and R. H. Pry, The hardening of metal crystals by precipitate particles, Acta Metall. 1, pp. 336-339 (1953).
5. L. Anestiev, R. Lazarova, P. Petrov, V. Dyakova, L. Stanev On the strengthening and the strength reducing mechanisms at aluminum

matrix composites reinforced with nano-sized TiCN particulates, Philosophical Magazine, 101:2, 129-153 (2021), DOI: 10.1080/14786435.2020.1821114.
6. J. H. Poynting, J. J. Thomson, A Text-Book of Physics, vol. 1, Properties of Matter, Charles Griffin and Company Limited, 1909.
7. A. Sommerfeld, Lectures on Theoretical Physics vol. 2, Mechanics of deformable bodies, Academic Press 1950.
8. A. T. Dinsdale and P. N. Quested, The viscosity of Al and its alloys – A review of data and models, Journal of Materials Science, 39 7221-7228 (2004).
9. S. P. Timoshenko and J. N. Goodier, Theory of Elasticity, Third Edition, McGraw-Hill, New York, 1970, ch. 13.
10. A. P. Boresi and R. J. Schmidt, Advanced mechanics of materials, Sixth Edition, John Wiley & Sons, Inc. New York, 2003, ch. 14.
11. R. G. Budynas A. M. Sadegh, Roark's Formulas for Stress and Strain, Ninth Edition, McGraw-Hill 2020, ISBN: 978-1-26-045376-8.
12. G. S. Ansell and F. V. Lenel, Acta metallurgica, 8, pp. 612-616 (1960).
13. P. Matysik, S. Jóźwiak, T. Czujko, Characterization of Low-Symmetry Structures from Phase Equilibrium of Fe-Al System Microstructures and Mechanical Properties, Materials 8, pp. 914-931 (2015); doi:10.3390/ma8030914.
14. Sh. Chou, J. Huang, D. Lii, H. Lu, The mechanical properties and microstructure of Al_2O_3/aluminum alloy composites fabricated by squeeze casting, Journal of Alloys and Compounds 436, pp. 124 - 130, (2007).
15. Zhou S.Q., Zhao W., Xiong W.H., Zhou Y.N. Effect of Mo and Mo2C on the microstructure and properties of the cermets based on TiCN. Acta Metall. Sin. 21, pp. 211-219 (2008).
16. V. Dyakova, private communication (2015).

CHAPTER II-7

CASE STUDY: STRENGTHENING AND STRENGTH-REDUCTION IN AN AL-TICN COMPOSITE

LUBOMIR A. ANESTIEV

The objectives of this part of the book are to study: (i) how the volume fraction of the reinforcement influences the microstructure and the mechanical properties of an Al composite reinforced with nano-sized TiCN, (ii) to test the validity of the theory of the strengthening and strength reduction developed in the preceding chapter, (iii) To reveal the mechanism(s) operative in a composite reinforced with nanosized particulates under tensile load, see Ch. II-6, and (iv) based on the experimental findings to determine the factors governing the strengthening and the strength reduction in the studied composite.

7.1 Materials

The research was carried out on aluminum reinforced with nano-sized TiCN. To avoid a possible decomposition of the reinforcement during the processing of the composite, the specimens were prepared by the powder metallurgy (PM) route, see Ch. II-1. As basic powders were used a commercially available Al powder (Al, min 99.5 wt. %; Fe, max. 1 wt. %) with a mean particle diameter of ~ 37 μm and a nano-sized TiCN powder with a particle diameter of ~50 nm. Before processing, the two basic powders, which subsequently served for reinforcement and matrix, were mixed in different weight proportions, w, (w = 2, 5, 10, 15, and 20 wt. %). After the mechanical mixing, each mixture was subjected to a *mill and mix* (M&M) procedure (see Chs II-1 and II-6) in a planetary, agate ball mill for 10 min, at rotating speed - 500 rpm, room temperature, and under inert gas atmosphere (Ar). (Ball weight to powder weight ratio (BPR) used was 0.4225; the total weight of the balls was 67.6 g while the weight of the

powders mixture was 160 g, per M&M cycle.) As explained in the preceding chapter, the purpose of the M&M procedure was to prevent the size-liquation (respectively, the accompanying agglomeration) of the reinforcement, by embedding the reinforcement particles onto the incentive powder surface. Thus ensuring: (i) easy handling of the as-produced green powder during subsequent processing and (ii) a homogeneous distribution of the reinforcement throughout the processed samples.

7.2 Processing of the green powders

The green powders, prepared as it was described in the preceding section, were compacted into bars at different compacting pressures by cold isostatic pressing. The as-compacted bars were hot extruded at temperatures varying between 0.8-0.85 of the aluminum melting temperature. A RUE 250 SS hydraulic press, equipped with a mold heater and with variable molds which allows a different degree of diameter reduction of the final product, the extrudate was used for that purpose. The extrusion ratio used for all extrudates was 6:1. The hold time of the extrudates in the mold was up to 20 minutes, which ensured: (i) fast equalization of the temperature through the mold-extrudates assembly; (ii) effective degassing of the pre-pressings. The as-produced extrudates were in the form of rods with a diameter of 12 mm. The friction between the mold and the extrudates was reduced by applying a high-pressure lubricant, “Vapor”. The aimed high-quality product, possessing high density, small-grained structure (achieved by avoiding the grain growth during the extrusion), good plasticity, high strength, and free of reinforcements' agglomerates, was insured by an optimization of the production process; the processing parameters were varied until the best possible mechanical parameters of the extrudates were obtained. The optimal combination of mechanical properties was achieved at: (i) Cold compaction at 600 MPa with a hold time under load 1 min and (ii) Hot extrusion at 470 ± 10 °C for 10 minutes and subsequent cooling in air.

7.3 Experimental methods

The tensile stress tests were carried out on a Zwick-Roell (Z100) testing machine in an ISO-certified lab, which specializes in mechanical testing of aluminum-based materials. The tensile test specimens (one of these is shown in Fig. II-2-8, Ch. II-2) were prepared from the extruded rods, which were cut in pieces at approximately 70 mm in length. The final

shape of the test specimens, according to the prescriptions of the ISO standard used, (total length 60 mm, sample length 30 mm, diameter 6 mm) was done mechanically, by lathing of the extruded rods. The tests were carried out at room temperature, as prescribed by the standard EN ISO 6298-1 Method B, with test parameters: Speed/yield point, 20 MPa s^{-1}, preload 5 MPa, and a test speed of 0.0067 s^{-1}. The current strain, ε (t), was determined by a laser extensometer.

The microstructure of the AMCs was studied by scanning electron microscopy (SEM/FIB LYRAI XMU, TESCAN) equipped with an EDX detector (Quantax 200, Brücker) and transmission electron microscopy (TEM/ JEOL-JEM 1011, 100 kV).

(i) *Preparation of the samples for the Mechanical tests.* The samples for the stress-strain (σ-ε) tests were prepared, as described above, from rods with different weight fractions of the reinforcement particles, TiCN (a test piece of those used in this case study is shown in Fig. II-2-8). Four samples from each of the weight fractions were prepared. Three of these were intended for the tensile tests (standard EN ISO 6892-1). The ones left were kept for reference purposes.

(ii) *Preparation of the metallography samples.* The SEM and the TEM specimens were prepared from the samples' pieces left after the tensile tests as well as from the reference samples. The specimens, made from the tensile test samples, were cut (ISOMET 1000, Bühler diamond disc saw) close to the yield site perpendicularly to the loading direction, while those made from the reference samples were cut perpendicularly to the direction of the extrusion.

The SEM specimens were prepared using conventional grinding and polishing techniques; wet grounding (grinding paper No. 3000), mechanical polishing with diamond paste, and etching, at room temperature, with 0.5 % water solution of Hydrofluoric acid.

The TEM specimens were prepared from plates from the specimens which were tensile tested and from those left for a reference. The plates, with thickness ~700 μm, were sliced perpendicularly to the direction of the tensile load. These were then mechanically thinned by grinding to foils of 20-30 μm (grinding paper, F2000) and polished with diamond paste (Struers DP P-1 μm paste). From the foils thus prepared, disks with a diameter of ~3 mm were formed, each of which was subsequently electropolished at room temperature in a solution of 20% $HClO_4$ and 80 % CH_3COOH (Struers Tenupol Electropolisher operating at 15 V) to the desired thickness.

7.4 Results from the tests

7.4.1 Results from the tensile tests

The obtained from the mechanical tests of the studied composites results, the yield, and the ultimate tensile strength, are summarized in Table 1.

As expected, the experimental data for $\sigma_{Y0.2\%}$ and σ_{UTS}, depends on the VF of the reinforcement, *f*, thus, correlating with the results of the authors, who studied the aluminum matrix composites (AMC) with nano-sized reinforcements before us; initially, the composite' yield strength increases with the increasing of the reinforcement's VF, after, $f \sim 0.05$ - 0.06 (~10 wt. % TiCN), however, the trend changes and it decreases to values slightly above those of the Al-matrix. The obtained results, therefore, clearly show that the addition of nano-sized TiCN particles into the pure Al-matrix results in a substantial increase of $\sigma_{Y0.2\%}$ and σ_{UTS}, compared to that of the matrix. For instance, the increase of $\sigma_{Y0.2\%}$ at w = 5-10 wt. % TiCN is up to 57 %, see Table 1.

Table II-7-1. Values of $\sigma_{Y0.2\%}$ (the yield strength), σ_{UTS} (the ultimate yield strength), and the elongation at break of the studied specimens measured at the mechanical tests: *w* - weight fraction of TiCN in wt. %; *f* - volume fraction of TiCN.

w wt. %	*f*	$\sigma_{Y0.2\%}$ [MPa]			σ_{UTS} [MPa]			Elongation at break [%]		
		Min.	Median	Max.	Min.	Median	Max.	Min.	Median	Max.
0	0	74	74	74	96	96	96	14	17	18
2	0.0121	96	105	107	148	149	150	19	22	24
5	0.0306	110	113	116	145	153	154	11	14	15
10	0.0625	106	113	114	142	142	146	10	11	15
15	0.0957	103	104	105	122	127	128	6.5	7.5	8
20	0.1304	97	98	failed	113	114	failed	6.5	7	failed

The notations; Min., Median, and Max., refer to the minimal, median, and the maximal value of the property measured.

Notice, that the measured by us 0.2% yield strength for the pure Al, $\sigma_{Y0.2\%}$ (see Ch. II-2), is higher than the values provided in most of the materials' handbooks e.g., [1], where this value, for pure polycrystalline aluminum, is given to be ~60 MPa. This difference of ~14 MPa is not fortuitous. Its origin is explained later in this chapter of the book.

7.4.2 Microstructure analysis, SEM

Fig. II-7-1 shows an SEM micrograph of one of the reference specimens, weight fraction of the reinforcement, w = 10 wt. % TiCN. The microstructure of the specimen consists of a matrix phase, fcc-Al, negligible quantity of the $FeAl_3$ precipitates, and TiCN particles with different sizes, seen on the figure as small spheres. Notice the homogeneous distribution of the reinforcement particles throughout the specimen and the absence of agglomerates, which result is attributed to the M&M procedure applied. The micro-grooves observed in the figure were formed when some of the reinforcing particles were dragged by the abrasive particles of the grinding paper. This is an important result showing that the lattices of Al and TiCN are partially or fully incoherent. Thence, it could be speculated that the adhesive force between TiCN particles and the Al matrix is not strong enough to resist the shear force generated by the friction. The analysis of the experimental data carried out in Chapter 7.4, however, proved the preceding conclusion incorrect.

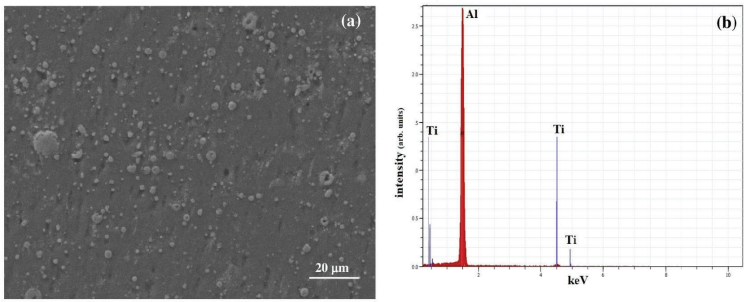

Figure II-7-1 (Fig. II-7-1a) SEM micrograph taken from a reference specimen (w = 10 wt. %). (Fig. II-7-1b) EDX-scan of the same specimen. No peaks associated with the iron were detected. (Both figures are supplied by R. Lazarova) The presence of larger particles, larger than the size specified in the previous subsection is unavoidable due to the Ostwald coarsening, which in this case occurs because of the differences in the particles' sizes (larger particles grow with time at the expense of the smaller ones with which these are in contact). Regrettably, even in vacuumed containers, the process cannot be avoided.

The presence of iron in the basic Al powder requires evaluating the influence of the $FeAl_3$ – precipitates on the mechanical properties of the composite. The first step is to confirm or reject, the presence of the $FeAl_3$ in the specimens. For that purpose, an elemental (SEM-EDS) analysis of the reference specimens was carried out. The results for the Al + 5 wt.% TiCN reference sample, are shown in Fig. II-7-1b. Two elements were detected; aluminum and titanium (in the figure the Al-peaks are colored in red, those of the Ti are in blue). The Fe peaks, if any, should have been located at, L_α - 0.705 keV and K_α - 6.398 keV. As seen no peaks associated with the iron are detectable. Concurrently, the volume fraction of the $FeAl_3$ [1] in the specimens, f_{FeAl3} was also estimated. The result is:

$$f_{FeAl3} = \frac{w_{FeAl3}}{\frac{\rho_{FeAl3}(100 - w_{FeAl3})}{\rho_{Al}} + w_{FeAl3}}, \quad (1)$$

where w is the weight fraction (in weight %) and ρ is the density of the Al and $FeAl_3$ constituents. Taking into account that $w_{FeAl3} = \frac{137}{56} w_{Fe}$ and that w_{Fe} is less than 1% (as given by the producer), for f_{FeAl3} is obtained, ~1.22 %. Thus, the cumulative area occupied by the $FeAl_3$ phase in Fig. II-7-1a should be ~1.22 % [2]. Since $FeAl_3$ was not detected by the EDS it could thus be concluded that it is probably in the form of ultra-fine precipitates. In the "precipitation strengthening" section of Ch. II-4 was shown that the strengthening effect generated by a precipitated phase depends on the precipitates' radii and their volume fraction. Recall that for the precipitates, which radius is less than a certain critical value $\langle r_p \rangle_{crit}$, the strengthening effect increases with the increase of the precipitate's radii as:

$$\Delta\sigma_Y = C_t \left(\frac{f \langle r_p \rangle}{b} \right)^{1/2}, \quad (2)$$

[1] Some recent studies carried out mainly by researchers of the CALPHAD group argue that the actual chemical formula of the $FeAl_3$ phase is Fe_4Al_{13}. Yet, in many handbooks, even the latest ones [3], that phase is still referred to as $FeAl_3$.

while for precipitates, which radii exceed $\left\langle r_p \right\rangle_{crit}$, the strengthening effect decreases with the precipitate's radii as:

$$\Delta\sigma_Y \cong \frac{C_l}{\left\langle r_p \right\rangle} \frac{1}{f^{-1/2} - 1} \quad \text{(see Eq. 3 in the preceding chapter).} \qquad (3)$$

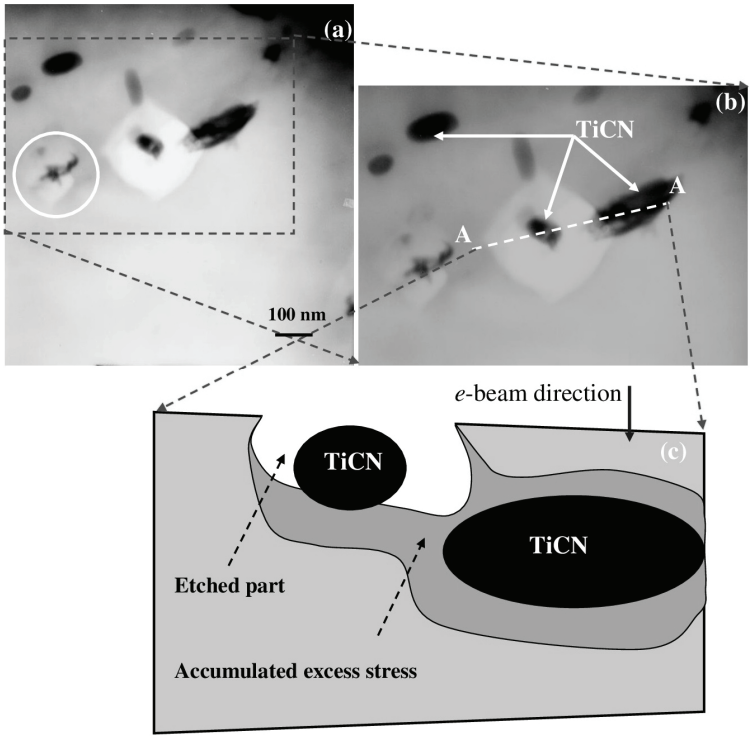

Figure II-7-2 A TEM micrograph showing embedded in the Al-matrix particles of the reinforcement. The bright halos around the reinforcement particles, the one in the center of Fig. II-7-2b and the one in Fig. II-7-2a, encircled in white, are due to deeper penetration of the etching agent in the Al-matrix during the electropolishing of the foil. The sketch in Fig. II-7-2c shows a cutoff of the foil along the A-A (the broken line) and is intended to illustrate the origin of the halos seen in the micrograph [4].

Here, in C_t and C_l, we grouped these parameters relevant to the physical properties of the precipitate and the matrix that do not contribute directly to the mechanical properties of the composite, i.e., those which are independent on $\langle r_p \rangle$ and f. By taking into account that the precipitates' sizes are less than the SEM resolution, i.e., r<20-50 nm, it follows that in the case studied should be operative Eq. 2. By substituting in Eq. 2 the estimated value for f_{FeAl3}, f_{FeAl3}~1.22 %, it follows that the contribution of the $FeAl_3$ precipitates to the composite strengthening should be insignificant.

7.4.3 Microstructure analysis, TEM

All TEM studies of the specimens were carried out in bright field mode (BF-mode, see Section 3.9.2 in Ch. II-3). During the TEM sessions, the samples were equally positioned (e-beam, perpendicular to the foil's plane). Fig. II-7-2 and 3 show TEM-micrographs obtained from samples that have undergone a tensile load (w = 10 wt.% TiCN; f = 0.0625).

In Fig. II-7-2 are seen several particles of the TiCN reinforcement embedded in the Al-matrix. Two of those, the one in the center of Fig. II-7-2b and the one in Fig. II-7-2a, circled in white, are of special interest because of the bright halos surrounding them. The presence of a halo suggests that the Al-matrix around the reinforcement particles is much easily etched. Bearing in mind, that the etching depth depends implicitly on the free energy of the etched material [5], it could be concluded that in the vicinity of the reinforcement particles the free energy of the Al-matrix is significantly higher, compared to those parts located at a distance from the reinforcement. In the case here, the matrix consists of pure Al. Therefore, the only reason for the differences observed should be the tensile loading, which has led to an accumulation of excess stress near the reinforcement particles. The absence of a halo around the remaining particles is explained by the inaccessibility of the etching agent to their stress zones, as illustrated in Fig. II-7-2c.

The micrograph in Fig. II-7-3a shows a net of cracks in the Al-matrix formed between some of the reinforcement particles; the cracks are seen as broken whitish lines. One notes the similarity between the microstructures shown in Fig. II-7-3a and Fig. II-7-2; in both figures around the reinforcement-particles are seen bright halos. The value of Fig. II-7-3a, however, is that it shows wherefrom the cracks originate, namely, from the overstressed regions of the matrix. Fig. II-7-3b shows a TiCN particle, with a diameter of 45-50 nm, surrounded by a tangle of dislocations (in

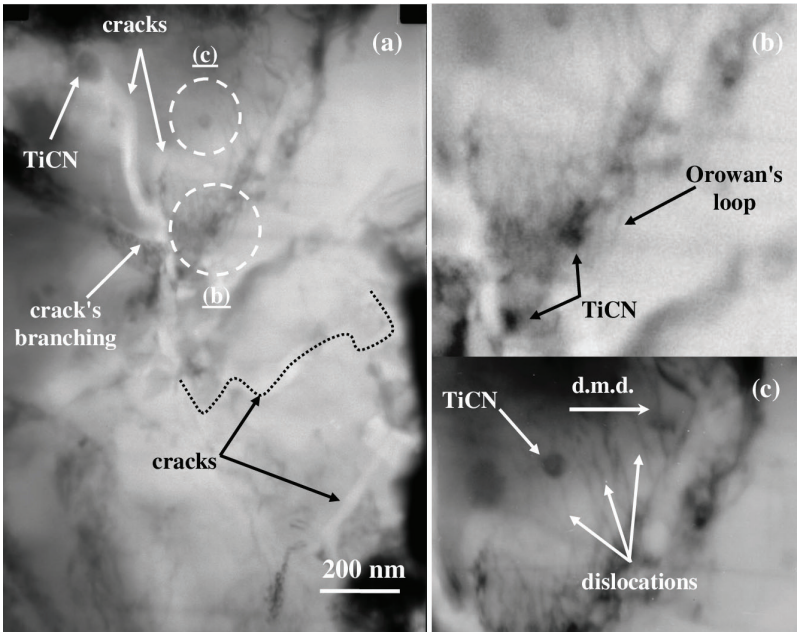

Figure II-7-3 A TEM micrograph showing cracks formed in the Al-matrix. It is readily noticed that the cracks start and branch in the vicinity of the reinforcement particles. The dotted black line (Fig. II-7-3a) follows one of those cracks along its length. The enlargements on the right side of Fig. II-7-3a show: (Fig. II-7-3b) an Orowan's loop with a TiCN particle at the center; (Fig. II-7-3c) series of linear dislocations, one of which at the moment of cutting through a TiCN particle (indicated with an arrow). The arrow (top center of Fig. II-7-3c) indicates the tentative movement direction of the dislocations that originated during the tensile loading of the specimen (d.m.d. stays for dislocations movement direction). The circles (in broken lines) indicate the locations of the enlargements shown in Fig. II-7-3b and II-7-3c.

Fig. II-7-3a the location of that particle is marked with a broken line circle). It can be presumed that the dislocations of the entanglement have been generated during the tensile loading of the specimen and subsequently have been entrapped around the particle. A dislocation loop (Orowan's loop), formed outside the tangle, is also readily detected. In Fig. II-7-3c is shown a smaller TiCN particle, 25-30 nm in diameter (In Fig. II-7-3a its

location is just above the particle shown in Fig. II-7-3b). In this case, however, the dislocations behaved differently. Instead of tangling, or bowing, around that particle, the dislocations did cut through it. The process is illustrated in Fig. II-7-3c, where one of the dislocations is captured at the moment of shearing through the particle. From the minute disruptions, seen on the dislocation lines at the right side of the particle in Fig. II-7-3c, it could be figured out that the dislocations' movement direction (d.m.d.) is from left to right (as indicated by the arrow).

The dislocation behavior, as observed in Fig. II-7-3c, is in good agreement with the theory of precipitate strengthening (see Section 4.2 in Ch. II-4). Recall that an obstacle (precipitate or reinforcement particle) is overcome from the dislocation by two different mechanisms. Which of these mechanisms would be operative depends on the size of the obstacle. In the case when the obstacle size is below some critical value $\langle r_p \rangle_{crit}$ (critical radius), the dislocation shears through the obstacle, while when the obstacle size is above that critical radius, the dislocation overcomes the obstacle by forming a dislocation loop around it (Orowan, Section 4.5, Ch. II-4). In the TEM-micrographs (Fig. II-7-3b and 3c of the paper) we noticed that both mechanisms are present; in Fig. II-7-3b (bowing) and in Fig. II-7-3c (shearing). Thus, from the micrographs shown, it could be deduced that the critical radius of the TiCN particles, embedded in the Al-matrix, is between 30 and 50 nm. $\langle r_p \rangle_{crit}$ could be readily evaluated by substituting in Eq. 18a (Ch. II-4) L_s with its equal, $L_s \cong \left(\frac{2\pi}{3f}\right)^{1/2} \langle r_p \rangle$ and equating the obtained result with tangential stress valid for low $|\eta_{ord}|$ at the late stage of precipitation (see third eqn. in Subsection (iv) in Section 4.3, Ch.II-4, p. 216, see also [6]). The result obtained is:

$$\langle r_p \rangle_{crit} = \frac{\alpha E b^2}{(8\pi/3)^{1/2}(1+\nu)U_{APBE}}. \qquad (4)$$

Here: α is a constant ($\alpha \sim 1$). Recall that the antiphase boundary energy U_{APBE} (Jm^{-2}) varies depending on the degree of the coherence between the lattices of the reinforcement and the matrix being; U_{APBE} = 0.1 Jm^{-2}, for fully coherent lattices and U_{APBE} = 1 Jm^{-2} for non-coherent. Replacing in Eq. 4 E = 398 GPa [5], ν = 0.23 [7], b = 2.5 Å, and assuming semi-

coherence between the Al - TiCN lattices, U_{APBE} = 0.5 Jm^{-2}, for the critical radius is obtained, $\left\langle r_p \right\rangle_{crit}$ ~14 nm, or a critical diameter of ~28 nm. The so evaluated critical diameter matches fairly well with that determined from the micrographs. From this, it can be concluded that the lattices of the Al matrix and that of the TiCN are semi-coherent, in contradiction to the conclusion made at the analysis of Fig. II-7-1.

Due to the specificity of the foils examined (Recall that these are made of specimens that have undergone tensile loading.), the preparation of quality TEM foils and their study was accompanied by problems, of which one should be aware. Some of these are listed below:

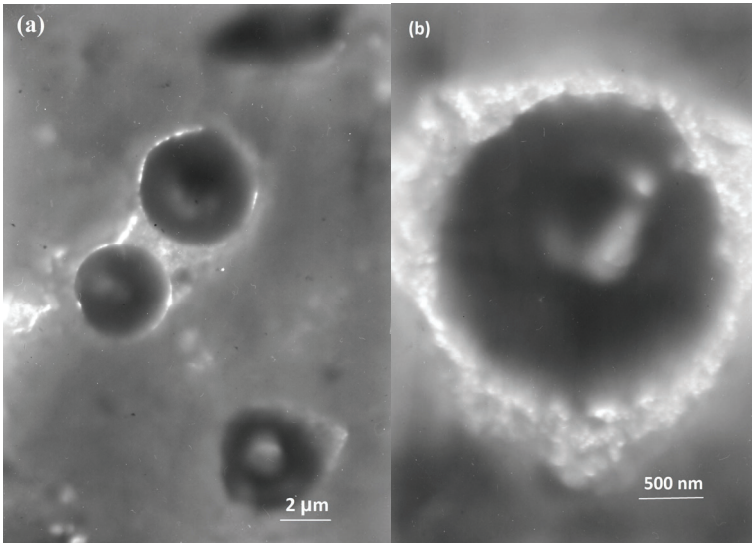

Figure II-7-4 (Fig. II-7-4a) a TEM micrograph of a composite (w = 10 wt. % TiCN) after a tensile test. Notice the differences in the Al-matrix microstructure between the two particles (center) and the particle (bottom-right). The bright region, between the two particles, is due to the accumulated stress in the matrix. (Fig. II-7-4b) a TEM micrograph of the microstructure around a single TiCN particle in a composite (w = 10 wt. % TiCN) after tensile loading. Notice the difference in the Al-matrix microstructure surrounding the particles. V. Dyakova [8]

(i) The tensile loading of the composite leads to a considerable overstressing of the Al-matrix near the reinforcement particles, thus, resulting in an uneven distribution of the plastic deformation throughout the sample. At electropolishing these parts of the Al-matrix are etched deeper, Fig. II-7-4 (see also [5]), thus, forming around reinforcement a mushy zone of voids and remnants of the Al-matrix. In some cases, the voids could penetrate the whole thickness of the foil (Fig. II-7-4b). As a result, the adhesion forces, keeping the particles and the matrix together, are not strong enough which leads to the separation of some of the particles from the foil. Because of that, the TEM analysis should be carried out on the thicker parts of the film. As a result, the obtained images are without sufficient contrast, e.g., Fig. II-7-3b and Fig. II-7-3c and it takes several TEM hours while a sufficiently good image of the desired part of the sample is obtained.

(ii) A serious problem, usually encountered when working at low magnifications, is the *e*-beam diffraction (the Fraunhofer diffraction [9], which occurs when the electrons are transmitted through the mushy zone formed around the reinforcement. (Recall that due to the accumulated around the reinforcement stress the Al-matrix is etched easier and much deeper.) In this case, the diffracted *e*-beam is imaged on the TEM micrograph as a bright halo around the mushy zone, and the reinforcement particles' edges, which is well seen in Fig. II-7-4b. Regrettably, this unwanted "optical" effect is unavoidable. Yet, when working with higher magnifications this unwanted effect is damped [9] and the quality of the micrographs return to their normal.

(iii) Another issue is the plastic deformation induced in the sample during the preparation of the foil. However, these could be readily avoided keeping in mind that the depth of the damage produced inside the specimen during mechanical thinning is three times the grit size of the abrasive used [10]. Hence, using fine grinding paper at the mechanical thinning of the sample would eliminate the risk of inducing unwanted mechanical deformations in the TEM-foil.

(iv) The differences in the corrosion resistance of the matrix and the reinforcement could also lead to a problem, e.g., the protruding of the reinforcement above the matrix, or vice versa. The quality of the image, in this case, will be unaffected only if the protrusions are within the depth field of the microscope [10], which for a TEM are within 0.1 μm. Otherwise, the defocused parts of the foil will be blurred, hence, with low contrast.

Therefore, one should be aware of the problems above that could arise when studying composites with nano-sized reinforcement by TEM. In the

present case study two of the problems, those listed above as, (i) and (ii) were frequently encountered by us.

The micrographs shown in Fig. II-7-2 to II-7-4, allow drawing the following conclusions: (i) At tensile loading, the stress accumulated in the Al-matrix near the reinforcement particles, correlates with the VF of the reinforcement. That is readily seen in Fig. II-7-4a; notice the brighter field between the two particles (the center of the micrograph). As above, this is a result of the deeper penetration of the etchant into the foil, which of its turn, is due to the accumulated stress in the matrix. In contrast, the matrix around the particle at the bottom of the same figure, which is at a considerable distance from the two at the center, is not etched to a penetration. From these experimental facts, it could be readily concluded that; when the reinforcement particles are close to each other, which is the case at higher VF of the reinforcement, the accumulated stresses between them are much higher, whereas, when these are sufficiently separated from each other, i.e. at lower VF, the accumulated stresses in the matrix around them is much lower. (ii) The stress field in the Al-matrix matches the geometry of the reinforcement particles (as can be seen in Fig. II-7-2). Notice that the sharp edges of the reinforcement particle, seen at the center of that micrograph, have had produced a wider stress field. This is attributed to the stress concentration generated around the sharper edges of that particle, thus, confirming the conclusions drawn in Section 6.3 of the preceding chapter. (iii) The intensity of the stress field formed around the reinforcement particles during tensile loading gradually increases and reaches its maximum at the reinforcement-matrix boundary (Fig. II-7-4b). A result predicted by the theory of elasticity; $\sigma \approx \left(\left\langle r_p \right\rangle / r \right)^3$ (Remember that r is the distance from the reinforcement particle center) (iv) The reinforcement particles with a size of ~ 40 nm and larger serve as impenetrable (non-deformable) obstacles to the free migration of the generated during the tensile loading dislocations, while those under 20-30 nm in diameter are sheared by the moving dislocations, thus supporting the predictions of the theories discussed in Sections 4.3 and 4.6 in Ch. II-4.

7.5 The strengthening mechanisms operative in this case study

Some of the strengthening mechanisms, explaining the strengthening in composites reinforced by structurally incoherent with the matrix reinforcement additives, were already discussed in Ch. II-4. However, only a few of these, listed in Ch. II-4 could be considered as operative in

the present case study: (i) thermal mismatch effect (TME) strengthening, (ii) the precipitation strengthening due to the formation of $FeAl_3$, (iii) the grain boundary strengthening, or the Hall-Petch effect, and (iv) the Orowan strengthening.

(i) *The thermal mismatch effect* (TME). The arguments presented and the conclusions drawn in Section 4.10, Ch. II-4 suffice in excluding, in the present case study, the TME from the list of possible strengthening mechanisms.

(ii) *The precipitation strengthening (formation of $FeAl_3$)*: As of above, it was proved that the VF of the $FeAl_3$ should be less than ~1.2%. Moreover, due to the high dispersion of the $FeAl_3$ precipitates, it could be readily assumed that these are easily sheared by the moving dislocations, thus having a negligible contribution, if any, to the strengthening of the composite.

(iii) *The contribution of the grain boundary strengthening (the Hall-Petch effect)*: The grain size influence on the mechanical properties was discussed in Section 4.7, Ch. II-4. Recall that the Hall-Petch strengthening mechanism is based on the presumption that the grain boundaries act as obstacles to the migration of the dislocations. Based on that presumption, HP succeeded in obtaining a functional dependence (see Eq. 32 in Section 4.7) that couples together the yield strength of the material with the grain size, showing that the former increases with the decrease of the grain size. From the preceding follows that; if the pure matrix and the matrix in the composite possess similar grain structure the contribution of the Hall-Petch effect on the yield strength could be readily eliminated by subtracting, their yield strengths.

In the present study, the tensile test samples were produced from the same Al-powder in a way to eliminate the grain coarsening, see the "Materials and Methods" section of this chapter. It could be thus concluded that the grain size distribution in the Al-matrix should match the size distribution of the basic Al powder used. Thence, if the matrices of the studied composites have the same average grain size (MGS), the contribution of the Hall-Petch effect on the yield strength of the composite can be readily eliminated by using the relative yield strength, $\Delta\sigma_{Y0.2\%}=\sigma_{Y0.2\%}(f)-\sigma_{Y0.2\%}(0)$, instead of the nominal one, $\sigma_{Y0.2\%}(f)$. (Recall that, $\sigma_{Y0.2\%\,Al} = \sigma_{Y0.2\%}(0)$; $\sigma_{Y0.2\%} = \sigma_{Y0.2\%}(f)$, where f = 0-0.1304).

At this stage of the study, two important questions should be answered: (a) what is the increase of the composite's yield strength, due to the Hall-Petch effect, and (b) is our presumption that the average grain size (MGS) in the composites with different VF of the reinforcement correct.

(a) The first of the questions above is readily answered by subtracting the yield strength found in the literature for pure Al from that measured in this study. The average value of the former is given in [1] to be about 60 MPa, while that measured by us is 74 MPa. Therefore, it could be concluded that in our case the contribution of the Hall-Petch effect to the composite' strengthening is ~14 MPa.

(b) To check, whether the equal-MGS condition is met in our study, the MGS of the pure Al and the Al+10 wt.% TiCN reference specimens were measured (R. Lazarova [4]). The measurements were performed on five visual fields by quantitative metallographic analysis. The embossed micrographs of the specimens studied are shown in Fig. II-7-5; (Fig. II-7-5a) a specimen prepared from pure Al, (Fig. II-7-5b) a specimen prepared from a composite reinforced with 10 wt.% TiCN. The measured by Lazarova MGS of the Al-matrix in the samples studied was: ϕ_{Al} = (1.925428 ± 0.569684) μm and $\phi_{Al+10\%\ TiCN}$ = (1.93358 ± 0.601238) μm, i.e., a difference less than 0.01 μm. Thence, the addition of the reinforcement did not in any way affected the Al grain size of the composite, and in the study here the contribution of the Hall-Petch effect to the yield strength could be readily eliminated by using the relative yield strengths, $\Delta\sigma_{Y0.2\%(f)}$, instead of the nominal ones, $\sigma_{Y0.2\%(f)}$.

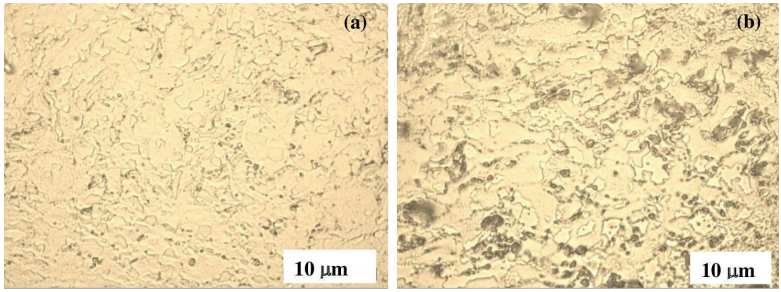

Figure II-7-5 OM micrographs showing the grain microstructure in two specimens prepared from the reference samples; (Fig. II-7-5a) pure Al and (Fig. II-7-5b) a composite reinforced with 10 wt.% TiCN (Figures 5a and 5b are provided by R. Lazarova).

By eliminating the contributions of the CTE-mismatch, the precipitation strengthening, and the Hall-Petch effect, the net increase or the decrease of $\Delta\sigma_{Y0.2\%(f)}$ with VF of the reinforcement would be, therefore, due to the only mechanism left - Orowan's strengthening mechanism.

(iv) *The Orowan strengthening*. The basics of Orowan's strengthening mechanism and the mathematical dependencies obtained were discussed in detail in Ch. II-4. In essence, this theory presumes that; when a moving dislocation encounters a non-deformable obstacle, e.g., a reinforcement particle, the dislocation bows around the obstacle and bypasses it by forming a dislocation loop around it. In the preceding chapter an equation, combining the theories of Orowan, Fisher, Hart, and Pry (FHP), Ardell and Melander, was obtained that allows accounting for the strengthening effect of nano-sized particulates embedded in a metal matrix:

$$\sigma_{str}\left(f\right)=\frac{0.84Gb\ln\left(\Lambda/r_0\right)}{2\pi\left(1-\nu\right)^{1/2}\left\langle r_p\right\rangle}\frac{1}{\left(\frac{2\pi}{3f}\right)^{1/2}-2}= \\ =\frac{0.134Gb\ln\left(\Lambda/r_0\right)}{\left(1-\nu\right)^{1/2}\left\langle r_p\right\rangle}\frac{1}{2.094f^{-1/2}-2} \tag{5}$$

.

Recall Eq. 23b from Ch. II-6 that states that $\langle r_s \rangle$ is approximately equal to the mean radii of the reinforcement, $\langle r_p \rangle$ (see the preceding chapter) and that *N* is the number of loops, left around the reinforcement particles after the dislocations did bow around them.

Remember that: (i) the strengthening increases as a result of (a) The reduction of the effective distance between the particles after the formation of every dislocation loop (not to be confused with the geometric distance between the particles). Thence, the smaller the effective distance between the particles, then the higher is the force required to push the next incoming dislocation, see Fig. II-7-4a. (b) The interaction of the incoming dislocations with the dislocation' loops already formed around the reinforcement particles, which results from the stress increase in the matrix around the reinforcement (Recall the discussion over the results shown in Fig. II-7-2 and Fig. II-7-4).

(ii) The strengthening depends not only on the volume fraction, *f* but also, on the mean radii of the reinforcement, $\langle r_p \rangle$. From Eq. 5 implicitly follows that at, $\langle r_p \rangle \to 0$, $\sigma_{str} \to \infty$, which is physically impossible ($\langle r_p \rangle = 0$, means that there is no reinforcement in the matrix). This result suggests that Eq. 5 is no longer valid below some critical value of $\langle r_p \rangle_{crit}$, i.e., the mechanism of the dislocation interaction with the reinforcement

changes from bowing to shearing of the dislocations through the reinforcement (see Section 4.2).

7.6 Testing the strengthening and strength-reduction theory: Results

In the preceding chapter, it was shown that by combining Eq.5 and the Griffiths theory of cracks formation it is possible to evaluate the increase and the decrease of the yield strength of the composite as a function of the VF of the reinforcement, its size, $\langle r_p \rangle$, and the mechanical properties of the matrix:

$$\Delta\sigma_Y(f) = \frac{0.067NEb\ln(\Lambda/r_0)}{(1+\nu)(1-\nu)^{1/2}\langle r_p\rangle}\frac{1}{2.094f^{-1/2}-2} - \frac{K_I S}{\sqrt{\pi}} f^{\frac{3}{2}} H_V(\sigma_{cr},\sigma_{sr}) \cdot \quad (6)$$

It was also argued that by plotting the results from the mechanical testing, $\Delta\sigma_Y$ vs. $\xi = \frac{\left(2.094 - 2f_{\max}^{1/2}\right)^2 f_{\max}}{0.698\left(2.094f^{-1/2}-2\right)} - f^{\frac{3}{2}}$, it could be possible to evaluate some important characteristic parameters of the mechanisms involved.

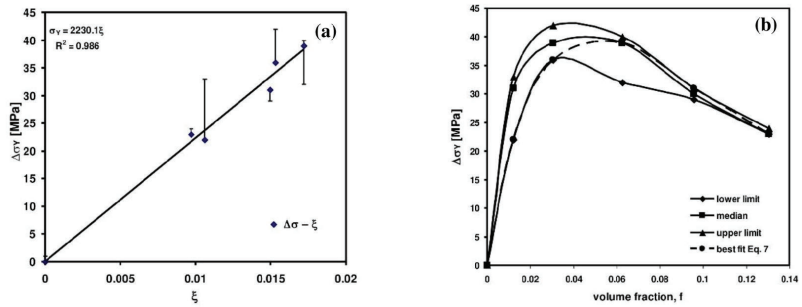

Figure II-7-6 Plots of the tensile test data listed in Table 1: (Fig. II-7-6a) the best linear fit (the solid line) of the experimental data in $\Delta\sigma_Y - \xi$ coordinates, (The error bars show the scattering of the $\Delta\sigma_{Y0.2\%}$.); (Fig. II-7- 6b) plots, in $\Delta\sigma_{Y0.2\%}$ - f_{TiCN} coordinates, of the experimental data (the solid lines) and the predicted by the Eq. 7 (the dashed line) values of $\Delta\sigma_Y(f)$ (N = 3.71 and $S \approx 0.79$ μm$^{-1/2}$).

Recall, that the evaluation of these parameters could be done in two ways: (i) Directly, by nonlinear regression. This approach, however, requires a considerable amount of experimental data points, which are not always available. (ii) Graphically by a linearization procedure as shown in Appendix II-B of the preceding chapter.

Fig. II-7-6a shows a plot of the experimental data from Table 1 in $\Delta\sigma_Y - \xi$ coordinates. The best fit of the experimental data is given by a linear equation, $\Delta\sigma_Y = 2230\,\xi$, or in the original coordinates:

$$\Delta\sigma_Y = 2230\left[\frac{\left(2.094 - 2f_{\max}^{1/2}\right)^2 f_{\max}}{0.698\left(1.84 f^{-1/2} - 2\right)} - f^{\frac{3}{2}}\right]. \qquad (7)$$

The values of, $f_{\max}$, $\frac{K_I S}{\sqrt{\pi}}$, and $\frac{0.067\,NEb\ln\left(\Lambda/r_0\right)}{\left(1+\nu\right)\left(1-\nu\right)^{1/2}\left\langle r_s\right\rangle}$, determined from plotting the experimental data listed in Table 1, are collected in Table 2. The error bars in Fig. II-7-6a indicate the scattering of the $\Delta\sigma_{Y0.2\%}$ experimental data.

In the equation above, the structure parameters *b*, Λ and r_0 could be obtained experimentally, while *E* and K_I are tabulated mechanical properties. Thence, from the experimental data listed in Table 1, two of the important parameters that govern the strength/strength-reduction in the composite studied, namely, *N* and *S* could be readily evaluated; By substituting, $K_{IAl} \approx 5$ MPa [11] in $\frac{K_I S}{\sqrt{\pi}}$ = 2230 MPa, for the parameter *S,* was obtained, $S \approx 0.79\ \mu m^{-1/2}$. After substituting, $E_{Al} = 70.6$ GPa, and $\nu = 0.345$ [1], $b_{Al} = 0.286$ nm [12], $\left\langle r_p\right\rangle \approx 25$ nm and $\ln\left(\Lambda/r_0\right) \approx 2.3$, in $\frac{0.067\,NEb\ln\left(\Lambda/r_0\right)}{\left(1+\nu\right)\left(1-\nu\right)^{1/2}\left\langle r_p\right\rangle}$ = 393 MPa, for the average number of the dislocation loops per a reinforcement particle, we found, $N = 3.71$. The last result is in agreement with the conclusions of Humphreys and Hirsch [13], and Hazzledine and Hirsch [14] who estimated that no more than four to five loops can be formed around a particle at room temperature.

Fig. II-7-6b shows the plots of $\Delta\sigma_{Y0.2\%} = \sigma_{Y0.2\%}(f) - \sigma_{Y0.2\%}(0)$, for the measured maximal, minimal, and median values of the yield stress as a function of VF (the solid lines). The dashed line shows the values

of, $\Delta\sigma_Y(f)$, predicted by Eq. 7 (calculated with the estimated in the present research N and S). The predicted by solving Eq. 7 values for $\Delta\sigma_Y(f)$ is within the scatter limits of our experimental data, as seen, in Fig. II-7-6b.

The obtained results could be accepted as proof that Eq. 6 correctly describes the dependence, $\Delta\sigma_Y(f)$. Additionally, these results proved correct the used by us: (i) Melander-Ardell version of the Orowan's equation (MAO) and (ii) the validity of the functional dependence, $\sigma_{cr} f^{\frac{3}{2}}$, proposed by FHP (for details about the MAO and FHP equations see Section 4.5 in Ch. II-4).

As already mentioned in the preceding chapter, the graphical method is very sensitive to the accuracy with which is determined, $f_{\max}$. Thus, if a sufficient number of experimental points are available, it is strongly advisable to use nonlinear regression methods for determining the parameters $f_{\max}$, N, and S. However, when the number of experimental points is limited, the graphical method is the only possible choice.

The theory developed, Eq.6, was also tested on the experimental data of Pan Ma et al. [15], H. Su et al. [16], and Khorshid et al. [17]. The results obtained are shown in Table 2 together with these obtained in the present study. The plots in $\Delta\sigma_Y - \xi$ coordinates of the experimental data of H. Su et al. and Khorshid et al. resulted in unreasonably high values for, $\frac{K_I S}{\sqrt{\pi}}$ and $\frac{0.067\, NEb \ln\left(\Lambda/r_0\right)}{\left(1+\nu\right)\left(1-\nu\right)^{1/2}\left\langle r_p \right\rangle}$, respectively, unrealistic values for, N and S. The presumed explanation of these results is the presence of agglomeration of the reinforcement reported by these authors in the samples studied by them. (For the correlation between the mechanical properties of the composite and agglomeration, refer to Section 6.2 in the preceding chapter) The plotting of the experimental data of Pan Ma et al. in the $\Delta\sigma_Y - \xi$ coordinates, however, yielded, $N\approx 8$, and $S\approx 0.45$ $\mu m^{-1/2}$, which is slightly above the limit evaluated by Humphreys, Hazzledine, and Hirsch [13, 14]. These authors also reported agglomeration of the reinforcement, but in their case, it was confined in the specimens with a weight fraction of the reinforcement above 10 wt. % (see the preceding chapter about the possible sources of agglomeration in composites). Because of their case, the agglomeration did not affect all of the specimens studied, the obtained values for N and S, are quite satisfactory.

Table II-7-2 A list of the values for, $\frac{0.067\,NEb\ln(\Lambda/r_0)}{(1+\nu)(1-\nu)^{1/2}\langle r_s\rangle}$, $\frac{K_I S}{\sqrt{\pi}}$ (denoted in the Table for the sake of brevity as *B* and *C*, respectively), *N*, *S*, and $f_{\max}$, obtained from the experimental data of different authors.

Matrix	Reinforcement used	*B* [MPa]	*C* [MPa]	*N*	*S* [$\mu m^{-1/2}$]	f_{max}	R^2	Reference
Al	Al_2O_3	2392	62123	26	25.0	0.008	0.986	H. Su et al. [16]
Al	Al_2O_3	4189	40450	42	1.58	0.027	0.989	Khorshid et al. [17]
Al-12Si	Al_2O_3	758	6600	8	0.45	0.032	0.94	P. Ma et al. [15]
Al	TiCN	393	2230	4	0.79	0.059	0.986	This case study [4]

7.7 Summary of the results obtained from the case study

The results obtained could be summarized as follows:

(1) The technological procedure M&M applied at the initial stages of the MMC's production, allows: (i) avoiding both weight and size liquation of the reinforcement during the preliminary stages of the composite production, (ii) subsequent easy handling of the as-prepared green powder mixture Al-TiCN and (iii) production of composites with a relatively homogeneous distribution of the reinforcement particles in the matrix, see Fig. II-7-1.

(2) From the analysis carried in the preceding chapter and the data obtained in this study, it looks like that the combination, M&M procedure with hot-extrusion, excels over the methods used so far for the production of composites reinforced with nano-sized particulates.

(3) The present study showed that the increase of the yield strength of the composite is due mainly to two of the strengthening mechanisms considered; the Hall-Petch grain size effect and the Orowan's strengthening mechanism. The contribution to the yield strength of these two strengthening mechanisms, however, is not on an equal basis. The Hall-Petch effect adds to the strengthening effect ~10-14 MPa, while the Orowan's strengthening mechanism contributed above ~45 MPa, i.e., approximately three to four times that of the Hall-Petch grain size effect.

(4) The hypothesis that the strengthening effect is due to two mechanisms acting in opposite directions proved correct. By combining a group of mechanisms acting toward the strengthening of the composite with a mechanism leading to a reduction of the strength it was possible to obtain a relation, Eq. 6, that allows a description, in mathematical terms,

of the combined action of the strengthening and the strength–reduction processes. It was confirmed that the strength-reduction is governed by two processes; (i) stress accumulation around the reinforcement particles until the strength limit of the matrix is exceeded, (ii) relieving of the accumulated stress by the formation of micro-, or nano-, cracks in the matrix, see Fig. II-7-3a, and Fig. II-7-4a and II-7-4b. Thence it could be argued that the yield strength of a composite is readily described by Eq. 6 which combines, (a) Orowan's strengthening model (as modified by FHP, Melander, and Ardell (Ch. II-4), and (b) the crack formation mechanism in brittle materials proposed by Griffiths (Ch. II-2).

(5) The results obtained confirm that the reinforcing effect depends on the size of the reinforcement, as predicted by the theory of precipitation strengthening (Ch. II-4).

References to Ch. II-7

1. E. A. Brandes and G. B. Brook (eds.), Smithells Metals Reference Book, 7th ed., Butterworth-Heinemann, Oxford, 1999.
2. W. Rostoker and J. R. Dvorak, Interpretation of metallographic structures, Academic Press, New York - London, 1965, ch. 5.
3. Encyclopedia of Al and its alloys, Edited by G. E. Totten, M Tiryakioglu, O. Kessler, CRC Press (Taylor and Francis group) vol.1 2019.
4. L. Anestiev, R. Lazarova, P. Petrov, V. Dyakova, L. Stanev, On the strengthening and the strength reducing mechanisms at aluminum matrix composites reinforced with nano-sized TiCN particulates, Philosophical Magazine, 101:2, 129-153 (2021), DOI: 10.1080/14786435.2020.1821114.
5. N. Perez, Electrochemistry and Corrosion Science, 2nd ed., Springer International Publishing, Switzerland 2016, ch. 1.4 Galvanic Corrosion.
6. P. Haasen, Mechanical properties of solid solutions, in Physical metallurgy 4th ed., vol. 3, R. W. Cahn and P. Haasen eds., North-Holland, Amsterdam, 1996, ch.23.
7. Y. Sun, Ch. Lu, H. Yu et all, Nanomechanical properties of TiCN and TiCN/Ti coatings on Ti prepared by Filtered Arc Deposition, Materials Science and Engineering A 625, 56–64 (2015).
8. V. Dyakova, private communication (2018).
9. M. Born and E. Wolf, Principles of Optics, 6th ed., Pergamon Press, 1980, ch. 8.5 Fraunhofer diffraction at apertures of various

forms; ch. A.II.4 The application of optical principles to electron optics.
10. D. B. Williams and C. B. Carter, Transmission Electron Microscopy: A Textbook for Materials Science, 2nd ed., Springer Science-Business Media, LLC, 2009, Ch. 10.3. A Forming a Thin Slice from the Bulk Sample.
11. Sh. Chou, J. Huang, D. Lii, H. Lu, The mechanical properties and microstructure of Al_2O_3/aluminum alloy composites fabricated by squeeze casting, Journal of Alloys and Compounds 436, pp. 124 - 130 (2007).
12. K. Kallip, L. Kollo, M. Leparoux, and C. M. Bradbury, Nanoparticulate reinforced aluminum alloy composites produced by powder metallurgy route, Advanced Composites for Aerospace, Marine and Land Applications II, pp. 165–174 (2015).
13. J. Humphreys and P. B. Hirsch, The deformation of single crystals of copper and copper-zinc alloys containing alumina particles II. Microstructure and dislocation-particle interactions, Proceedings of the Royal Society (London) A. 318, pp. 73-92 (1970).
14. P. M. Hazzledine and P. B. Hirsch, A Coplanar Orowan Loops Model for Dispersion Hardening, Philosophical Magazine 30, pp. 1331-1351 (1974).
15. P. Ma, Y. Jia, P. K. Gokuldoss, Zh. Yu, S. Yang, J. Zhao, and Ch. Li, Effect of Al_2O_3nanoparticles as reinforcement on the tensile behavior of Al-12Si composites, Metals 7, pp. 359-370 (2017).
16. H. Su, W. Gao, Zh. Feng and Zh. Lu, Processing, microstructure and tensile properties of nano-sized Al_2O_3particle reinforced aluminum matrix composites, Materials and Design 36, pp. 590–596 (2012).
17. M. T. Khorshid, S.A. J. Jahromi and M. M. Moshksar, Mechanical properties of tri-modal Al matrix composites reinforced by nano- and submicron-sized Al_2O_3 particulates developed by wet attrition milling and hot extrusion Materials and Design 31, pp. 3880–3884 (2010).